

DEPARTAMENTO DE ASTROFISICA

Universidad de La Laguna

Interaction between Massive Stars and the Interstellar Medium in Galactic H II regions

Thesis submitted by
Sergio Simón Díaz
as a requirement for the degree of
Doctor of Physical Science.



INSTITUTO DE ASTROFISICA DE CANARIAS
December 2005

Examination date: December 19th, 2005

Thesis supervisors: Prof. Artemio Herrero Davó & Dr. César Esteban López

© Sergio Simón Díaz 2005

ISBN: 84-689-6245-7

Depósito legal: TF-27/2006

Some of the material included in this document have been already published in
Astronomy & Astrophysics.

*A mis padres y hermanos,
a Irene.*

*Con la Música,
con la Danza.*

”Yo tengo una teoría. El exceso de conocimiento desequilibra la mente. Se hace un esfuerzo tan grande para adquirir conocimientos que no queda espacio para el sentido común”

— Iain Pears — La cuarta verdad

AGRADECIMIENTOS

La memoria es frágil y el transcurso de una vida es breve y sucede todo tan deprisa, que no alcanzamos a ver la relación entre acontecimientos, no podemos medir la consecuencia de los actos, creemos en la ficción del tiempo, en el presente, el pasado y el futuro, pero puede ser también que todo ocurra simultáneamente.

La casa de los espíritus – Isabel Allende –

Eran las dos de la tarde. En la Higuera un calufo que te cambas, y había que subir al IAC a escuchar una charla más. ¡Chiquita pereza! Pero subí ...

Gracias a Artemio Herrero por haberme engatusado aquel día con las Estrellas Masivas Azules. Pones esto aquí, miras que sale por allá, y finalmente comparas con lo de más acullá. ¡Chos!, parecía fácil, pero han sido 5 años. Gracias a César Esteban, por compartir la aventura. Espero poder unificar vuestras enseñanzas en un sólo camino. Gracias por acogerme y abrirme las puertas a la comunidad de astrofísicos estelares y nebulares.

Gracias a Danny Lennon por ofrecerme trabajo en La Palma mientras terminaba la tesis. Curioso eso de aprender inglés en La Palma ... Danny, gracias por escuchar mis ideas y mostrarme otra forma de investigar.

Gracias a toda la gente del IAC a los que en algún momento he pedido ayuda. También a los que no. A Fernando Moreno, por su papel de portavoz en el verano de 2000 (nunca terminé aquel puzzle). A Nieves y Lourdes. A Eva, Tanja y Judith. A Isa, Elito y Joaquín. A Rosi y Jose. Gracias a Chris Evans y la gente del ING, en especial a Robert Greimel, Romano Corradi, Sam Rix, Pierre Leisy y Mischa Schirmer.

Un agradecimiento muy especial a aquellos que de alguna manera u otra han colaborado con el desarrollo de la tesis. Gracias a Héctor Castañeda, por haber sido arbitro interno de la tesis. A Mónica Rodríguez; espero haber hecho buen uso de tus datos. A Paco Najarro; mucho se ha discutido y todavía queda mucho por discutir. A Christophe Morisset, por los modelos CLOUDY-3D y acercarse a Tenerife a enseñarnos cómo se usa el código. A Robert Ryans y Philip Dufton, por los modelos TLUSTY. A Jorge García Rojas y Ángel R. López Sánchez, por ser mis apoyos nebulares. A Alfred Rosemberg, Luis Corral y Ángel de Vicente. A Miriam García, por los modelos WM-*basic*. A Joaquim Puls, por compartir sus conocimientos sobre el modelado de las atmósferas estelares. A Charo Villamariz, por tantas charlas sobre tantas cosas. Y un "gracias" más grande si cabe para Miguel A. Urbaneja y Carrie Trundle.

Muchas gracias a Grażyna Stasińska por haberme acogido durante unas semanas en Meudon. Trabajar contigo es un placer. A Luc Jamet.

A Roi. A Judith por aquel primer café. A Carmen y sus clases de danza. A Cristina Campos por llevarme y mostrarme que con el tiempo a mi también me saldrá bonito. A Mecano, por volver (aunque sea como fantasmas del pasado) y hacerme un poco más amenos esos ratitos en La Palma. A Jose Caballero, Rakel Oreiro, Jorge Quintero, Jesús y Nieves, Paca y Álex.

A Miguel M., Fer, Marta S., Jose, Irune, Miguel G., Stephanie, Juanjo, Cheky y Ana, Marta F., Mar, Mila y Prado, lo único en Madrid que Gallardón no ha podido poner patas arriba. Por demostrarme una y otra vez que las cosas buenas nunca acaban. ¿Podeis hacer que vuelva a ser normal? ¡Seguro que sí!

A mi padre. Gracias por demostrarme que nunca es tarde para tomar decisiones importantes en la vida y perseguir un sueño. ¡Ánimo!, quizá algún día caminemos juntos por Montmartre mientras nos contamos cómo nos va. A mi madre. Escribir una tesis es un trabajo arduo, pero lo que tú has hecho durante este tiempo lo es mucho más. ¡Enhorabuena!, el resto está dentro de tí. A Carlos. ¡Te encontré! A Pili, la mejor hermana pequeña del mundo.

Irene, esto ya casi está. Y dentro de muy poquito tú. Sólo de pensar en lo que nos espera después me hacen los ojos chiribitas. Si escribo aquí todo lo que te querría decir, estos agradecimientos ocuparían mil páginas. A tí te doy las gracias de otra manera, ¿vale?

Sergio Simón Díaz

SINOPSIS

Esta tesis está enfocada hacia el estudio de la interacción de las estrellas masivas con el medio interestelar ionizado en dos regiones HII galácticas. Se presentan dos estudios bien diferenciados. El primero trata de la comparación de abundancias químicas en la región de formación estelar asociada con la Nebulosa de Orión (M42), obtenidas a partir de métodos estelares y nebulares. El segundo se dirige hacia la construcción de un modelo de fotoionización detallado de la nebulosa de Marian (M43) mediante la comparación de las predicciones de los modelos con un gran número de observables de distinto tipo.

Para los propósitos de esta tesis, se ha obtenido un conjunto de datos observacionales de varios tipos. Estos datos incluyen espectroscopia de rendija larga en el rango óptico de las estrellas masivas presentes en las nebulosas M42 y M43, e imagen en filtro estrecho de la nebulosa M43. Además se han recuperado los datos espectroscópicos de M43 utilizados por M. Rodríguez en un estudio previo de esta nebulosa.

Se ha hecho uso del modelo de atmósfera estelar de última generación FASTWIND para establecer los parámetros estelares y las abundancias de oxígeno y silicio de las estrellas de Orión. La fiabilidad de las abundancias obtenidas se basa en un análisis detallado previo que se realiza para la estrella τ Sco, una estrella B0.2V con líneas estrechas (debido a su baja $v \sin i$). Se ha encontrado buen acuerdo entre la abundancia estelar de oxígeno obtenida para las estrellas de Orión y aquella estimada previamente por Esteban et al. (2004) para el contenido nebuloso en fase gaseosa. Este resultado sugiere un factor de deposición en polvo para el oxígeno nebuloso en M42 menor del que se venía considerando hasta ahora. Las abundancias estelares de silicio son mayores que las que se obtienen a partir del estudio del espectro FUV de M42. Este resultado permite confirmar el depósito de cierta cantidad de silicio nebuloso en granos de polvo.

La nebulosa M43 es una región H II aparentemente esférica ionizada por una sola estrella (HD 37061, B1V). Los parámetros estelares de la estrella ionizante, obtenidos mediante el análisis de su espectro óptico con `FASTWIND` se han utilizado como entrada del modelo de atmósfera estelar `WM-basic` para modelar su distribución de flujo ionizante. Esta distribución espectral de energía, junto con las abundancias nebulares obtenidas a partir del análisis del espectro óptico de M43, y los parámetros morfológicos y fotométricos inferidos de las imágenes de la nebulosa en filtros estrechos, se han utilizado como entrada del código de fotoionización `CLOUDY` para construir modelos de la nebulosa "a medida". Se han considerado dos tipos de modelos esféricos: con densidad constante y con una ley de densidad obtenida a partir del ajuste del perfil de brillo superficial en H_{α} . Finalmente, se han dado los primeros pasos en el modelado de la nebulosa mediante el código `CLOUDY-3D`, un código pseudo-3D que permite construir modelos con geometrías de tipo "ampolla".

CÓDIGOS DE LA UNESCO: 2101.06, 2101.10, 2101.12, 2101,11

ABSTRACT

This thesis focuses on a comprehensive study of the interplay between the massive stars and their surrounding ionized interstellar medium in two Galactic H II regions. Two different studies are presented: the comparison between stellar and nebular abundances for the star forming region associated with the Orion nebula (M42), and the effect of considering different hypothesis on the modeling of the ionized nebula M43, comparing the output of the models with as many observational constraints as possible.

A set of different types of observational data has been compiled for the aims of this thesis. These consist of long-slit stellar optical spectroscopy of the massive stars inside the nebulae M42 and M43, along with narrow band imagery of the Galactic H II region M43. Additionally, some nebular optical spectroscopic data of M43 have been recovered from a previous study by M. Rodríguez.

The state-of-the-art stellar atmosphere code `FASTWIND` has been used to derive the stellar parameters and oxygen and silicon abundances of the Orion stars. The reliability of the derived abundances is based on a very detailed abundance analysis developed for the star τ Sco, a B0.2V star with a very low $v \sin i$. A very good agreement has been found between the stellar oxygen abundances and those obtained by Esteban et al. (2004) for the gas-phase. This result suggests a lower dust depletion factor of oxygen than previous estimations for the Orion nebula. The stellar silicon abundances are larger than that predicted from the FUV spectrum of M42. This result is compatible with some nebular silicon being depleted onto dust grains.

M43 is an apparently spherical H II region ionized by a single star (HD 37061, B1V). The resulting stellar parameters from the analysis of the ionizing star of M43 with `FASTWIND` have been used as input of the stellar atmosphere code `WM-basic` to derive a detailed ionizing flux distribution. This spectral energy distribution, along

with the nebular abundances derived from the analysis of the optical spectrum of M43, and the photometric and morphological nebular parameters obtained from narrow band imagery, have been used to build a tailored photoionization model of the nebula with `CLOUDY`. Two types of spherical models, either with constant density or a density law derived from the H_α surface brightness distribution are considered. Additionally, the predictions of these models are compared with those resulting from a blister model generated with the pseudo-3D code `CLOUDY-3D`.

UNESCO CODES: 2101.06, 2101.10, 2101.12, 2101.11

CONTENTS

Agradecimientos	vii
Sinopsis	ix
Abstract	xi
1 Introduction	1
1.1 Chemical abundances from H II region studies	2
1.2 Chemical abundances from massive star studies	4
1.3 Do stellar and nebular abundances agree?	7
1.4 Modeling H II regions and starbursts	8
1.5 Outline of thesis	11
2 Observations	13
2.1 Introduction	13
2.2 Stellar observational dataset	14
2.3 Nebular observational dataset	21
2.3.1 Long-slit spectroscopy	21
2.3.2 Narrow band imagery	22
3 Dealing with Stellar Atmosphere Codes	29
3.1 Introduction	29
3.2 Stellar model atmosphere codes	32
3.3 Quantitative spectral analysis: FASTWIND	37
3.3.1 The application FASTWIND	37
3.3.2 Stellar parameters determination: methodology	43
3.3.3 Stellar abundances determination: methodology	46
3.4 Modeling ionizing fluxes: WM- <i>basic</i>	52

3.4.1	Using WM- <i>basic</i>	52
3.4.2	A comparison between FASTWIND and WM- <i>basic</i> results	54
3.5	General analysis strategy	59
4	Nebular spectroscopic studies	61
4.1	Introduction	61
4.2	Physical conditions of H II regions	62
4.3	Nebular abundances	63
4.4	Total H α luminosity and H α surface brightness distribution	64
4.5	A nebular photoionization code: CLOUDY	65
4.5.1	Input for CLOUDY	66
4.5.2	Comparing the output of CLOUDY models with the observational constraints	68
5	Stellar abundances in B0.5V stars	71
5.1	Introduction	71
5.2	Line identification and measurement of equivalent widths	73
5.3	Oxygen abundances	77
5.3.1	First approach	77
5.3.2	Detailed multiplet study	79
5.3.3	Effect of the stellar parameters over the derived oxygen abundances	90
5.3.4	Comparison between FASTWIND, CMFGEN and TLUSTY results	92
5.4	Silicon abundances	95
5.4.1	Microturbulence from the Si analysis	97
5.4.2	Effect of the stellar parameters over the derived silicon abundances	98
5.5	Summary and conclusions	99
6	Massive stars in the Orion nebula	101
6.1	Introduction	102
6.2	The Orion nebula and its associated stellar population	103
6.3	Massive stars in Orion: observational dataset	104
6.4	Rotational velocities and stellar parameters	105
6.4.1	Rotational velocities. The Fourier method	105
6.4.2	Stellar parameters	107
6.4.3	Results of the stellar parameters study	120
6.5	Modeling θ^1 Ori C: the main ionizing star of M42	122
6.5.1	A historical review	122

6.5.2	Preliminary study of the spectrum	123
6.5.3	Determination of the $v \sin i$ of θ^1 Ori C	127
6.5.4	Modeling of θ^1 Ori C	129
6.6	Stellar abundances in Orion B0.5V stars	132
6.6.1	Oxygen abundance determination	132
6.6.2	Silicon abundance determination	134
6.6.3	Oxygen and silicon abundances in the reference stars	136
6.6.4	Oxygen and silicon abundances in the Orion stars	139
6.7	Comparing with nebular results	141
7	The apparently spherical H II region M43	143
7.1	Introduction	143
7.2	Spectroscopic analysis of the ionizing source	145
7.2.1	Stellar parameters	145
7.2.2	Spectral energy distribution	147
7.3	Obtaining useful information from the INT-WFC images	153
7.3.1	Total H_α luminosity and H_α surface brightness profile	154
7.3.2	Other narrow band filters	156
7.4	Nebular physical parameters and abundances revised	157
7.5	Photoionization models	159
7.5.1	Characteristics and input of the models	160
7.5.2	Observational constraints and strategy	162
7.5.3	Spherical constant density models	167
7.5.4	Density law models	178
7.5.5	Spherical vs. blister models	181
7.6	Summary and conclusions	184
8	Conclusions	187
A	Determination of stellar $v \sin i$	193
A.1	Testing the Fourier method. Some theoretical cases	195
A.1.1	The Fourier method	195
A.1.2	Rotational and macroturbulent profiles	195
A.1.3	The Fast Fourier Transform (FFT) and its computational properties	196
A.1.4	Some theoretical tests	197
A.2	Applying the Fourier method to real OB stellar spectra	201
B	Stellar spectroscopy of binary systems	203

C Glossary of terms	207
Bibliography	211

CHAPTER
ONE

INTRODUCTION

*No sé si esta historia es verdad,
me lo han asegurado seriamente:
si no lo es,
está bastante bien inventada.*

- Michael Ende -

FROM birth, massive stars ($M_{\star} > 8-10 M_{\odot}$) are closely related to the surrounding interstellar medium (ISM) from which they are born. In the collapse of the parent molecular cloud only a few of these massive stars are formed compared to the total number of low mass stars (the number of stars formed per unit of mass scales $\propto M_{\star}^{-2.35}$, Salpeter 1955). However their influence over the ISM is very important. Apart from nova and supernova type phenomena, these stars are the most luminous stellar objects in the Universe, not only in terms of the amount of radiation emitted, but also due to the mechanical energy released in their stellar winds. The intense radiation emitted by these hot massive stars in the ultraviolet and extreme ultraviolet (UV/EUV) range ionizes the ISM and generates what is called a H II region. This appears before our eyes as a diffuse nebula surrounding the stars, and before the eyes of a spectroscopist as an emission line spectrum. Moreover, the mechanical energy deposited by the stars in the ISM in the form of stellar winds and finally as a supernova explosion will produce remarkable effects over the star forming region. Finally, the chemical composition of the surrounding ISM will be polluted by the resulting elements generated in the stellar interior. In this way, the cycle in which the original material from the cloud, processed in the stellar interior, is returned back to the ISM with a modified chemical abundance pattern, is closed.

The lifetime of massive stars is very short in terms of stellar evolutionary time-scales ($\sim 10^6 - 10^7$ years); H II regions are bounded to these stars, so their lifetime is of the same magnitude. Therefore, these are young objects that reflect the present chemical composition of the galactic zone where they are located (in contrast to what happens with lower mass stars and their associated nebular objects, the planetary nebulae; these objects present a larger evolutionary scale so they reflect the chemical composition of the epoch when the stars were formed modified by the possible contamination due to the stellar evolution). The evolutionary characteristics of massive stars imply that both objects (massive stars and their associated H II region) must share the same chemical composition. However, there are certain cases in which this is not completely fulfilled:

1. Strong stellar mass-loss may expose underlying layers already contaminated on the surface of the star.
2. Rotating models for massive stars by Maeder & Meynet (2000) predict products from the CNO-bicycle reaching and polluting the outer layers of these stars. Mixing of nuclear processed material at the stellar surface will increase with stellar mass, age, initial rotational velocity and decreasing metallicity. Observational evidences of this surface contamination have been found in several studies of OBA-type stars and fast rotators (viz. Walborn 1972b, McErlean et al. 1999, Korn et al. 2000, Venn et al. 2002, Villamariz et al. 2002, Bouret et al. 2003)
3. The gas-phase nebular abundances of certain elements can be affected by depletion onto dust grains (mainly Si, O, Mg, Fe, C). In this case, although the total gas+dust abundances in the nebula must agree with the massive stellar ones, the gas-phase abundances, derived through a spectroscopic study of the H II region, could be somewhat lower.
4. Mass transfer in close binary evolution may contaminate the surface of the star accreting material.

1.1 Chemical abundances from H II region studies

Traditionally, chemical abundance studies in spiral (including the Milky Way) and irregular galaxies have been based on the emission line spectra of H II regions. This is logical since H II regions are luminous and have high surface brightness (in the emission lines) compared to individual stars in galaxies. A H II region is an efficient machine for converting EUV radiation of hot massive stars into a few narrow emission lines, leading to a very luminous object in the optical/IR bands. Therefore it

is relatively easy to obtain high quality spectroscopic observational data, even with small and medium size telescopes. This has made possible both the detailed study of individual nebulae (viz. Esteban et al. 2004), and the determination of radial abundance gradients in the Milky Way (viz. Shaver et al. 1983, Afflerbach et al. 1997, García-Rojas et al. 2004, Esteban et al. 2005) and other spiral galaxies (viz. Vilchez et al. 1988, Kennicutt et al. 2003, Bresolin et al. 2004, Cedrés et al. 2004), imposing observational constraints to the chemical evolution models of these galaxies.

There are two different approaches for deriving chemical abundances in H II regions (see Stasińska 2004 for an excellent review on the subject): the *direct* method and *statistical* or *strong line* methods. The former is based on the fact that the abundance ratio of two ions can be obtained from the observed intensity ratio of lines emitted by these ions (the electron temperature $-T_e-$ and density $-N_e-$ of the ionized nebula are required for this method). To derive the total abundances, the ionic abundances of the main ions for each element need to be known; if the lines of one of these main ions cannot be observed, then element abundances are calculated through the so-called ionization correction fractions, ICFs. The ICFs are calculated either by using empirical calibrations (e.g. Torres-Peimbert & Peimbert 1977) or by modeling the H II region with a photoionization code (Stasińska 1990, Mathis & Rosa 1991). *Statistical* or *strong line* methods were developed to study those cases in which the electron temperature cannot be measured (mainly in the high metallicity regime, or when the quality of the data or the observed spectral range is not enough to measure the temperature sensitive lines). These methods are based on the construction of nebular abundance indicators making use of strong lines, easily measurable in the emission line spectrum of the ionized gas. However, these indicators must be calibrated. Many calibrations exist in the literature, viz. Pagel et al. 1979, Skillman 1989, McGaugh 1994, Vilchez & Esteban 1996, Díaz & Pérez-Montero 2000, Pilyugin 2000.

Although this is a commonly used methodology, it is not without some difficulties and problems. For example, it is known that optical recombination lines (ORL) in ionized nebulae indicate higher abundances than collisionally excited lines (CEL). Temperature fluctuations, density condensations and abundance inhomogeneities have been proposed to solve the ORL/CEL problem, however this explanation is not completely satisfactory (see Esteban 2002 for a review). In a comparison of results from *direct* and *strong line* methods in the spiral galaxy M101, Kennicutt et al. (2003) find that empirical calibrations yield oxygen abundances that are systematically higher than the T_e -based abundances by amounts ranging from 0.1 to 0.5 dex. Moreover, in H II regions, the oxygen abundances derived from *strong line* "empir-

ical” abundance indicators depend strongly upon the choice of calibration (see e.g. Kobulnicky et al. 1999). Stasińska (2005) has recently shown that for metal rich nebula, the derived abundances based on a direct measurement of the T_e deviate systematically from the real ones.

Finally, one must keep in mind other sources of uncertainties in nebular abundance determinations such as the atomic data, reddening corrections and the possible depletion of elements onto dust.

1.2 Chemical abundances from massive star studies

Stellar spectroscopy has been a very valuable tool for studying the composition and evolution of stars in our Galaxy. Blue massive stars can be easily identified at large distances due to their high luminosities ($\sim 10^{4.5} - 10^6 L_\odot$) and hence are an important complement to spectroscopy of H II regions, since they sample similar spatial and temporal distributions. Therefore, massive stars offer a unique opportunity for the study of abundance gradients in the Milky Way and other nearby galaxies as an alternative method to classical H II region studies, with clear advantages in some aspects, like the extension of the analysis to more α -elements, and to the Fe-group and s-process elements. However the amount of energy that is released by these stars is so large that it produces dramatic effects not only on the surrounding ISM but also on the star itself. These stellar objects show mass outflows during their whole lifetime (so called stellar winds) and their atmospheres departure from LTE conditions, two facts that make the modeling of atmospheres of hot massive stars more complicated.

It has not been until very recently that the development of massive star model atmospheres and the growth of the computational efficiency has allowed a reliable abundance analysis of these objects. This fact has been reinforced with the construction of medium and large sized ($\geq 4\text{m}$) ground based telescopes which have made it possible to obtain enough good quality data within reasonable observing times, whilst space telescopes have opened up the observable window to the UV and FIR spectral ranges. In addition, multi-object spectrographs attached to large-size telescopes have made it possible to increase the number of targets which can be observed during one run (e.g. the FLAMES-VLT spectrograph).

Some examples of studies of abundance gradients in Local Group spiral galaxies through massive stars are those by Smartt & Rolleston (1997), Gummersbach et al. (1998), Rolleston et al. (2000), Smartt et al. (2001a) and Daflon & Cunha (2004) — Milky Way — ; Monteverde & Herrero (1998), Monteverde et al. (2000) and

Urbaneja et al. (2005b) — M33 — ; Venn et al. (2000) and Trundle et al. (2002) — M31 —. Studies of radial abundance gradients in spiral galaxies have been performed even beyond the Local Group, at distances up to 2 Mpc (Urbaneja et al. 2003, 2005a). The most comprehensive works in the Magellanic Clouds are those by Korn et al. (2000, 2002) and the Queen’s group (Rolleston et al. 1996, McErlean et al. 1999, Lee et al. 2005). At present, a large effort is being devoted towards the understanding of the influence of mass-loss and rotational velocities on massive star evolution in the international FLAMES collaboration (P.I. S. Smartt). Studies of massive star abundances have even reached galaxies at ~ 7 Mpc (Bresolin et al. 2001), although in this case it was not possible to derive individual abundances for the different elements.

A reliable stellar abundance study is mainly based on a correct stellar atmosphere modeling, however there are other effects that can affect the final results and must be carefully taken into account; they are summarized below.

STELLAR ATMOSPHERE MODELING

Different assumptions about the physics used in the stellar atmosphere modeling can be considered (e.g. plane-parallel or spherical geometry, LTE/NLTE and/or line blocking/blanketing effects). The reliability of these assumptions depends on the specific study one wants to develop. For example, some earlier works assumed that line blanketing effects were more important over the region of photospheric lines formation than departures from LTE, so the use of Kurucz’s LTE blanketed models (Kurucz 1979) were preferred to those NLTE codes without the line blanketing effects (e.g. Mihalas & Auer 1970). However, it was soon demonstrated that the assumption of LTE could introduce systematic errors into the results (Becker & Butler 1988). Kurucz’s models were then combined with a detailed NLTE description in the exact calculation of the level populations (resulting in pseudo-NLTE abundances, see for example Gies & Lambert 1992, Cunha & Lambert 1992, 1994).

Improvements in computational methods, as well as an increase in computer efficiency, have made it possible to model the atmospheres of hot luminous stars taking into account not only strong NLTE effects and hundreds of thousands of metallic lines producing the so-called line blanketing (Hubeny & Lanz 1995), but also winds with expanding spherical geometries (Santolaya-Rey et al. 1997; Hillier & Miller 1998; Pauldrach et al. 2001; Puls et al. 2005). This makes it possible to carry on fully consistent NLTE line blanketing stellar abundance analyses within acceptable computational times.

ATOMIC MODELS AND ATOMIC DATA

State-of-the-art NLTE model atmosphere codes have arrived at such a high level of numerical sophistication that, together with the capability of the current computers, they permit calculations which include line spectra from all elements from hydrogen up to the iron group. The need of reliable atomic data has become a critical problem for further progress. A NLTE description of the atomic processes related to the interaction of the radiation with the stellar plasma requires a fully detailed description of atomic models and precise atomic data. This includes a definition of the energy levels and the whole set of continuum and line processes, either collisional or radiative, of all the atomic species that want to be included in the line synthesis. A major effort has been devoted in the last years to calculate and compile atomic data, as well as to construct detailed atomic models (see reviews by Rauch & Deetjen 2003, Lanz & Hubeny 2003 and Nahar 2003 in the proceedings to the international workshop on Stellar Atmosphere Modeling).

ESTABLISHMENT OF THE STELLAR PARAMETERS AND MICROTURBULENCE

For a given abundance, the equivalent width of metal lines depends on the effective temperature and gravity of the star, as well as on microturbulence. Therefore a precise determination of stellar parameters and microturbulence is important prior to the development of a reliable stellar abundance analysis. The most precise method to derive T_{eff} and $\log g$ in massive stars is based on a completely spectroscopic approach, in which through an iterative process, gravity is determined by means of a visual comparison of the observed and synthetic hydrogen Balmer lines, and effective temperature through its effect on the ionization equilibrium of different ions of the same elements (normally, in the case of OB-type stars, either by a visual comparison of the He I-II lines, or by using theoretical ratios of Si II-III or Si III-IV lines). This method has been widely used (viz. Herrero et al. 1992; Gummertsbach et al. 1998; McErlean et al. 1999). Some other studies derive effective temperatures and gravities for these stars using Strömgren dereddened color indices and H_{γ} line profiles (see Daflon et al. 1999, for a recent application of this method).

Stellar parameters are somewhat dependent on the assumption of the physics used in the stellar atmosphere modeling. For example, the papers by Herrero et al. (2002), Crowther et al. (2002), and Martins et al. (2002) showed that the SpT - T_{eff} calibrations used previously (Vacca et al. 1996) needed to be revised to lower effective temperatures for a given spectral type. Recent analyses by Repolust et al. (2004), Massey et al. (2004) and Martins et al. (2005) reinforce this result.

Microturbulence is a free parameter that was included in stellar abundance analyses for trying to solve the discrepancy found in line abundances derived from weak and strong lines. Although it was firstly thought that this free parameter would be unnecessary when NLTE effects were considered, many studies have shown that although it is smaller in those cases, neither is zero (e.g. Gies & Lambert 1992, find that the derived microturbulence is reduced from 30 to 15 km s⁻¹ when a NLTE description is included in the formal solution for the analysis of B-type Supergiants). Villamariz & Herrero (2000) have shown that the hydrogen and helium spectrum of OB stars (and therefore the derivation of their stellar parameters) may be affected by microturbulence in the case of supergiants, but its influence is usually negligible for dwarfs with strong Stark broadened lines.

Its physical meaning is assumed to be related with small scale turbulent motions of the stellar plasma, however some questions about its behavior in stellar atmospheres still remains unclear (e.g. McErlean et al. 1999, find that lines from Si III indicate smaller microturbulences than do the lines of O II). Nevertheless, microturbulence is commonly used in stellar abundance analysis as a free parameter.

1.3 Do stellar and nebular abundances agree?

Nebular abundance studies are limited by the ORL/CEL discrepancy, atomic data, ICFs, reddening and dust depletion. Stellar absorption spectra of massive stars allow us to estimate chemical abundances with an accuracy comparable with that obtained from nebular studies. However, stellar absolute abundances may contain systematic errors due to uncertainties in the atmospheric parameters and atomic data, or because of simplifications in the model atmosphere analysis. To minimize these errors differential analyses are performed with respect to a star with similar spectral type and luminosity class (see Smartt et al. 1996, Monteverde et al. 2000). Nevertheless, as suggested by Korn et al. (2002), systematic errors are arguably more important than the random ones at the current level of accuracy reached for the stellar abundance studies, and the identification of these systematic errors may be addressed by an integral approach: *by studying the stellar and gas component of H II regions in tandem.*

Two types of studies can be addressed to follow that suggestion: the comparison of radial abundance gradients in spiral galaxies or mean abundances in irregular galaxies (*global approach*), and the comparison of absolute abundances in the same galactic region (*local approach*). Values found in the literature for the oxygen abundance gradient in the Galaxy range from -0.04 to -0.08 in the nebular case (Shaver

et al. 1983, Afflerbach et al. 1997, Deharveng et al. 2000, Pilyugin 2003, Esteban et al. 2005) and from -0.03 to -0.07 in the stellar case (Gummersbach et al. 1998, Rolleston et al. 2000, Daflon & Cunha 2004). One could conclude that results from both methodologies are in agreement within the intrinsic uncertainties, however this may not be the case when comparing results from individual studies. For example, in a recent study Esteban et al. (2005) derive an oxygen abundance gradient through nebular optical recombination lines of $-0.044 \pm 0.010 \text{ dex kpc}^{-1}$, a value that is not in agreement with that by Rolleston et al. (2000) derived through B-type stars ($-0.067 \pm 0.008 \text{ dex kpc}^{-1}$) and only in marginal agreement with the value of $-0.031 \text{ dex kpc}^{-1}$ by Daflon & Cunha (2004).

In the extragalactic case, the comparison of stellar and H II region oxygen abundances (based on direct determinations of the electron temperature of the nebulae) in M33 by Urbaneja et al. (2005b) shows a very good agreement, however Trundle et al. (2002) and Urbaneja et al. (2003, 2005a) show that abundance gradients in M31 and NGC300 derived from stellar and nebular studies tend to be coherent but very dependent on the calibration used in the strong line nebular methods.

Examples of the comparison between stellar and nebular abundances in the same Galactic region or mean abundances in the Magellanic Clouds are found in Cunha & Lambert (1992, 1994), Korn et al. (2002), and Trundle et al. (2004, and references therein). Although within the typical errors of the stellar and nebular analyses the abundances determined in each method are fairly consistent, more work remains necessary. For example, until now, there has not been a consistent detailed comparison of stellar and nebular abundances in the same local star forming region.

A combined study of nebular and stellar abundances will allow to address various interesting astrophysical tasks such as the reliability of the derived abundances in both methodologies; the possible depletion of nebular elements onto dust grains; to check the strong line nebular methods; or to extend the abundance studies to regions where one of both methodologies is difficult to be applied (viz. the outermost regions of spiral galaxies, where the H II regions are fainter and difficult to observe, or obscured star forming regions).

1.4 Modeling H II regions and starbursts

The physical characteristics and ionization structure of H II regions are strongly dependent on the spectral energy distribution of the ionizing stars. Therefore, ionized nebulae are potential tools to check the validity of the emergent energy distribution predicted by stellar atmosphere models. Moreover, the emission line spectrum of

these nebulae can be used to characterize the associated underlying massive stellar population in those cases where it cannot be well resolved. However, the problem is complicated by the fact that the ionization structure also depends on the nebular density distribution and the chemical abundances.

There are many studies that derive the properties of the stellar population associated to GHR (giant H II regions) or starburst comparing with photoionization models where the ionizing source is a stellar cluster (see e.g. Stasińska & Leitherer 1996). In these studies, some assumptions over the stellar population must be made:

1. The initial mass function (IMF)
2. The star formation history (SFH)
3. A M_* - SpT - T_{eff} calibration
4. The global ionizing flux and spectral energy distribution (SED)

By comparing the model predictions with constraints from the observation of the ionized region, it is possible to derive important physical parameters such as the metallicity, the IMF and the star formation rate.

The massive star population powering H II regions or starbursts can be characterized in three different ways: assuming an IMF (if the stellar population cannot be resolved), determining spectral types through photometry or low resolution spectroscopy, or obtaining the stellar parameters of each one of the stars by fitting the observed spectrum with model atmosphere codes. Once the stellar population is defined, the global ionizing flux distribution must be modeled using model atmosphere codes (as it cannot be obtained directly from observations). Therefore, theoretical model atmospheres are a crucial ingredient for the photoionization modeling of H II regions and starbursts. Model atmosphere codes that have been commonly used in this field are those by Kurucz¹, which are plane-parallel, LTE, line-blanketed models. Kurucz models are preferred to those NLTE codes without the line blanketing effects (e.g. Mihalas), due to the fact that the blocking of UV flux by hundreds of thousands of metal lines in the Lyman continuum ($\lambda < 911 \text{ \AA}$) affects strongly the emergent ionizing flux. However it is known that for massive hot stars the NLTE effects are important, and the presence of winds can affect the stellar emergent flux (viz. Gabler et al. 1989; Najarro et al. 1996; Sellmaier et al. 1996).

¹In some cases the ionizing flux distribution of the stars are modeled through blackbodies.

Some work has been devoted to study the impact of the recent generation of NLTE, line blanketed, spherically expanding model atmosphere codes (Santolaya-Rey et al. 1997, Schaerer & de Koter 1997, Hillier & Miller 1998, Pauldrach et al. 2001) on the ionization structure of H II regions, either by comparing samples of H II regions with model grids (Sellmaier et al. 1996, Stasińska & Schaerer 1997, Giveon et al. 2002, Morisset et al. 2004), or by detailed model fitting of individual H II regions (Luridiana et al. 1999, Stasińska & Schaerer 1999, Oey et al. 2000ab, Morisset et al. 2002, Relaño et al. 2002, Jamet et al. 2004). These studies are based on the modeling of H II regions with photoionization codes whose input is the ionizing flux distribution of the stellar population, the nebular density distribution and the nebular abundances. Usually, some assumptions have to be made, such as the number and spectral types of the stars powering the nebula (by assuming an IMF or deriving the spectral types through photometry or low resolution spectroscopy, as commented above). The nebular density is assumed to be constant and equal to the electron density N_e derived from nebular spectroscopy (or re-scaled assuming some filling factor); in more satisfactory models, it is derived from the H_α surface brightness assuming a spherical geometry.

However, these assumptions are not always fully justified. Cerviño et al. (2002) showed that if the total initial mass of a cluster is less than $\sim 10^4 M_\odot$, statistical fluctuations around the mean IMF can strongly affect the main diagnostics of the cluster, such as the $EW(H_\beta)$ or the determined ionizing spectrum. The determination of the total ionizing flux distribution of the cluster depends on SpT- T_{eff} calibrations that have been revised recently (Martins et al. 2002; Herrero et al. 2002; Repolust et al. 2004; Martins et al. 2005). On the other hand the possibility that the apparent spherical nebulae were actually blisters makes questionable the assumption on the density distribution. The successful *blisters* (Israel 1978) or *champagne flow* (Tenorio-Tagle 1979) models are based on the idea that an expanding H II region formed near the edge of a molecular cloud will eventually breakout into the less dense medium. In particular, the development of an internal density gradient in the ionized gas is predicted by these models. Morisset et al. (2005) show that the ionization structure of a H II region differs drastically when considering a blister model or its *spherical impostor* (a spherical nebula reproducing the same H_α surface brightness). Therefore, geometries other than spherical must be investigated in photoionization models.

The total H_β luminosity of the H II region or starburst is an important parameter that is directly linked to the stellar population via the total number of ionizing photons. Nevertheless, this is only valid if the H II region is ionization bounded (i.e. the ionizing photons do not escape from the nebula). Oey & Kennicutt (1997)

find that many H II regions in the LMC are density bounded. This result has also been found by Relaño et al. (2002) in NGC346, the most luminous H II region in the SMC, and Stasińska & Izotov (2003). The release of photons could explain the ionization of the diffuse interstellar medium (Zurita et al. 2000).

The aperture correction problem has also to be taken into account when comparing the output from photoionization models with the observed nebular spectrum. In other words, the observed spectra must be compared to computed spectra corresponding to the part of the nebula seen through the slit (Luridiana et al. 1999). If the slit size and position are controlled parameters in resolved H II regions, then they can be used to constraint the results of the photoionization model at increasing distances from the central source.

As suggested by Stasińska & Schaerer (1997), the best approach would be to test all these situations in extremely well defined situations. However, what remains clear is that again an *integral approach*, the study of both objects (massive stars and H II regions) in tandem, can help to improve the techniques in both fields.

1.5 Outline of thesis

This thesis focuses on a comprehensive study of the interplay between the massive stars and their surrounding ionized interstellar medium in two Galactic H II regions. Two different studies are presented: the comparison between stellar and nebular abundances for the star forming region associated with the Orion nebula (M42), and the effect of considering different hypothesis on the modeling of the ionized nebula M43, comparing the output of the models with as many observational constraints as possible.

This thesis is structured as follows: After the presentation of the observations used in thesis (Chapter 2), the various tools that have been considered for the studies presented here are described. The analysis of the optical spectra of the massive stars is performed using the recent generation of model atmosphere codes; these are introduced in Chapter 3, together with the methodology followed to derive stellar parameters and abundances and modeling stellar ionizing flux distributions. Two different tools for studying ionized nebulae powered by stellar objects are presented in Chapter 4: the spectroscopic approach gives the mean physical properties and abundances of the nebulae along the line of sight below the slit; the photoionization modeling approach allows a detailed study of the ionization structure of the nebulae. The following step is to apply the proposed methodology to real cases. In Chapter

5 the slow rotator B0.2V star τ Sco is used as *benchmark test* for the abundance analyses of early B-type main sequence stars with the stellar atmosphere code FASTWIND. A detailed spectroscopic study of a group of massive stars inside the Orion nebula is presented in Chapter 6; stellar parameters as well as oxygen and silicon abundances are derived for these stellar objects. The stellar abundances are compared with nebular results. In Chapter 7, the de Marian nebula (M43) has been selected to build a tailored photoionization model for a well resolved, apparently spherical galactic H II region with a single ionizing star. Finally, the conclusions of this work are summarized. Complementary topics are presented in appendices.

OBSERVATIONS

Quiero tener contacto
con la realidad,
pero
la realidad no me gusta.
- Tontxu -

The observational dataset used for this thesis is presented in this chapter. The bulk of the observations consist of long-slit stellar and nebular optical spectroscopy and are supplemented with narrow band imagery of the Galactic H II region M43.

2.1 Introduction

This chapter presents the observations that were obtained for the aims of this thesis, along with some comments on target acquisition and the reduction processes. Several types of observables have been used here, comprising stellar and nebular spectroscopy and narrow band imagery.

In Chapters 6 and 7, the optical spectra of the OB stars located inside the H II regions M42 and M43 are used to derive their stellar parameters through the analysis of the H and He I-II lines. Additionally, many metal lines are present in this optical range (viz. C,N,O,Si and Mg), therefore a stellar abundance analysis is feasible with the same spectra (see Chapters 5 and 6). The usual requirements for the

forementioned analyses are intermediate spectral resolution ($R \sim 7000-10000$) and a high signal-to-noise ratio ($SNR \geq 150-200$) in the spectral range between 4000 and 5050 Å together with a spectral window centered on H_α . The spectral resolution and SNR must be sufficient to accurately measure the equivalent widths of the metal lines that appear in the stellar spectra. The Intermediate Dispersion Spectrograph (IDS) attached to the Cassegrain focus of the 2.5m Isaac Newton Telescope (INT) had an adequate configuration¹ for reaching these specifications in a reasonable observing time. One observing run was requested successfully, and all the stars needed for this study were observed with adequate quality (see Section §2.2).

Two types of observations have been used for the analysis of the Galactic H II region M43 (Chapter 7): medium resolution long-slit nebular spectroscopy to study its chemical composition and physical characteristics, and narrow band imagery of the nebula, to study its photometric and morphological parameters. Both the spectroscopic and photometric datasets were obtained with the INT. The spectroscopic data (IDS spectra) have been recovered from Mónica Rodríguez's thesis (Rodríguez 1998), and nebular images were obtained with the Wide Field Camera² (WFC, an optical mosaic camera attached to the prime focus of the INT), in service time.

2.2 Stellar observational dataset

The bulk of the stellar spectroscopic observations used here were carried out with the Isaac Newton 2.5m Telescope (INT) at the Roque de los Muchachos Observatory in La Palma on 21 December 2002. The long-slit Intermediate Dispersion Spectrograph (IDS) was used with the 235 mm camera and two different gratings. The spectral region between 4000 and 5050 Å was observed using the H2400B grating, which resulted in an effective spectral resolution $R \sim 7500$ (equivalent to a 0.23 Å/pixel resolution and ~ 2.6 pixel FWHM arc lines). For the H_α region the H1800V grating was used, resulting in a similar spectral resolution (0.3 Å/pixel, $R \sim 8000$). To obtain the appropriate wavelength coverage with these configurations, three exposures were required; two settings in the blue and one in the red. To avoid saturation on the strong nebular emission lines contaminating the stellar spectra, several short exposures were taken when necessary. Additionally, a large number of bias, flat fields and arcs were obtained for use in the reduction process.

¹ IDS is not offered any longer to visiting astronomers since August 2003. Information about the instrument can be found in <http://www.ing.iac.es/Astronomy/instruments/ids/>

²<http://www.ing.iac.es/Astronomy/instruments/wfc/>

HD	Name	SpT	m_v	A_v	M_v
Orion stars					
HD 37020	θ^1 Ori A	B0.5V	6.73	1.89	-3.4
HD 37022	θ^1 Ori C	O7V _p	5.12	1.74	-4.9
HD 37023	θ^1 Ori D	B0.5V	6.71	1.79	-3.3
HD 37041	θ^2 Ori A	O9V	5.07	1.12	-4.3
HD 37042	θ^2 Ori B	B0.5V	6.41	0.73	-2.6
HD 37061	NU Ori	B1V	6.84	2.09	-3.5
Reference stars					
HD 47839	15 Mon	O7V	—	—	-4.8
HD 214680	10 Lac	O9V	—	—	-4.4
HD 149438	τ Sco	B0.2V	—	—	-3.3

TABLE 2.1 — Identification, spectral type and photometric visual data of the studied objects. The A_v and m_v values for Orion stars from Preibisch et al. (1999). The M_v values for these stars have been calculated considering a distance $d = 450 \pm 50$ pc to the Orion nebula. Data for HD 214680 and HD 47839 are from Herrero et al. (1992). Photometric data for HD 149438 is from Humphreys (1978). Uncertainties in m_v , A_v and M_v are 0.01, 0.03 and 0.3 respectively.

The reduction of the spectra was done using the IRAF reduction package, following long-slit standard techniques³ that comprise:

- Bias subtraction
- Correction of the small scale sensitivity variation of the CCD by using a normalized combined flat field on each spectral region.
- Subtraction of the sky and nebular contribution (see below)
- Aperture extraction.
- Wavelength calibration

At this point, the different exposures for the same spectral region of each target are combined, taking care that there is not a relative shift in wavelength between them. The signal-to-noise ratio (SNR) reached for the spectra — estimated as the square root of the total number of counts for a given wavelength — varies with wavelength, but is usually about 200-250 in the blue region and 250 in the H_α region (see Table 2.2). An atlas of these spectra is presented later in Figures 2.3 and 2.4; the two blue regions have been coadded.

³See e.g. *A User's Guide to Reducing Slit Spectra with IRAF*, by P. Massey, F. Valdes, J. Barnes (15-Apr-1992)

HD	4000 - 4550	4500 - 5050	H α
HD 37020	170-280	210	220
HD 37022	170-330	280	290
HD 37023	220-450	450	320
HD 37041	200-275	230	210
HD 37042	160-220	250	230
HD 37061	170-300	250	250
HD 214680	140-190	200	160
HD 47839	89-120	160	260

TABLE 2.2 — *SNR* achieved for the target spectra for each one of the three spectral ranges observed with the INT+IDS.

Special care has to be taken, in the reduction process, due to the nebular contamination of the stellar spectra. The stars studied are located inside H II regions, so the stellar spectra are contaminated by the nebular emission spectrum. It would be desirable to remove this nebular contribution, as it fills the cores of the Balmer H and He I lines. However this is not an easy task, despite having long-slit observations, as the nebular emission has spatial structure that complicates its subtraction (especially in the Balmer H lines, where there is a strong nebular contribution. See Figure 2.1). If this contamination is not correctly removed an over or under subtraction will appear. After trying various possibilities it was concluded that the best solution for this problem is not to subtract the nebular emission at all, instead those regions where the emission lines contaminate the stellar lines were ignored in the fitting process of the synthetic lines to the final spectrum. For the Balmer H and He I lines this is satisfactory, as emission lines are narrower than absorption lines. Nebular contributions are more difficult to separate from metal lines. However the stellar metal lines used in the abundance analyses presented here have a negligible contamination from nebular lines.

The last step of the reduction process is the normalization of the spectra⁴. This final step was done using our own software developed in IDL: a normalization function is defined with a cubic splines fit to some selected continuum points, and the spectrum is then divided by this function. The selection of the continuum points is arbitrary, but one must take into account that they cannot be located where there is an interstellar band or over the wings of the H, He I-II or metal lines, and must adequately trace the curvature of the non-rectified spectrum.

⁴In some cases, if the observed star is not single, spatially unresolved components may be included in the slit. Spectral features showing this binarity can appear in the spectrum of the star, and the normalized spectrum can be affected by binarity effects (see Appendix B)

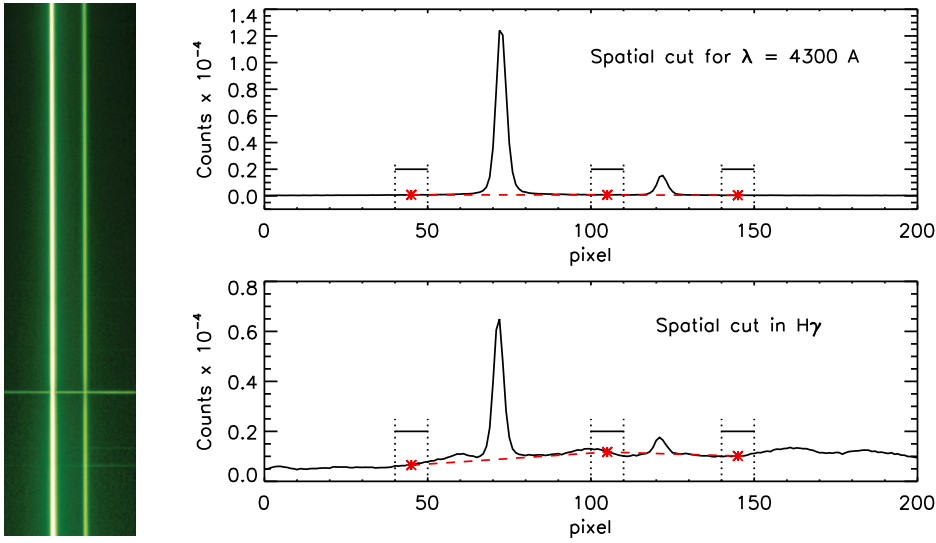


FIGURE 2.1 — (Left) Partial section of the CCD showing the bi-dimensional spectrum (horizontal: spatial direction; vertical: dispersion direction) of HD 37020 + HD 37021 + M42. The broad vertical white lines correspond to the stellar continuum emission. Vertical cuts outside the stellar emission give the nebular spectra at various distances from the star. Horizontal lines represents spatial cuts in one of the narrow nebular emission lines. (Upper right) Spatial cut for a given wavelength where there is no nebular emission. The spectrum for each star is extracted fitting a gaussian curve and subtracting the sky and nebular contribution. In this case the nebular and sky contribution in the stellar zone is estimated by a linear fit to adjacent zones. (Lower right) Spatial cut in $H\gamma$. The structure of the nebula in this wavelength complicates the subtraction of the nebular emission.

In the normalization process of the INT-IDS $H\alpha$ spectra it was found that the blue wing of the $H\alpha$ line is affected by a feature that has previously been identified as a broad diffuse interstellar band, DIB (Herbig 1995). Therefore, the normalization of the $H\alpha$ spectra has to be done taking care of not selecting a continuum point inside this DIB because it would produce an incorrect result. Figure 2.2 illustrates this problem. The presence of the mentioned DIB will be taken into account in the fitting process to derive the stellar parameters (see Chapters 6 and 7).

The INT observations consist of the brightest three stars in the Trapezium cluster (θ^1 Ori A, C, D) inside the Orion nebula (M42) together with the two nearby stars θ^2 Ori A and B, and NU Ori (the ionizing source of M43). Two standard stars were included in this set, 10 Lac and 15 Mon (O9V and O7V respectively). The spectrum for the other standard star, τ Sco, was kindly provided by Dr. Gehren. This is a slow rotating B0.2V star, ideal for a preliminary abundance analysis study.

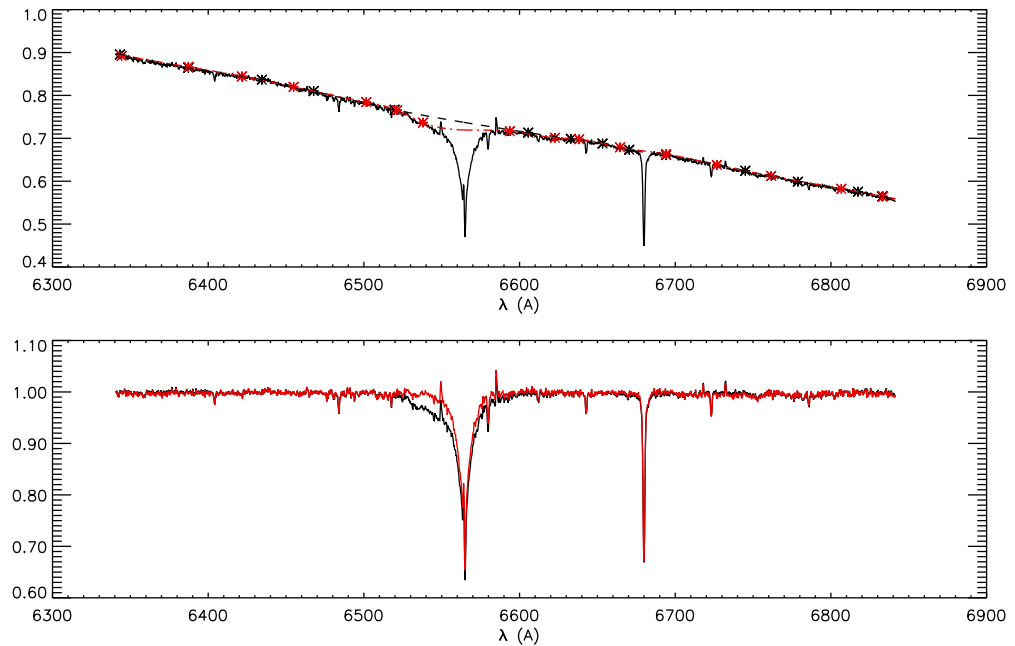


FIGURE 2.2 — Two possible solutions in the normalization of the INT-IDS H α spectrum of HD 37042. The normalization function indicated by the black dashed line in the upper figure follows the general trend of the continuum over the H α line; this option produces the blue wing of H α to be extended far away from the line in the normalized spectrum. For the red dashed-dotted normalization function, a continuum point is selected in the blue wing of the H α line, where a diffuse interstellar band is located; this option produces an incorrect solution.

The spectrum was obtained with CASPEC, attached to the ESO 3.6m telescope. The *SNR* of this spectrum is ~ 200 -300 in the blue region and ~ 150 in the H α region.

The main ionizing source of the Orion nebula, HD 37022 (θ^1 Ori C) is known to have variable spectral features varying in phase or antiphase with a period of 15.4 d (Conti 1972, Stahl et al. 1993, Walborn & Nichols 1994, Stahl et al. 1996). For the study of the spectral variability of this star, some FEROS spectra have been used (some of which were downloaded from the FEROS database and other kindly provided by Dr. Stahl). These observations were carried out with FEROS at the ESO 1.52m telescope in La Silla. The instrument is designed for high-dispersion spectroscopy with $R \sim 48000$ over the spectral range 3700-9200 Å. The achieved *SNR* is 300 at about 4500-5000 Å. The study of this star is presented in Chapter 6. The various phase observations that have been used for the variability study are summarized in Table 6.4 of that chapter.

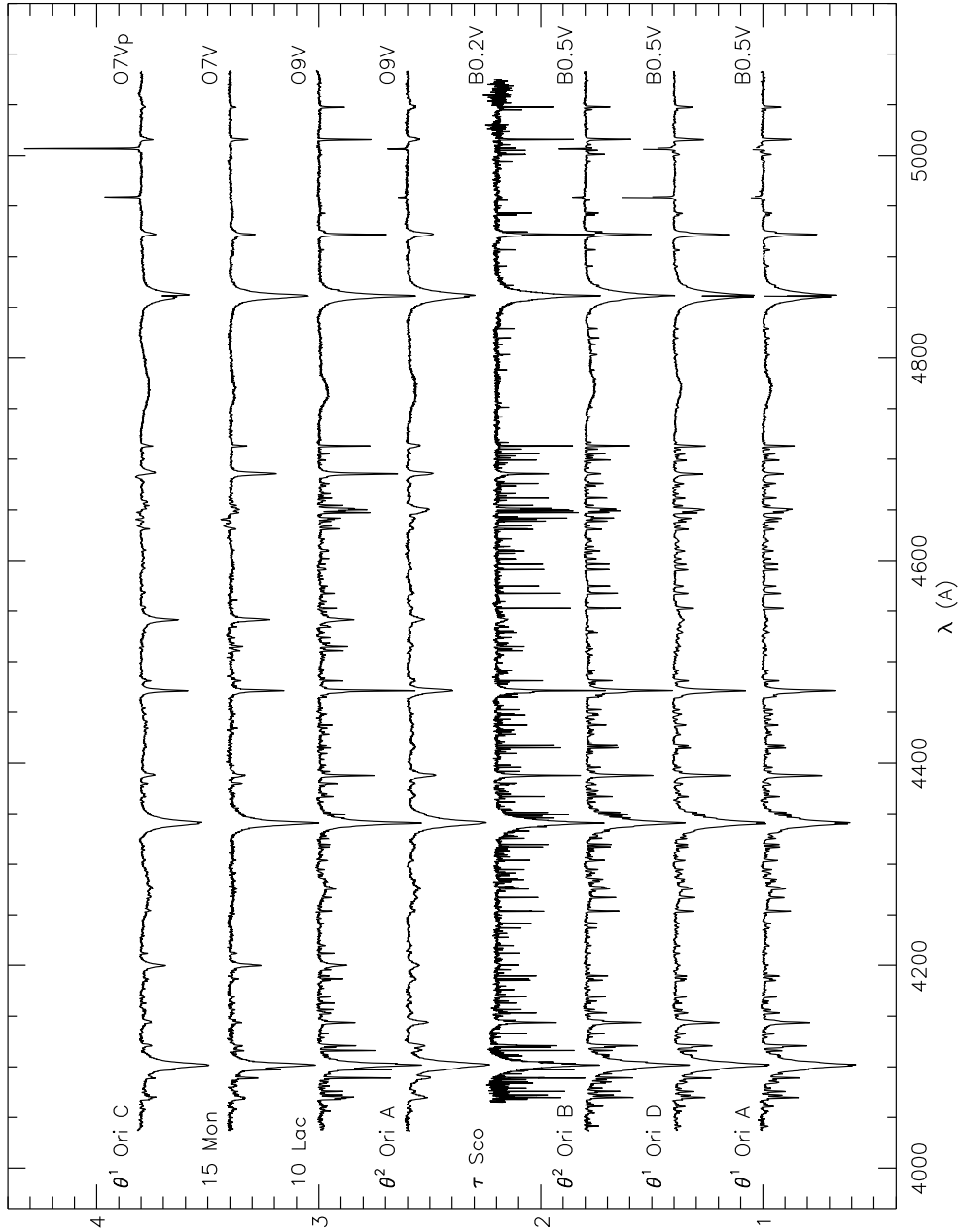


FIGURE 2.3 — Atlas of the INT+IDS spectra in the 4000-5000 Å region used for this study. The τ Sco spectrum is from CASPEC. Several narrow nebular emission lines appear in the spectra of the Orion stars. In these stars, the cores of the hydrogen Balmer lines are contaminated by the nebular lines. Nebular H_{β} and $[O\text{ III}]\lambda\lambda 4960,5007$ lines have been arbitrarily diminished in the θ^1 Ori A and D plotted spectra for the sake of clarity. Many metal lines can be distinguished along with the broad H and He lines in the O9 - B0.5 spectra. The high rotational velocity of θ^2 Ori A causes the metal lines of this O9V star to be shallower, broader and more blended when compared to the other O9 target. The known inverted P-Cygni He II $\lambda 4686$ profile can be seen in the θ^1 Ori C spectrum.

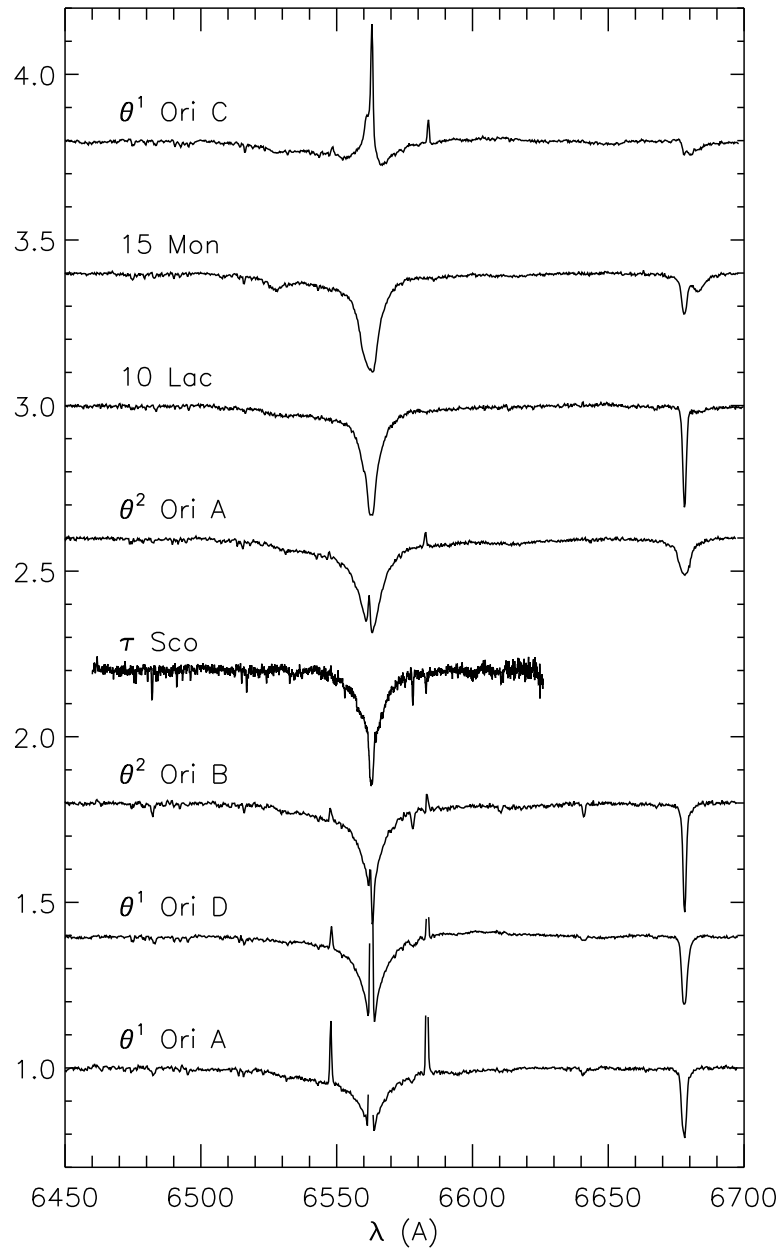


FIGURE 2.4 — Atlas of the INT+IDS spectra centered in H_{α} . The τ Sco spectrum is from CASPEC. Nebular H_{α} and [N II] emission lines have been arbitrarily diminished in the θ^1 Ori A and D plotted spectra for the sake of clarity. Two emission components can be distinguished in the θ^1 Ori C H_{α} line: the narrow one is associated with the nebula, the other one is variable and it is associated with the star (see Section §6.5, Chapter 6).

2.3 Nebular observational dataset

2.3.1 Long-slit spectroscopy

For the study of the Galactic H II region M43 (an apparently spherical nebula close to the Orion nebula) presented in Chapter 7 some of the INT-IDS spectroscopic data from Mónica Rodríguez's thesis (long-slit spectroscopy of several Galactic H II regions) have been recovered. Specifications on her observing runs and the reduction and calibration process can be found in Rodríguez (1999), here we only describe the main characteristics of the M43 spectra concerning our study.

The INT-IDS long-slit observations cover the spectral range $\lambda\lambda 3985\text{-}8810$ Å (taken in three different exposures covering the spectral ranges $\lambda\lambda 3985\text{-}5825$ Å, $\lambda\lambda 5680\text{-}7020$ Å and $\lambda\lambda 6970\text{-}8810$ Å). The selected slit width of $1''.4$ results on a spectral resolution of 4 Å/pixel. Five spectra at different positions from the central star were obtained by dividing the original ~ 2 arcmin length slit into shorter sections (see Figure 2.5 and Table 2.3). Two new columns with extra information have been added to the information provided by Rodríguez (1999): the actual distance from the star to the apertures (since the quoted positions refer to the telescope pointing position in the observing run, which do not fit in with the position of the star); and the non extinction corrected H_α/H_β line intensity ratios, that will be used to estimate the extinction correction for the H_α images.

Since the original line intensity data for these spectra have only been published in Rodríguez's thesis (Rodríguez 1998), the extinction corrected intensities have been summarized below in Table 2.4 for the set of lines of interest.

Slit	Position (")	Size (")	$F(H_\beta) \times 10^{12}$	τ_β	R_V	d (")	$[I(H_\alpha)/I(H_\beta)]_0$
M43-1	+21	28.8	2.03	1.55	5.5	45	4.04
M43-2	+63	26.2	1.42	1.45	5.5	88	4.54
M43-3	+89	25.6	0.59	1.54	5.5	115	5.55
M43-4	-54	17.9	2.01	1.60	6.0	7	4.22
M43-5	-16	23.0	1.97	1.63	6.0	11	4.23

TABLE 2.3 — Relevant data for the five slit sections used by Rodríguez (1999, her Table 2; extended with two extra columns with additional information) for the spectroscopic study of M43. The quoted positions are relative to $\alpha = 05\ 35\ 28.8$, $\delta = -05\ 16\ 19$ (positive numbers indicate shifts to the west). Integrated H_β line fluxes ($\text{erg cm}^{-2} \text{s}^{-1}$) are not corrected for extinction. d corresponds to the distance from the star to the closer side of each slit section to the star position. Non extinction corrected H_α/H_β line intensity ratios have been calculated using the $[\text{N II}] \lambda 5755$ line, present in both blue spectral ranges.

λ (Å)	Ion	$[I(\lambda)/I(H\beta)] \times 100$				
		M43-1	M43-2	M43-3	M43-4	M43-5
4069	[S II]	2.7 ± 0.1	4.4 ± 0.1	4.3 ± 0.4	1.55 ± 0.02	1.8 ± 0.1
4102	H δ	25.5 ± 0.2	25.62 ± 0.09	25.6 ± 0.1	24.6 ± 0.2	25.6 ± 0.1
4340	H γ	46.6 ± 0.1	45.43 ± 0.1	46.5 ± 0.1	46.6 ± 0.2	46.5 ± 0.1
4860	H β	100.0 ± 0.3	100.0 ± 0.2	100.0 ± 0.2	100.0 ± 0.7	100.00 ± 0.05
4959	[O III]	2.97 ± 0.02	4.30 ± 0.04	12.5 ± 0.1	2.98 ± 0.1	3.62 ± 0.1
5007	[O III]	8.88 ± 0.03	13.07 ± 0.05	37.6 ± 0.2	8.98 ± 0.1	10.92 ± 0.1
5518	[Cl III]	0.237 ± 0.004	0.22 ± 0.02	0.344 ± 0.009	0.259 ± 0.009	0.28 ± 0.02
5538	[Cl III]	0.177 ± 0.004	0.16 ± 0.02	0.15 ± 0.03	0.163 ± 0.009	0.21 ± 0.02
5755	[N II]	0.793 ± 0.008	0.977 ± 0.008	1.23 ± 0.08	0.80 ± 0.02	0.76 ± 0.02
5755	[N II]	0.82 ± 0.03	0.88 ± 0.06	0.95 ± 0.06	0.78 ± 0.03	0.76 ± 0.06
5876	He I	0.96 ± 0.03	0.82 ± 0.06	2.02 ± 0.09	0.90 ± 0.03	3.41 ± 0.03
6300	[O I]	1.78 ± 0.03	2.75 ± 0.06	6.0 ± 0.1	1.74 ± 0.06	1.34 ± 0.03
6312	[S III]	0.58 ± 0.03	0.58 ± 0.06	0.43 ± 0.09	0.55 ± 0.06	0.73 ± 0.03
6548	[N II]	34.72 ± 0.09	36.8 ± 0.1	39.4 ± 0.3	35.6 ± 0.2	33.7 ± 0.2
6563	H α	292.2 ± 0.9	292.2 ± 0.8	307 ± 1	290 ± 1	291.9 ± 0.3
6584	[N II]	112.9 ± 0.3	121.1 ± 0.3	128.6 ± 0.5	114.9 ± 0.6	109.7 ± 0.1
6678	He I	0.23 ± 0.03	0.18 ± 0.02	0.74 ± 0.06	0.20 ± 0.02	0.99 ± 0.02
6717	[S II]	23.93 ± 0.08	36.2 ± 0.1	40.01 ± 0.2	24.2 ± 0.1	19.58 ± 0.02
6731	[S II]	24.06 ± 0.06	36.2 ± 0.1	40.5 ± 0.2	24.4 ± 0.1	20.33 ± 0.02
7066	He I	0.211 ± 0.008	0.19 ± 0.01	0.6 ± 0.04	0.19 ± 0.01	0.81 ± 0.01
7136	[Ar III]	0.61 ± 0.01	0.72 ± 0.01	1.94 ± 0.07	0.62 ± 0.03	2.91 ± 0.05
7320	[O II]	1.92 ± 0.04	2.41 ± 0.03	3.4 ± 0.1	1.9 ± 0.1	2.10 ± 0.04
7330	[O II]	1.53 ± 0.04	1.85 ± 0.05	2.63 ± 0.09	1.54 ± 0.07	1.67 ± 0.04
8579	[Cl II]	0.41 ± 0.01	0.539 ± 0.009	0.63 ± 0.03	0.40 ± 0.01	0.360 ± 0.007
8599	Pa14	0.74 ± 0.01	0.69 ± 0.01	0.85 ± 0.04	0.71 ± 0.01	0.94 ± 0.02
8751	Pa12	1.06 ± 0.03	1.10 ± 0.01	1.1 ± 0.04	1.08 ± 0.03	1.13 ± 0.03

TABLE 2.4 — Extinction corrected intensities for the set of lines of interest in the spectral ranges $\lambda\lambda 3985\text{--}5825$ Å, $\lambda\lambda 5680\text{--}7020$ Å and $\lambda\lambda 6970\text{--}8810$ Å. Selected from Tables A.14–A.18 presented in Mónica Rodríguez’s thesis (Rodríguez 1998)

2.3.2 Narrow band imagery

The spectroscopic observational dataset for the study of M43 was complemented with narrow band imagery obtained with the Wide Field Camera (WFC) attached to the prime focus of the INT. The WFC consists of 4 thinned EEV $2k \times 4k$ CCDs with a pixel size of $13.5\mu\text{m}$ corresponding to $0''.33/\text{pixel}$. The edge to edge limit of the mosaic neglecting the ~ 1 arcmin inter-chip spacing is 34.2 arcmins. Figure 2.5 shows a section of the fourth WFC–CCD with an H α image of M43 and the location of the five slit sections used by Rodríguez (1999); the whole region covered by the WFC also includes part of the nearby M42 nebula (see Figure 2.7).

The observations were taken on 25 March 2005, during a service night. Ten images in filters H_α and Sloan r' with an offset of 30 arcsec between them were obtained. Since the night was photometric, one field with Landolt standard stars was observed at two different air masses during the night for the flux-calibration of the H_α and Sloan r' images. Additionally, five images in $[O\text{ III}]$ and $[S\text{ II}]$ filters were obtained⁵. Table 2.5 summarizes the log of the observations. Figure 2.6 shows the transmission curves of the different filters and the position of the brightest nebular lines in the spectral range between 4800 and 7300 Å.

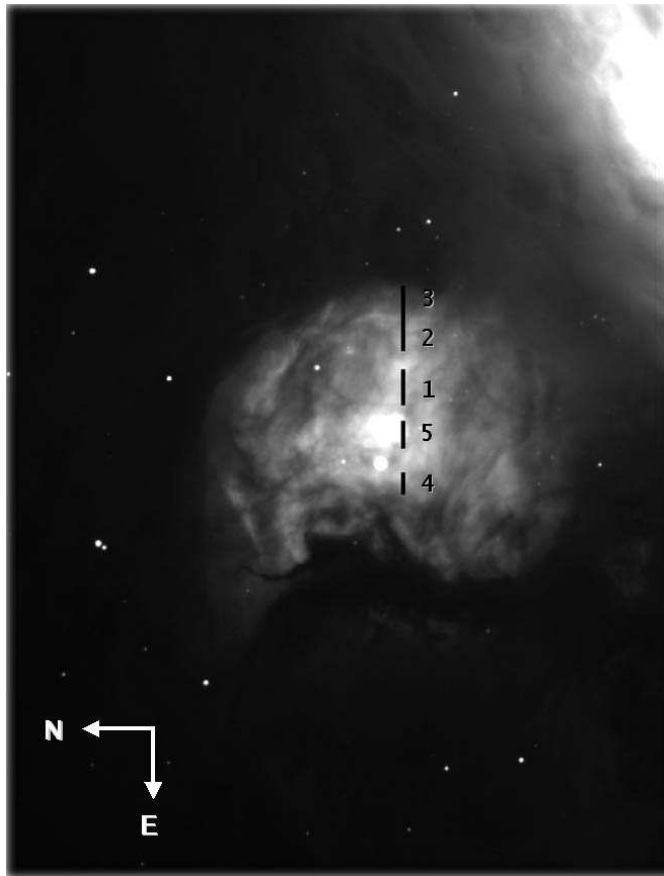


FIGURE 2.5 — INT-WFC M43 image in H_α with the position of the different slit sections used by Rodríguez (1999). Same number identifications will be used in the study presented in Chapter 7 (this thesis).

⁵Since only the surface brightness profiles of the nebula in these lines are of interest, the $[O\text{ III}]$ and $[S\text{ II}]$ images are not flux calibrated.

Filter	λ_0	FWHM	t_{exp}	Target
H α	6568	95	10 x 30 s	M43
Sloan r'	6240	1347	10 x 3 s	M43
[O III]	5008	100	5 x 12 s	M43
[S II]	6725	80	5 x 12 s	M43
H α	6568	95	3 x 70 s	0918+029D
Sloan r'	6240	1347	3 x 10 s	0918+029D

TABLE 2.5 — Journal of observations.

The reduction of the images was done using the IRAF reduction package, following standard techniques. These consist of the correction of the rough images from the bias level and the flat field response of the CCDs; then the dithered images from each filter are aligned and combined together using an unsaturated star in the adjacent field.

To obtain the flux calibrated pure H α images, two different approaches were used. The first one considers the subtraction of the continuum adjacent to the H α line with the field star method applied to the H α and Sloan r' images. Since there are some intrinsic uncertainties associated with this method, which implies that the correction factors could be underestimated or overestimated, the validity of this result was checked by considering another method. This alternative technique uses the H α images along with the long-slit spectroscopic information by Rodríguez (1999).

CALIBRATION OF THE H α IMAGES: FIRST APPROACH

The steps followed to obtain the flux calibrated pure H α emission images are presented below:

- The H α and Sloan r' images are flux calibrated using the standard star observed at two different airmasses.
- The Sloan r' image, multiplied by a correction factor, is subtracted from the H α image. In Figure 2.6 it can be seen that the H α and Sloan r' filters have different FWHM. The correction factor, estimated using the stars in the field, corrects the broad Sloan r' filter to the FWHM of the narrow H α filter and takes into account the different exposure times of the two images.

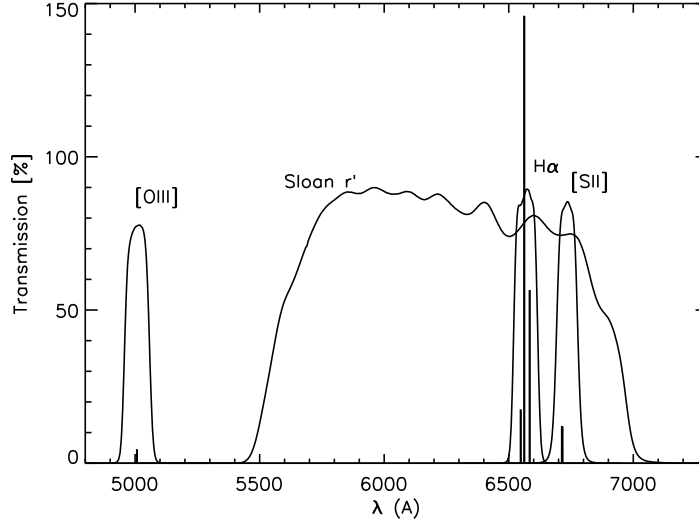


FIGURE 2.6 — Characteristics of the filters used for obtaining narrow band images of M43 with INT-WFC. The brightest nebular lines ([O III] λ 5007, H α , [N II] λ 6548, 6584 and [S II] λ 6717, 6731) are also shown in the plot.

- The H α filter also includes the nearby [N II] lines (see Figure 2.6), so the H α images must be corrected by this [N II] contamination. The H α and [N II] line intensities measured from the spectroscopic observations (see Table 2.4) have been used along with the H α filter transmission curve to estimate this correction factor.

$$F_c(\text{H}\alpha) = cf(\text{N II}) F_m(\text{H}\alpha) \quad (2.1)$$

being F_c the corrected flux, F_m the measured flux, and

$$cf(\text{N II}) = \frac{I(\text{H}\alpha)}{I(\text{N II } 6548) t_{6548} + I(\text{N II } 6584) t_{6584} + I(\text{H}\alpha) t_{\text{H}\alpha}} \quad (2.2)$$

the correction factor due to the N II lines, where t is the H α filter transmission value for the wavelengths corresponding to the H α and [N II] lines, and I are the non extinction corrected intensities. Table 2.6 summarizes these values along with the derived correction factors for each slit section. A mean $cf(\text{N II})$ value of 0.658 has been considered for correcting the H α images of nebular N II lines emission.

- Finally, the flux calibrated H α images must be corrected for extinction.

The weak point of this method is the following. Since the Sloan r' filter also includes the H_α line, as well as another nebular emission lines like $[N II]$ and $[S II]$, the final pure H_α emission could be underestimated when the Sloan r' image is subtracted from the H_α image. Some tests using the long-slit nebular spectra of M43 have shown that this underestimation can be $\sim 6-15\%$, depending on the correction factor considered for the Sloan r' images.

To check this calibration, a second different technique has been applied to calibrate the H_α images.

Line	Transmission (%)	M43-1	M43-2	M43-3	M43-4	M43-5
H_α	0.875	100.	100.	100.	100.	100.
$[N II] \lambda 6548$	0.843	11.9	12.6	12.8	12.2	11.5
$[N II] \lambda 6584$	0.880	38.8	41.6	42.1	39.8	37.7
<i>c.f.</i> (N II)		0.66	0.65	0.65	0.66	0.67

TABLE 2.6 — Spectroscopic information used for removing $[N II] \lambda\lambda 6548, 6584$ contamination from the H_α image. The non extinction corrected intensities for the $[N II]$ lines, relative to $H_\alpha = 100$ are from Rodríguez (1998). The derived *c.f.* (N II) values for each slit section have been calculated using Equation 2.2.

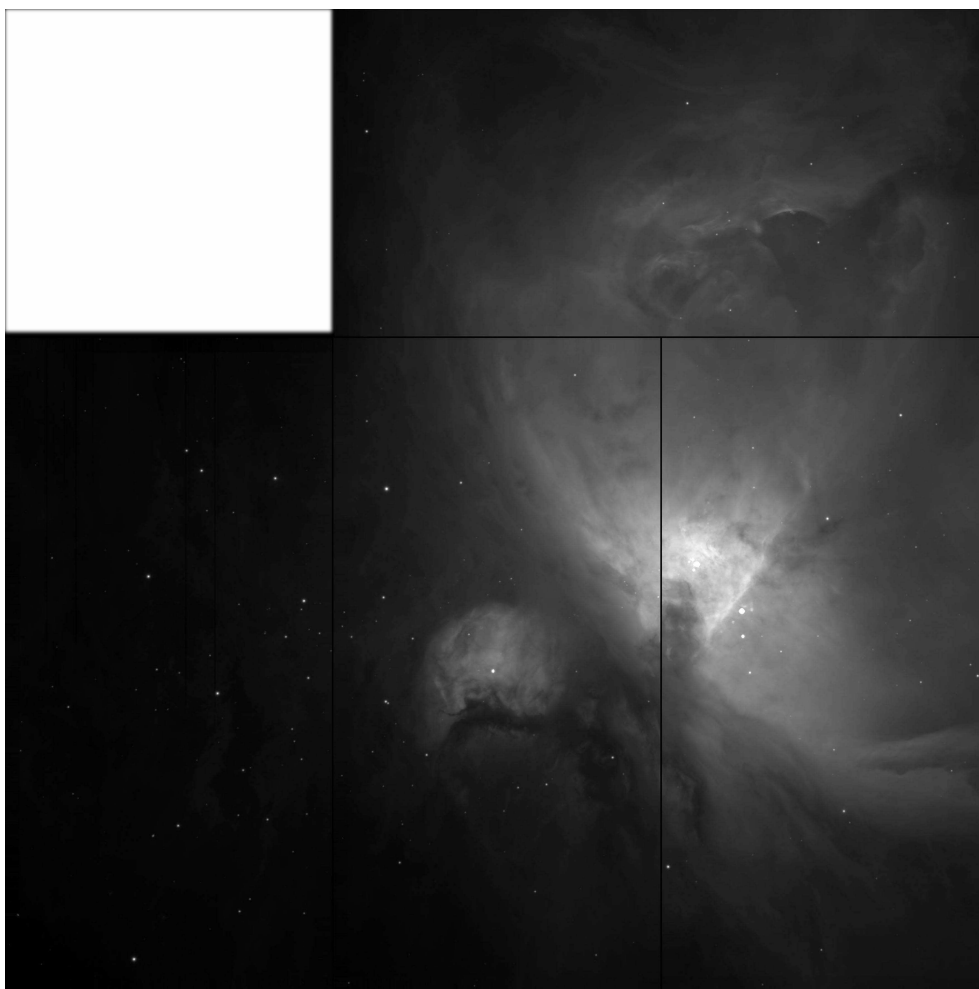
CALIBRATION OF THE H_α IMAGES: SECOND APPROACH

This second technique uses the long-slit spectroscopic information by Rodríguez (1999) to calibrate the H_α images. These are the steps followed in this case:

- The various H_α fluxes associated with the different slit sections are calculated with the H_β fluxes summarized in Table 2.3 and the corresponding non extinction corrected $I(H_\alpha)/I(H_\beta)$ ratios.
- The H_α image is multiplied by a correction factor to convert the total number of counts inside the slit M43-1 to the corresponding $F(H_\alpha)$ for this slit section.
- The information from the other slit sections is used to check the validity of this calibration. The differences found are below 15%.
- Again, the flux calibrated H_α images must be corrected for extinction.

COMPARISON OF RESULTS FROM BOTH METHODS

The values derived through both techniques for the integrated non extinction corrected H_α flux are in quite good agreement: $(3.8 \pm 0.4) \times 10^{-9} \text{ ergs}^{-1}\text{cm}^{-2}$ and $(4.2 \pm 0.2) \times 10^{-9} \text{ ergs}^{-1}\text{cm}^{-2}$ respectively. As it was expected, the value given by the first method is $\sim 10\%$ lower than the other one. A final value of $(4.0 \pm 0.4) \times 10^{-9}$ will be considered. In Chapter 7 (Section §7.3), this value is corrected by distance and extinction, estimating the integrated H_α luminosity of M43.

FIGURE 2.7 — INT-WFC image of M42 and M43 nebulae in H_α

DEALING WITH STELLAR ATMOSPHERE CODES

... y entonces dice el Físico
— *para medir el volumen de una vaca* —
"Supongamos que es una esfera".
- Un chiste -

In this chapter the model atmosphere codes used in this thesis will be summarized, stressing their main characteristics. The strategy followed for determining the stellar parameters and abundances, as well as modeling the ionizing flux distribution of massive stars is based on the analysis of their optical spectra using the recent generation of spherical, line-blanketed model atmosphere codes.

3.1 Introduction

THE outer layers of blue luminous stars are characterized by strong NLTE conditions, spherically extended geometries and the effect of hundreds of thousands of flux absorbing metal lines present in the UV range. The high luminosity and low density of these objects results in the radiative transitions dominating over the collisional ones producing significant departures from LTE conditions. The presence of strong extended stellar winds invalidates the hypothesis of plane-parallel geometry. Finally, these stars emit the bulk of their radiative flux in the EUV and UV ranges, where hundreds of thousands of metal lines are located, producing blocking of the emergent flux in these spectral windows, backwarming of the inner layers due to the scattering of radiation, and redistribution of the radiation to lower energies (in the so called line blocking and line blanketing effects). The radiative driven wind theory states that the interaction of the radiation with the opacity of these metal lines is

what drives the material of the outer layers of these stars, producing the stellar wind (Lucy & Solomon 1970; Castor, Abbot & Klein 1975).

All the above effects must be taken into account when modeling the atmospheres of blue luminous stars. An ideal model atmosphere code should consider all of these problems in a detailed manner. However this would require an enormous computational effort. To avoid this, depending on the specific object one wants to treat, some of the physical processes can be relaxed without affecting the reliability of the model output. For example, if one wants to study photospheric lines in stars with high surface gravity, a plane-parallel geometry can be considered as an approximate solution to the problem. Obviously this simplification is not valid to treat lines formed in the outer parts of the atmosphere, affected by the stellar wind.

Previous codes by Mihalas & Auer (1970) considered plane parallel, NLTE, H-He atmospheres (i.e. unblanketed models). Kurucz (1979, 1991) included line blanketing effects in his grid of plane parallel models (ATLAS9), however neglecting NLTE conditions. ATLAS9 has been widely used not only for the study of low mass stars, but also in the high mass regime regarding different aspects: Vacca et al. (1996) presented a SpT - T_{eff} - $Q(\text{H}^0)$ calibration based on Kurucz (1991) models, the QUB¹ group extensively used ATLAS9 models in the 90's for deriving stellar parameters and abundances of B-type stars in the Galaxy and the Magellanic Clouds; many studies on H II regions modeling also used these model atmospheres (e.g. Stasińska & Leitherer 1996). Kunze (1994, cf. Kunze et al. 1992) included up to 9 of the most abundant elements (H, He, C, N, O, Ne, Mg, Al, Si, S, Ar) to account for line blanketing effects in NLTE plane parallel models (however, the iron group elements were not included in this calculation). The main limitation during these years was the enormous computational effort that was required by a NLTE line blanketed calculation. Much effort has been devoted to improve the computational methods applied in stellar codes (e.g. Workshop on "Stellar atmosphere modeling", Tübingen, 2002); the resulting advances together with the increase in the efficiency of computers during the last decades, have made the modeling of atmospheres of hot luminous stars possible in reasonable computational times.

All models mentioned above assume a plane parallel geometry, however in some cases stellar wind effects are highly important. For very low density winds, the extension of the atmosphere is negligible and plane-parallel geometry can be used, however strong UV resonance lines can be affected by the extension and the mass outflow. For increasing density winds, the region where the continuum and the lines

¹Queen's University of Belfast

are formed can be affected by wind effects. Strong recombination lines in the optical (e.g. H_{α} , $He\ II\ \lambda\ 4686$) and IR begin to show contamination by the outflow, going from partial re-filling to complete emission (see review on winds from massive star by Kudritzki & Puls 2000). Winds are also able to modify the ionizing radiation of hot stars dramatically (Gabler et al. 1989; Najarro et al. 1996; Sellmaier et al. 1996), an effect that has important consequences for the ionization of the interstellar medium by hot stars. Finally, also the IR, (sub)millimeter and radio continua are strongly affected.

During the last years, several groups have worked in parallel on different codes that consider various approximations for the global solution depending on the specific problem. There are two main families of model atmosphere codes for massive stars: the plane-parallel, hydrostatic models and those so-called "unified models" (Gabler et al. 1989) in which spherically symmetric geometry with a smooth transition between the photosphere and the wind is considered. All of these account for the NLTE and line blanketing effects (although also offer the possibility of calculating LTE and/or unblanketed models). TLUSTY (Hubeny & Lanz 1995) is the plane-parallel code widely used nowadays; FASTWIND (Santolaya-Rey et al. 1997, recently updated, see Puls et al. 2005), COSTAR (Schaerer & de Koter 1997), CMFGEN (Hillier & Miller 1998), and WM-*basic* (Pauldrach et al. 2001), belonging to the second category² take into account winds with expanding spherical geometries.

LINE BLANKETING EFFECTS

It has been mentioned above that line blanketing effects are important in the modeling of blue luminous stars, but what is it exactly and how does it affect the structure and the emergent fluxes of stellar models? Blue luminous stars emit the bulk of their radiation in the (E)UV range, a spectral range affected by the presence of hundreds of thousands of metal lines producing line blocking and line blanketing effects. Although both effects are related, they affect in two different ways the structure and emergent flux of the stellar atmosphere. The opacity of the large amount of lines reduces the emergent (E)UV flux (line blocking), but also, as there is less frequencies available for the effective transport of the flux outwards in the atmosphere, the temperature gradient increases (producing the so-called backwarming effect). Obviously, these effects have drastic consequences on the ionization stratification and the emergent fluxes. The first consequence is that the backwarming effect affects

²CMFGEN and WM-*basic* did not originally belong to "Unified Model Atmospheres", particularly CMFGEN that originally only described the wind (whilst WM-*basic* was slightly more "unified"). However the statement can be taken as correct for current versions.

the ionization in the line formation region of the diagnostic lines, leading to higher ionization (e.g. the He II lines are stronger and therefore a lower T_{eff} is needed to fit the observed lines when models with line blanketing are considered). On the other hand, fluxes are not only affected by the change in T_{eff} , but also (and this is the main effect) by line blocking. Lyman continuum fluxes are reduced and hence, as the total emergent luminosity must be conserved (which means that the product of the flux times r^2 has to be conserved), IR and radio fluxes are enhanced.

These line blanketing effects have a large impact on derived luminosities, radii and masses of massive stars, due to the change in the emergent flux at a given temperature (see review by Herrero & Najarro 2005). Additionally these changes have a significant effect on the ionization of the surrounding material predicted by photoionization models.

3.2 Stellar model atmosphere codes

This section presents the stellar model atmosphere codes applied in this thesis. The work developed here mainly aims to a spectroscopic analysis of blue massive stars located inside H II regions to derive their stellar parameters, abundances and ionizing flux distributions (to be followed by a study of the surrounding nebula). The two latter determinations are performed by means of `FASTWIND`, a unified model atmosphere optimized for the analysis of optical and IR spectra of massive stars. `FASTWIND` is designed for fast computations but makes only an approximate treatment of the opacity from metals and hence the emergent flux in the spectral window where line blocking is important, is only approximate. The ionizing flux distributions are therefore modeled using `WM-basic`, another spherically extended stellar atmosphere code aimed to the precise study of the (E)UV range, with a very detailed treatment of the line blanketing effects over this spectral range. Indeed it is from this code (`WM-basic`) that the approximate treatment of line blanketing has been developed for `FASTWIND`. Therefore this code is consistent with the parameters determined with `FASTWIND` in the optical.

In Chapter 5, `FASTWIND` results from a detailed oxygen abundance analysis for the star τ Sco are compared with those derived from another two stellar atmosphere codes widely used by the scientific community; these are the spherically extended code `CMFGEN` and the plane parallel code `TLUSTY`. In Chapter 7, the spectral energy distributions (SED) predicted by `WM-basic` and `CMFGEN` for the star HD 37061 are compared.

The main characteristics of the codes FASTWIND and WM-*basic*, as well as the codes TLUSTY and CMFGEN, used for the comparisons, are presented below:

FASTWIND (Santolaya-Rey et al. 1997, Puls et al. 2005)

FASTWIND (Fast Analysis of STellar atmospheres with WINDs) is a *fast performance* code developed for calculating NLTE line-blanketed model atmospheres for hot stars with winds. It is optimized for treating optical and IR spectroscopic analyses of normal stars with $T_{\text{eff}} \gtrsim 8500$ K (OBA-stars) of all luminosity classes and wind strengths.

The main objectives that have guided the developers of FASTWIND since the initial version of the code are: easy to use, robust, and fast and portable performance. Since the first version, presented in Santolaya-Rey et al. (1997) to the latest one, described very recently (Puls et al. 2005), many improvements have been included in the code (the main ones are an approximate treatment of the line blanketing/blocking effects and a consistent calculation of the T-structure by means of the thermal balance of electrons). Obviously, the motivations which have driven the development of FASTWIND have been and still are those mentioned above (a fast performance to be of highest priority in the age of multiobject spectrographs where hundreds of spectra are obtained simultaneously and require fast analysis). The required computational efficiency is obtained by applying appropriate physical approximations to processes where high accuracy is not required (regarding the objective of the analysis: optical/IR lines).

The characteristics of the code have been extensively described in Santolaya-Rey et al. (1997), and Puls et al. (2005). The main points regarding the use of FASTWIND in this thesis are emphasized in Section §3.3.

FASTWIND has been tested and applied for a variety of different spectral types and luminosity class objects. Urbaneja et al. (2003, 2005a,b), Trundle et al. (2004) and Trundle & Lennon (2005) have centered their studies on B supergiants in the Magellanic Clouds, the spiral galaxies M33 and M31, or even galaxies beyond the Local Group; Herrero et al. (2002) and Repolust et al. (2004) have determined new effective temperature scales for Galactic O stars (either supergiants or dwarfs); Massey et al. (2004) derived a similar scale as a function of metallicity studying O stars in the Magellanic Clouds; in this thesis I will present a detailed analysis of the Trapezium cluster stars ionizing the Orion Nebula (also published in Simón-Díaz et al. 2005).

WM-basic (Pauldrach et al. 2001)

WM-basic is a detailed NLTE atmospheric model for hot luminous stars with homogeneous, stationary, and spherically symmetric radiation driven winds.

This code aims mainly at the prediction of EUV/UV fluxes and profiles, through a sophisticated and consistent description of line blocking and blanketing. However the bound-bound radiative rates are calculated in Sobolev approximation (including continuum interactions) and the code does not include broadening terms, hence the optical lines usually considered for the stellar parameter determination are not reliable for diagnostic purposes.

The solution of the hydrodynamics produced by the scattering and absorption of Doppler shifted metal lines provides a realistic stratification of the density and velocity, particularly in the transonic region. The line contribution to the radiative acceleration is parameterized following the formulation by Castor, Abbot & Klein (1975) — CAK — (see also Pauldrach et al. 1986) that uses the concept of line-force multiplier:

$$M(t) = \kappa t^{-\alpha} \left(\frac{n_e}{W(r)} \right)^\delta \quad (3.1)$$

Where t is a dimensionless depth parameter defined in the Sobolev approximation, $t \equiv v_{\text{th}} \chi_{\text{Th}} / (dv/dr)$ with v_{th} the thermal velocity of the ion and χ_{Th} the electron opacity, n_e is the electron density, $W(r)$ is the geometrical dilution factor and κ , α and δ are the force multiplier parameters. κ represents the number of lines with strengths above some critical value, α defines the slope of the line strength distribution and δ is included to account for changes in the wind ionization structure.

Detailed atomic models are considered for all the important ions of the 149 ionizations stages of 26 elements (H to Zn, apart from Li, Be, B and Sc), resulting in a total of 5000 levels. More than 30000 bound-bound transitions for the NLTE calculations and more than 4 million lines for the line-force and blocking calculations are accounted for. Additional line data were taken from the Kurucz (1992) line list: approximately 20000 lines for ions of Mn, Fe, Co and Ni.

The authors have developed a fast numerical method which accounts for the blocking and blanketing influence of all metal lines in the entire sub- and supersonically expanding atmosphere. The line blocking effects are treated by means of an Opacity Sampling technique in the initial iterations and a detailed radiative line transfer (an

exact solution of the transfer equation in the observer's frame) used for the final iterations. Line blanketing effects over the temperature structure are treated using a flux correction procedure in deeper layers ($\tau_R \geq 0.1$) and the thermal balance of electron heating and cooling in the outer layers.

This code allows the user to account for the EUV and X-ray radiation produced by cooling zones which originate from the simulation of shock heated matter.

Some examples of studies where *WM-basic* has been applied are those by García & Bianchi (2004) and Bianchi & García (2002) who determine the stellar and wind parameters of a sample of Galactic early type O stars by analyzing the UV and FUV spectra; Smith et al. (2002) present a grid of ionizing fluxes for O and WR stars for the use with evolutionary synthesis codes and single star H II region analyses. Finally, Rix et al. (2004) combine the evolutionary spectral synthesis code *STARBURST99* with the output from *WM-basic* for obtaining integrated UV stellar spectra of star forming regions (to be applied in the study of high redshift galaxies)

CMFGEN (Hillier & Miller 1998)

CMFGEN is a NLTE, line blanketed code with spherical geometry and mass loss. Radiative transfer is treated "exactly" in this code (all lines are treated in comoving frame, even those from iron group elements), meaning that no opacity redistribution or sampling techniques are used. Therefore this code can be used for spectroscopic studies from the (E)UV range to the (F)IR, even though it is very time consuming (whilst a *FASTWIND* model takes 20-30 minutes, *CMFGEN* takes anything from 3-7 hours).

The approach driving this code is the inclusion of as many lines as possible in order to fully describe the effects of line blanketing while minimizing the number of level populations to be explicitly solved (using the idea of super levels first pioneered by Anderson 1989). The number of superlevels and their links to the real atomic levels is easily modified. This allows flexibility in testing the accuracy associated with various superlevels assignments.

CMFGEN was originally designed for the analysis of very dense winds, so the treatment of the photospheric density stratification was approximate. At present, the velocity and density structures are not self-consistently computed but has to be given as input, either as input data or parameterized (see in Martins et al. 2004, an example of how these structures are included in the code).

CMFGEN has been applied to the spectroscopic study of massive stars in various spectral windows. From FUV, UV and optical spectroscopy (Hillier et al. 2003; Bouret et al. 2003; Evans et al. 2004; Martins et al. 2004) to NIR and FIR spectroscopy (Najarro et al. 2004; Lenorzer et al. 2004). Martins et al. (2002, 2005) have presented a new effective temperature scale of O stars (somewhat different to the previous one by Vacca et al. 1996 and consistent with those by Herrero et al. 2002, García & Bianchi 2004, Repolust et al. 2004 and Massey et al. 2004).

TLUSTY (Hubeny 1988, Hubeny & Lanz 1995)

TLUSTY is a code for calculating plane parallel, horizontally homogeneous, stellar model atmospheres in radiative and hydrostatic equilibrium. Departures from LTE are allowed for a set of occupation numbers of selected atomic and ionic energy levels. The program is fully data oriented as far as the choice of atomic species, ions, energy levels, transitions and opacity sources is concerned (there are no default opacities built in). The model atmosphere code is completed with SYNSPEC, a program for obtaining the formal solution (i.e. calculating the synthetic spectrum) from a given model atmosphere.

The basic concepts, equations and numerical methods used are described in Hubeny (1988). The new developments included in subsequent versions are described in detail in Hubeny & Lanz (1992, 1995) and Hubeny et al. (1994). One of the most important features of the new version of the program (v. 200) is that it allows for a fully consistent, NLTE metal line blanketing. Treatment of line blanketing is done either by means of Opacity Distribution Functions (ODF) or Opacity Sampling (OS).

In order to construct realistic NLTE model atmospheres for O-type stars, Lanz & Hubeny (2003) included about 100000 individual atomic levels of over 40 ions of H, He, C, N, O, Ne, Si, P, S, Fe and Ni in the calculation of their OSTAR2002 grid. The levels are grouped into about 900 NLTE superlevels. A total of 8000 lines of the light elements and about 2 million lines of Fe III-Fe VI and Ni III-Ni VI are accounted for in the calculations.

TLUSTY and SYNSPEC codes, the OSTAR2002 grid and all the atomic data files used on it can be downloaded from <http://tlusty.gsfc.nasa.gov>. There is also a very complete user's guide available.

3.3 Quantitative spectral analysis: FASTWIND

3.3.1 The application FASTWIND

In this thesis, FASTWIND is used to derive the stellar parameters and abundances of O and early-B main sequence stars through the analysis of their optical spectrum. Its fast performance makes it possible to create grids covering the required large space of stellar parameters with low computational times. This advantage is also valid to generate microgrids for the abundance analysis study (e.g. a total of up to 9-16 models are needed when the curve of growth method is used, see below).

Here, the main tasks concerning the use of FASTWIND are described, together with the steps that have to be followed for generating synthetic spectra to compare with the observations.

TEMPERATURE STRUCTURE

The establishment of the temperature stratification from a rigorous treatment of radiative equilibrium is a very time-consuming process as the radiative equilibrium equation is strongly coupled with the formulae governing the physics of the stellar atmosphere (namely the hydrodynamic, statistical equilibrium and radiative transfer equations). Following the fast performance philosophy of this code, the temperature is not derived directly from the radiative equilibrium equation. The basic idea for reducing the computational effort is decoupling the calculation of the temperature stratification from the rest of the problem.

Originally, the code used an approximate T-stratification defined by the NLTE-Hopf functions (Santolaya-Rey et al. 1997). The three parameters that characterize these functions, the so-called NLTE-Hopf parameters (q_0, q_∞, γ), are included ad-hoc, with the only requirement that the defined T-structure must conserve the total flux along the atmosphere within an error $\leq 3\%$. Above some point in the atmosphere, where the temperature reaches a given fraction of the T_{eff} , the temperature is held at this fixed value, resulting in an isothermal wind. The NLTE-Hopf parameters depend mainly on T_{eff} , $\log g$ and metallicity (Z) and are therefore different for pure HHe and line-blanketed models (as this is a flux conservative method, the correct amount of line blanketing is "automatically" obtained if the NLTE-Hopf parameters are selected correctly). Usually they are estimated by a *trial and error* process based on an initial grid of values determined from alternative model atmosphere codes viz. TLUSTY, ATLAS9, etc (note discussion is Santolaya-Rey et al. 1997, about translation of plane parallel Hopf parameters to spherical dimensions).

A very recent update of FASTWIND (Puls et al. 2005) allows to calculate the temperature structure self-consistently through a flux correction method in the lower atmosphere and the thermal balance of electrons method (Kubát et al. 1999) in the outer one. The computational effort required by this method is somewhat higher than the original one³, however three improvements justify it:

- Although the initial guess of the T-stratification still use the NLTE-Hopf parameters, the method converges the model to a final temperature structure that is independent on this initial guess. Therefore the final T-stratification is now user-independent (note below comment on density structure).
- The flux is conserved better in this method (usually $\leq 1\%$, see Table 3.1).
- The T-structure in the outer part of the atmosphere is now calculated. This is particularly important for the IR-spectroscopy, since the IR is formed above the stellar photosphere and depends critically on the run of T_e in those regions, where the first method is no longer applicable.

Figure 3.1 shows a comparison of the final T-structures resulting in both methods along with the flux conservation reached. The initial guess of the temperature (i.e. initial Hopf parameters) is the same for both models. The agreement between both T-structures is fairly good for $\tau_R \geq 10^{-2}$ (for the selected NLTE-Hopf parameters), however the flux conservation is better in the "temperature correction method".

VELOCITY LAW FOR THE WIND

FASTWIND does not solve the hydrodynamic equations. Instead, the velocity law for the wind (the outer expanding atmosphere) is specified by a prescribed β -type velocity law depending on two parameters, β and v_∞ :

$$v(r) = v_\infty (1 - b/r)^\beta \quad (3.2)$$

The inner atmosphere (photosphere) is in pseudo-hydrostatic equilibrium, with a velocity law following from the equation of continuity. Both parts are connected by a smooth transitions in the sonic region (see Santolaya-Rey et al. 1997 for a detail description of the hydrodynamics considered in FASTWIND).

³A model with H, He, O and Si atoms considered explicitly takes ~ 10 min when the temperature structure is held fixed and ~ 30 min when the temperature correction method is activated.

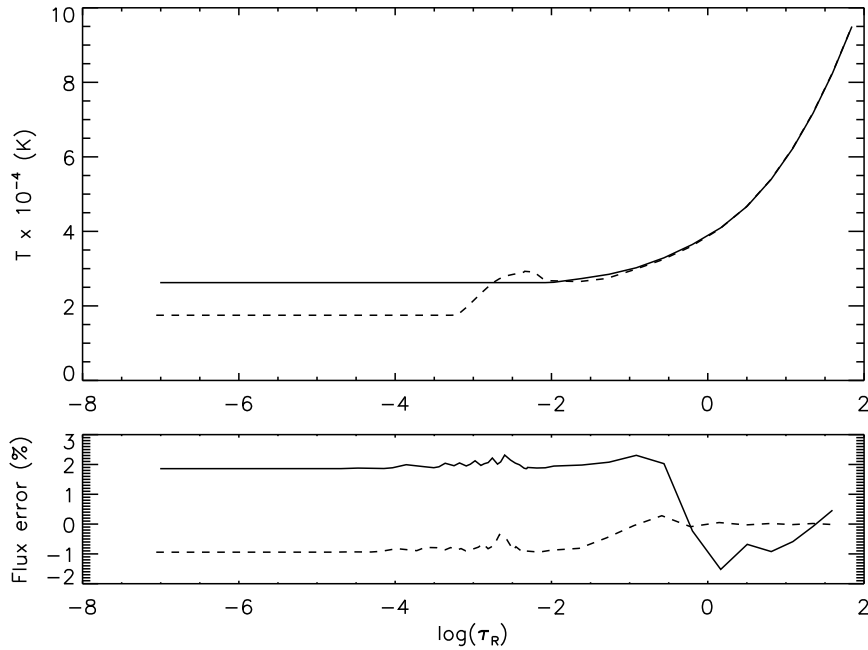


FIGURE 3.1 — Example of the final FASTWIND T-structure for a model with $T_{\text{eff}} = 35000$ K, $\log g = 4.0$ and $\log Q = -13.5$. (Upper panel) The initial (solid) T-stratification, defined by the NLTE-Hopf function, is modified to the final (dashed) structure. (Lower panel) The flux conservation is better in the whole atmosphere when the temperature is self-consistently calculated (red). The flux conservation for the case when the initial T-structure is not updated is shown as a black curve.

The density stratification is derived from both velocity laws and the equation of continuity, and it is highly dependent on the initial Hopf parameters, as the density structure is not recalculated for the final convergence of the temperature structure.

ATOMIC MODELS

Information concerning the physical state of the plasma in objects for which LTE is not valid can be extracted from spectra only if radiative and collisional rates for atoms and ions are known. NLTE model atoms for statistical equilibrium computations consist of a compilation of energy levels and radiative and collisional transition data; spectrum synthesis demands accurate wavelengths, transition probabilities and line-broadening data. Therefore, model atoms are included with a different degree of complexity in the various steps followed in a model atmosphere calculation.

Hydrogen and helium are the most important atoms affecting the physical structure of the stellar plasma, followed by the line blanketing effects due to metals. To calculate an exact blanketed model atmosphere one should include both hydrogen and helium atoms and the metallic species in detail (e.g. TLUSTY and CMFGEN). This implies that rate equations must be solved with the consideration of all radiative and collisional transitions between levels of important ions, which is a very consuming task. In order to save significant computational effort, FASTWIND considers an approximate treatment of the line blanketing/blocking effects. The code distinguishes between explicit elements that are included in detail and can be synthesized later when solving the formal solution, and background elements producing the line blanketing and whose occupation numbers are calculated by means of an approximate solution of the NLTE rate equations. Data for the background ions are taken from Pauldrach et al. (2001; WM-*basic*) and are provided in a fixed form. Lines of these elements cannot be synthesized unless they are included explicitly.

Fine structure is accounted for in the formal solution, where a better sampling for the frequency grid is considered, the occupation numbers are separated according to their statistical weights and broadenings are specified in detail. Obviously, the formal solution can only be applied to levels that have been explicitly included (i.e. the occupation numbers for these levels have previously been calculated).

An important characteristic of FASTWIND concerning the treatment of model atoms is that when one element is included explicitly, it is no longer considered as a background element. Therefore, if the detailed definition of the explicitly included element is not the same than that used in the background (c.f. it considers a different number of ions) the line blanketing effects can be affected. Nevertheless, it is supposed that the blanketing is principally produced by Fe and Fe-group elements, so including C, N, O, Si, or Mg explicitly should not produce any effect (see Figure 3.2 and comment on Section §3.3.2).

The main advantage of the "approximate line blanketing" method is that the computational time required for the calculation of a NLTE line blanketed model atmosphere is reduced. For good cases, while running TLUSTY or CMFGEN models for the T_{eff} and $\log g$ determination using the optical H-He line requires about 5 and 8 hours respectively, FASTWIND models only need ~ 10 min. In FASTWIND models only H and He are required to be included explicitly, and since the statistical equilibrium equations have only to be solved for the explicit elements, the computational time is reduced. Moreover, for an abundance analysis, only the elements for which one wants to synthesize lines (e.g. Si or O) have to be included explicitly, along with hydrogen and helium.

Following the philosophy of the NLTE, hydrostatic, plane-parallel line formation code DETAIL (Butler & Giddings 1985), FASTWIND is completely "*data driven*". The code itself is independent of any specific data except for the implicit consideration of the background elements producing the line blanketing. This allows for new model atoms to be included and subsequently updated without complication. The atomic models that have been considered for the FASTWIND analyses presented in this thesis are described below. Wavelengths and transition probability data for those oxygen and silicon lines accounted for in the formal solution and used in the abundance analysis of early B-type stars are summarized in Tables 5.1 and 5.2 (Chapter 5).

- **HYDROGEN AND HELIUM:** The H and He model atoms (hereafter combined as A10HHe) consist of 20 NLTE levels for H I and He II, and 49 NLTE levels for He I (Puls et al. 2005 and references therein). Hydrogen and helium lines are affected by Stark broadening, so this is taken into account in the formal solution. As optical lines from these ions are used for the T_{eff} and $\log g$ determination by means of a visual comparison of the synthetic and observed profiles (see Section §3.3.2), an accurate definition of the Stark broadening is required.
- **OXYGEN:** The oxygen model atoms now available for use with FASTWIND were introduced by Urbaneja (2004). Two versions for the oxygen model atom have been used for our stellar abundance analyses. The original simpler version (hereafter O23-3) is basically the O I-IV model by Becker & Butler (1988, see Urbaneja 2004 for a more detailed description of this model and the update cited below). Becker & Butler (1988) used data by Henry (1970) for the O II radiative bound-free transitions (RBF), and energy levels by Moore (1971). M.A. Urbaneja updated this model in his thesis (hereafter O23-op), including up to 60 levels for O III and replacing the original RBF transitions by the OPACITY PROJECT data for the lower ten levels. The energies of these first 10 levels were changed to be consistent with the OP data.
- **SILICON:** The original silicon model atom include the Si II, Si III and Si IV ions with total number of NLTE levels 34, 28 and 18 respectively. Trundle et al. (2004) found that the initial 12-level Si II model, described by Becker & Butler (1990) produced severe discrepancies for the analyses of mid to late B-type stars (B2 - B9) when comparing with TLUSTY models. Therefore, this Si II model was replaced with a more complete 34-level ion and the discrepancies disappeared. However for the stars studied in this thesis (with spectral types earlier than B1), the Si II ion is only a trace ion, so the initial Si II-IV model has been stripped down to a simpler Si III-IV model (hereafter Si34).

FUNDAMENTAL STELLAR PARAMETERS

Several parameters can be varied to calculate different models. These are the usual ones, also used in the plane-parallel models: effective temperature, gravity, microturbulence, helium abundance and metallicity (T_{eff} , $\log g$, ξ_t , $\epsilon(\text{He})$ and Z respectively), plus four additional parameters: the stellar radius, R , that accounts for the sphericity, and the mass loss rate, the exponent of the velocity law and the wind terminal velocity (\dot{M} , β and v_∞ respectively) that characterize the wind properties. The parameter space can be reduced by considering that models with the same wind-strength parameter, $Q = \dot{M} (Rv_\infty)^{-1.5}$ show almost identical wind effects on the optical lines for a given β value (Puls et al. 1996). Finally, for the abundance analysis, the abundances for the elements of interest must be indicated, $\epsilon(X)$. The abundances for the metals that are not included explicitly are calculated scaling the solar abundances from Grevesse & Sauval (1998) with the metallicity.

GENERATING GRIDS OF MODELS AND SYNTHETIC SPECTRA

Once the atomic models have been selected one can proceed to generate grids of models for the analyses. Each model is defined by a large number of parameters (T_{eff} , $\log g$, $\epsilon(\text{He})$, R , ξ_t , v_∞ , β , \dot{M} , Z and $\epsilon(X)$ of the elements that are considered explicitly), so creating a grid that covers the whole space of parameters implies a highly computational effort. To reduce it, it is convenient to make some previous assumptions concerning the grid needed. For example, as it has been mentioned above, models with the same Q parameter show almost identical optical lines, and as the analyses presented here are centered on these optical lines, then three parameters can be merged together (R , v_∞ and \dot{M}). The stars that will be analyzed with this grid are Galactic stars, so the metallicity is fixed to a solar value. Finally, the helium abundance will be fixed to a normal value ($\epsilon(\text{He}) = 0.09$) and the parameter β to 0.8 (Repolust et al. 2004). The resulting subgrid reduces the number of parameters that will be varied to T_{eff} , $\log g$, ξ_t , Q and $\epsilon(X)$.

At this point, the methodology separates in two different steps, and each one needs the calculation of different grids:

1. The stellar parameters determination, based on the analysis of the optical H and He I-II lines.
2. The abundance analysis, based on the curve of growth method.

Both steps are described in following sections, along with the grids calculated in each case.

3.3.2 Stellar parameters determination: methodology

The technique used for the derivation of the stellar parameters in O and early B main sequence stars is already standard and has been described elsewhere (viz. Herrero et al. 2002, Repolust et al. 2004). The analyses are based on visual fitting of hydrogen Balmer lines and He I and He II lines with synthetic lines previously convolved with the corresponding broadening profiles (namely instrumental and rotational profiles, although traditionally the former may also include other extra-broadenings, like the macroturbulence). Through the He I/He II ionization equilibrium, the effective temperature can be estimated; the wings of the upper Balmer lines (H_γ , H_δ) are useful for the determination of the gravity. Information about the stellar wind is mainly provided by H_α . It should be pointed out here that the different parameters and diagnostics are not independent and therefore some iteration is needed until a consistent solution is found.

Once the observed lines are fitted with the modeled ones, effective temperature, gravity, He abundance and $\log Q$ are determined. As mentioned by Villamariz & Herrero (2000), the HHe spectra of OB dwarfs is only slightly influenced by the microturbulence and hence it is considered as an ad-hoc parameter ($\xi_t \sim 0 - 10 \text{ km s}^{-1}$) in the stellar parameters determination. Note however that the adopted microturbulence may not exactly coincide with the microturbulence derived from the abundance analysis (see next section).

The code also provides for the corresponding model the emergent flux distribution and then mass, radius and luminosity can be calculated if M_V is known:

$$5 \log \frac{R}{R_\odot} = 29.57 - (M_V - V) \quad (3.3)$$

$$\log \frac{L}{L_\odot} = 2 \log \frac{R}{R_\odot} + 4 \log \frac{T_{\text{eff}}}{T_\odot} \quad (3.4)$$

$$\log \frac{M}{M_\odot} = 2 \log \frac{R}{R_\odot} + \log \frac{g_{\text{true}}}{g_\odot} \quad (3.5)$$

where V is the integral of the stellar flux over λ , weighted by the V-filter function of Matthews & Sandage (1963), and g_{true} accounts for the "centrifugal correction" (see Repolust et al. 2004).

Errors in T_{eff} and $\log g$ can be established generating a microgrid around central values; visual comparisons between modeled lines and observations allow us to determine the range of possible values for these parameters. Errors in R , M and L are calculated considering the propagations of the uncertainties in T_{eff} , $\log g$ and M_{v} .

Taking into account

$$y = \log x \quad \sigma_y = \sigma_{\log x} = \frac{\sigma_x}{x} \log e \quad (3.6)$$

and

$$a = b + c \quad \sigma_a^2 = \sigma_b^2 + \sigma_c^2 \quad (3.7)$$

the uncertainties for the radii, mass and luminosity are:

$$\frac{\Delta R}{R} = \frac{\Delta M_{\text{v}}}{5 \log e} \quad (3.8)$$

$$(\Delta \log L)^2 = \left(2 \frac{\Delta R}{R} \log e\right)^2 + \left(4 \frac{\Delta T}{T} \log e\right)^2 \quad (3.9)$$

$$\left(\frac{\Delta M}{M}\right)^2 = \frac{1}{(\log e)^2} \left[\left(2 \frac{\Delta R}{R} \log e\right)^2 + (\Delta \log g_{\text{true}})^2\right] \quad (3.10)$$

where

$$M_{\text{v}} = m_{\text{v}} - 5 \log d + 5 - A_{\text{v}} \quad (3.11)$$

$$(\Delta M_{\text{v}})^2 = (\Delta m_{\text{v}})^2 + \left(5 \frac{\Delta d}{d} \log e\right)^2 + (\Delta A_{\text{v}})^2 \quad (3.12)$$

A GRID OF HHE BLANKETED MODELS

Prior to creating a grid of blanketed models from which to determine the stellar parameters, we should be sure that the "approximate line blanketing" method is independent on the number of explicit elements considered. If the method works properly then, as the stellar parameters are determined through the visual fitting of the H, He I and He II lines, only the hydrogen and helium model atoms must be explicitly considered (reducing therefore the computational time required for each

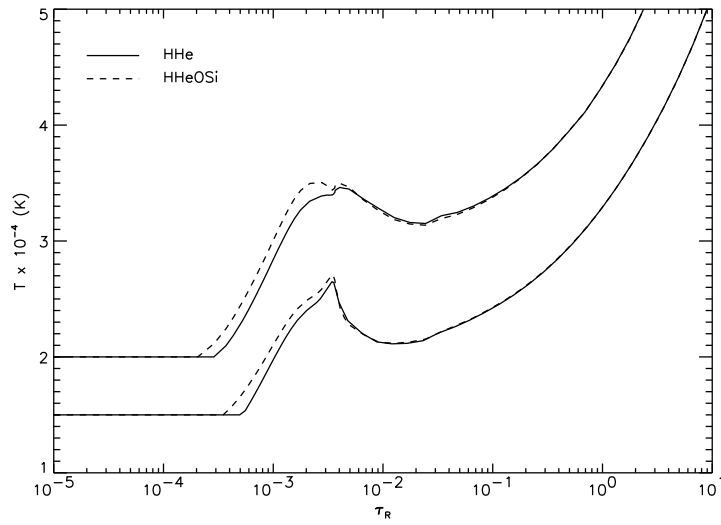


FIGURE 3.2 — Comparison of the effect of including oxygen and silicon as explicit elements on the T-structure. Two cases are considered: $T_{\text{eff}} = 30000$ K and 40000 K ($\log g = 4.0$, $\epsilon(\text{He}) = 0.09$, $\log Q = -13.5$). The agreement is almost perfect in the region where the diagnostic lines are formed ($-2 \leq \log \tau_{\text{R}} \leq 0$).

model). Figure 3.2 shows the effect of the inclusion of oxygen and silicon as explicit atoms over the temperature structure. Although there are some differences in the outer part of the stellar atmosphere ($\log \tau_{\text{R}} \geq -2.5$), this discrepancy does not affect the diagnostic H and He lines used for the stellar parameter determination. These lines are formed below $\log \tau_{\text{R}} \sim -2$, where both T-structures are in almost perfect agreement.

A grid of HHe FASTWIND models covering the stellar parameter space summarized below was calculated:

- $T_{\text{eff}} \in [28000, 40000]$ K with steps of 1000 K.
- $\log g \in [3.9, 4.1]$ dex with steps of 0.1 dex.
- $\xi_{\text{t}} = 0, 5, 10$ km s^{-1}
- $\log Q = -13.5, -13.0$
- $\epsilon(\text{He}) = 0.09$
- Model atom: A10HHe

To calculate this set of models, FASTWIND requires a grid of Hopf parameters covering the same range of stellar parameters. Table 3.1 summarizes the grid of Hopf parameters used along with the errors associated with the flux conservation when the temperature correction method is used and when it is not activated. The improvement of the flux conservation when using the temperature correction method is clear. Whilst for the original case these errors are between 1-3 %, the T-correction method improve this conservation to values < 1 %, independently on the initial set of Hopf parameters (if these are not very far away from the converged solution). Note that the density structure is calculated from the first temperature stratification, very dependent on the initial set of Hopf parameters. Hence, if the Hopf parameters are far away from the converged solution, the model may be erroneous even though the error in the flux conservation reach very low values when the T-correction method is applied.

3.3.3 Stellar abundances determination: methodology

There are two different approaches to the abundance analysis in stellar objects. Computation of a complete spectral interval in which all the observed lines are included is called a synthesis⁴. This method is one of the few techniques that can be applied when blending is severe. In the case of massive stars it is applied in fast rotators (e.g. Villamariz et al. 2002), in UV studies (e.g. Bouret et al. 2003) or when the spectral resolution is not good enough for resolving individual lines (for example, in extragalactic studies beyond the Local Group, see Urbaneja et al. 2005a). This method requires a correct broadening of the line profiles. The second method, the curve of growth, is based on the behavior of the line strength with an increase in the chemical abundance of the absorber. A graph specifying the change in the equivalent width of a line versus the element abundance is called a *curve of growth*.

Opposite to the synthesis method, the curve of growth method does not require any knowledge of the exact rotational and macroturbulent broadening mechanisms affecting the line profile, as it is based on the measurement of line equivalent widths. This is not the case for the microturbulent broadening; microturbulence is a free parameter that was included in the stellar abundance analyses to solve the discrepancy found in the line abundances derived from weak and strong lines. Its physical meaning is supposed to be related with small scale turbulent motions of the stellar plasma and affects mainly the strong lines close to saturation.

⁴When the synthetic spectrum is directly compared to the observed one, we call this the direct synthesis method

T_{eff}	$\log g$	$\log Q$	Y_{He}	q_{∞}	q_0	γ	Max. flux err. (%)	
							Orig.	T-corr.
28000	3.9	-14.00	0.10	1.21	0.31	1.30	3.7	0.38
29000	3.9	-14.00	0.10	1.19	0.34	1.30	3.0	0.41
30000	3.9	-14.00	0.10	1.18	0.37	1.30	2.4	0.43
31000	3.9	-14.00	0.10	1.18	0.39	1.46	1.7	0.56
32000	3.9	-14.00	0.10	1.17	0.42	1.62	1.6	0.64
33000	3.9	-14.00	0.10	1.15	0.44	1.90	2.4	0.76
34000	3.9	-14.00	0.10	1.10	0.45	2.30	2.9	1.04
35000	3.9	-14.00	0.10	1.05	0.47	2.70	2.8	0.97
36000	3.9	-14.00	0.10	1.01	0.48	3.26	3.3	1.11
37000	3.9	-14.00	0.10	0.97	0.49	3.82	3.6	0.92
38000	3.9	-14.00	0.10	0.94	0.49	4.36	3.8	0.85
39000	3.9	-14.00	0.10	0.92	0.50	4.88	4.2	0.83
40000	3.9	-14.00	0.10	0.90	0.50	5.40	4.0	0.76
28000	4.0	-14.00	0.10	1.21	0.31	1.30	3.4	0.37
29000	4.0	-14.00	0.10	1.19	0.34	1.30	3.4	0.38
30000	4.0	-14.00	0.10	1.18	0.37	1.30	3.0	0.39
31000	4.0	-14.00	0.10	1.18	0.39	1.46	2.5	0.46
32000	4.0	-14.00	0.10	1.17	0.42	1.62	2.1	0.57
33000	4.0	-14.00	0.10	1.15	0.44	1.90	1.6	0.70
34000	4.0	-14.00	0.10	1.10	0.45	2.30	1.6	0.87
35000	4.0	-14.00	0.10	1.05	0.47	2.70	1.5	0.94
36000	4.0	-14.00	0.10	1.01	0.48	3.26	2.7	1.10
37000	4.0	-14.00	0.10	0.97	0.49	3.82	2.5	1.04
38000	4.0	-14.00	0.10	0.94	0.49	4.36	2.7	0.90
39000	4.0	-14.00	0.10	0.92	0.50	4.88	3.2	0.85
40000	4.0	-14.00	0.10	0.90	0.50	5.40	3.2	0.84
28000	4.1	-14.00	0.10	1.21	0.31	1.30	3.6	0.36
29000	4.1	-14.00	0.10	1.19	0.34	1.30	3.8	0.36
30000	4.1	-14.00	0.10	1.18	0.37	1.30	3.4	0.36
31000	4.1	-14.00	0.10	1.18	0.39	1.46	3.2	0.41
32000	4.1	-14.00	0.10	1.17	0.42	1.62	2.9	0.50
33000	4.1	-14.00	0.10	1.15	0.44	1.90	2.5	0.64
34000	4.1	-14.00	0.10	1.10	0.45	2.30	2.5	0.69
35000	4.1	-14.00	0.10	1.05	0.47	2.70	2.6	0.85
36000	4.1	-14.00	0.10	1.01	0.48	3.26	2.5	0.89
37000	4.1	-14.00	0.10	0.97	0.49	3.82	2.6	0.85
38000	4.1	-14.00	0.10	0.94	0.49	4.36	2.1	1.05
39000	4.1	-14.00	0.10	0.92	0.50	4.88	2.1	0.93
40000	4.1	-14.00	0.10	0.90	0.50	5.40	2.4	0.93

TABLE 3.1 — Grid of Hopf–NLTE parameters used for the grid of FASTWIND models. Last columns present the maximum error associated with the flux conservation for both ”original” and ”temperature correction” cases.

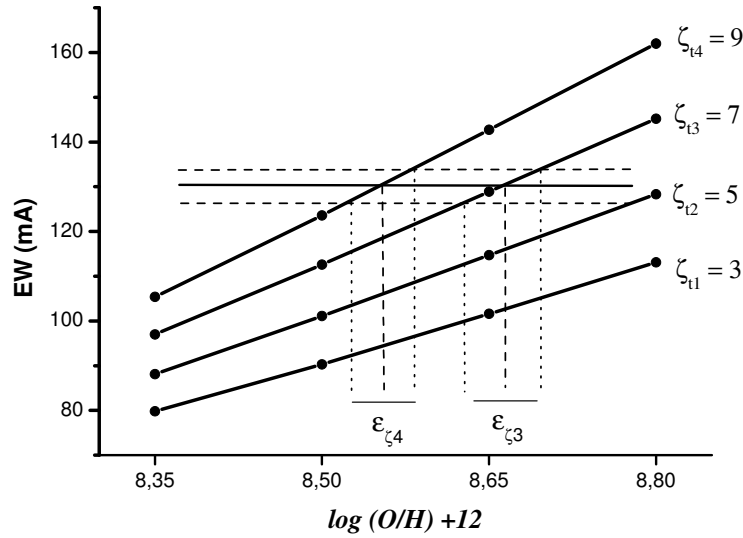


FIGURE 3.3 — Example of a curve of growth for the $O\ II\ \lambda 4414$ line in the star τ Sco (HD 149438). A grid of 16 models has been considered (4 microturbulences and 4 oxygen abundances). The observed EW of the line and its uncertainty are plotted as horizontal lines. Two examples of abundances (and their uncertainties) derived for microturbulences 7 and 9 km s^{-1} are plotted as vertical lines. See also Figures 3.4 and 3.5

In this thesis the curve of growth method will be applied for deriving stellar abundances. Once the stellar parameters have been derived, a grid of FASTWIND models combining different abundances and microturbulence values is calculated (only the abundance for the studied element and the microturbulence are varied, the remaining parameters are left fixed). In this way, the curves of growth for each line can be constructed by plotting the theoretical equivalent width for each abundance and microturbulence versus the abundance (see Figure 3.3). From the observed equivalent width and its error, an abundance (and its uncertainty) can be derived for each line and microturbulence. The individual line abundances are dependent on the microturbulence, that affects more the strong lines than the weak ones. Figure 3.4 shows the $\log \epsilon - EW$ diagrams for two different microturbulences in the study of HD 149438. The microturbulence value that minimizes the dependence of the line abundances on the line strength in the $\log \epsilon - EW$ diagrams (i.e. produces a zero-slope) will be the adopted microturbulence⁵.

⁵These diagrams can also be used as a diagnostic tool to check the reliability of the different lines for the abundance determination (see Chapter 5).

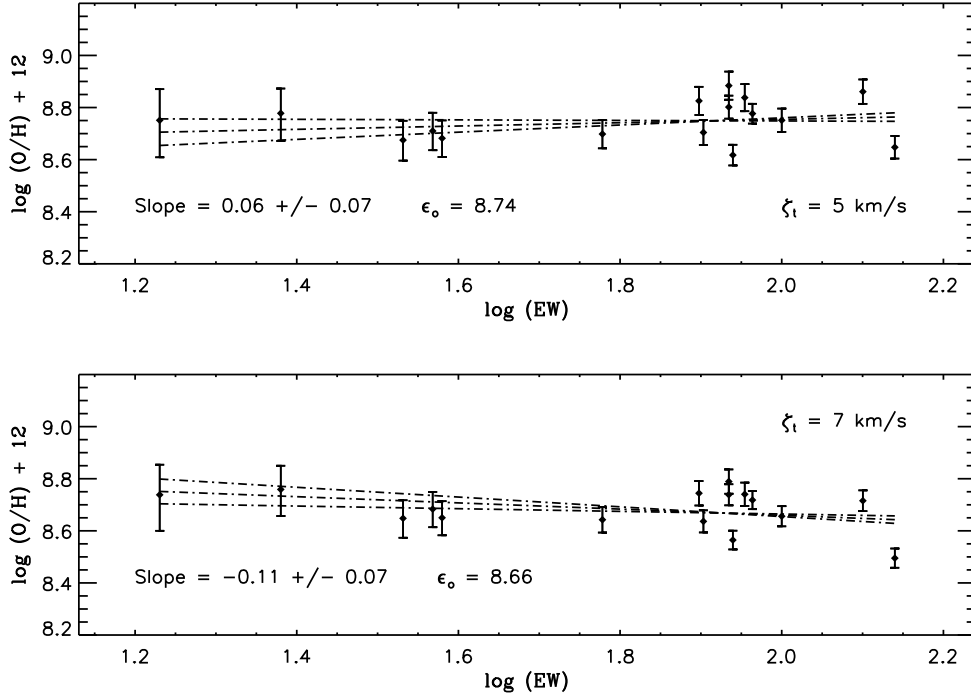


FIGURE 3.4 — Example of $\log \epsilon$ - EW diagrams in the study of HD 149438. A slope, its uncertainty, and a mean abundance are derived for each microturbulence. See also Figure 3.5.

Figure 3.5 shows the dependence of the slope and the total abundance on the microturbulence. Uncertainties in the microturbulence are obtained considering the errors derived for the slope (due to errors in the individual line abundances). This step also allows to estimate the contribution of the uncertainty in the microturbulence to the total oxygen abundance. This uncertainty depends mainly on the quality of the spectra (in the example shown in Figure 3.5 this is ~ 0.03 dex).

In the last step, abundance values for each line as well as their uncertainties are calculated for the adopted microturbulence. The final abundance value is estimated through a weighted mean of the linear individual line abundances ($10^{\epsilon_i - 12}$), and its uncertainty (σ_w) is that associated with this mean⁶.

⁶ $x_w = \frac{\sum (x_i / \sigma_i^2)}{\sum 1 / \sigma_i^2}$ $\sigma_w = (\sum 1 / \sigma_i^2)^{-1/2}$

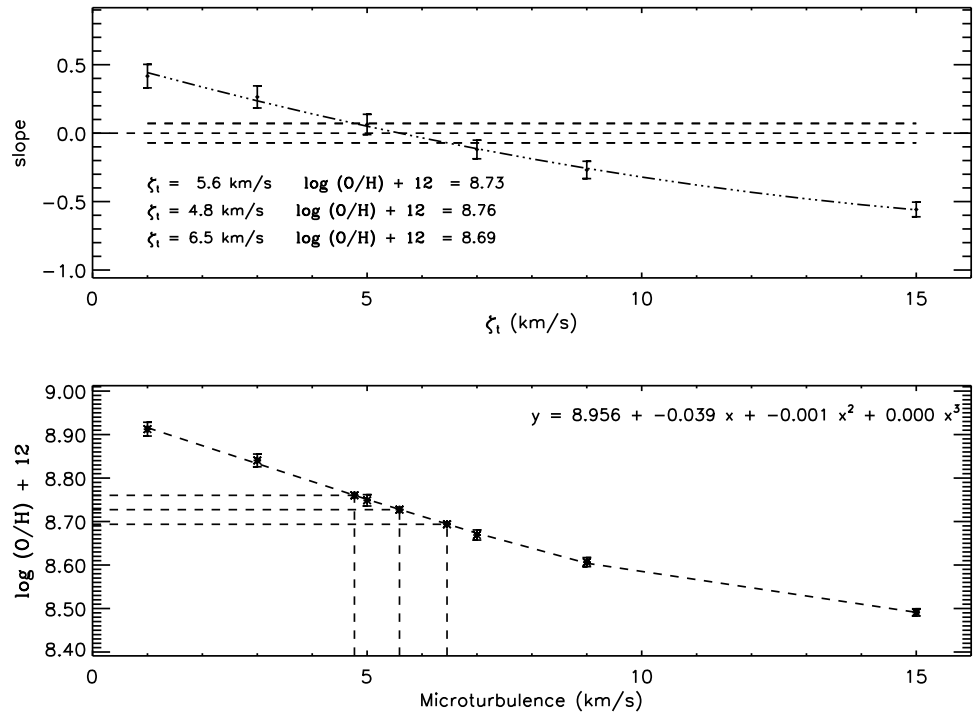


FIGURE 3.5 — Third step in the determination of the abundance. The final microturbulence and abundance are derived from the zero-slope. The uncertainty in the zero-slope determination produce a certain uncertainty in the microturbulence which hence results in an uncertainty in the final abundance. This uncertainty will be combined with those produced by the other sources of error affecting the abundance determination (see text).

The final uncertainty in the total abundance takes into account four different sources of errors: those associated with the statistical analysis, those derived from the error in the determined microturbulence and finally those referred to the uncertainty in the stellar parameters and atomic data. All these sources of error are added quadratically to that emerging from the final abundance uncertainty (see Villamariz et al. 2002).

A GRID OF HHeOSi BLANKETED MODELS FOR THE ABUNDANCE ANALYSIS

The abundance analysis by means of the curve of growth method requires a set of models (combining different values of microturbulence and abundance) for a given set of stellar parameters. A grid of HHeOSi blanketed models for the abundance analysis of B1- O9 main sequence stars has been generated with the following characteristics:

1. Effective temperatures between 29000 and 36000 K with steps of 1000 K. Three values for the $\log g$: 3.8, 4.0 and 4.2. $\log Q = -13.5$
2. Microturbulences: 1, 3, 5, 7, 9, 11 km s^{-1}
3. Abundances: O: [-3.50, -3.35, -3.20, -3.05] & Si: [-4.85, -4.70, -4.55, -4.40]⁷
4. Model atom: A10HHe023-3Si34⁸

The final grid consists of files with the EW of the different oxygen and silicon lines for the different values of microturbulence and abundance (one file for each set of stellar parameters). The use of this grid is very easy: once the stellar parameters of the target have been determined through the HHe analysis, and the observed oxygen and silicon equivalent widths have been measured one only needs to proceed as it has been specified above with the appropriate set of modeled equivalent widths.

⁷Abundances are combined in pairs for each model, as it is assumed that the modeled oxygen line equivalent widths are independent of the silicon abundance and vice versa.

⁸ This model atom combines the A10HHe, 023-3 and Si34 model atoms described above (see Section §3.3.1)

3.4 Modeling ionizing fluxes: *WM-basic*

3.4.1 Using *WM-basic*

The author of *WM-basic*, Adi Pauldrach, has created an easy-to-use Windows interface for running the code. This is distributed as freeware and can be downloaded from the website <http://www.usm.uni-muenchen.de/people/adi/adi.html>.

The code produces the ionizing fluxes and UV synthetic spectra (see Section §3.2). The input of *WM-basic* consists of the set of stellar parameters (T_{eff} , $\log g$, R , $\epsilon(\text{He})$ and Z). Based on the results of consistent calculations of the line force as a function of the stellar parameters and abundances, an initial guess of the force multiplier parameters (κ , α and δ) is automatically estimated. All this information is used by the code to guess the wind parameters, \dot{M} and v_{∞} . This estimation of the mass-loss rate and the terminal velocity is based on the approximate radiation driven wind theory (Kudritzki et al. 1989).

Note that although the force multiplier parameters can be used as free parameters, the actual values of κ , α and δ are constrained by the physics of the problem, and cannot take arbitrary values. For example, α represents the slope of the cumulative line force distribution function, which can actually be obtained at each point once the problem has been solved. However, if necessary, values could be slightly varied in order to reproduce known values of \dot{M} and v_{∞} .

THE IONIZING FLUX DISTRIBUTION

The emergent flux distribution predicted by *WM-basic* is normalized to correspond to the effective temperature at the photospheric radius. This means that although the shape of the flux given in the output file is that emerging from the "outside" of the wind (H_{ν} , typically at about 100 stellar radii), it is scaled as if it did emerge at a stellar radius of 1. Therefore, the luminosity calculated from this emergent spectral energy distribution SED is:

$$L = \int L_{\nu} d\nu = 16\pi^2 R_{\star}^2 \int H_{\nu} \frac{c}{\lambda^2} d\lambda \quad (3.13)$$

and the number of ionizing photons for an ionic specie is defined by:

$$Q(X^{+i}) = \int_{\nu_0}^{\infty} \frac{L_{\nu}}{h\nu} d\nu = 16\pi^2 R_{\star}^2 \int_0^{\lambda_0} \frac{H_{\nu}}{h\lambda} d\lambda \quad (3.14)$$

where ν_0 is the frequency of the ionization edge for the ion X^{+i} .

Figures 3.7 and 3.8 show the ionizing flux distributions for models with different T_{eff} and a $\log g = 4.0$ dex. The output of the codes *WM-basic* and *FASTWIND* have been plotted for comparison. The *FASTWIND* emergent flux in the $F(\text{UV})$ range is the result of the approximated treatment of the line blanketing/blocking effects; on the other hand, *WM-basic* results in a more detailed emergent flux in this spectral range, including all the strong and weak lines which produce the blocking of the stellar emergent flux. A comparison between the emergent fluxes and some other tests for checking the consistency between both codes are presented in the next section.

In the study presented in Chapter 7, the SED predicted by *WM-basic* is used as input of the photoionization code *CLOUDY*. Usually, a photoionization code has some predefined incident continua (e.g. blackbody), but there is also the possibility to include an user defined incident continuum as input (e.g. the output from a stellar atmosphere code). In this case, the shape and the intensity of the continuum must be specified as a table of points. The frequency grid used for defining the stellar incident continuum is interpolated by the photoionization code to a predefined frequency grid (normally a mesh with nearly logarithmically increasing widths). Therefore, two points must be taken into account for a correct link of the stellar atmosphere output to the photoionization code input:

1. The ionization edges must be consistently located according with the final interpolated grid used by the photoionization code (e.g. the hydrogen Lyman jump must be located at 1 Ryd).
2. The interpolation between the original frequency mesh from the stellar code and the final one considered by the photoionization code must be correctly done (the flux integrals must be conserved).

The best way to account for the first point is to convert the frequency grid of the stellar atmosphere SED to Rydbergs (Ryd). The second point is important when using SEDs defined in a very detailed manner, like the ones predicted by *WM-basic* or *CMFGEN*. These codes produce very detailed emergent fluxes accounting for the blocking of a huge amount of lines and hence these have to be rebinned to the final grid taking care of the conservation of the flux integrals:

$$F(x_c) = \sum_{i=n_1}^{n_2} \frac{[f(i+1) + f(i)][x(i+1) - x(i)]}{2x_0} \quad (3.15)$$

where $x_0 = x(n_2) - x(n_1)$ and $x_c = 0.5 [x(n_2) + x(n_1)]$. This interpolation will also be used when comparing emergent fluxes from different codes producing frequency sampling with different steps.

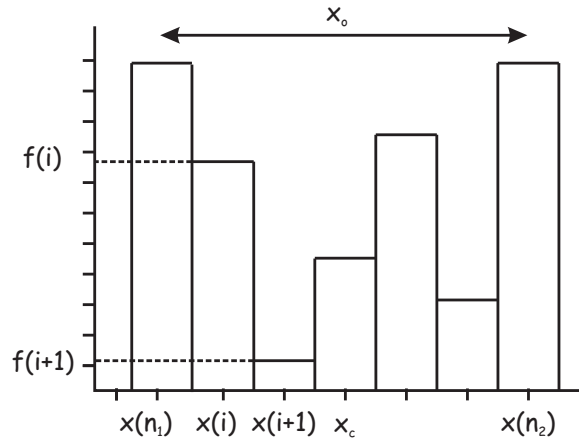


FIGURE 3.6 — A detailed emergent flux defined between the points $x(n_1)$ and $x(n_2)$ can be rebinned to the point x_c by applying Formula 3.15. This procedure conserves the flux integrals

3.4.2 A comparison between FASTWIND and WM-*basic* results

Since both codes FASTWIND and WM-*basic* will be used together for modeling spectral energy distributions, it is important to be sure that both give coherent results. The main comparisons regarding the combined use of FASTWIND and WM-*basic* in this thesis are emphasized in this section (note a more extensive comparison between both codes in Puls et al. 2005).

In Section §3.3.2 it has been shown that the radius of a star is determined from its absolute visual magnitude and the modeled emergent flux passing through the V-filter. Therefore for consistency, both FASTWIND and WM-*basic* models must result in the same V-fluxes when the same stellar parameters are considered as input. If this is correct, as the same radius, $\log g$ and T_{eff} are used, the total luminosity and mass consistency is automatically fulfilled. Table 3.2 shows the differences found in the predicted V magnitude for a grid of WM-*basic*⁹ – FASTWIND models. The agreement between both codes is very good, differences in the predicted V magnitudes are normally below 0.05, which results in differences in derived radii $\leq 3\%$.

⁹The WM-*basic* grid of models has been provided by Miriam García

T_{eff} (K)	V_{FW}	V_{WM}	ΔV	$\Delta R/R$ (%)	$\Delta L/L$ (%)	$\Delta M/M$ (%)
28000	-28.8316	-28.8081	-0.02	-1.1	-2.2	-2.2
30000	-28.9788	-29.0628	0.08	3.9	7.7	7.7
32000	-29.1243	-29.1820	0.06	2.7	5.3	5.3
34000	-29.2509	-29.3012	0.05	2.3	4.6	4.6
36000	-29.3603	-29.3592	-0.00	-0.1	-0.1	-0.1
38000	-29.4431	-29.4938	0.05	2.3	4.7	4.7
40000	-29.5142	-29.5264	0.01	0.6	1.1	1.1
42000	-29.5828	-29.5794	-0.00	-0.2	-0.3	-0.3
44000	-29.6437	-29.6555	0.01	0.5	1.1	1.1
46000	-29.6981	-29.6894	-0.01	-0.4	-0.8	-0.8

TABLE 3.2 — Comparison of V synthetic magnitudes predicted by FASTWIND and WM-*basic* in models with different effective temperatures, $\log g = 4.0$ dex, $v_{\infty} = 2300 \text{ km s}^{-1}$, $\dot{M} = 0.1 \times 10^{-6} M_{\odot} \text{ yr}^{-1}$ and $R = 9 R_{\odot}$. The same parameters have been considered in both calculations. Note that differences in the predicted V produce deviations in the inferred radii, luminosities and masses.

To compare ionizing fluxes and calculate $Q(X^{+i})$, formula 3.15 has been applied for rebinning the WM-*basic* spectral energy distributions to the wavelength grid considered in FASTWIND. Figures 3.7 and 3.8 show the ionizing emergent fluxes predicted by FASTWIND and WM-*basic* for some of the models summarized in Table 3.2. These plots are accompanied with a comparison of the number of ionizing photons for various ionic species resulting from both SEDs.

The first order approach to define the emergent ionizing flux distribution is the measurement of the total number of hydrogen ionizing photons. For the second order approach, the measurement of the total number of He^0 ionizing photons is also required. These are two important quantities that define the physical properties and ionization structure of an H II region (along with the density distribution of the nebular material). For example, in a ionization bounded nebula, its total $L_{\text{H}\alpha}$ and size will depend on the total $Q(\text{H}^0)$ associated with the ionizing stars and the nebular density. Finally, the exact ionization structure of the various ionic species will depend on these two quantities and the detailed emergent flux distribution (again the nebular density distribution is important).

From the visual comparison of emergent fluxes, the agreement is quite good between both FASTWIND and WM-*basic* models, except for some strong absorption and emission features not considered in FASTWIND and the spectral range below 350 \AA in the highest T_{eff} cases (as mention by Puls et al. 2005). The diagrams showing the comparison of number of ionizing photons for various ionic species bet-

ter show the discrepancies between both SEDs. These are the main conclusions of this comparison:

- The agreement is quite good (with differences $< 10\%$) for $Q(\text{H}^0)$, $Q(\text{O}^0)$, $Q(\text{N}^0)$, $Q(\text{S}^+)$ and $Q(\text{Cl}^+)$, showing that both SEDs are fairly similar between H and He I Lyman jumps (504-912 Å). In some cases FASTWIND predicted $Q(\text{S}^+)$ and $Q(\text{Cl}^+)$ departure from WM-*basic* results, due to the presence of absorption features not considered in FASTWIND models.
- For $Q(\text{He}^0)$, the agreement is also good, however there are some cases in which the discrepancy is larger than 10%. These are related to the presence of a strong absorption line close to the He I Lyman jump, again not considered in FASTWIND.
- For the other ions with ionization energies above that of He^0 , the results are dependent on the different slope predicted by both codes between 212 and 500 Å, and/or the absorption and re-emission features which are missing in the mean opacity approach used in FASTWIND.
- Finally, the major discrepancy is found below the He^+ edge.

Therefore, it can be concluded that the consistency between both codes, FASTWIND and WM-*basic* is quite good in terms of predicted V magnitudes and total number of hydrogen ionizing photons, however the shape of the SED may be quite different for certain cases. The presence of strong absorption and re-emission features in this spectral range may also affect the number of ionizing photons for certain ions. These discrepancies are related to the approximations used in the model calculation itself or to the effect of the opacity sources considered (i.e. the amount of lines producing the line blocking). Some possible explanations for the discrepancies found between FASTWIND and WM-*basic* spectral energy distributions have been discussed by Puls et al. (2005). At this point it is important to remark that FASTWIND has not been developed for the analysis of the (E)UV spectral range.

How important are these differences in terms of the ionization of the surrounding interstellar medium? Can the study of H II regions help to discriminate between the predictions of the various stellar atmosphere codes? A longstanding idea is to test the atmospheres of hot stars using nebular lines, and this would be better performed by studying well defined situations. To this aim, in Chapter 7 a detailed study of the Galactic H II region M43 and its ionizing star is presented.

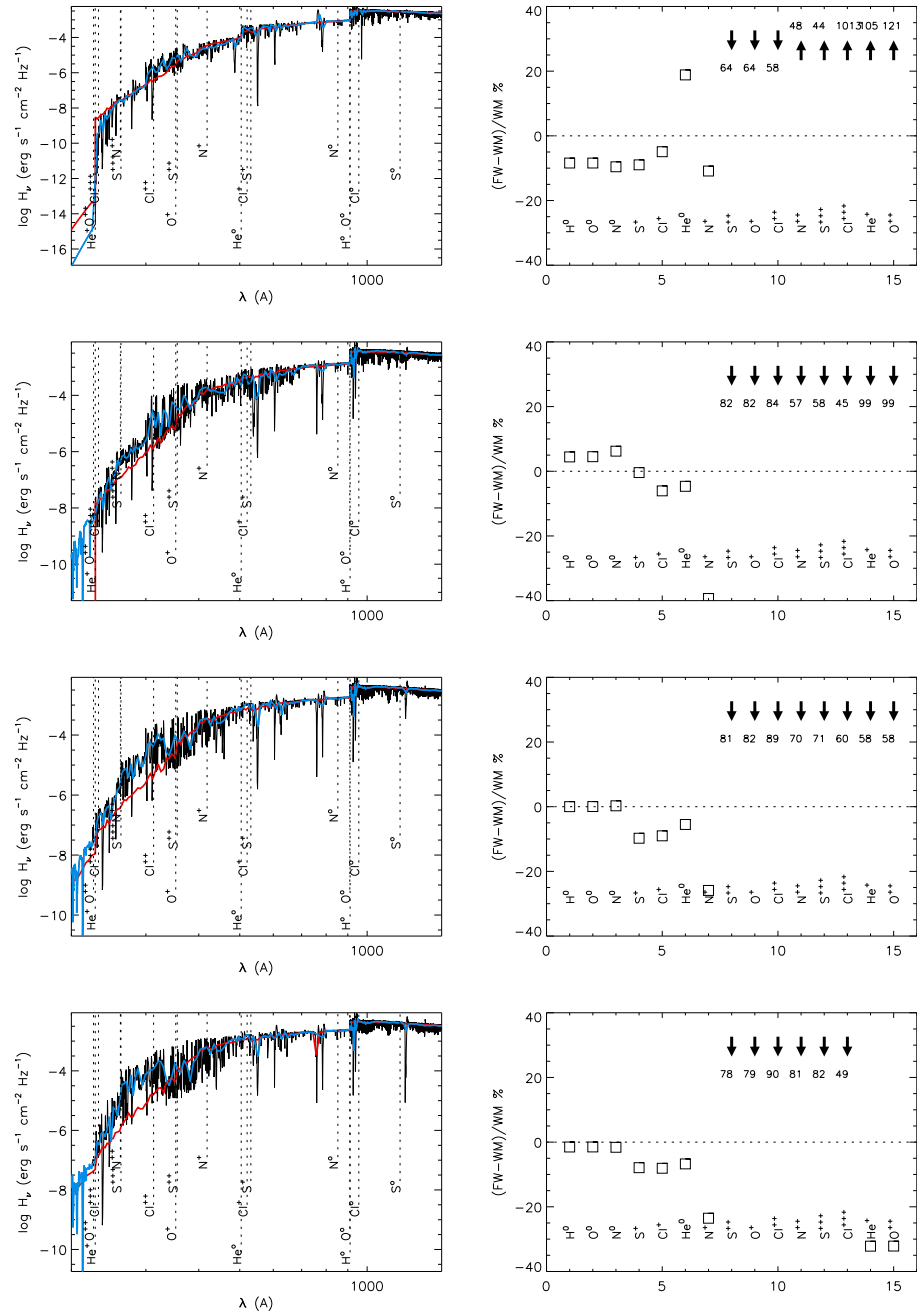


FIGURE 3.8 — Same than 3.7. From top to bottom, $T_{\text{eff}} = 36000, 38000, 40000, 42000$ K.

3.5 General analysis strategy

We can now define the general strategy that will be followed in this thesis for the stellar analyses.

FASTWIND and *WM-basic* will mainly be used for the analyses. The stellar parameters will be determined by means of a visual fitting of the FASTWIND synthetic H, He I-II lines to the observed ones. Previously, the rotational broadening has to be determined from the observed spectra. For these analyses a grid of line-blanketed HHe models will be used (see Section §3.3.2) and the synthetic spectra will be convolved with the corresponding instrumental and rotational profiles depending on the spectrum. Uncertainties on the stellar parameters will be estimated again through a visual comparison of the observed spectra with models close to the best one. Finally, radii, masses and luminosities will be calculated, as well as their uncertainties.

In §3.4.2 we have shown that FASTWIND and *WM-basic* models are consistent in terms of predicted V magnitudes and total number of hydrogen ionizing photons. FASTWIND allows us to determine the spectral parameters from the optical spectra, but the modeled ionizing flux distribution is approximated and probably not very reliable. *WM-basic* gives more precise and detailed ionizing flux distributions but no reliable optical lines are calculated, so the stellar parameters calculated previously with FASTWIND (T_{eff} , $\log g$, $\epsilon(\text{He})$, Z and R) will be used as input for *WM-basic* models.

The modeled ionizing flux distributions will be used as input for the photoionization code CLOUDY (see Chapter 4). The sampling of the ionizing flux distributions will be normally more precise than what is required for CLOUDY so they must be adapted to the CLOUDY frequency grid (see Section §3.4.1)

Once the stellar parameters of a star have been determined, if we want to proceed to the abundance analysis, a microgrid will be constructed for these stellar parameters varying the element abundance and the microturbulence. In this case, the atomic models of the elements we want to study must be included explicitly, as well as the information for the formal solution. With the theoretical equivalent widths we will construct the curves of growth and follow the methodology presented in Section §3.3.3 to obtain the stellar abundances of the various elements.

NEBULAR SPECTROSCOPIC STUDIES

A brief introduction to some of the nebular methods to derive the physical conditions and abundances of ionized nebulae is presented.

Some ideas about the photoionization code `CLOUDY` and the methodology that will be followed for the study of the Galactic H II region M43, developed in Chapter 7 are also presented.

4.1 Introduction

THE interpretation of spectroscopic observations of H II regions can address many fundamental questions in Astrophysics. For instance, H II regions can provide information about the present-day chemical abundances of the galactic regions where they are located. The spectra of H II regions are dominated by emission lines that are sensitive to details of the emitting gas and the properties of the ionizing stellar population. Therefore the emission line spectrum of these nebulae can be used to characterize the associated underlying massive stellar population in those cases where it cannot be well resolved. In addition, since the physical conditions in these photoionized nebulae are governed by a number of atomic processes, they provide a *natural laboratory* to test atomic physics theories.

This chapter is structured in two main parts. In the first part (Sections §§4.2 and 4.3), a brief introduction to some of the nebular methods used to derive the physical conditions and abundances of ionized nebulae is presented. These are fairly well understood and explained in several textbooks (viz. Osterbrock 1989). These textbooks, along with the excellent reviews by Ferland (2003) and Stasińska (2004) have been mostly used to this aim. The second part (Section §§4.5) is devoted to present some ideas about the photoionization code CLOUDY and the methodology that will be followed for the study of the Galactic H II region M43, developed in Chapter 7.

4.2 Physical conditions of H II regions

A H II region is an ionized cloud of gas formed around one or more massive stars. Energetic photons of OB-type stars ionize the gas, which is heated by the residual kinetic energy of the photoelectrons. The photoelectrons collide with ions and cause internal excitations, which decay to produce collisionally excited emission lines (e.g. [O III] λ 5007, [N II] λ 6584, [S II] λ 6716) and cooling of the gas. The electrons eventually recombine with ions. The degree of ionization at each point in the nebula is fixed by the equilibrium between photoionization and recapture. In the recombination process, recaptures can occur to excited levels, and excited atoms thus formed then decay to lower and lower levels by radiative transitions, eventually ending in the ground level. Recombination lines are formed during this process. Note that, for example, the recombination of H^+ gives rise to excited atoms of H^0 and hence leads to the emission of the H I spectrum (likewise, He^+ recombines and emits the He I spectrum).

Energy conservation sets the spectrum of a photoionized gas. Energy from the stellar continuum is reprocessed into other forms of light. The heating rate is affected by gas temperature and the shape of the ionizing radiation field. Thermal losses occur through recombination, free-free radiation and emission of collisionally excited lines (being this last one the dominant process). Both heating and cooling rates have nearly the same density dependence, which implies that the temperature will not strongly depend on density. The equilibrium temperature will be determined by a mix of ingredients across a real nebula.

Electron temperature (T_e) is expected to be usually rather uniform in nebulae. Its variations are mostly determined by the mean energy of the absorbed stellar photons and by the populations of the main cooling ions.

The nebular geometries result from the structure of the parent molecular cloud. The morphology of H II regions is normally rather complex on all scales. Typical hydrogen densities $N(\text{H})$ are $10^3 - 10^4 \text{ cm}^{-3}$ for compact H II regions. In the case of extragalactic H II regions, the hydrogen average densities are lower, typically 10^2 cm^{-3} since giant H II regions encompass also zones of diffuse material.

TEMPERATURE AND DENSITY MEASUREMENTS FROM EMISSION LINES

Ions of p^2 electronic configuration, of which O^{++} and N^+ are the best examples, have energy level structures that result in emission lines from two different upper levels with considerably different excitation energies occurring in the optical wavelength region. It is clear that the relative rates of the corresponding lines depend very strongly on T_e , so these lines ratios may be used to measure the electron temperature (T_e). Examples of line ratios used to derive the T_e are $[\text{O III}] (\lambda 4959 + \lambda 5007)/\lambda 4363$ and $[\text{N II}] (\lambda 6584 + \lambda 6583)/\lambda 5755$.

The electron density in a nebula may be measured by observing the effects of collisional de-excitation. This can be done by comparing the intensities of two lines of the same ion (as for O^+ and S^+ , with p^3 electronic configuration), emitted by different levels with nearly the same excitation energy so that the relative excitation rates of the two levels depend only on the ratio of collisional strengths. If the two levels have different radiative transition probabilities or different collisional de-excitation rates, the relative populations of the two levels will depend on the density, and the ratio of intensities of the lines they emit will likewise depend on the density. The best examples are $[\text{O II}] \lambda 3729/\lambda 3726$ and $[\text{S II}] \lambda 6716/\lambda 6731$.

4.3 Nebular abundances

Abundances of metals with respect to hydrogen are mostly derived using the intensity ratio of collisionally excited lines (CEL) with respect to H_β . The intensity ratios of optical and ultraviolet collisional lines are strongly dependent on electron temperature. These lines are among the strongest in the spectrum, owing to the large impact cross section. The challenge here is to have a good estimate of the electron temperature because the emission of a collisionally excited line is proportional to the product $T^{-1/2} \exp(-\chi/kT)$, where χ is the difference in excitation potential of the upper and lower levels of the transition.

On the other hand, the intensity ratios of recombination lines (RL) are almost independent of temperature. Therefore, ratios of recombination lines are capable

of determining with great accuracy abundances that are nearly independent of the physical conditions along a line of sight. Because the strengths of recombination lines are proportional to their abundances, hydrogen and helium are the only elements common enough to produce prominent recombination lines. However, with very deep spectroscopy, it is now possible to distinguish very faint recombination lines produced by the heavy elements (see e.g. Esteban et al. 2004).

It has been known for several decades that abundances measured by recombination lines are systematically larger than those deduced from forbidden lines. This is not a small problem; the deduced abundances can vary from 0.3 dex to more than 1 dex for planetary nebulae and about 0.10-0.30 dex for H II regions. The explanations most often invoked are: temperature fluctuations, incorrect atomic data, fluorescence excitation, upward bias in the measurement of weak line intensities, blending with other lines, abundance inhomogeneities. Non of them is completely satisfactory, some are now definitely abandoned. Recent discussions and reviews about this problem can be found in Stasińska (2002), Liu (2002, 2003), Esteban (2002) and Torres-Peimbert & Peimbert (2003).

The gas-phase nebular abundances of certain elements can be affected by depletion onto dust grains (viz. Si, Fe, C, Mg, O). Therefore analyses of the emission of line spectrum only provide lower limits for the abundance of these elements.

4.4 Total H_α luminosity and H_α surface brightness distribution

The total H_α luminosity and the H_α surface brightness distribution are two important constraints in the modeling of H II regions. In an ionization bounded nebula composed by pure hydrogen, the total number of recombinations per unit time balances the total number of ionizing photons emitted by the star per unit time, or during recombination to the ground level. During the recombination process captures to the excited levels decay to lower levels by radiative transitions. Therefore the total luminosity in i.e. H_α line is a direct measure of $Q(H^0)$. If the nebula is density bounded, part of the ionizing continuum emerging from the stars will escape from the nebula and the total H_α luminosity will be smaller. At first approximation:

$$L_{H\alpha} \leq \frac{\epsilon(H\alpha)}{\alpha_B(H^0, T_e)} Q(H^0) \quad (4.1)$$

where α_B is the H recombination coefficient to the excited states (case B), T_e represents an average electron temperature of the nebula and $\epsilon(H_\alpha)$ is the emission coefficient of H_α .

The surface brightness in a recombination line is given by:

$$S(\text{line}) = \int \left(\frac{j_{\text{line}}}{N_e N_{\text{ion}}} \right) N_e N_{\text{ion}} dl \quad (4.2)$$

where the term in braces is the effective recombination coefficient for a line. This coefficient is determined by the atomic physics that describes the capture of an electron by an ion and its subsequent cascade to the ground state. It is a weak function of density, and has a roughly T^{-1} dependence on temperature (see Osterbrock 1989).

For the case of a H I recombination line, since $N_e \sim N(\text{H}^+) = N_{\text{H}}$, equation 4.2 can be written as:

$$S(\text{HI}) = \int \left(\frac{j_{\text{HI}}}{N_e N_{\text{ion}}} \right) N_{\text{H}}^2 dl \quad (4.3)$$

Therefore, the surface brightness distribution in a H I recombination line (i.e. H_α) is mainly characterized by the hydrogen density distribution of the ionized nebular gas.

By assuming a nebula with spherical geometry, it is possible to determine the radial density law that would reproduce the H_α surface brightness profile. The way to do this is to assume a hydrogen radial density distribution, $N_{\text{H}}(r)$, and to apply the following equation:

$$S_{\text{H}\alpha}(x) = 2 \sum_{y=0}^{y_{\text{max}}} \left(\frac{j_{\text{H}\alpha}}{N_e N_{\text{ion}}} \right) N_{\text{H}}^2(r_{x,y}) \Delta y \quad (4.4)$$

where x is the projected distance from the ionizing source, $r_{x,y} = \sqrt{x^2 + y^2}$, Δy is the integration step along the y -axis; and $y_{\text{max}}(x) = \sqrt{R_{\text{max}}^2 - x^2}$. The meaning of these quantities are better illustrated in Figure 4.1. By trial and error one can find the hydrogen density distribution that is a better fit to the observed H_α surface brightness profile.

4.5 A nebular photoionization code: CLOUDY

Photoionization codes are built to take into account all the major physical processes that govern the ionization and temperature structure of nebulae. The most popular one is CLOUDY developed by G. K. Ferland and collaborators. CLOUDY is a large-scale spectral synthesis code designed to simulate fully physical conditions within an astronomical plasma and then predict the emitted spectrum. This photoionization code was born in August 1978 and it has been in continuous evolution and improvement since then. The code is distributed as freeware and can be downloaded from

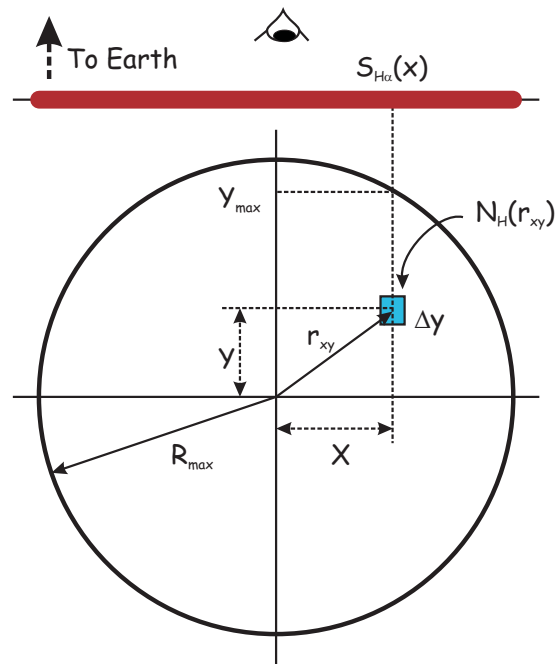


FIGURE 4.1 — This figure illustrates the meaning of the quantities used in Equation 4.4

the website <http://www.nublado.org>. The most recent version of CLOUDY is C05.07.06 (released 2005 Jul 08). In this thesis a previous version (v.96.01) has been used.

The computational methods, along with the characteristics of the code are described in Ferland et al. (1998) and the three volume documentation that accompanies the source code *Hazy, a Brief introduction to Cloudy 96*. The calculation is explicitly one dimensional, with results depending only on the depth coordinate.

4.5.1 Input for CLOUDY

Only a few parameters need to be specified to predict the full spectrum of a photoionized cloud: the shape of the radiation field emitted by the central object, the flux of photons striking the illuminated face of the cloud, the cloud's density (and how it varies with depth), and the gas chemical composition. In return, the full spectrum, with the continuum over a broad range of wavelengths, and the intensities of about one hundred of emission lines are predicted.

CHARACTERIZING THE IONIZING SOURCE

The spectral energy distribution of the ionizing source is defined by two quantities, its shape and its intensity. The shape of this energy distribution in a real star is mainly defined by its T_{eff} , $\log g$ and metallicity, although may also be dependent on the wind characteristics. Since the ionizing spectral range of the SED is not directly observable, models are used, and hence the predicted shape is also dependent on the characteristics of the stellar atmosphere models (e.g. models with or without the consideration of line blanketing effects predict different emergent ionizing fluxes). The intensity of the spectral energy distribution emerging from the star mainly depends on the stellar radius and effective temperature of the star (i.e. its luminosity).

The continuum shape should be specified between energies of 1.001×10^{-8} Ryd and 7.354×10^6 Ryd (≈ 100 MeV). There are several CLOUDY commands to specify this continuum shape (e.g. `black body t=4.6` refers to a continuum defined by a blackbody with $T = 40000$ K). CLOUDY also offers the possibility of entering the continuum as a table of points using the command `interpolate`. CLOUDY interpolates upon this table using straight lines in log-log space. This option will be used in this thesis, since the shape of the ionizing continuum will be previously calculated using stellar atmosphere codes. In Chapter 3 (Section §3.4.1) it was indicated how the original frequency grid used by the stellar atmosphere models to describe the SED is adapted for a correct link to the photoionization code input. This takes into account the discontinuities at the ionization threshold for the H^0 and He^0 and the conservation of the flux integrals.

GEOMETRY AND DENSITY DISTRIBUTION OF NEBULAR GAS

Both the geometry and the density distribution are important physical properties of the H II regions that cannot be directly inferred from the observations. The 3D geometries of the nebulae are projected into the plane of the sky, resulting in apparent 2D geometries. On the other hand, only a mean density associated with the part of the nebula that is seen through the slit can be derived when a spectroscopic density indicator (e.g. $N_e[\text{S II}]$) is used.

In CLOUDY, the geometry is always spherical, but can be changed to effectively plane parallel by making the inner radius much larger than the thickness of the cloud.

Many different density distributions can be computed with CLOUDY. Density is specified in CLOUDY by indicating how the hydrogen density changes with radius or depth.

Some interesting definitions related to the geometry and density distribution description of the nebular gas are presented below:

Density bounded nebula: The nebula is said to be density or matter bounded if the outer limit to the emission-line region is marked by the outer edge of the cloud.

Radiation bounded nebula: The nebula is said to be radiation bounded if the outer limit to the emission-line region is defined by a hydrogen ionization front, so both warm ionized and cold neutral regions exist. All the ionizing photons emitted by the ionizing source are absorbed inside the nebula. Therefore the intensity or luminosity of a recombination line is set by the luminosity of the ionizing continuum, with relatively little dependence on cloud properties.

Filling factor (ϵ): The definition of this quantity is based on the idealization of the H II regions as containing small clumps of high density material which occupy a fraction ϵ of the total volume of the H II region, and which are surrounded by low density material whose contribution to the measured emission of the H II regions is negligible (Osterbrock 1989).

Covering factor (cf): This quantity is defined as the fraction of 4π sr covered by gas, as viewed from the central source of ionizing radiation.

GAS COMPOSITION AND DUST GRAINS

Abundances must be specified by number relative to hydrogen. These are gas-phase abundances, and do not include material locked onto dust grains.

CLOUDY also allows for the inclusion of dust grains. This only affects the physics of the nebula but it doesn't either produce depletion of the included nebular gas-phase abundances nor reddening of the predicted intensity lines.

4.5.2 Comparing the output of CLOUDY models with the observational constraints

One of the possibilities offered by CLOUDY is to show the volume emissivity of up to 100 emission lines as function of depth into the cloud, $\epsilon(r)$. Integrating these emissivities over the volume of the ionized plasma, the total luminosities can be derived (actually this can also be one output in CLOUDY). However when the H II region

is spatially resolved, and the aperture used to obtain the observed spectrum (i.e. a fiber or a slit) is smaller than the actual size of the nebula, an aperture correction must be applied to CLOUDY results.

This is the case for the study of M43 that will be presented in Chapter 7. We count with five slit sections (with sizes that are smaller than the apparent size of the nebula) located at different angular distances from the ionizing star in the plane of the sky.

We have developed an IDL procedure to calculate, from the output of CLOUDY, quantities directly comparable with the observational spectroscopic constraints. Basically it computes the predicted surface brightness profiles for the different lines by applying the formula:

$$S_B(x) = 2 \sum_{y=0}^{y_{max}} \epsilon(r_{x,y}) \Delta y \quad (4.5)$$

where $\epsilon(r)$ is the volume emissivity ($\text{erg cm}^{-3} \text{s}^{-1}$) of the corresponding line at a distance r to the ionizing source and x and y are given in cm. Note that $r_{x,y}$, Δy and $y_{\max}(x)$ have the same meaning as in Equation 4.4.

Let's assume that (I_1/I_2) is the intensity ratio of two lines corresponding to a certain slit section whose center is located at an angular distance α (in arcsec) to the star. This quantity can be directly compared with the $S_{B1}(x)/S_{B2}(x)$ ratio. Note that first one has to assume a certain distance to the nebula (d) to transform angular distances to linear distances. This can be done by applying the following equation:

$$x(\text{cm}) = \alpha(\text{arcsec}) \frac{d(\text{pc})}{206265} 3.086 \times 10^{18} \quad (4.6)$$

STELLAR ABUNDANCES IN B0.5V STARS

*Pon a cocer las lentejas
(que habrás puesto en remojo en la vispera)
en agua con sal y un chorrito de aceite de oliva
junto con un cebolla y una zanahoria*

Ensalada de lentejas - Arguiñano -

Quantitative stellar spectroscopy of B-type stars has been increasingly used to investigate the chemical composition of our own Galaxy, other galaxies in the Local Group and even beyond. Some work has been devoted to study the coherence of results from these stellar analyses and those from nebular spectroscopic studies. However, until now it has not been consistently done in the same stellar forming region. This will be addressed in Chapter 6 for the case of the Trapezium cluster stars inside the Orion nebula. Previously, in this chapter τ Sco — a B0.2V star with a very low $v \sin i$ — is used as a *benchmark test* for the abundance analyses of early B-type stars with the stellar atmosphere code FASTWIND. A comparison between oxygen abundances derived using three different codes (FASTWIND, CMFGEN, and TLUSTY) is also presented in this chapter.

5.1 Introduction

As a result of their properties, the advent of medium and large size telescopes, and the development of stellar atmosphere codes for massive stars, quantitative spectroscopy of B-type stars has been increasingly used to investigate the present day

abundance patterns of our own Galaxy (e.g. Gies & Lambert 1992, Gummersbach et al. 1998, McErlean et al. 1999, Rolleston et al. 2000, Daflon & Cunha 2004), other Local Group galaxies like the Magellanic Clouds (Lennon et al. 1991, Dufton et al. 2000, Korn et al. 2002, Trundle et al. 2004), M33 and M31 (Monteverde et al. 1997, 1998, 2000, Smartt et al. 2001b, Trundle et al. 2002, Urbaneja et al. 2005b), and even galaxies beyond the Local Group (Urbaneja et al. 2003, 2005a).

Many are the advantages that make these stars very useful to address a number of astrophysical problems (see review by Herrero 2003). As a direct consequence of their high luminosities, they can be observed in distant regions of the Galaxy and nearby galaxies; their spectra show many — however, well separated — C, N, O, Si, Mg, S, Al and Fe photospheric metal lines and hence are perfect targets for stellar abundance analyses. Photospheres of B main sequence stars are not normally contaminated by core-processed material so their derived stellar abundances can be compared directly with those from H II regions. Finally, B-type supergiants may exhibit modified surface abundances caused by CNO-cycled material reaching the surface due to mixing and mass loss processes, and hence they are a key test of stellar evolution models.

A reliable determination of absolute stellar abundances is based on a correct determination of the physical conditions in the region of the stellar atmosphere where the lines are formed along with the emergent stellar flux going through these layers. A correct definition of the model atoms is also needed. Absolute abundances may contain systematic errors due to uncertainties in the atmospheric parameters and atomic data, or because of simplifications in the model atmosphere analysis (e.g. the assumption of LTE). To minimize these errors differential analyses are performed with respect to a star with similar spectral type and luminosity class (e.g. Smartt et al. 1996, Monteverde et al. 2000). However, as suggested by Korn et al. (2002), systematic errors are arguably more important than the random ones at the current level of accuracy reached for the stellar abundance studies.

In this chapter τ Sco — a B0.2V star with a very low $v \sin i$ — is used as a *benchmark test* for the oxygen and silicon absolute abundance analyses of early B-type stars with the stellar atmosphere code FASTWIND. This study will be able to address different tasks:

- To establish a suitable set of oxygen and silicon lines for the stellar abundance analysis of early B-type stars.

- To check the reliability of the oxygen and silicon model atoms used for the analyses.
- To identify common problems associated with the determination of stellar abundances by means of the curve of growth method.
- To study the effect of the uncertainties in the derived stellar parameters over the final abundances.

The results presented in this chapter, will lay the foundations for the abundance analysis of the Trapezium cluster stars inside the Orion nebula. In the forthcoming chapter a detailed study of the Orion stars, along with a consistent comparison of abundances derived through both stellar and nebular methodologies will be presented.

This chapter is structured as follows: In Section §5.2, the spectrum of τ Sco is used for the identification of the O II and Si III-IV lines present in the spectra of early B-type stars. The oxygen abundance analysis is performed in Section §5.3, where the *detailed analysis by multiplets* approach is also presented and how it can help to identify problems with the model atoms. A comparison of results from the oxygen abundance analysis by means of three commonly used stellar atmosphere codes (FASTWIND, CMFGEN, and TLUSTY) is presented in Section §5.3.4. The silicon abundance analysis is performed in Section §5.4. Finally, the summary and the conclusions are presented in Section §5.5

5.2 Line identification and measurement of equivalent widths

As indicated in Chapter 3 (§3.3.3), stellar abundances can be derived following two different approaches: spectral synthesis and the curve of growth method. This second approach has been widely used in the abundance analysis of early type stars through their optical spectra. For the application of this methodology, the stellar spectra must have enough good quality and low $v \sin i$ to make sure that the lines do not lead to blending problems and it is possible to measure the equivalent width of the metal lines accurately. This is not always feasible but, if it is possible, it is worth to use this method because the reliability of the derived abundances is better, as intrinsic uncertainties can be systematically controlled.

When this methodology is used it is important to correctly identify the lines that are going to be used and to remove all the lines whose equivalent widths can be affected by the presence of lines of other elements. The CASPEC spectrum of τ Sco (Figure 5.1; see Chapter 2 for a description of its characteristics) has been used

for the identification of the O II and Si III-IV lines present in the spectra of early B-type stars. For the line identification, the NIST Atomic Spectra Database (v.3.0) has been used. The whole set of lines, divided into multiplets, is shown in Tables 5.1 and 5.2. Their $\log gf$ values (basically taken from NIST database) and some comments on the possibility of blending are also summarized in those tables¹.

To measure the equivalent widths we use our own software developed in IDL. A least squares profile fitting procedure was used, with Gaussian profiles fitting the line and polynomials of degree one to fit the local continuum. Errors in the measurements due to the uncertainty in the position of the local continuum (estimated as $\pm 1/SNR$, Villamariz et al. 2002) have also been considered. Equivalent widths of all the lines listed in Tables 5.1 and 5.2 have been measured for τ Sco (see Tables 5.3 and 5.6, respectively). The estimated value of the uncertainty in the measurement of the EWs is ~ 5 mÅ and ~ 10 mÅ for some problematic lines.

Configurations	Terms	Label	λ (Å)	$\log gf$	Notes
3s 4s - 3s 4p	3S - 3P_0	Si III 4552	4552.622	0.292	
		Si III 4567	4567.840	0.070	
		Si III 4574	4574.757	-0.406	
3s 4d - 3s 5f	1D - 1F_0	Si III 4716	4716.654	0.491	Weak
3s 4f - 3s 5g	3F_0 - 3G	Si III 4813	4813.33	0.823	Weak
		Si III 4819	4819.72	0.938	Weak
		Si III 4829	4828.88	0.071	Weak
4s - 4p	2S - 2P_0	Si IV 4089	4088.862	0.194	+ O II
		Si IV 4116	4116.104	-0.106	
5d - 6f	2D - 2F_0	Si IV 4212	4212.396	0.380	
			4212.414	0.562	
5f - 6g	2F_0 - 2G	Si IV 4631	4631.241	1.216	+ N II
5g - 6h	2G - 2H_0	Si IV 4654	4654.323	1.479	
5f - 6d	2F_0 - 2G	Si IV 4950	4950.111	-0.129	Very weak

TABLE 5.1 — Preliminary set of Si III-IV lines selected for the analysis, divided by multiplets. Lines have been identified cross-correlating the line list from the NIST Atomic Spectra Database with the spectrum of the low $v \sin i$ star τ Sco. Possible blends with lines from other species are identified with a '+'. $\log gf$ values are from the NIST database. These values have been considered for the formal solution in FASTWIND models.

¹Oxygen lines located in the wings of Balmer lines have not been included in Table 5.2. The measurement of the equivalent widths of these lines is complicated and therefore they are useless for their application in the curve of growth method.

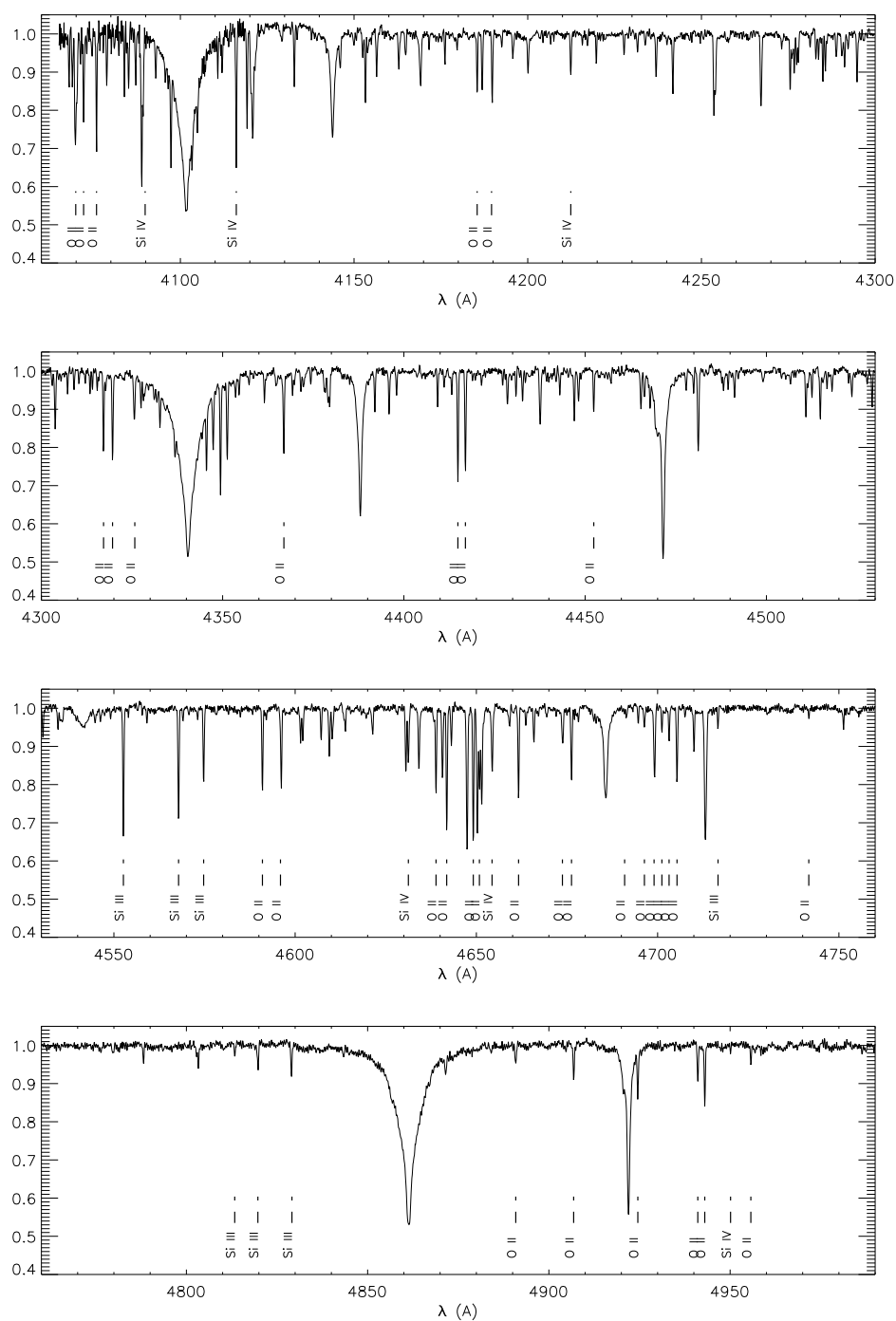


FIGURE 5.1 — Blue CASPEC spectrum of τ Sco. The oxygen and silicon lines used for the abundance analysis are indicated. Note that the spectral region between 4000 and 4110 Å — where the O II $\lambda\lambda$ 4069, 4072, 4075, 4078 lines are located — has worse quality than the rest of the spectrum.

Terms	NIST	Label	λ (Å)	$\log gf$	Notes
<hr/>					
2s ² 2p ² (³ P) 3s - 2s ² 2p ² (³ P) 3p					
<hr/>					
⁴ P- ⁴ D ₀	64	O II 4638	4638.856	-0.332	+ C II + Si III
		O II 4641	4641.810	0.055	+ N III
		O II 4650	4649.135	0.308	x C III (if $v \sin i$ high)
		O II 4651	4650.638	-0.362	x C III
		O II 4661	4661.632	-0.278	
		O II 4673	4673.733	-1.090	+ C III
		O II 4676	4676.235	-0.394	
⁴ P- ⁴ P ₀	65	O II 4696	4696.352	-1.380	Very weak
		O II 4317	4317.139	-0.386	+ C II
			4317.696	-0.142	
		O II 4319	4319.630	-0.380	+ N III + C II
			4319.866	-0.502	NIST 191
O II 4366			4366.895	-0.348	
			4366.530	-0.929	
		O II 4325	4325.761	-1.098	x H _γ + C III
² P- ² D ₀	72	O II 4414	4414.899	0.172	
			4414.456	-1.483	NIST 189
		O II 4416	4416.975	-0.077	+ Si IV
		O II 4452	4452.378	-0.788	
<hr/>					
2s ² 2p ² (¹ D) 3s - 2s ² 2p ² (¹ D) 3p					
<hr/>					
² D- ² F	99	O II 4590	4590.974	0.350	
		O II 4596	4595.957	-1.033	
			4596.177	0.200	
<hr/>					
2s ² 2p ² (³ P) 3p - 2s ² 2p ² (³ P) 3d					
<hr/>					
⁴ D ₀ - ⁴ F	90	O II 4069	4069.623	0.150	+ C III
			4069.882	0.344	
		O II 4072	4072.153	0.552	
		O II 4076	4075.862	0.693	+ C II
O II 4078			4078.842	-0.284	
² D ₀ - ² F	118	O II 4705	4705.346	0.477	
		O II 4741	4741.704	-0.989	Very weak
⁴ S ₀ - ⁴ P	130	O II 4891	4890.856	-0.436	
		O II 4906	4906.830	-0.160	
		O II 4924	4924.529	0.074	x He I λ 4922 (if $v \sin i$ high)
² P ₀ - ² D	148	O II 4941	4941.072	-0.054	
		O II 4943	4943.005	0.239	
		O II 4956	4955.707	-0.573	Very weak
<hr/>					
2s ² 2p ² (¹ D) 3p - 2s ² 2p ² (¹ D) 3d					
<hr/>					
² F ₀ - ² G	161	O II 4185	4185.440	0.604	
		O II 4189	4189.788	0.717	+ S II
			4189.581	-0.828	
² D ₀ - ² F	172	O II 4699	4699.011	0.418	
			4698.437	-0.883	
			4699.218	0.270	NIST 118
O II 4703			4703.161	0.263	
² P ₀ - ² P	188	O II 4691	4691.419	-0.309	
			4690.888	-0.610	
		O II 4701	4701.179	0.088	
			4701.712	-0.611	

TABLE 5.2 — Preliminary set of O II lines selected for the analysis, divided by multiplets. See comments on Table 5.1. When the blending with lines from other species is clear from the τ Sco spectrum, it is marked with a 'x'.

5.3 Oxygen abundances

Up to forty five O II lines can be clearly distinguished in the CASPEC spectrum of τ Sco (covering the spectral window between 4050 Å and 5050 Å). These lines span a large range of equivalent widths, and hence O II is a good barometer of microturbulence. Table 5.3 summarizes the equivalent widths for the O II lines; these are shown in ascending order for a better identification of the different lines in the $\log \epsilon(\text{O}) - EW$ plots presented along the chapter. No O III lines have been identified in the observed spectral range.

Line	EW	$\log EW$	Line	EW	$\log EW$
O II λ 4741	9	0.95	O II λ 4705	78	1.89
O II λ 4691	12	1.07	O II λ 4676 *	79	1.90
O II λ 4956 *	17	1.23	O II λ 4366 *	80	1.90
O II λ 4696	19	1.28	O II λ 4590	80	1.90
O II λ 4701	21	1.32	O II λ 4638 *	86	1.93
O II λ 4891 *	24	1.38	O II λ 4319 *	86	1.93
O II λ 4703	31	1.49	O II λ 4596	87	1.94
O II λ 4906 *	34	1.53	O II λ 4072	89	1.95
O II λ 4452 *	37	1.57	O II λ 4699	89	1.95
O II λ 4941 *	38	1.57	O II λ 4661 *	90	1.95
O II λ 4078	45	1.65	O II λ 4317 *	92	1.96
O II λ 4924	48	1.68	O II λ 4076	96	1.98
O II λ 4673	51	1.71	O II λ 4416 *	100	2.00
O II λ 4185	53	1.72	O II λ 4414	106	2.02
O II λ 4325	58	1.76	O II λ 4641 *	126	2.10
O II λ 4943 *	60	1.78	O II λ 4650	138	2.14
O II λ 4189	66	1.81	O II λ 4069	152	2.18

TABLE 5.3 — Ascending ordered equivalent widths (mÅ) for τ Sco O II lines. Uncertainties in the measurement of the EW are ± 5 mÅ. O II λ 4651 line is blended with two C III lines and it is not possible to measure its equivalent width. O II λ 4069, 4072, 4076 and 4078 lines are located in a spectral region where the CASPEC spectrum of τ Sco has a worse quality. The lines marked with an asterisk (*) are those used for the study presented in Section §5.3.4

5.3.1 First approach

For this first approach, the whole set of observed O II lines summarized in Table 5.3 will be included in the analysis. The synthetic lines are obtained by means of the stellar code FASTWIND (v.8.5, with temperature correction option activated²) and the oxygen model atom A10HHe023–3 defined in Chapter 3 (§3.3.1).

²See Chapter 3

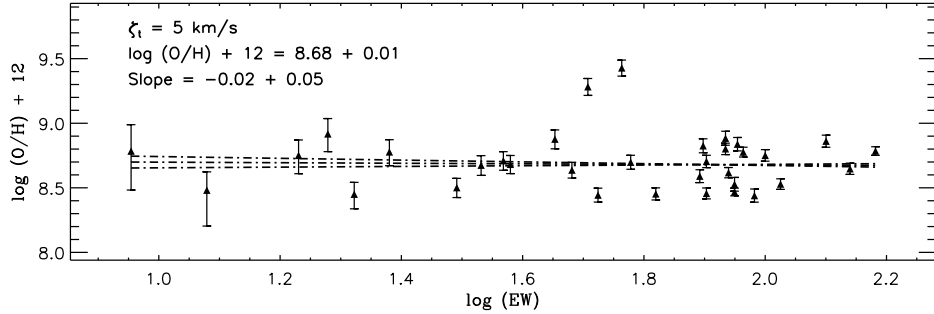


FIGURE 5.2 — Oxygen abundance vs. equivalent width diagram for the star τ Sco. A microturbulence of 5 km s^{-1} , close to that resulting in the zero slope, has been considered. Uncertainties in the oxygen abundance and the slope are those associated with the linear fit (the abundance error due to the scatter of individual line abundances has not been added). Two lines can be clearly distinguished having higher abundances than the remaining ones (see text)

A grid of FASTWIND models with fixed stellar parameters³ ($T_{\text{eff}} = 32000 \text{ K}$, $\log g = 4.0$, $\epsilon(\text{He}) = 0.09$, $\log Q = -13.5$ and $Z = Z_{\odot}$) and different values of oxygen abundance and microturbulence⁴ is calculated for this analysis. A fixed microturbulence of 5 km s^{-1} is considered in the model calculation, while it is varied in the formal solution. Although the EW of the metal lines is slightly dependent on the microturbulence assumed for the model calculation, this approach is good enough for the purpose of the study presented below. The calculation of the theoretical equivalent widths of the O II lines is performed separately for each one of the lines, so possible contamination by lines from other elements are not considered (the model produces pure O II equivalent widths).

Figure 5.2 shows the $\log \epsilon(\text{O})$ - $\log EW$ diagram for a microturbulence of 5 km s^{-1} , corresponding to a slope value close to zero. Two lines can be clearly identified yielding higher abundances compared with the remaining ones. These lines, O II $\lambda 4673$ and O II $\lambda 4325$, were identified as possibly contaminated by other C III lines and must be ruled out in the analysis.

The scatter in the line abundances is normally assumed to be associated with the errors in the departure coefficients from different multiplets in the modeling process, or even with the uncertainties of the calculated line oscillator strengths. This disper-

³The stellar parameters for τ Sco have been derived through a visual fitting of the optical H and He I-II lines (see Chapter 6)

⁴See Chapter 3, Section §3.3.3.

sion is added to the uncertainty of the final abundance; however, as it will be shown below, it can also have an important effect over the final abundance value through the derived microturbulence. Therefore, although the equivalent widths of the whole set of O II lines ranges from the order of a few mÅ to more than a hundred mÅ, and would be perfect for the determination of the microturbulence, some authors prefer not to trust the microturbulence resulting from the zero slope fit of these lines since they come from different multiplets. Instead, assuming that the microturbulent velocity should be the same for all the species, they suggest to use the Si III $\lambda\lambda$ 4552, 4567, 4574 triplet for deriving the microturbulence (e.g. McErlean et al. 1999). However, it will be shown in the following sections that it is feasible to determine the microturbulence using lines from different O II multiplets if a detailed multiplet analysis is performed, and that this makes the final derived abundance more reliable, as inherent problems related to the model atom can be detected.

5.3.2 Detailed multiplet study

Where are the different metal lines formed in the stellar atmosphere? Are lines from different multiplets formed in different regions, and lines from the same multiplet in the same region? In that case, are lines from different multiplets affected by different values of microturbulence? These are important questions to answer to know if either it is feasible to use lines from different multiplets for the determination of the microturbulence or not.

Let's study a simple case to try to answer those questions: the line formation region in a plane parallel stellar atmosphere. For this case the monochromatic optical depth is defined by:

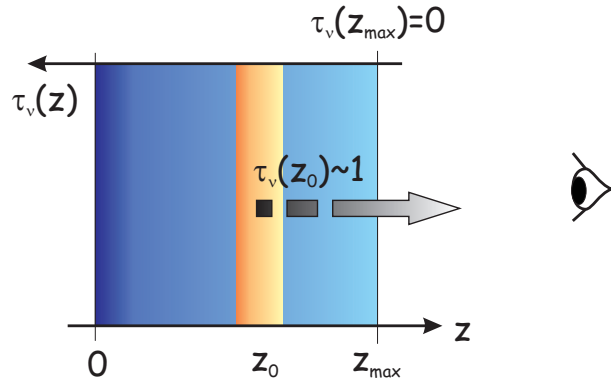
$$\tau_\nu(z) = \tau_\nu^c(z) + \tau_\nu^l(z) = - \int_z^{z^{max}} (\kappa_\nu^c + \sigma_\nu^c) dz - \int_z^{z^{max}} \chi_\nu^l dz \quad (5.1)$$

where z increases upwards in the stellar atmosphere (i.e. towards an external observer, see Figure 5.3), κ_ν^c and σ_ν^c are the continuous absorption and scattering coefficients, and χ_ν^l is the line absorption coefficient. The later, in NLTE and assuming *complete redistribution*, is defined by:

$$\chi_\nu^l = \frac{\pi e^2}{m_e c} b_l n_l^* f_{lu} \phi(\nu - \nu_0) \left[1 - \frac{b_u}{b_l} e^{-h\nu/KT} \right] \quad (5.2)$$

where b_l and b_u are the NLTE departure coefficients for the lower and upper level respectively, n_l^* is the lower level LTE population, f_{lu} is the line transition oscillator strength, and ϕ the line profile.

FIGURE 5.3 — In a plane parallel stellar atmosphere the emergent spectrum at frequency ν is formed in the region of the atmosphere around z_0 , where the optical depth achieves the condition $\tau_\nu(z_0) \sim 1$



Let's assume that the condition $\tau_\nu(z_0) \sim 1$ defines the point z_0 where the atmosphere becomes optically thin for this frequency (then it is said that the emergent spectrum at this frequency is formed in z_0). This is a simplification⁵ but it will be considered for illustrative purposes. The smaller the total absorption coefficient, the deeper in the atmosphere is formed the emergent spectrum at this frequency. This produces, for example, in the case of a OB star, the optical continuum being formed deeper than the UV continuum. The sharp variation of the line profile makes the line core being formed in a different location than its wings. Therefore, the region where a line becomes optically thin is defined by the points where the line core achieves an optical depth $\tau_\nu^c + \tau_\nu^l \sim 1$ (upper limit) and the optical depth of the adjacent continuum $-\tau_\nu^c$ achieves the same condition (lower limit). In the spectral window between the hydrogen Balmer and Paschen jumps the continuum absorption coefficient varies smoothly with frequency, and hence it can be assumed that the wings of all the optical lines are formed over the same region in the stellar atmosphere (where the optical continuum forms).

Figure 5.4 shows the points at which the line cores of the O II lines attain an optical depth of unity in a model for τ Sco. It can be clearly seen that the formation depths of these lines cover over a large region in the stellar atmosphere between $\log \tau_R \sim -3$ and -1 , independently of the multiplet. Therefore, it can be assumed that all the optical O II lines from different multiplets are formed approximately over the same region. This means that there is not a real physical reason hindering the use of lines from different multiplets for deriving the microturbulence. Actually, part of the reason why the microturbulence derived using lines from different multiplets may be erroneously calculated is related to the way the lines are calculated by the stellar

⁵ Actually photons at a given frequency escape from a larger region $[\tau_\nu^A, \tau_\nu^B]$ with $\langle \tau_\nu \rangle \sim 1$

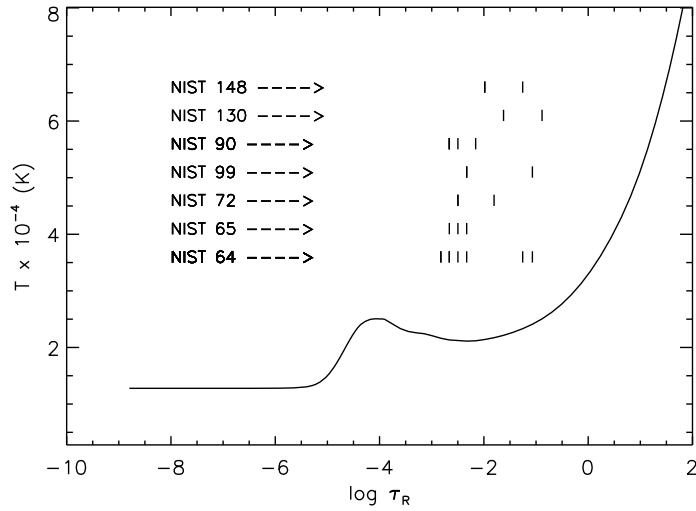


FIGURE 5.4 — The points where the core of the O II lines becomes optically thin ($\tau_{\nu}^c + \tau_{\nu}^l \sim 1$) have been overplotted to the temperature structure of the FASTWIND model used for the analysis of τ Sco. Lines are grouped into different multiplets.

atmosphere code. Lines from the same multiplets come from sublevels that are grouped together in the model calculation (only the departure coefficients of levels with quantum numbers n and L are calculated in a first approximation, then they are split according to the statistical weights of the J sublevels in the formal solution). If there was an error in the calculation of the departure coefficient of some level this would produce an error in the global transition, and hence in the lines within this multiplet with respect to other multiplets. The final result is a dispersion between results from different multiplets. Nevertheless lines within a multiplet would be consistently calculated. Obviously, this dispersion can affect the derived zero-slope microturbulence and hence the final abundance (see e.g. the case presented in Figure 5.10).

To minimize the effect of the line abundance dispersion in the microturbulence determination, the best would be to consider lines from only one multiplet that spread over a large range in EW s. However this is not always possible or, even more, could be dangerous (if some line is contaminated by another line, its EW is not accurately measured or has an erroneous $\log gf$ value). For the case of O II, any single multiplet has a small range in equivalent width, and hence the value of ξ_t is not well constrained. The use of several multiplets will contribute to derive an accurate value for microturbulence.

Figure 5.5 shows the $\log \epsilon(\text{O})$ - EW diagrams for the lines in τ Sco, but this time separated by multiplets. From these plots several interesting conclusions can be derived (see also Table 5.4):

- Some of the multiplets cannot be used separately for deriving the microturbulence because the equivalent width baseline is very small (viz. NIST 65, 99 and 161).
- The bad quality of the spectrum can produce errors in the measurements of the EW s, and then a large dispersion in the line abundances within one multiplet (e.g. NIST 90; these lines are located in a region of the observed spectrum of τ Sco with a worse quality).
- Lines with small EW present large uncertainties in the line abundance. This affects the derived microturbulence and its uncertainties. These lines should be only considered if they are in agreement with the remaining lines in the multiplet (e.g. O II λ 4741 in multiplet 118 and O II λ 4696 in multiplet 64).
- Sometimes discrepancies are found between the abundances of lines from the same multiplet, even in cases where the EW of the lines are accurately measured and no known line contamination is present in the spectrum (e.g. O II $\lambda\lambda$ 4414, 4416 in multiplet 72). This may be related with the atomic data.
- The global solution traces rather well the mean behavior of the different multiplets (see however below).
- Two of the multiplets are producing systematically lower abundances (NIST 161 and 188). These multiplets have (1D) 3p levels (with very close energies, see Figure 5.8) as lower levels, and hence it can be argued that is the calculation of the departure coefficients for those levels what is producing this difference in the line abundances. Following this argument, lines O II $\lambda\lambda$ 4703, 4699⁶ (NIST 172), corresponding to (1D) 3p (2D_0) - (1D) 3d (2F_0) transition should show the same behavior. Figure 5.6 shows that this is the case, with all these lines giving lower abundances than the remaining ones.

⁶The line O II λ 4699 is formed by three components, two of them from multiplet 172 and the third one from multiplet 118. The former two components are affecting the line in the same way than those from multiplets 161 and 188

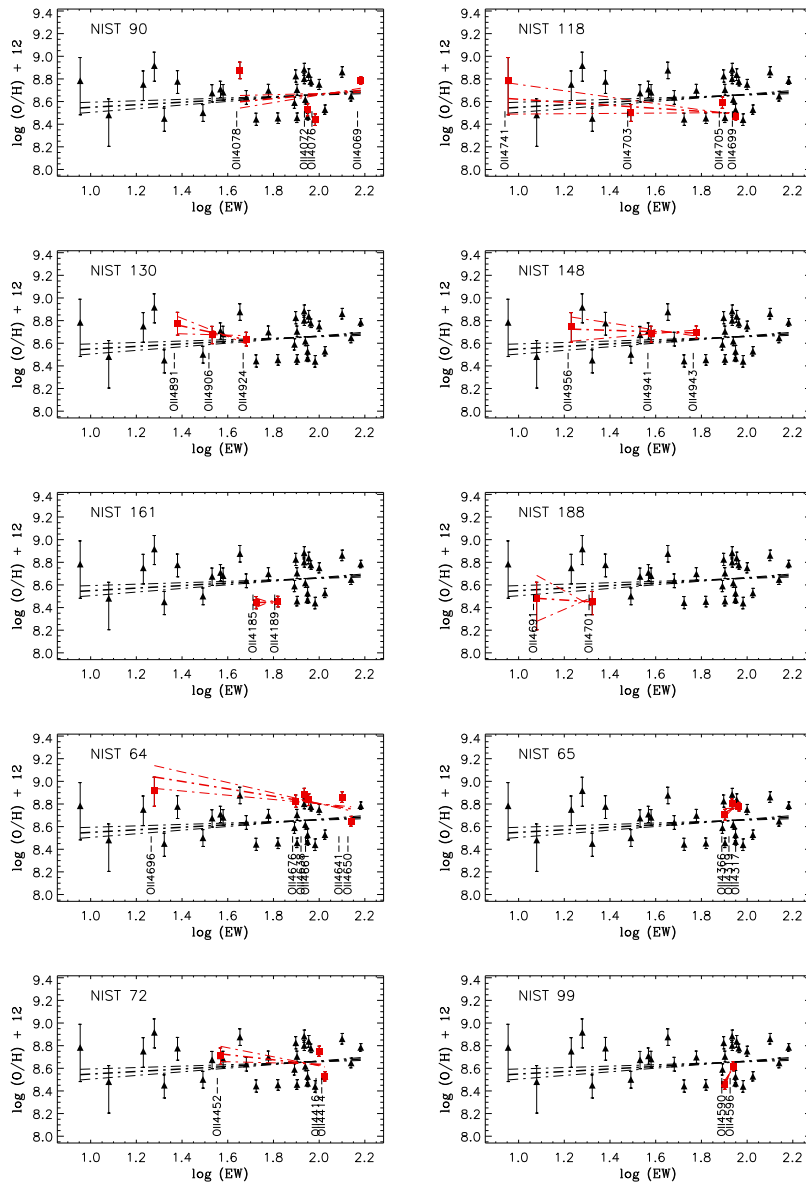


FIGURE 5.5 — Oxygen abundance - EW diagrams for the lines of the different multiplets. Black triangles represent the whole set of lines (except $O\ II\ \lambda\ 4673, 4325$) for a microturbulence of $5\ \text{km s}^{-1}$. Overplotted as red squares, lines belonging to the multiplet indicated in the upper left corner. The resulting slope for a microturbulence of $5\ \text{km s}^{-1}$ has been plotted for each separate analysis.

Multiplet (NIST)	# lines	EW range (dex)	Comments
90	4	0.55	High dispersion. Probably due to the bad quality of the τ Sco CASPEC spectrum in this zone
118	4	1.00	Large EW range. The line O II λ 4741 is too weak to be reliable.
130	3	0.30	Low dispersion. Reliable
148	3	0.60	Low dispersion. Reliable
161	2	0.10	EW range very small. Lower abundances than the mean.
188	2	0.20	EW range small. Lower abundances than the mean
64	6	0.85	Large EW range. Reliable. However O II λ 4650 line abundance lower than the remaining ones in the multiplet. Higher abundances than the mean.
65	3	0.07	EW range very small.
72	3	0.45	Reliable. However some discrepancy between O II λ 4414 and O II λ 4416 lines.
99	2	0.10	EW range very small.

TABLE 5.4 — Notes on the detailed analysis by multiplets

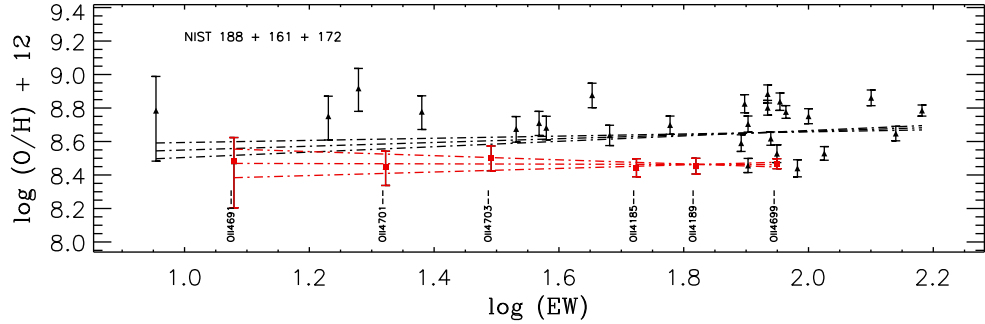


FIGURE 5.6 — Abundances derived for lines from multiplets NIST 188, 161, 172 (red) are compared with those from the remaining ones. Although the microturbulence derived from this set of lines is also $\xi_t \sim 5 \text{ km s}^{-1}$, the corresponding oxygen abundance is ~ 0.15 - 0.20 dex lower.

Final suitable O II line dataset

All the information provided by the detailed analysis by multiplets allows us to select a final suitable set of O II lines for the abundance analyses of B0.5V stars with FASTWIND and the A10HHe023–3 model atom (see Table 5.5). We have decided to rule out lines from multiplets 188, 161, 172 (which produce lower abundances than the mean, see above). Lines from multiplet 90 are also ruled out in this case (the CASPEC spectrum of τ Sco has worst quality in the spectral region where these lines are located). However, these will be considered in the analyses of the other B0.5V stars (see Chapter 6).

Figure 5.7 compares the results from the study with the whole set of O II lines and that including only the selected set of lines. The zero slope fit is achieved for a similar value of the microturbulence, however there is a difference in global abundance of ~ 0.05 dex.

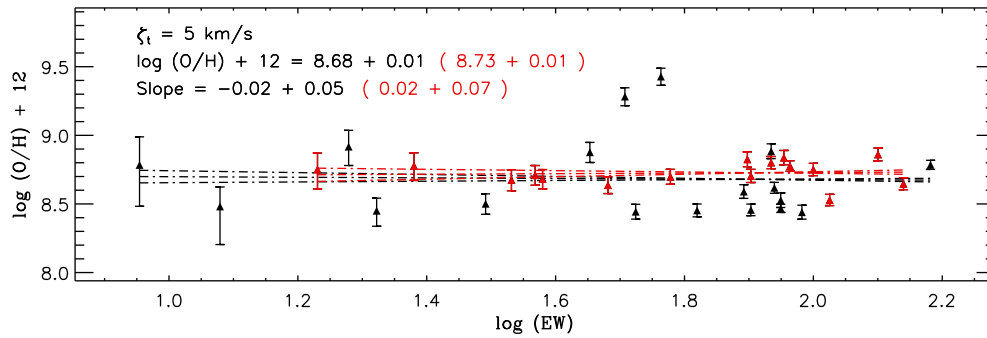


FIGURE 5.7 — Comparison of results using two different sets of O II lines. (Black) Whole set of lines summarized in Table 5.3. (Red) Final suitable set of lines, where lines from multiplets NIST 161, 172 and 188, along with O II $\lambda\lambda$ 4673, 4325 (blended) and O II λ 4741 (too small equivalent width) have been excluded.

Multiplet	Lines	Multiplet	Lines
NIST 64	O II $\lambda\lambda$ 4638, 4641, 4661, 4676	NIST 90 (*)	O II $\lambda\lambda$ 4072, 4076, 4078
NIST 65	O II $\lambda\lambda$ 4317, 4319, 4366	NIST 130	O II $\lambda\lambda$ 4941, 4943, 4956
NIST 72	O II $\lambda\lambda$ 4416, 4452	NIST 148	O II $\lambda\lambda$ 4891, 4906

TABLE 5.5 — Final suitable set of O II lines dataset. (*) These lines have been ruled out in this case (see text).

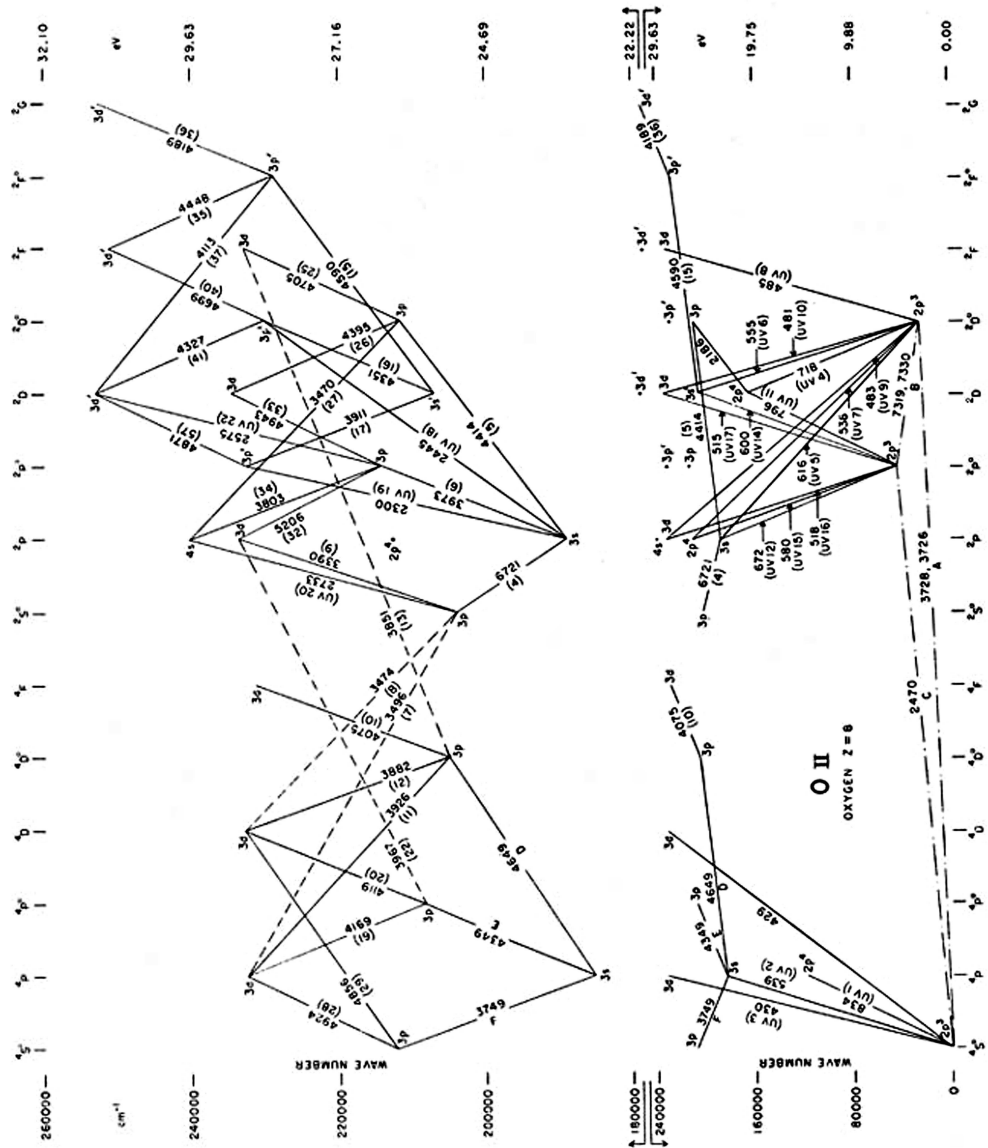


FIGURE 5.8 — Atomic energy level data for O II presented as a Grotrian diagram (downloaded from <http://spider.ipac.caltech.edu/staff/rosalie/grotrian.html>). This ion has two spin systems (quartet and doublet)

Problems with the atomic data

To illustrate the advantages of the detailed analysis by multiplets, this section will show how this methodology can help to identify model atom inconsistencies. Below, a problem that was found when an update of the oxygen model atom A10HHe023-3 was considered in the analyses is presented.

The oxygen model atom A10HHe023-3 used in the analyses of the previous section is a simplified version of the O I-IV model by Becker & Butler (1988) where the O I ion has been removed. M.A. Urbaneja updated this model in his thesis (Urbaneja 2004, hereafter A10HHe023+op), including up to 60 levels for O III and replacing the original RBF transitions by the OPACITY PROJECT data for the lower ten levels. The energies of these first 10 levels were also slightly modified to be consistent with the OP data (see Chapter 3 for a more extensive description of these model atoms).

Figure 5.9 shows the $\log \epsilon(\text{O})$ - $\log EW$ diagrams for three different microturbulences. The set of lines considered for this analysis is basically that summarized in Table 5.3, except for the O II $\lambda\lambda$ 4741, 4691 (with very low EW) and O II $\lambda\lambda$ 4673, 4325 (contaminated by lines from another ions). In this case, the scatter of the line abundances is larger than the one found in the analysis from the previous section, and the zero-slope is reached for a microturbulence larger than 15 km s^{-1} , instead of 5 km s^{-1} .

What originates this difference respect to the analysis with the A10HHe023-3 model atom? After studying different possibilities, as the effects of the inclusion of a larger number of O III levels, or the change in the treatment of the RBF transitions in the O II model atom, the answer to this question was found by means of a detailed analysis by multiplets. Figure 5.10 shows the comparison between the results from both model atoms in the same model atmosphere conditions and the same value of microturbulence (only the oxygen model atom is different in both calculations). Some of the line abundances are only slightly varied, nevertheless there is a set of lines (either with large or small equivalent widths) with very different line abundances. A more careful look at those lines with a change in their abundances (and hence in their modeled equivalent width) show that these lines correspond to multiplets with lower levels $3s^4P$, $3s^2P$ and $3p^4D_0$ (levels 6, 7 and 10 respectively in the O II model atom, exactly the three levels that a) are lower levels in one of the analyzed transitions and b) their energy levels were changed to use the OP data).

The explanation to this large difference has been found to be related to the O II level energies indicated by the OPACITY PROJECT data. The energies from the OP

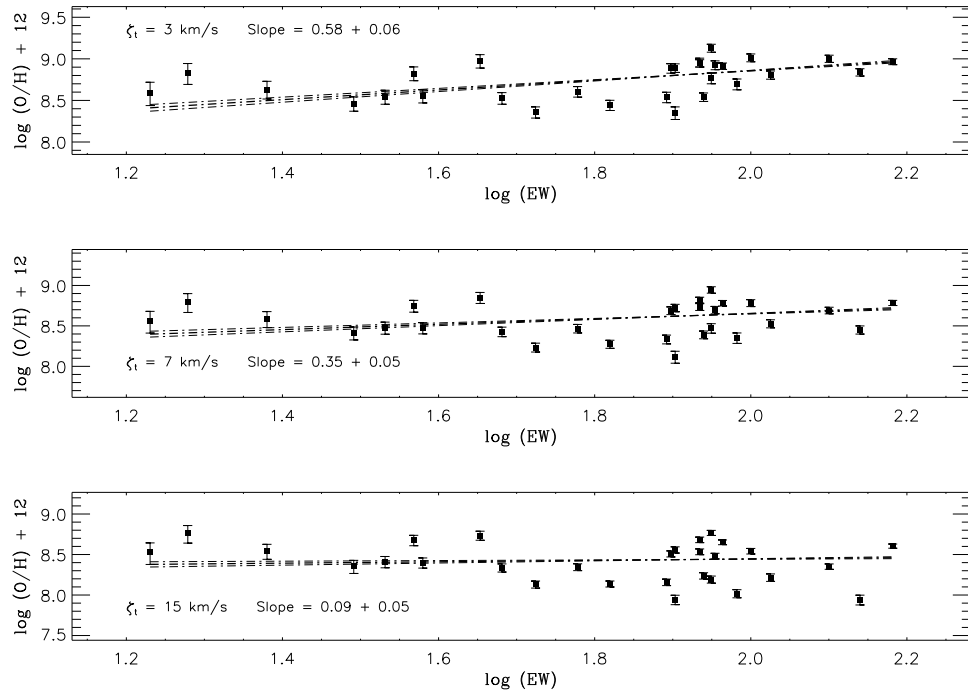


FIGURE 5.9 — Oxygen abundance analysis for τ Sco using the A10HHe023+op model atom. In this case, the zero slope is reached for a microturbulence slightly larger than 15 km s^{-1} . What is producing this large difference relative to the analysis using the A10HHe023-3 model atom?

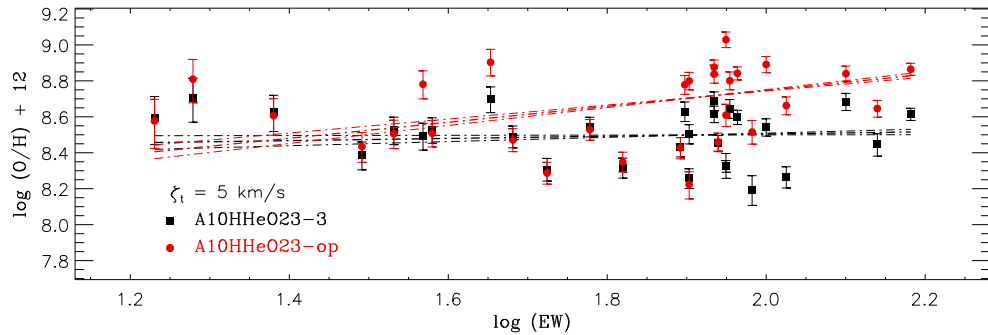


FIGURE 5.10 — Comparison of the O II line abundances resulting from the consideration of the oxygen A10HHe023-3 (black squares) and A10HHe023+op (red circles) model atoms. A microturbulence of 5 km s^{-1} has been considered in both calculations

data are the result of calculations and are somewhat different to the experimental ones derived from the analyses of optical spectra by Moore (1971). The set of level energies which are used for the model atom by Becker & Butler are the experimental one, so in order to make the A10HHe023+op model atom consistent with the data from the OPACITY PROJECT, the energies of the first 10 levels of O II must be changed to those indicated by the OP data (see Figure 5.11). This produces an inconsistency in the transitions involving those levels. Figure 5.11 illustrates this argument. The difference in excitation energies for the A10HHe023+op model atom is $\sim 1-2\%$ for those transition between levels 1 to 10 (e.g. transition 6 - 10, or resonance transitions), however this difference is larger for transitions combining levels with changed energies and the original ones (e.g. transitions 6 - 12, 7 - 13 and 10 - 19, with differences up to 5%). The result of this inconsistency is that lines from some of the multiplets are not correctly modeled⁷. This produces an artificial trend in the $\log\epsilon(\text{O})$ - EW diagrams (see Figures 5.9 and 5.10).

As a result of this study it can be concluded that when the A10HHe023+op model atom is used, the microturbulence and the final oxygen abundance derived for τ Sco (and hence, the other early B-type stars) is erroneous. For the analyses presented in the next chapter, the A10HHe023-3 model atom will be preferred although it is simpler.

This problem, which is associated with an incorrect definition of the oxygen model atom, reinforces the suggestion that it is dangerous to use lines coming from different multiplets for deriving the microturbulence through the zero slope in the $\log\epsilon(\text{O})$ - $\log EW$ diagrams; however even if we do not trust the microturbulence given by the O II lines analysis and use that resulting from other ions, the final oxygen abundance would be erroneously larger.

Therefore, we conclude the utility of this detailed analysis by multiplets for determining the reliability of the model atoms in different situations and defining the suitable set of lines that can be used for the abundance analyses. We propose to use this approach in cases with good spectral resolution and SNR before moving towards those cases where the stellar spectrum is observed with worse resolution and/or SNR .

⁷M.A. Urbaneja is working in the solution of this problem. The new version corrects the difference in energies by shifting the OP cross sections edges to the energies in Becker & Butler oxygen model atom.

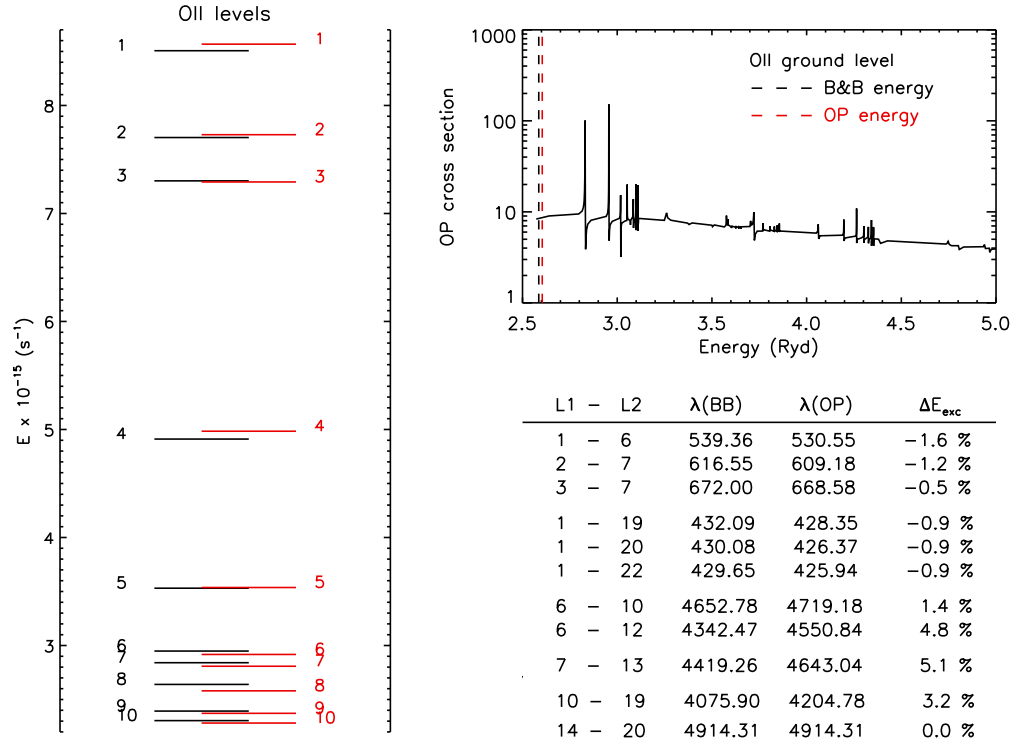


FIGURE 5.11 — (Left) Diagram showing the energies of the O II levels considered in the model atom by Becker & Butler (black) and in the OPACITY PROJECT database (red). (Lower right) The difference in energies produces a discrepancy in the excitation energies of some of the optical and UV transitions. (Upper right) Photoionization cross section for the O II fundamental level as defined by the OP data.

5.3.3 Effect of the stellar parameters over the derived oxygen abundances

Monteverde et al. (2000) and Villamariz et al. (2002) presented a very thorough study about uncertainties in the stellar abundance analysis. Here, we will present a different, more visual approach, for showing the effect of the stellar parameters uncertainties on the abundance analysis process through the curve of growth method. This work is based on previous works by A. Herrero, I. Monteverde, M.R. Villamariz and M.A. Urbaneja, collaborators of the "*Estrellas Masivas Azules*" group at the Instituto de Astrofísica de Canarias (IAC).

Figure 5.12 shows the effect of a change of ± 1000 K and ± 0.2 dex, in T_{eff} and $\log g$ respectively, over the O II line abundances. The whole set of lines summarized in Table 5.2 has been included in the analysis (except O II $\lambda\lambda$ 4325, 4673) and the model atom A10HH ϵ 023-3 has been considered. The same value of microturbulence ($\xi_t = 5 \text{ km s}^{-1}$) has been considered in all cases.

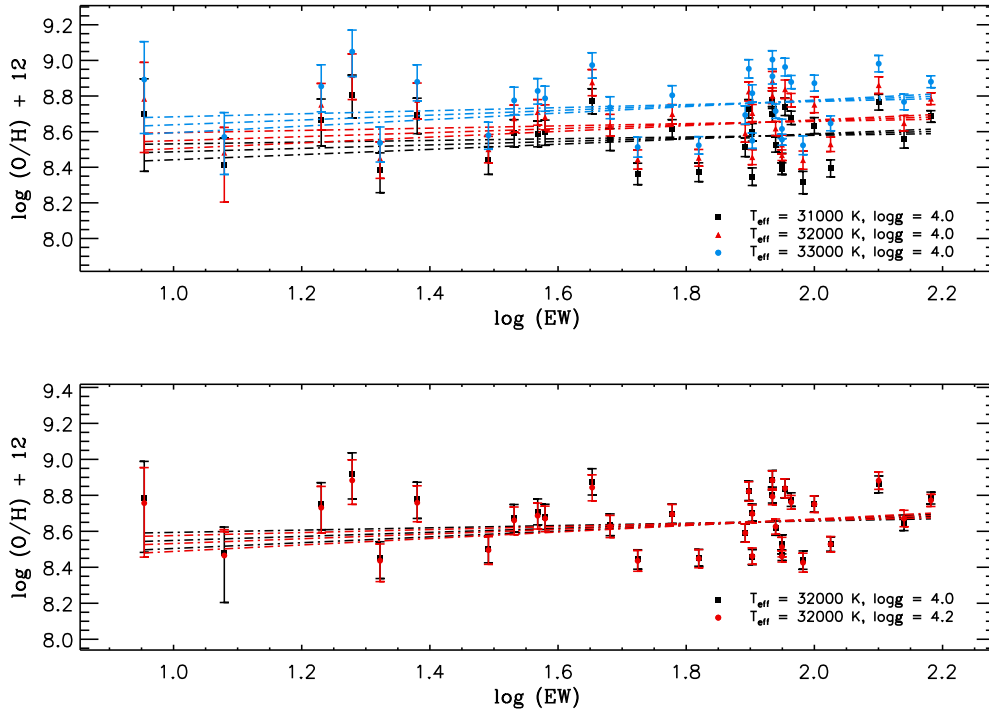


FIGURE 5.12 — Effects of the variation of T_{eff} (up) and $\log g$ (down) over the oxygen abundances for the case of τ Sco. The same value of microturbulence ($\xi_t = 5 \text{ km s}^{-1}$) is always considered.

From these comparisons we can conclude:

1. Within these range of stellar parameters, O II lines become fainter as T_{eff} gets higher, therefore line abundances become larger for models with higher effective temperatures. The behavior is the opposite for the gravity.
2. A change in T_{eff} or $\log g$ produces a shift in the abundance of every line, however the slope is only slightly varied.

3. The effect of a change in the effective temperature over the line abundances ($\Delta \log \epsilon(\text{O}) \sim 0.08$ dex for $\Delta T_{\text{eff}} \sim 1000$ K) in these range of stellar parameters is larger than the effect of a change in the gravity ($\Delta \log \epsilon(\text{O}) \sim 0.02$ dex for $\Delta \log g \sim 0.2$ dex).
4. The discrepancy found in §5.3.2 between the abundance derived from multiplets 188, 161, 172, and the global trend stands still if a different value of T_{eff} or $\log g$ is considered.

5.3.4 Comparison between FASTWIND, CMFGEN and TLUSTY results

FASTWIND, CMFGEN, and TLUSTY are three commonly used stellar atmosphere codes. In Chapter 3 (§3.2) it has been commented that both CMFGEN and TLUSTY produce a more complete treatment of the line blanketing effects than FASTWIND does. To check the reliability of FASTWIND results and to study the consistency between the abundances derived through these stellar atmosphere codes, this section compares the results of the oxygen abundance analyses performed with these codes for the star τ Sco. Note that, although TLUSTY is a plane parallel model atmosphere, this assumption can be considered as valid in the case of stars with large gravities where the effects of sphericity and mass loss are almost negligible (this is the case of the stars that will be studied in this thesis). Therefore, a comparison with TLUSTY results is also meaningful.

A grid of models with fixed stellar parameters and different oxygen abundance and microturbulence has been calculated with each one of the codes. The stellar parameters used for the grids are $T_{\text{eff}} = 32000$ K, $\log g = 4.0$ dex, $\epsilon(\text{He}) = 0.09$ and $Z = Z_{\odot}$. Additionally, FASTWIND and CMFGEN requires information about the wind characteristics ($\log Q = -13.5$). CMFGEN and TLUSTY models were calculated by F. Najarro (CSIC) and R. Ryans (QUB) respectively. Information about the model atoms considered in TLUSTY can be found in <http://star.pst.qub.ac.uk/>.

FASTWIND and TLUSTY models produce pure O II equivalent widths, however in the case of CMFGEN, the equivalent width of the lines have been calculated from the final spectrum once the formal solution is performed. Since these formal solution includes lines from other elements than oxygen, the equivalent widths of the O II may be contaminated by the presence of other nearby modeled lines. This has been taken into account for the selection of lines that will be used in the analyses.

The same set of O II lines has been used for the abundance analysis by means of the curve of growth method. These are the lines labeled with an asterisk (*) in

Table 5.3. Figure 5.13 shows the $\epsilon(\text{O})$ - $\log EW$ diagrams for the microturbulence in the grid of models that produces a slope value close to zero for each one of the FASTWIND, TLUSTY, and CMFGEN analyses.

Below, the results of the analyses are presented, along with some comments on problematic lines:

- **FASTWIND ANALYSIS:** Comments on this analysis has been presented in previous sections. A $\xi_t = 8.5 \pm 1.5 \text{ km s}^{-1}$ and $\epsilon(\text{O}) = 8.72 \pm 0.04 \text{ dex}$ is derived using the whole set of common lines.
- **TLUSTY ANALYSIS:** In this case, $\text{O II } \lambda\lambda 4891, 4906$ and $\text{O II } \lambda\lambda 4317, 4319$ lines (multiplets 130 and 65 respectively) must be ruled out from the analysis. There is some unidentified problem with the lines from multiplet 130. The large abundance derived for the other two lines may be related with the fact that TLUSTY calculations do not include the second component of these lines (see Table 5.2). A $\xi_t = 4.5 \pm 1.0 \text{ km s}^{-1}$ and $\epsilon(\text{O}) = 8.86 \pm 0.03 \text{ dex}$ is derived using the remaining lines.
- **CMFGEN ANALYSIS:** In this case, $\text{O II } \lambda\lambda 4891, 4906$ (multiplet 130) lines must be ruled out from the analysis. CMFGEN also produces too large equivalent width for this two lines, and hence the derived abundance is too low. A $\xi_t = 2 \pm 2 \text{ km s}^{-1}$ and $\epsilon(\text{O}) = 9.0 \pm 0.1 \text{ dex}$ is derived using the remaining lines.

Once the problematic lines have been identified and ruled out, derived abundances can be directly compared. It is found that from TLUSTY and CMFGEN analyses, a larger value of oxygen abundance is derived compared to the one derived from FASTWIND analysis. This discrepancy is mainly related to the large dependence of the derived abundances on the effective temperature in this range of stellar parameters (corresponding to early B type main sequence stars). In this range TLUSTY and CMFGEN produce larger He II lines than FASTWIND does for a given T_{eff} , and hence a lower effective temperature (~ 1000 - 2000 K) would be estimated for $\tau \text{ Sco}$ when using these stellar atmosphere codes. Since CMFGEN and TLUSTY models have been calculated using a larger T_{eff} than the one that is required to fit the observed lines, and the equivalent width of the O II modeled lines is smaller for larger effective temperatures, the oxygen abundance required to fit the observed O II lines will be larger. This discrepancy can be minimized if the analysis is performed consistently for each one of the codes (i.e. using the stellar parameters derived from the HHe analysis).

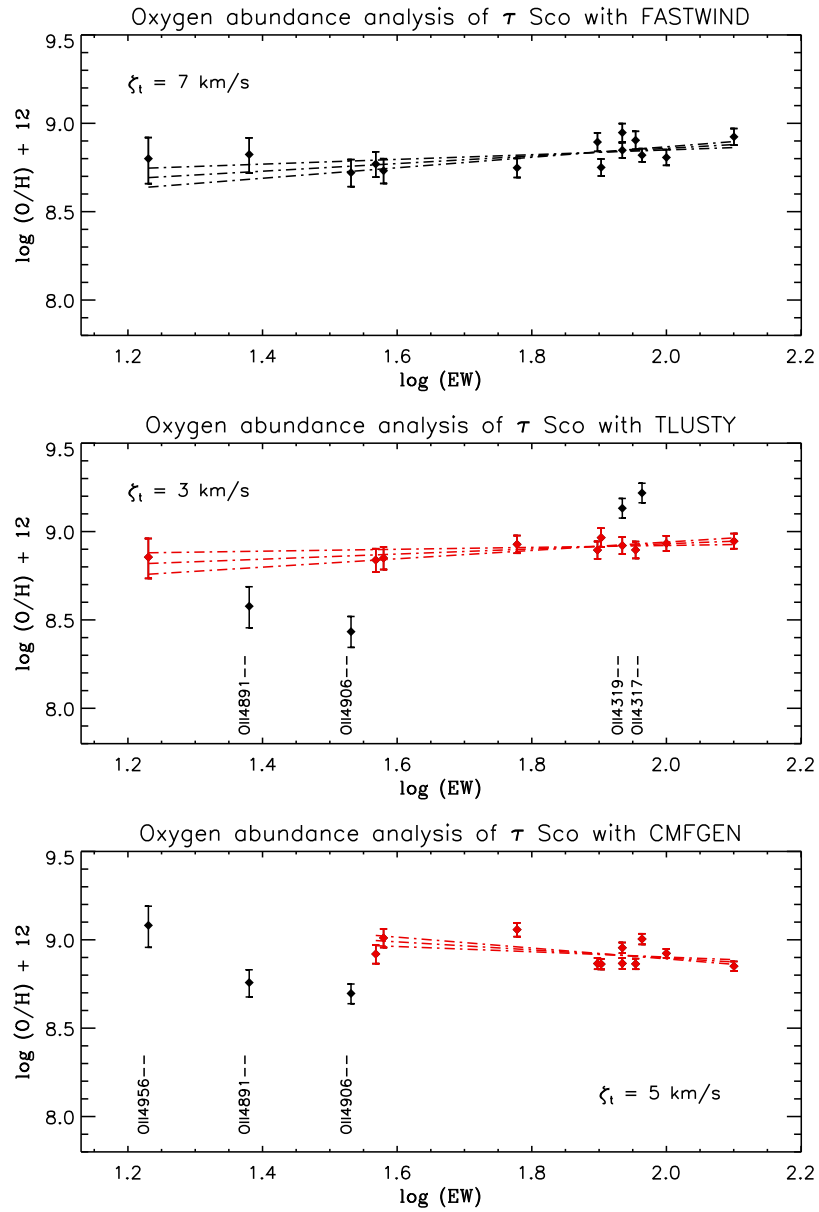


FIGURE 5.13 — Oxygen abundance analysis for τ Sco using three commonly used stellar atmosphere codes (FASTWIND, TLUSTY and CMFGEN). The same set of lines is initially used in the analyses, however the marked lines have been ruled out in TLUSTY and CMFGEN analyses.

5.4 Silicon abundances

Spectra of early B-type stars contain lines from two different ionizing states of silicon. Table 5.1 resumes the whole set of Si III-IV lines identified in the spectrum of τ Sco, divided by multiplets. Their equivalent widths are summarized in Table 5.6.

The silicon model atom — A10HHeSi34 — used for the analyses has been defined in Chapter 2. A grid of FASTWIND models with fixed stellar parameters (see section 5.3) and different values for silicon abundance and microturbulence is calculated in the same way than the one generated for the oxygen abundance analysis (see Section §5.3).

Line	EW	$\log EW$	Line	EW	$\log EW$
Si III λ 4813	16	1.20	Si IV λ 4950	6	0.78
Si III λ 4716	18	1.26	Si IV λ 4212	42	1.62
Si III λ 4819	30	1.48	Si IV λ 4631	64	1.81
Si III λ 4829	37	1.57	Si IV λ 4654	78	1.89
Si III λ 4574	73	1.86	Si IV λ 4116	125	2.10
Si III λ 4567	115	2.06	Si IV λ 4089	185	2.27
Si III λ 4552	126	2.10			

TABLE 5.6 — Ascending ordered observed equivalent widths (mÅ) for τ Sco Si III and Si IV lines. Uncertainties in the measurement of the EW are ± 5 mÅ.

A similar approach through a detailed analysis by multiplets (and, in this case, also by ionizing state), will allow us to define the suitable set of lines for the silicon abundance analyses. Figure 5.14 shows the $\log \epsilon(\text{Si})$ - EW diagrams for the whole set of lines and three different microturbulences. The analysis is done independently for Si III and Si IV lines. For the case of Si III lines, zero slope is reached for a microturbulence of 6 km s^{-1} when the whole set of lines is considered. However, for this microturbulence there is a dependence of the line abundances with the equivalent width for the lines Si III $\lambda\lambda$ 4552, 4567, 4574 (zero slope is reached for this multiplet for a microturbulence of 1 km s^{-1}). It could be assumed that there is some inconsistency in the atomic data for the Si III λ 4574 line, however the change in $\log gf$ needed to fit this line to the remaining ones is too large to be reasonable. Considering the microturbulence derived through the Si III $\lambda\lambda$ 4552, 4567, 4574 multiplet, the other Si III lines have systematically lower abundances. These lines (Si III $\lambda\lambda$ 4813, 4819, 4829 and Si III λ 4716) come from 4d-5f and 4f-5g transitions, close to the highest levels considered in the model atom and hence could be affected by boundary conditions. This discrepancy has been previously pointed

out by Becker & Butler (1990). In their paper, these authors include a short discussion on the reliability of the different synthetic lines for the determination of the stellar temperature. If they adopt the reproduction of the observed Si III $\lambda\lambda$ 4552, 4567, 4574 triplet as a good criterion, they find the theoretical EW of the lines from the other triplet Si III $\lambda\lambda$ 4813, 4819, 4829, as well as the Si III λ 4716 line, to be systematically too strong.

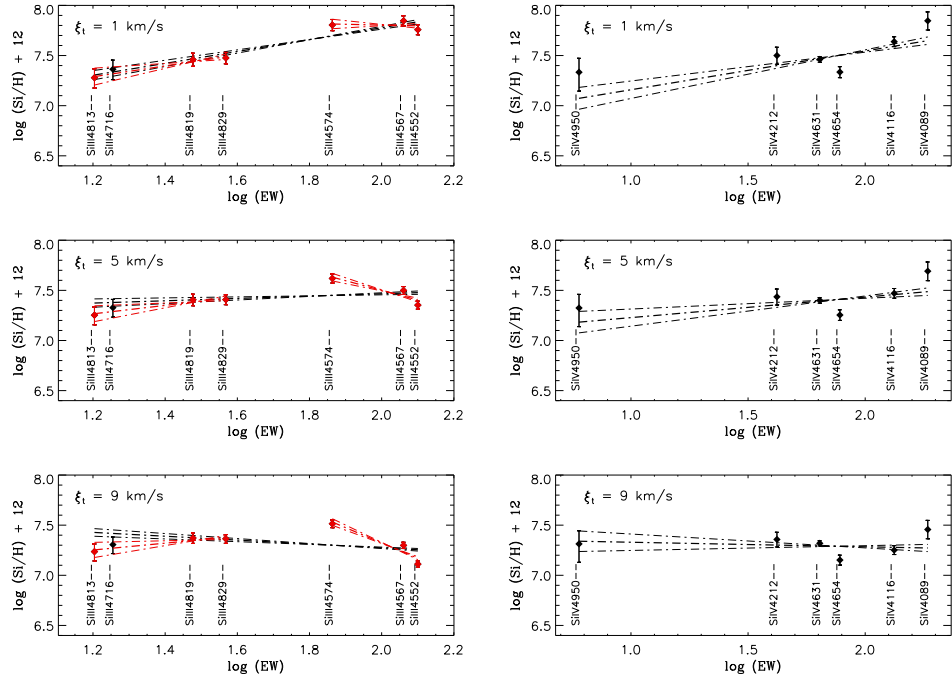


FIGURE 5.14 — Detailed silicon abundance analysis. (Left) Black line fits the whole set of Si III lines; linear fits to different multiplets are show as red lines. (Right) Linear fit to the Si IV lines.

The behavior of Si IV lines is as follows: Si IV λ 4089 is known to be contaminated by another O II line (and hence, as this O II line is not considered in the formal solution, the line abundance derived using this line is too high and not taken into account); Si IV λ 4950 seems to follow the general trend, however it is very weak and can affect drastically the global result; the remaining four lines are consistent (although Si IV λ 4654 gives slightly lower abundances than the remaining three).

The final suitable set of lines for the silicon abundance analyses of B0.5V stars with FASTWIND and the silicon model atom A10HHeSi34 consists of Si III $\lambda\lambda$ 4552, 4567, 4574 and Si IV $\lambda\lambda$ 4116, 4212, 4631 lines.

5.4.1 Microturbulence from the Si analysis

The triplet Si III $\lambda\lambda$ 4552, 4567, 4574 is commonly used to establish the microturbulence in B-type stars. In this case it is found that the microturbulence derived from the oxygen analysis is somewhat larger ($\sim 5-7 \text{ km s}^{-1}$) than what it derived from Si III analysis. A similar problem has been previously found in the analysis of B-type supergiants (McErlean et al. 1999, Trundle et al. 2002), who establish a normal value for microturbulence in B supergiants of $\sim 10-12 \text{ km s}^{-1}$ (derived from silicon analyses), being larger the microturbulence derived from oxygen ($\xi_t \sim 15-20 \text{ km s}^{-1}$).

Table 5.7 shows how the derived oxygen and silicon abundances depend on the microturbulence. These abundances have been calculated for $\xi_t = 1$ and 5 km s^{-1} , the values inferred from the O II and Si III analyses respectively. The difference in the final abundances are ~ 0.15 dex (oxygen) and ~ 0.3 dex (silicon) depending on the considered microturbulence.

Which microturbulence do we trust? Shall all the elements be affected by the same microturbulence? These remain as open questions. More work is needed to understand if these differences in the derived microturbulences are real, or only a result of the modeling process (as an illustrative example of the second possibility it can be considered the case studied in Section §5.3.2, in which a bad definition of the oxygen model atom results in a microturbulence derived from O II lines larger than 15 km s^{-1} , while the correct one is $\sim 5-10 \text{ km s}^{-1}$). Meanwhile, in the analyses presented in the forthcoming chapter, a different microturbulence will be considered for each element.

	$\xi_t = 1 \text{ km s}^{-1}$	$\xi_t = 5 \text{ km s}^{-1}$
$\log(\text{O}/\text{H}) + 12$	8.93	8.77
$\log(\text{Si}/\text{H}) + 12$	7.80	7.48

TABLE 5.7 — Effect of the microturbulence on the derived oxygen and silicon abundances. Abundance values correspond to a stellar model atmosphere with $T_{\text{eff}} = 32000 \text{ K}$ and $\log g = 4.0$ dex. Only the Si III $\lambda\lambda$ 4552, 4567, 4574 triplet is considered for the silicon abundance. Note comment about S III/Si IV ionization balance in next section

5.4.2 Effect of the stellar parameters over the derived silicon abundances

Figure 5.15 and Table 5.8 show the effect of varying the stellar parameters over the derived silicon abundances. A microturbulence $\xi_t = 1 \text{ km s}^{-1}$ has been considered in all cases (estimated from the zero-slope of the Si III triplet). These are the conclusions that can be derived from this comparison:

- Similar to the oxygen case, the slope in the $\log \epsilon(\text{Si})$ - EW diagrams is only slightly dependent on the stellar parameters, and hence the derived microturbulence.
- In this case the uncertainties associated with a change of 1000 K and 0.1 dex in effective temperature and gravity are 0.2 and 0.05 dex respectively.
- The agreement between silicon abundances derived from Si III and Si IV (i.e. the ionization balance for Si IV/Si III, see Figure 5.15) is achieved for $T_{\text{eff}} = 31000 \text{ K}$, $\log g = 4.0 \text{ dex}$. There is a difference of $\sim 1000 \text{ K}$ respect to the effective temperature derived from the HHe analysis.
- There is a difference of $\sim 0.20 \text{ dex}$ between the silicon abundance that is derived considering the Si III lines along with the stellar parameters derived from the HHe analysis ($T_{\text{eff}} = 32000 \text{ K}$, $\log g = 4.0 \text{ dex}$), and the value corresponding to the Si IV/Si III ionization balance (see Figure 5.15). This later value ($\epsilon(\text{Si}) = 7.67 \text{ dex}$) is assumed to be the correct one.

	$\log g = 4.0 \text{ dex}$	$\log g = 4.2 \text{ dex}$
$T_{\text{eff}} = 31000 \text{ K}$	Si III: 7.62 ± 0.03 Si IV: 7.64 ± 0.02	Si III: 7.61 ± 0.03 Si IV: 7.80 ± 0.03
$T_{\text{eff}} = 32000 \text{ K}$	Si III: 7.80 ± 0.03 Si IV: 7.48 ± 0.03	Si III: 7.78 ± 0.02 Si IV: 7.60 ± 0.03
$T_{\text{eff}} = 33000 \text{ K}$	Si III: 8.06 ± 0.03 Si IV: 7.93 ± 0.03	Si III: 7.36 ± 0.03 Si IV: 7.45 ± 0.02

TABLE 5.8 — Effect of varying the stellar parameters on the silicon abundances. Si III and Si IV analysis has been considered separately for a microturbulence of 1 km s^{-1} .

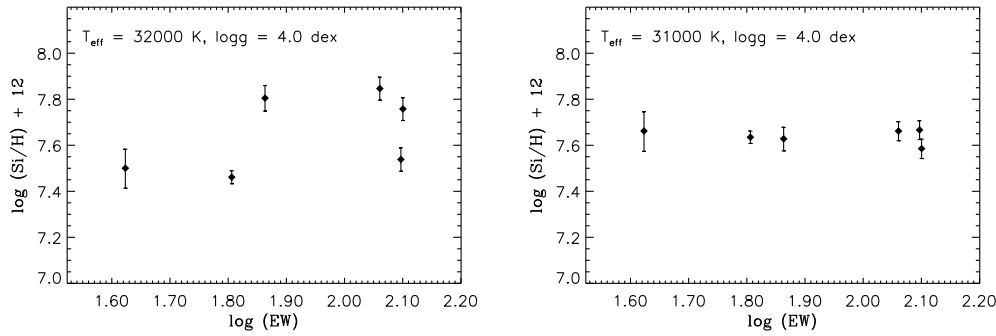


FIGURE 5.15 — Effect of varying the effective temperature on the silicon abundance. Only the Si III $\lambda\lambda$ 4552, 4567, 4574 and Si IV $\lambda\lambda$ 4212, 4631, 4116 have been considered. The plot shows the results for a microturbulence of 1 km s^{-1} .

5.5 Summary and conclusions

The results of a detailed oxygen and silicon abundance analysis for the low $v \sin i$ star τ Sco (B0.2V) have been presented. The study of this star has been used as a *benchmark test* for the stellar abundance analysis of early B-type stars with the stellar atmosphere code FASTWIND. The main points below summarize the results from this chapter:

- A set of oxygen and silicon lines, present in the spectral range between 4000 and 5000 \AA and useful for the abundance study in early B-type main sequence stars has been presented.
- The utility of the detailed analysis by multiplets approach as an initial step to identify problems in the model atoms has been shown. A suitable set of lines for the abundance analyses with FASTWIND has been established.
- It has been shown that it is feasible to use the whole set of O II lines to determine the microturbulence if firstly a detailed analysis by multiplets is performed.
- The A10HHe023–3Si34 model atom will be used for the analyses presented in the forthcoming chapter.
- The reliability of the oxygen abundance derived with FASTWIND has been studied, comparing it with the abundances derived by means of other two commonly used stellar atmosphere codes (CMFGEN and TLUSTY).

- The dependence of the oxygen and silicon abundance with the stellar parameters has been shown. The derived microturbulence does not depend on them, only the final global abundance.
- It has been mentioned that the microturbulence derived from the silicon analysis (1 km s^{-1}) is somewhat smaller than the one derived from the oxygen analyses ($\sim 5-7 \text{ km s}^{-1}$). This difference has been previously found for the case of B-type supergiants. The difference in the final abundances are ~ 0.15 dex (oxygen) and ~ 0.3 dex (silicon) depending on the considered microturbulence.
- The Si IV/Si III ionization balance is achieved for a $T_{\text{eff}} \sim 1000 \text{ K}$ lower than the value derived from the He II/He I analysis. The difference is within the uncertainties for the stellar parameters, however the effect of the derived silicon abundance through the Si III lines is large (~ 0.2 dex). The silicon abundance corresponding to the Si IV/Si III ionization balance is preferred.

THE NEAREST STAR FORMING REGION: THE ORION
NEBULA

*Orion, the hunter of Taurus the bull, and Lepus the hare.
Followed faithfully by his companions Canis Major, and Canis Minor,
he is the dominator of the northern sky*

- Greek Mythology -

Results of a detailed spectroscopic analysis of the massive stars associated with the Orion Nebula, together with reference stars used for comparison, are presented. The rotational velocities have been obtained using the Fourier analysis method, finding agreement with values derived from the usual method, based on linewidth measurements. The rotational velocity derived for θ^1 Ori C through this method is consistent with the variability of some of its spectral features that have a period of 15.42 days. By means of the fit of the H, He I and He II observed profiles with FASTWIND synthetic profiles, stellar parameters and wind characteristics have been derived. It is found that macroturbulence effects have to be included for a good fit to the He I-II lines in the spectrum of θ^1 Ori C.

By means of a very accurate study, oxygen and silicon abundances have been derived for the three B0.5V stars θ^1 Ori A, D and θ^2 Ori B. Final oxygen abundances are consistent with nebular gas-phase results presented in Esteban et al. (2004) and are lower than those given by Cunha & Lambert (1994). This new result suggest a lower dust depletion factor of oxygen than previous estimations for the Orion nebula.

6.1 Introduction

PHOTOSPHERES of OB main sequence stars are representative of the interstellar material from which they were born due to their relative youth. Therefore these objects and the associated ionized nebulae — H II regions — must share the same chemical composition, reflecting the very recent abundance pattern of the regions where they are located. The search of consistency between nebular and massive star abundances has been a longstanding problem. Since the abundance of certain elements varies with galactocentric distance in spiral galaxies, comparison of results from OB stars and H II regions must be made at the same galactocentric distance and most preferably in the same association (e.g. Gies & Lambert 1992, Cunha & Lambert 1992, 1994, Smartt et al. 2001b). The other possibility is to compare abundance gradients, this way the stellar and nebular objects may not be necessarily in the same region; abundances derived from both methodologies must show a similar trend with the galactocentric distance (e.g. Smartt & Rolleston 1997, Gummersbach et al. 1998). Alternatively, some studies compare directly stellar and nebular results from different regions in irregular galaxies (e.g. Korn et al. 2000, Trundle et al. 2004).

Recent works by Trundle et al. (2002) and Urbaneja et al. (2005a) have shown that abundance gradients in some spiral galaxies derived from stellar and nebular studies tend to be coherent but very dependent on the calibration used in the strong line nebular methods. Esteban et al. (2005) result for the Galaxy oxygen abundance gradient from eight H II regions are in marginal agreement with the value derived by Daflon & Cunha (2004) from approximately 69 early B-type main sequence stars situated in 25 Galactic open clusters/associations; however these values do not agree with previous estimations by Rolleston et al. (2000). Therefore, more work is needed to better understand the cause of these discrepancies. For example, until now there have not been systematic studies in the same star forming region that compare results obtained from detailed nebular and stellar studies. With this aim, we have selected the Orion nebula, a well studied and spatially resolved Galactic H II region with a cluster of a few massive stars inside it (the Trapezium cluster).

The study presented in this chapter is focused on a detailed and fully consistent spectroscopic analysis of the group of OB stars associated with the Orion Nebula for deriving their stellar parameters along with O and Si abundances using the stellar atmosphere code `FASTWIND`. The reliability of the derived stellar abundances is based on previous results presented in Chapter 5 for the narrow line B0.2V star τ Sco. Stellar abundances will be compared with those obtained in previous nebular spectroscopic studies of M42.

This chapter is structured as follows: a brief introduction to the Orion nebula and the observational dataset used for this study is presented in Sections §§6.2 and 6.3. The rotational velocities and the stellar parameters of the Orion stars and some other standard stars are calculated in Section §6.4. The study of the ionizing source of the Orion nebula, θ^1 Ori C, is presented separately in Section §6.5; this star is known to be spectroscopically variable, so a more extensive work is needed to derive its stellar parameters. Three B0.5V stars in Orion are used to develop a stellar abundance analysis (Section §6.6). Finally, the derived stellar abundances are compared with nebular results (Esteban et al. 2004, Rubin et al. 1993, Garnett et al. 1995) in Section §6.7.

6.2 The Orion nebula and its associated stellar population

The Orion complex contains the massive on-going star forming region closest to Earth, at about only 450 pc. The Orion nebula, M42, and its associated cluster of stars (the Orion Nebula Cluster, ONC) are part of this complex. It is a well known H II region (e.g. O'Dell 2001; Ferland 2001) ionized by a group of a few early type stars located in the core of the nebula (the Trapezium cluster stars, θ^1 Ori). Together with θ^1 Ori C (HD 37022, O7V), the main ionizing source, and a few more early B-type stars, a total membership of about 3500 low mass stars compose the ONC (Hillenbrand & Hartmann 1998). The youth of the cluster is obvious from the fact that it contains O stars still on the main sequence. An accurate assessment of the age is complicated due to uncertainties in the distance to the cluster, the spectral classification of the stars, the observed photometry, the amount of interstellar correction and the models for the protostars. However, some studies have ventured possible ages: Herbig & Terndrup (1986) established the age as being about 10^6 years; Hillenbrand (1997) demonstrate that the age of the cluster is small (less than 1 Myr) but there is not a good fit to a single age; from a comparison of observations with the protostars models by Palla & Stahler (1999), these authors conclude that the best fitting single age is 2×10^6 years.

Cunha & Lambert (1992, 1994) included some of the ONC stars in a survey of B-type stars in the Orion OB1 association¹. They presented a spectroscopic analysis of these stars for determining C, N, O, Si and Fe stellar abundances.

The most recent and complete analysis of the chemical composition of the Orion nebula has been presented by Esteban et al. (2004) who reanalyzes the emission line spectrum of the nebula to determine the physical conditions and abundances of

¹The Orion OB1 association contains four subgroups (Ia-Id) with different ages, and content of gas and dust (Blaauw 1964). The youngest group (Id) corresponds to the ONC.

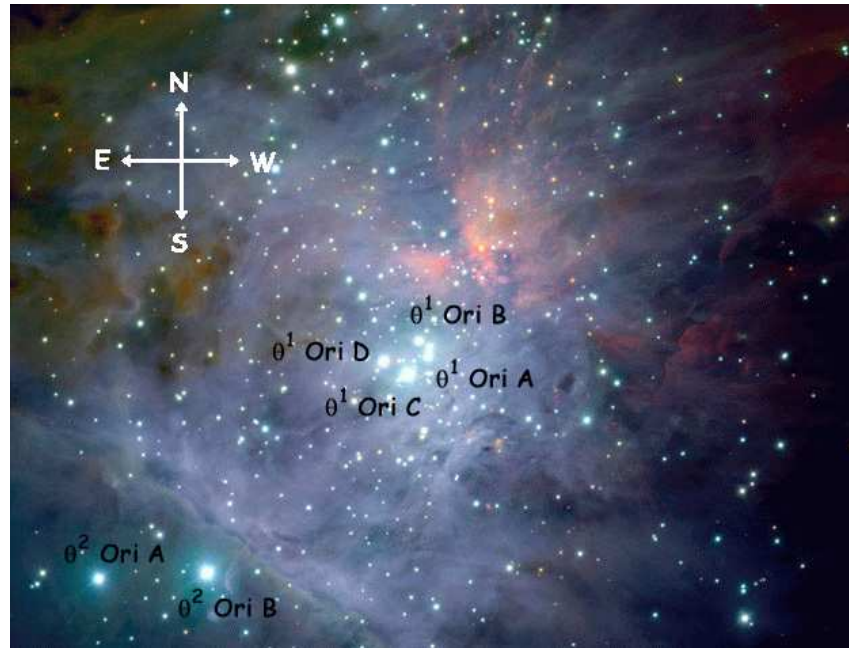


FIGURE 6.1 — Representative-color composite of 81 near-infrared light images taken with VLT’s ISAAC. The Trapezium cluster stars (θ^1 Ori) are shown in the center of the Orion nebula. The other two OB stars (θ^2 Ori A, B) are not normally included as members of the Trapezium cluster, however, they are part of the ONC. Credit: M. McCaughrean (AI Potsdam).

the ionized gas-phase. These authors use a wide variety of collisionally excited and recombination lines for the abundance determination.

6.3 Massive stars in Orion: observational dataset

The observational dataset consists on INT+IDS spectra of the O-early B type stars belonging to the stellar systems θ^1 Ori (the Trapezium cluster) and θ^2 Ori inside the Orion nebula. The ionizing source of the nebula (θ^1 Ori C) is known to be a spectroscopic variable star with a magnetic field. To study this variability, some FEROS spectra of the star at different phases have been considered. Finally, other three reference stars have been considered for comparison (10 Lac and 15 Mon were observed in the same run than the Orion stars; τ Sco is from CASPEC).

Some comments on the characteristics of these spectra and the reduction and normalization process have been previously presented in Chapter 2. Table 7.1 summarizes the spectral type and photometric visual data of the studied objects.

For a direct visual comparison of the observed profiles with the synthetic ones, the spectra have to be corrected from radial velocity shifts². In those cases in which metal lines are clearly distinguished, all these lines have been used for determining the shift needed to locate the whole set of spectral lines in its corresponding laboratory wavelength system (comparing with an atomic line list). If the $v \sin i$ is high the spectrum is compared with a previously corrected template.

6.4 Determination of rotational velocities and stellar parameters

6.4.1 Rotational velocities. The Fourier method

The analysis of stellar spectra makes use of a number of free parameters like the micro and macroturbulent velocities and the projected rotational velocity, $v \sin i$. The last one has acquired particular importance in recent times, because of the mixing that rotation may induce in the interior of massive stars (e.g. Maeder & Meynet 2000; Villamariz et al. 2002).

Conventionally, $v \sin i$ values are based on linewidth measurements of individual features, mainly metal lines apparently free of blends. As the principal broadening of these lines is stellar rotation, when this broadening is above the spectral resolution it is possible to determine $v \sin i$ from the FWHM of the line. Usually metal lines are used, however in cases of high rotational velocities or high temperatures metal lines may appear blended or very weak. Therefore, in these cases, if the $v \sin i$ is high, the whole He spectrum is used; if $v \sin i$ is not extremely high, only He I lines are used, as these lines are less affected by pressure broadening than He II lines. However, the $v \sin i$ derived must be tested with some metal lines (if available), as we cannot be completely sure that rotational broadening dominates over pressure broadening.

Although this method has been extensively used, some studies have shown that metal lines could be affected by other broadening mechanisms, such as macroturbulence (Conti & Ebbets 1977; Ebbets 1979; Ryans et al. 2002; Howarth 2004), in main sequence O-type and early and mid B-type supergiants stars. The $v \sin i$ derived by this method would be only an upper limit. It is not possible to distinguish between rotation and macroturbulence broadening through linewidth measurements. Even worse, sometimes it is found that different lines of the same star give very different rotational velocities, as in the case of HD 191612 (Walborn et al. 2003) which could be due to the different contribution of macroturbulence, rotation and pressure to the line broadening (Howarth 2004). However Fourier analysis methods

²Note that the corresponding radial velocity shift is not that associated with the real radial velocity of the star, as it has not been corrected from Earth motion.

HD	$v \sin i$ (km s ⁻¹)		
	This work		Other authors
	Fourier	FWHM	FWHM
HD 37020	55.0 ± 0.6	57 ± 3	56 ^a
HD 37022	24 ± 3	40 ± 11	53 ^b
HD 37023	49.0 ± 0.9	51 ± 3	51 ^a
HD 37041	131 ± 4	140 ± 11	110 ^b
HD 37042	34.0 ± 0.5	36 ± 3	10 ^c
HD 214680	30.0 ± 0.8	37 ± 4	35 ^b
HD 47839	67 ± 4	66 ± 6	67 ^b
HD 149438	< 13	16 ± 3	5 ^d , 19 ^e

TABLE 6.1 — Projected rotational velocity derived from the Fourier and FWHM analyses. References from the literature are: ^a Simón-Díaz et al. (2003), ^b Howarth et al. (1997), ^c McNamara & Larson (1962), ^d Schönberner et al. (1988), ^e Kilian et al. (1991)

could help to solve this problem and to determine more accurate and reliable rotational velocities (Smith 1976).

The Fourier method has only been marginally applied in the study of OB stars (e.g. Ebbets 1979). In this chapter, the strength of this method for determining rotational velocities in early type stars will be illustrated. Some notes on the characteristics and applicability of the Fourier method are presented in Appendix A. We have tested these method with theoretical and observational cases, and it works well for massive hot stars.

The lowest $v \sin i$ that can be determined through the Fourier method is given by the spectral resolution of the observed spectrum ($\Delta\lambda$ in Å/pixel, see Appendix A). The sampling of the computational Fourier transform cannot be extended beyond $0.5/\Delta\lambda$. The resolution in the IDS spectra is 0.23 Å/pixel, so the lowest $v \sin i$ that could be detected through the Fourier method is ~ 20 km s⁻¹. For θ^1 Ori C FEROS spectra the resolution is ~ 0.03 Å/pixel, so $v \sin i \geq 2$ km s⁻¹ for detection. For the τ Sco spectrum, the resolution is 0.1 Å/pixel, so the lowest detectable $v \sin i$ is 8 km s⁻¹.

The $v \sin i$ of the sample of stars has been determined through both the Fourier and FWHM methods. Results are presented in Table 6.1, along with some values found in the literature, for comparison. All the works referenced in that table use the FWHM method applied to the optical spectra of the stars except those by Howarth et

al. (1997), who use a cross correlation technique for IUE spectra, and Schönberner et al. (1988) who compare the observed spectrum of τ Sco with synthetic profiles.

Comments on the individual stars $v \sin i$ determination, along with the comparison between the values derived through Fourier and FWHM methods are presented in Section §6.4.2. Agreement between both methodologies is very good, indicating that the influence of macroturbulence in the line broadening of O-type stars is small. However there are some interesting cases (see the study of θ^1 Ori C in Section §6.5).

6.4.2 Stellar parameters

The analyses have been performed using the latest version of FASTWIND (Puls et al. 2005, v8.5). The methodology, based on the visual fitting of the H and He I-II synthetic profiles to the observed ones, is described in Chapter 3 (§3.3.2).

The low density in the winds of the studied objects makes the spectrum insensitive to changes in Q , so that only upper values can be determined in most cases. Microturbulence has no effect on the H/He spectrum of early type stars of large gravity, as has been shown by Villamariz & Herrero (2000). Therefore only effective temperatures, gravities and He abundances are determined in this step of the analysis. Of course, microturbulence is important for the derivation of metallic abundances and will be determined in the corresponding section.

Table 6.2 summarizes the derived parameters for the sample of stars. The fits corresponding to these values are shown in Figures 6.2 to 6.8. Some comments on the individual analyses are given below. A comparison between spectroscopic and evolutionary results are given in Section §6.4.3. The analysis of θ^1 Ori C is performed separately in Section §6.5.

HD	Name	T_{eff} ± 1000 K	$\log g$ ± 0.1 dex	$R (R_{\odot})$	$M(M_{\odot})$	$\log(L/L_{\odot})$	$\log Q$
HD 37020	θ^1 Ori A	30000	4.0	6.3 ± 0.9	14 ± 5	4.45 ± 0.13	< -13.5
HD 37022	θ^1 Ori C	39000	4.1	9.9 ± 1.4	45 ± 16	5.31 ± 0.13	—
HD 37023	θ^1 Ori D	32000	4.2	5.6 ± 0.8	18 ± 6	4.47 ± 0.13	< -13.5
HD 37041	θ^2 Ori A	35000	4.1	8.2 ± 1.1	39 ± 14	4.93 ± 0.13	< -13.5
HD 37042	θ^2 Ori B	29000	4.1	4.5 ± 0.6	9 ± 3	4.11 ± 0.13	< -13.5
HD 214680	10 Lac	36000	3.9	8.3 ± 1.1	20 ± 7	5.02 ± 0.13	< -13.5
HD 47839	15 Mon	40000	4.1	9.3 ± 1.3	40 ± 14	5.30 ± 0.13	-13.0
HD 149438	τ Sco	32000	4.0	5.6 ± 0.8	11 ± 4	4.47 ± 0.13	-13.0

TABLE 6.2 — Stellar parameters derived from FASTWIND analysis. Only an upper limit for $\log Q$ can be derived for these stars. The microturbulences considered for the HHe analysis in each star are shown in the corresponding fitting plots. A normal value for the He abundance has been considered for all the stars ($\epsilon=0.09$).

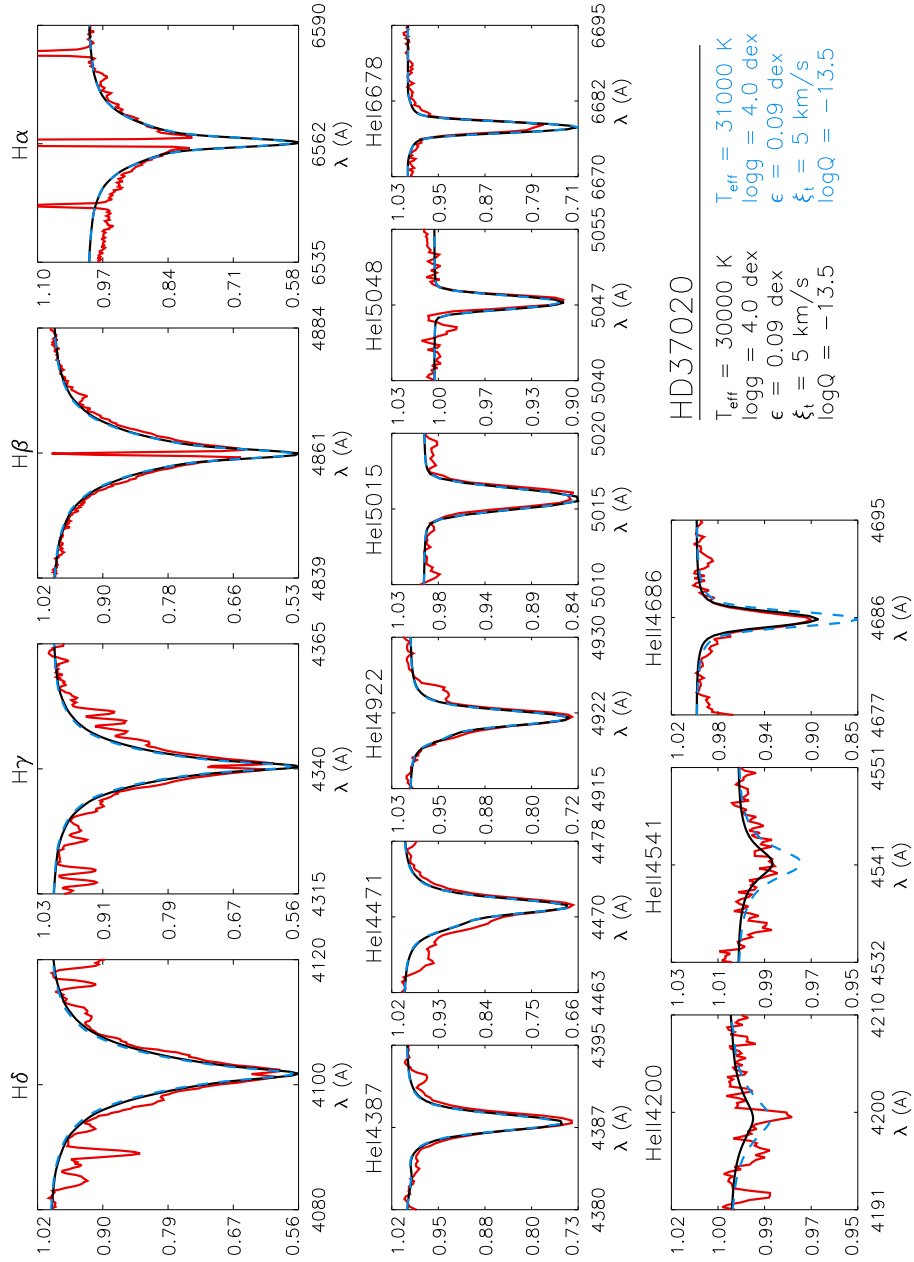


FIGURE 6.2 — Analysis of HD 37020 (θ^1 Ori A, B0.5V). Two models have been plotted for comparison with the observed spectrum. The adopted model has been represented with a solid line, while another model varying 1000 K in T_{eff} has been plotted with a dashed line. Note the core of the stellar Balmer lines contaminated with emission from the nebula. Only the wings of the Balmer lines are used for the fitting. The narrow line that appears in the core of the He II 4200 line is a N III absorption line; the red wing of the He I 4922 line is contaminated by an O II absorption line. The blue wing of the H $_{\alpha}$ line is affected by a diffuse interstellar band so it is not used for the fitting

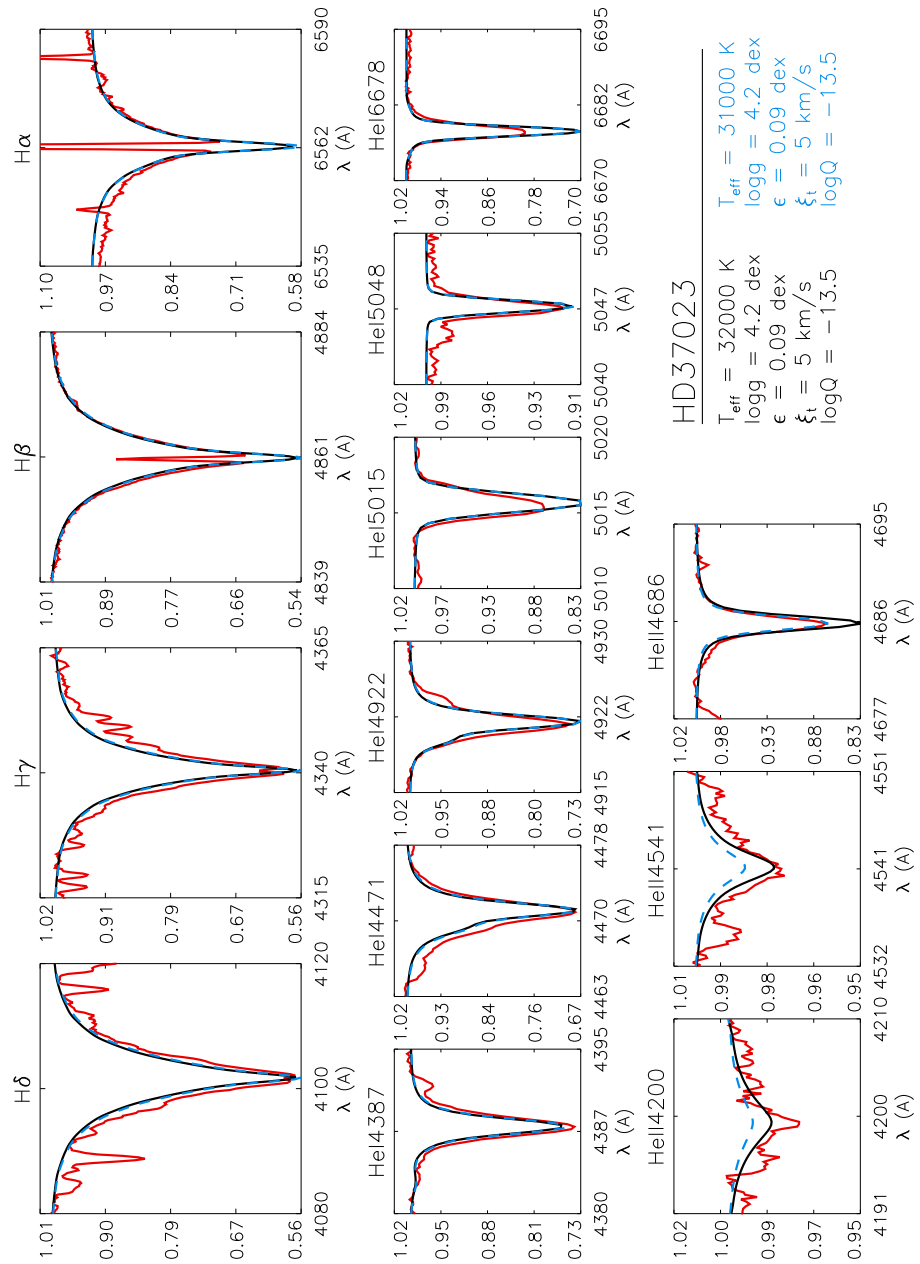


FIGURE 6.3 — As Fig. 6.2 for HD 37023 (θ^1 Ori D, B0.5V). A variation of 1000 K in T_{eff} has been considered in this case.

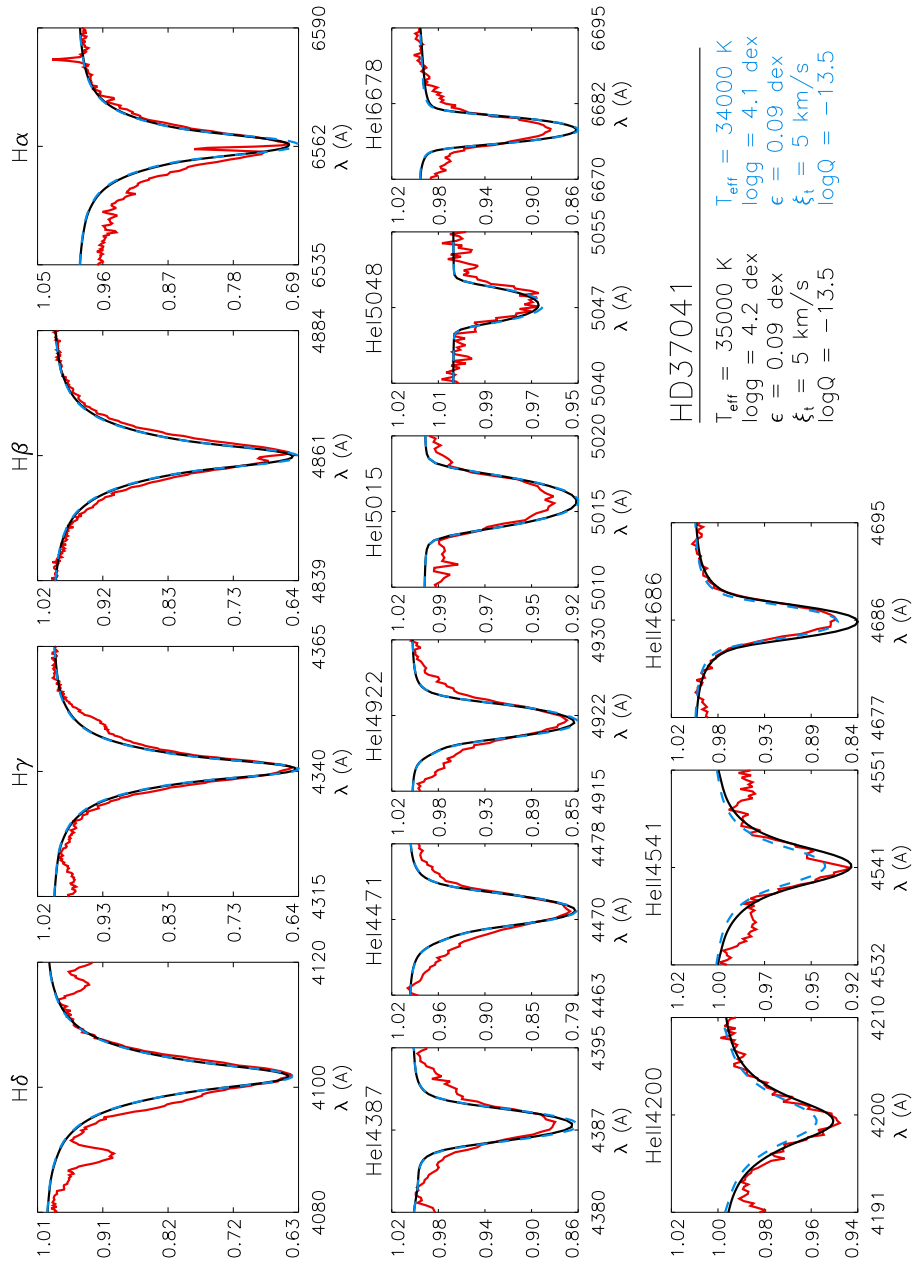


FIGURE 6.4 — As Fig. 6.2 for HD 37041 (θ^2 Ori A, O9V). A variation of 1000 K in T_{eff} and 0.1 dex in $\log g$ has been considered in this case. Note that the broad wings of the He I lines cannot be fitted correctly (see text)

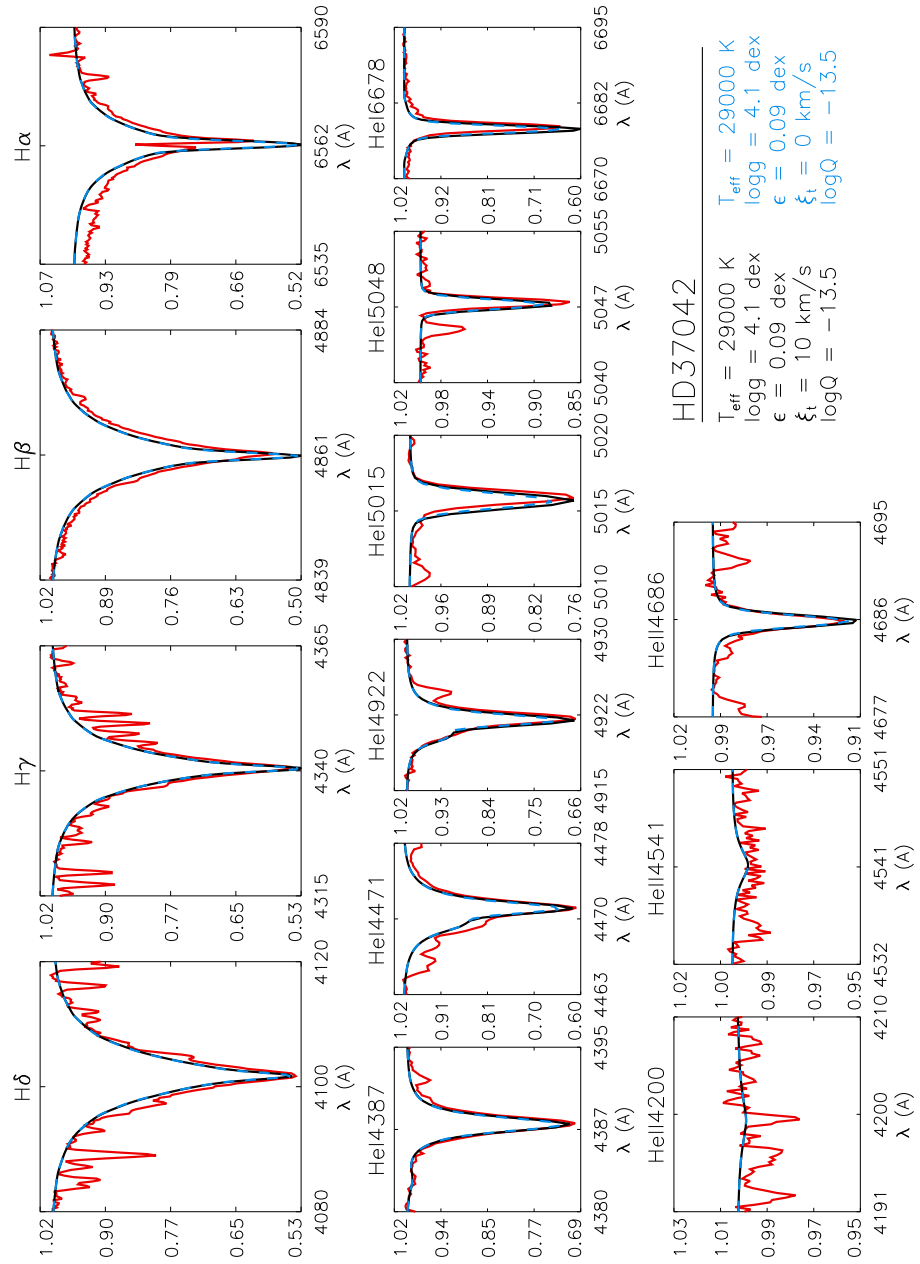


FIGURE 6.5 — As Fig. 6.2 for HD 37042 (θ^2 Ori B, B0.5V). For this star, the He I lines fit better if a microturbulence of 10 km s^{-1} is considered

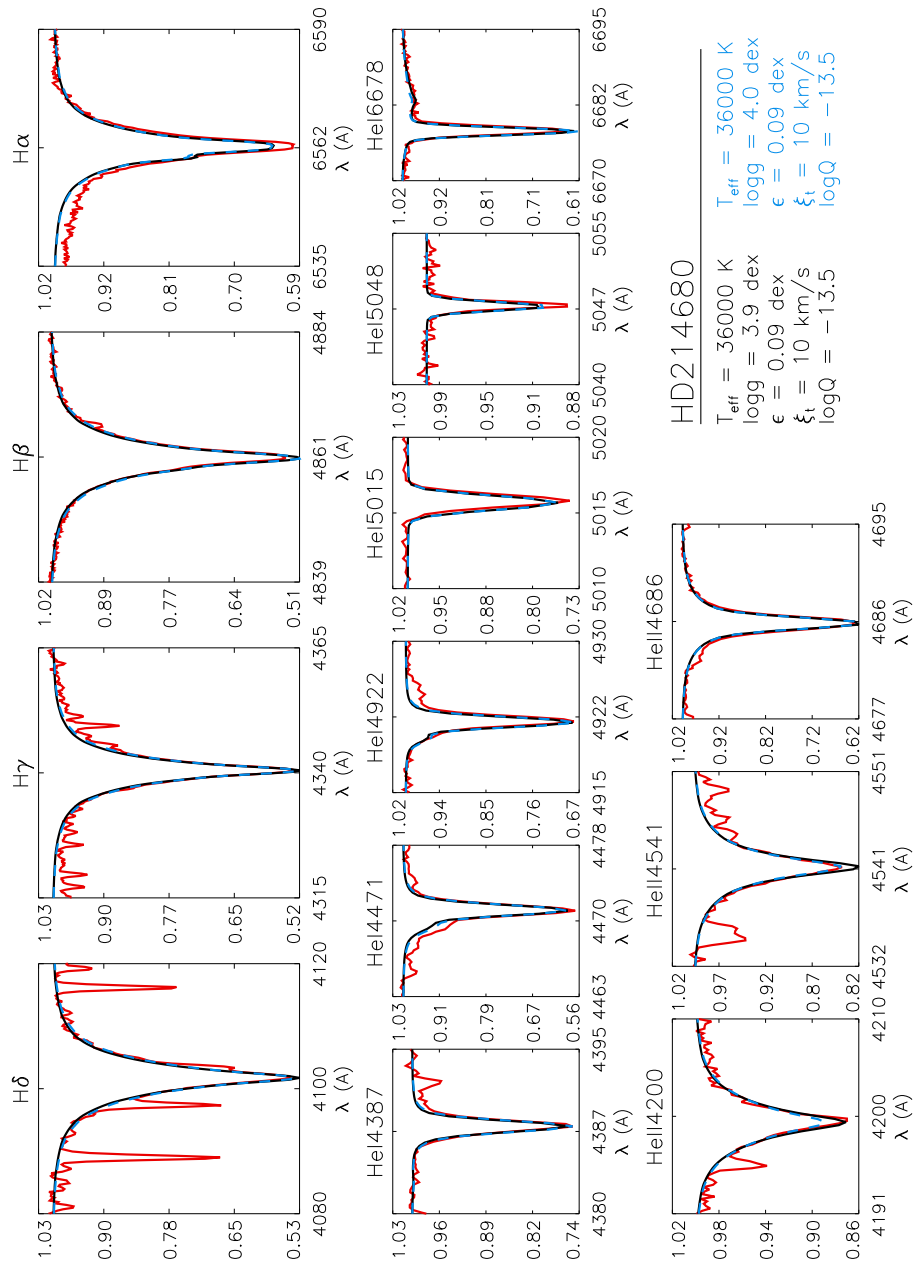


FIGURE 6.6 — As Fig. 6.2 for HD 214680 (10 Lac, O9V). A variation of 0.1 dex in $\log g$ has been considered in this case.

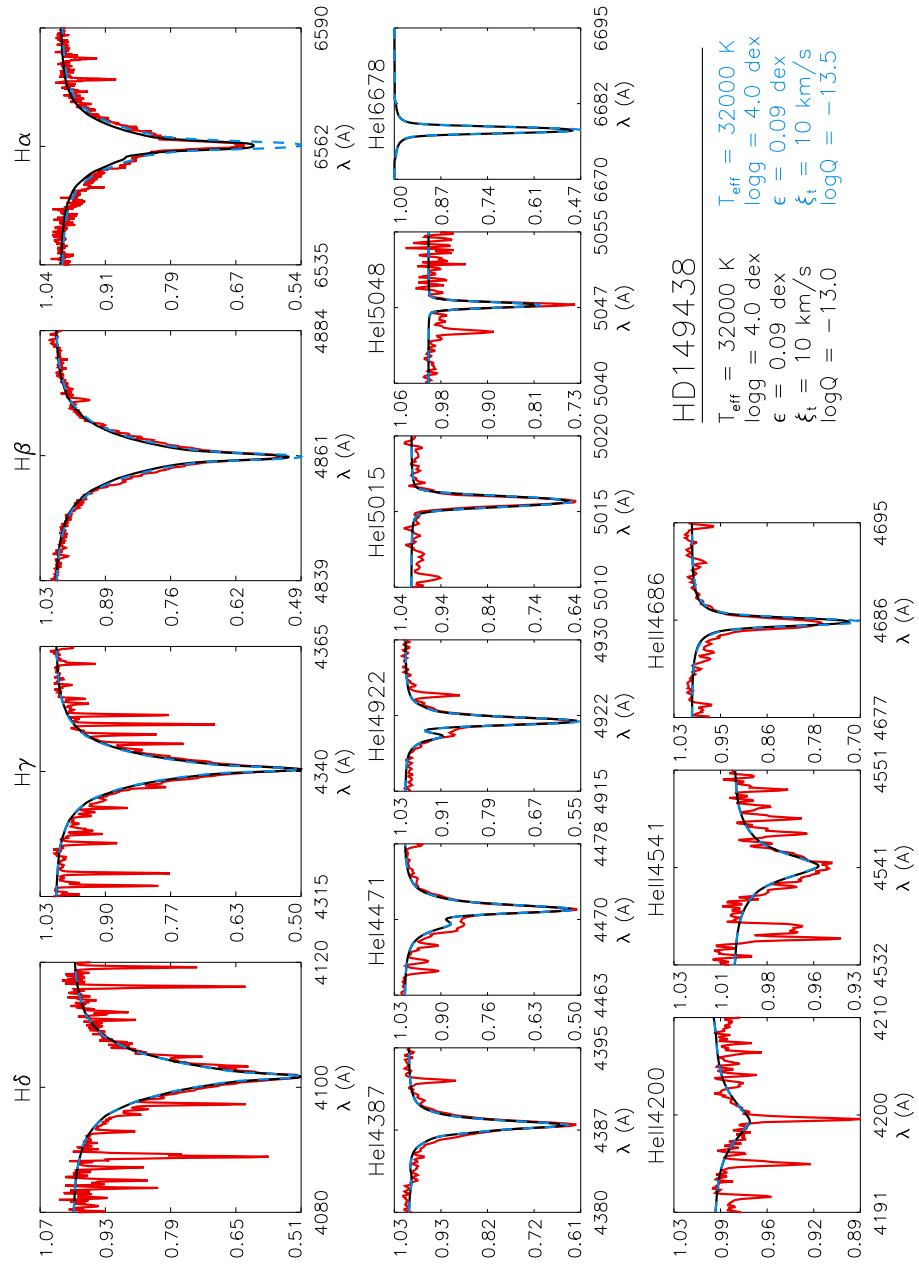


FIGURE 6.7 — As Fig. 6.2 for HD 149438 (τ Sco, B0.2V). A variation of 0.5 dex in $\log Q$ has been considered in this case. The $H\alpha$ line is not contaminated by nebular emission for this star and a more accurate value of $\log Q$ can be determined. The $\text{He I } \lambda 6678$ line is out of the observed range in the CASPEC spectrum of τ Sco.

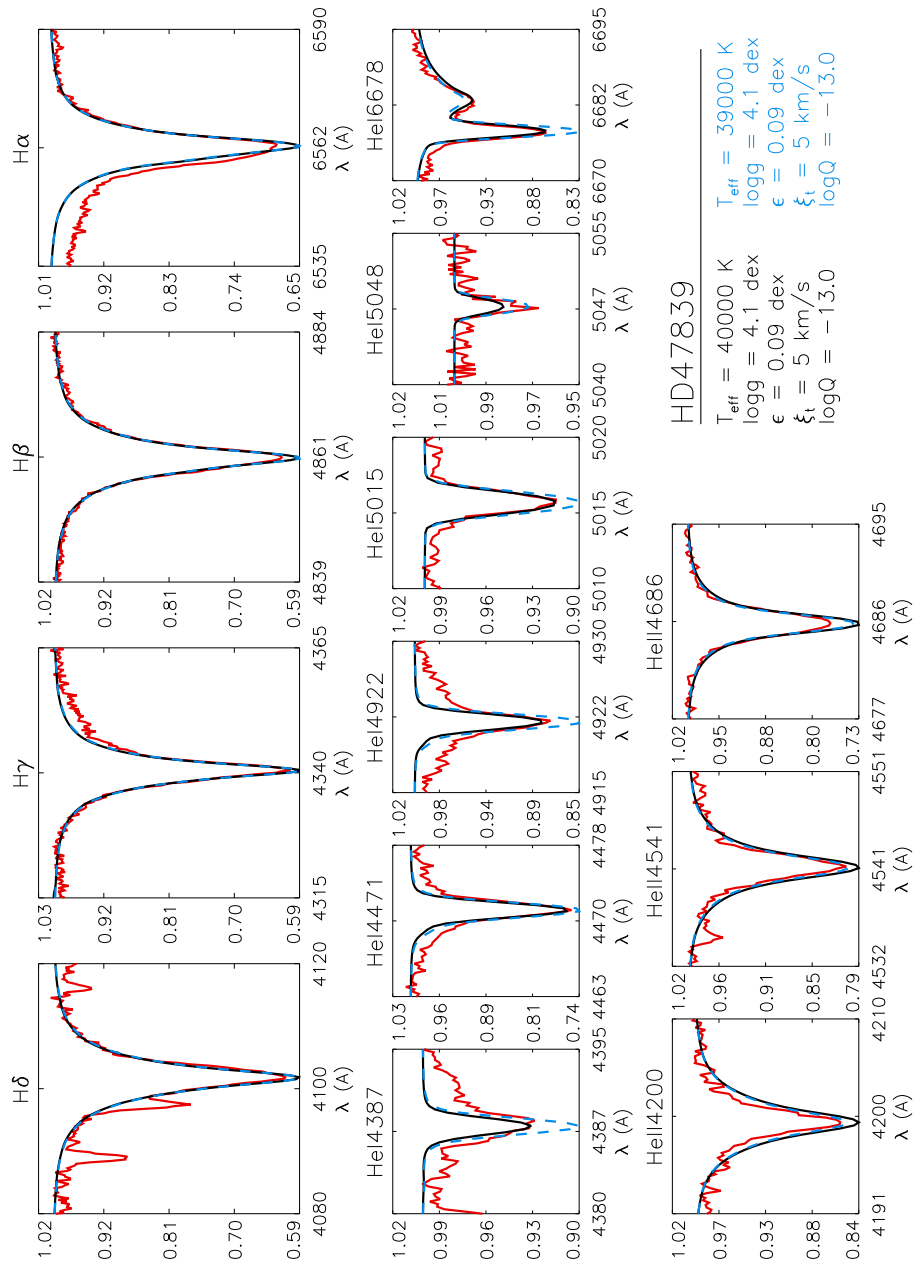


FIGURE 6.8 — As Fig. 6.2 for HD 47839 (15 Mon, O7V). A variation of 1000 K in T_{eff} has been considered in this case.

*Comments on the Trapezium cluster stars**HD 37020 (θ^1 Ori A)*

This is an eclipsing binary discovered by Lohsen (1975). The period is $P = 65.432$ d, the visual magnitude ranges between $6^m.7$ and $7^m.6$, and the eclipse lasts ~ 20 h. The primary is a B0.5V star which has many isolated metal lines. No lines of the secondary star have been found in the INT-IDS spectrum of the star. This fact, together with the characteristics of the binary system described before, suggest that the secondary is a cooler, smaller and less luminous star, and that the change in visual magnitude is due to the eclipse of the primary by its companion. Therefore the optical spectrum is mainly dominated by the B0.5V star.

The Fourier method has been applied to some O II, Si III-IV, N II and He I lines, deriving a $v \sin i = 55 \pm 0.6 \text{ km s}^{-1}$. Metal and He I lines are in agreement. The $v \sin i$ derived through the linewidth measurement method is consistent with this value (see Table 6.1).

Figure 6.2 shows the good fit of the FASTWIND profiles to the observed spectra for the parameters given in Table 6.2 (except for the forbidden component of He I $\lambda 4471$ line, which is not well reproduced throughout the analyses. Note also that the apparent bad fit of He II $\lambda 4200$ is due to the blend with the N III line at the same wavelength). We are very close to the applicability limit of the He I-II ionization equilibrium for deriving the T_{eff} as He II $\lambda 4200$ and He II $\lambda 4541$ lines are very faint; however these lines are still sufficiently sensitive to changes in T_{eff} and $\log g$ to derive the stellar parameters accurately. The stellar parameters obtained here are in very good agreement with those obtained by Cunha & Lambert (1992) using the Strömgren index c_0 and the wings of H_γ corresponding to Kurucz's (1979) LTE model atmospheres (this is not the case for the other two stars in common with these authors). A comparison of values is given in Table 6.3.

HD 37022 (θ^1 Ori C)

This is the main ionizing source of the Orion nebula. See Section §6.5 for a detailed study of this star.

HD 37023 (θ^1 Ori D)

This is the only star in the four Trapezium cluster stars (θ^1 Ori) without a binary companion (Preibisch et al. 1999).

Star	T_{eff} (K)	$\log g$ (dex)
HD 37020	29970 / 30000	3.92 / 4.0
HD 37023	32600 / 32000	4.70 / 4.2
HD 37042	31600 / 29000	4.70 / 4.2

TABLE 6.3 — Comparison of stellar parameters for HD 37020, HD 37023, HD 37042. First values refer to Cunha & Lambert (1992) determinations, second values to this work. There is excellent agreement for HD 37020, but poor agreement (specially for $\log g$) for the other two stars.

The Fourier method gives a $v \sin i = 49.0 \pm 0.9 \text{ km s}^{-1}$ for this star. Again, there is agreement with the linewidth measurement method.

Figure 6.3 shows the fitting of the HHe lines. Observed He I lines are slightly broader than theoretical ones. Table 6.3 shows the comparison between our stellar parameters and those derived by Cunha & Lambert (1992). In this case there is no agreement: although the T_{eff} are compatible, the $\log g$ they derived is very high with respect to our determination.

HD 37041 (θ^2 Ori A)

This is a single-lined spectroscopic binary (see Howarth et al. 1997). These authors find a single peak in the cross correlation function of the IUE spectrum, indicating that the spectrum of the primary is not seriously contaminated.

Comparing the spectrum of this O9V star with that of the standard star 10 Lac (also classified as O9V) it has been found that there are no unblended metal lines due to its high rotational velocity (except Si IV $\lambda 4089$, but it is in the blue wing of H δ). A good $v \sin i$ determination has been possible using the Fourier method with the He I lines. A $v \sin i = 131 \pm 4 \text{ km s}^{-1}$ has been derived. The Si IV line has been used to check the reliability of this value; a $v \sin i = 136 \pm 5 \text{ km s}^{-1}$ is obtained. He II lines do not give good results. A $v \sin i = 140 \pm 11 \text{ km s}^{-1}$ is derived applying the FWHM method to the He I $\lambda 5015$ line.

Figure 6.4 shows the fitting of the synthetic profiles with the observed ones. A $v \sin i = 131 \text{ km s}^{-1}$ has been considered for the H-He analysis. The wings of the He I lines cannot be well fitted. Note that although the strength of the whole set of He I-II is correctly fitted, the synthetic He I lines do not fit properly the wings of the corresponding observed lines.

HD 37042 (θ^2 Ori B)

A good agreement has been found between metal and He I lines when using the Fourier method. The $v \sin i$ derived is $34.0 \pm 0.5 \text{ km s}^{-1}$. The value obtained with the FWHM method is $36 \pm 3 \text{ km s}^{-1}$, in agreement with the former one.

A very good fit of the observed and synthetic FASTWIND profiles is obtained (see Figure 6.5). Again the forbidden component of He I $\lambda 4471$ is too weak. For this star, the He I lines fit better if a microturbulence of 10 km s^{-1} is considered.

This is the third star in common with Cunha & Lambert (see Table 6.3); it has also been found for this star (as for HD 37023) that the stellar parameters derived by these authors are very different from ours (they obtain a very high $\log g$ and an effective temperature $\sim 3000 \text{ K}$ higher).

*Comments on the reference stars**HD 214680 (10 Lac)*

This star has been previously considered as standard for stellar parameter determination through the H-He analysis (see Herrero et al. 2002 and references therein). The spectrum of the star, obtained from a new observing run covering a larger spectral range has been reanalyzed here (the He I $\lambda\lambda 5015, 5048, 6678$ and He II $\lambda 6683$ lines can be used for the new analysis). Since a new version of FASTWIND (slightly different from that used by Herrero et al.) is used here, the new analysis will be useful to check the consistency of this latest version of the code in this stellar parameters regime.

The projected rotational velocity has been accurately determined by means of the FWHM method ($v \sin i = 37 \pm 4 \text{ km s}^{-1}$). The Fourier method applied to the INT+IDS spectrum gives a $v \sin i = 30 \pm 0.8 \text{ km s}^{-1}$. This large difference could be due to the fact that the $v \sin i$ is close to the computational Fourier transform limit ($\sim 20 \text{ km s}^{-1}$ for this spectrum).

The whole set of HHe lines are perfectly fitted with the FASTWIND synthetic profiles (Figure 6.6). The parameters derived by Herrero et al. (2002) are $T_{\text{eff}} = 35500 \text{ K}$, $\log g = 3.95$ and $\epsilon = 0.09$. The new results are in agreement with those values.

HD 149438 (τ Sco)

This star was selected for comparison in the stellar oxygen abundance analysis of the B0.5V Trapezium cluster stars (see Section §6.6). It has been studied elsewhere (Martin 2004, Przybilla & Butler 2004, Kilian 1994, Schönberner et al. 1988, Becker & Butler 1988, Peters & Polidan 1985, Kane et al. 1980). Comparing isolated oxygen and silicon lines to a set of rotationally broadened profiles, Kilian et al. (1991) obtained a $v \sin i = 19 \text{ km s}^{-1}$ for this star. The Fourier method applied to the CASPEC spectrum only allow us to say that the $v \sin i$ is lower than 13 km s^{-1} ; this is because in this case the effect of the microturbulence over the broadening of the metal lines can be comparable with that produced by the rotation, so the first zero could be associated with the microturbulence instead of the $v \sin i$ (Gray 1973).

A very good fit with the synthetic FASTWIND profiles is obtained for this star (see Figure 6.7). In this case the problem with the forbidden component of the He I $\lambda 4471$ can be clearly seen. Table 6.11 (Section §6.6) summarized the stellar parameters obtained in this and previous work.

HD 47839 (15 Mon)

This star was selected for comparison with the main ionizing source in Orion (θ^1 Ori C). Some comments on the analysis of this star and the comparison with θ^1 Ori C are presented in Section §6.5. It was classified as O7V(f) by Walborn (1972a). Gies et al. (1993) pointed for the first time that this star is a spectroscopic binary with a period of 25 years. They estimated a mass for the primary of $M = 34 M_{\odot}$, and suggested that the secondary has a spectral type O9.5Vn (with very broad lines).

The spectrum of HD 214680 (O9V), convolved with a high $v \sin i$ ($\sim 350 \text{ km s}^{-1}$), has been used to recognize lines in the spectrum of HD 47839 not contaminated by the secondary star; three metal lines were found. Using these lines (Si IV $\lambda\lambda$ 4212, 4654 and N III λ 4379) a $v \sin i = 67 \pm 4 \text{ km s}^{-1}$ has been determined. A similar value has been derived applying the FWHM method to the same lines ($66 \pm 6 \text{ km s}^{-1}$).

The fitting of the H and He lines for the stellar parameters shows how the He I lines are contaminated by these from the secondary star. The derived value for the spectroscopic mass ($40 \pm 14 M_{\odot}$) is in good agreement with the dynamical mass derived by Gies et al. (1993). Herrero et al. (1992) derived a $T_{\text{eff}} = 39500 \text{ K}$, $\log g = 3.70$ and $\epsilon = 0.07$ for this star. Although it would be expected to obtain a lower T_{eff} due to the inclusion of line blanketing effects, the value we have obtained is slightly higher because there is also a large difference between the $\log g$ we derived

(4.0) and the one by Herrero et al. (3.7). There is also another difference; we do not need a lower He abundance for fitting the He lines. This could be due to a binarity effect³; when a composite spectrum is considered in a binary system, lines can appear diluted or magnified due to the combination of the fluxes of the primary and the companion. If the system is out of eclipse the total flux will be higher than when the primary is observed isolated, so when the spectrum is normalized all the lines will appear diluted (and then a lower He abundance is needed to fit the He lines and a lower gravity is derived).

6.4.3 Results of the stellar parameters study

From the optical spectra of the Orion stars only upper limits for the Q parameter can be achieved. These estimations are based on the effect of the wind on the He II $\lambda 4686$ and H $_{\alpha}$ lines (the later one is contaminated by the nebular contribution). Some tests have shown that the other H and He lines are not affected by the uncertainties in $\log Q$ for the range of values considered, so the derived parameters will not be affected.

Masses, radii and luminosities have been derived for all the studied targets (they are indicated in Table 6.2 along with their uncertainties). The main source of uncertainty for these parameters is that associated with the absolute magnitude (except for the case of the mass, that is also affected by uncertainties in $\log g$). An error in M_v of the order of 0.3 magnitudes propagates to the mass, radius and luminosity, giving uncertainties of $\sim 37\%$, 13% and 30% respectively.

The stars have been plotted on the HR diagram in Figure 6.9. Evolutionary tracks from Meynet & Maeder (2003), corresponding to initial masses between 9 and $120 M_{\odot}$ and initial rotational velocities of 0 km s^{-1} are also plotted. The figure is completed with isochrones from Schaller et al. (1992), corresponding to ages of 2, 2.5 and 3 Myr.

All stars are found in the Main Sequence close to the ZAMS, as it is expected because of their youth. Nevertheless, we can see the separation from the ZAMS increasing with luminosity, as pointed out by Herrero et al. (2004). The loci of the Orion stars is consistent with an isochrone at about 2.5 ± 0.5 Myr, derived from the tracks with zero initial rotational velocity, which is slightly older than the upper limit given by Palla & Stahler (1999, 2 Myr) and somewhat larger than other Trapezium age determinations found in the literature (e.g. Hillenbrand 1997, ≤ 1 Myr). However, it has to be considered that, at large initial rotational velocities, the ZAMS is slightly

³See Appendix B.

shifted to the right and modifies the derived ages. Hence, until the role of the initial rotational velocities is properly understood (for example, the distribution of initial rotational velocities in clusters), the use of isochrones for massive stars in very young clusters should be regarded with special caution.

A good agreement between gravities derived from the evolutionary tracks and those obtained from quantitative analysis of the spectra is found. There is a trend for the most massive stars to have larger spectroscopic than evolutionary masses, but the number of objects is too small to draw any general conclusion.

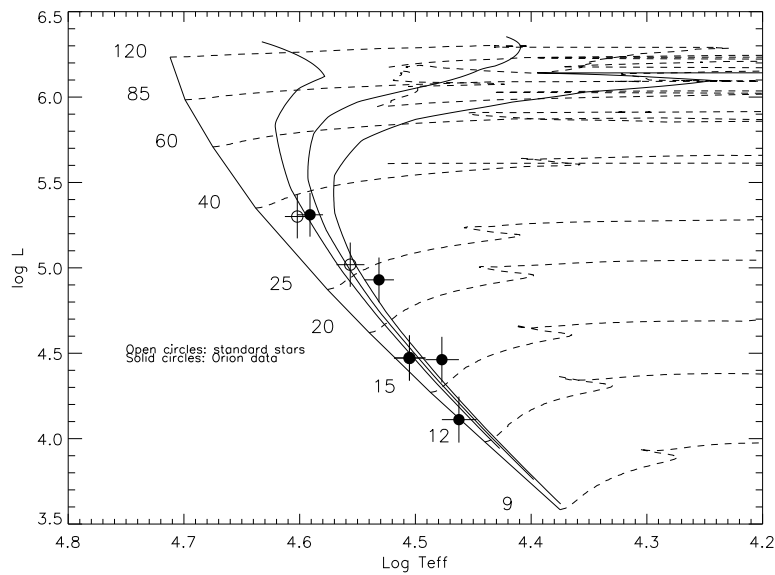


FIGURE 6.9 — HR diagram with the studied stars. Evolutionary tracks from Meynet & Maeder (2003). Isochrones from Schaller et al. (1992), corresponding to the ZAMS and ages of 2, 2.5 and 3 Myr.

6.5 Modeling θ^1 Ori C: the main ionizing star of M42

6.5.1 A historical review

This star is known to have variable spectral features varying in phase or antiphase with a period of 15.422 ± 0.002 d (Stahl et al. 1993; Walborn & Nichols 1994; Stahl et al. 1996). These variable features were discovered after Conti (1972) showed for the first time that θ^1 Ori C has a variable inverted P-Cygni profile in the He II 4686 line. Among them are H_α emission, variability in the equivalent width of some atmospheric and wind lines, and X-ray emission (Caillault et al. 1994; Gagné et al. 1997).

Different explanations for this variability have been postulated. The possibility of θ^1 Ori C being a binary and this binarity explaining the spectral variability has been dismissed (Stahl et al. 1996). The variability has been associated with the rotation of the star. Stahl et al. (1996) proposed the presence of a dipolar magnetic field in θ^1 Ori C, with the magnetic pole inclined 45° from the rotation axis (which is inclined 45° from the line of sight). The geometry of this system would imply alignment between magnetic pole and the line of sight at phase 0.5 and they would be perpendicular at phase zero (when maximum H_α emission is found). Babel & Montmerle (1997) proposed the magnetically confined wind-shock model (MCWS) to explain the variability in the star. According to this model, the radiatively line driven wind is confined by a dipolar magnetic field towards the magnetic equator of the system, generating a cold, dense disk due to the collision of material coming from both hemispheres, and a hot post-shock region.

The wind characteristics of θ^1 Ori C were determined by Howarth & Prinja (1989) and Stahl et al. (1996) through UV spectrum studies. The former derived a mass loss rate of $4 \times 10^{-7} M_\odot \text{yr}^{-1}$, the latter through the absorption in C IV lines, determined a terminal velocity somewhat greater than 2500 km s^{-1} .

It is common that O7V stars have stellar winds; what is not so common is the detection of magnetic fields in O stars. Donati et al. (2002) succeeded in the detection of Zeeman features in the spectrum of θ^1 Ori C through spectropolarimetric observations with the Anglo-Australian Telescope. They detected variability in the Stokes V profiles of some photospheric metal lines. This variability has a coherent modulation with the period derived from other variable features. However, the geometry derived was in contradiction with that from Stahl et al. (1996), with the magnetic pole aligned with the line of sight at phase zero (they found a maximum in the longitudinal component of the magnetic field at this phase).

6.5.2 Preliminary study of the spectrum

As this object is known to have spectral variability, it is very important to understand the cause of this variability and to determine which lines are reliable for the stellar atmosphere modeling before comparing synthetic and observed H - He profiles. Preliminary work with the INT+IDS spectrum showed that a better spectral resolution was needed to apply the Fourier method for obtaining the $v \sin i$. This spectrum did not allow us to have either a good enough sampling ($\Delta\lambda$), or to carry on a study of the variability, so we decided to use some FEROS spectra with better quality and covering all variability phases (see Table 6.4), that are available in the ESO archive.

Through the study of the FEROS spectra observed in the different phases we have found all the variable spectral features described in Stahl et al. (1996) and some new ones:

- **He II 4686:** Broad emission appears in the blue wing of the line (the so-called inverted P-Cygni profile, with maximum at $\phi \sim 0$). Broad emission is also present in the red wing (maximum at $\phi \sim 0.5$, minimum at $\phi \sim 0.8$).
- **Balmer lines:** These lines are affected by the same broad emission features as those in He II $\lambda 4686$. The emission features are stronger in H $_{\alpha}$ and H $_{\beta}$ than in the other Balmer lines
- **Metal and He I-II lines:** All the line strengths vary in phase, being larger at $\phi \sim 0$.

Name	Date	$MJD-2.400.000,5$	ϕ
f07341+51	16/10/98	51102.31	0.180
f85221	26/07/99	51385.43	0.539
f03551+61	08/10/98	51094.28	0.659
f04711+21	10/10/98	51096.39	0.796
f15241	28/11/98	51145.37	0.972

TABLE 6.4 — FEROS spectra used for the study of the spectral variability of θ^1 Ori C. All spectra have been downloaded from the ESO-FEROS database except f85221, kindly provided by O. Stahl. The different phases have been calculated from $MJD_0 - 2.400.000,5 = 48832,5$ (Stahl et al. 1996) and $P = 15.422$ days

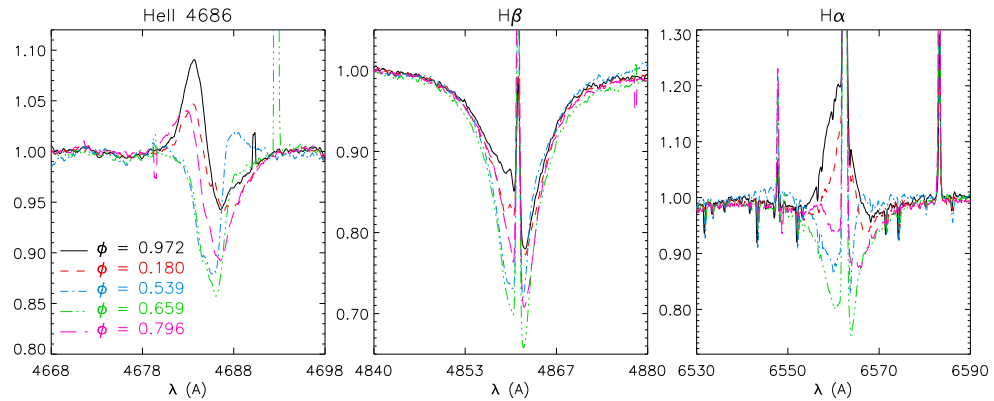


FIGURE 6.10 — The most representative phases have been selected to show the variability of the He II $\lambda 4686$, H β and H α lines in the θ^1 Ori C spectrum. The variable feature associated with the inverted P-Cygni profile discovered by Conti in the He II $\lambda 4686$ line is also present in the hydrogen Balmer lines. Another emission feature can be clearly seen in the red wing of these lines at phase ~ 0.5 . The narrow emission features in the Balmer lines are nebular lines.

This variability can be easily explained considering the model proposed by Stahl et al. (1996) and developed by Babel & Montmerle (1997). This model assumes that θ^1 Ori C is an O7V star with a disc produced by the confinement of the wind by a dipolar magnetic field through the magnetic equator. Consequently, a cool disc with material falling back to the stellar surface is formed. Figure 6.11 illustrate the geometry proposed by this model.

If it is considered that at phase zero the cool disc is seen edge-on, the blue shifted emission appearing in He II $\lambda 4686$, H α and the other hydrogen Balmer lines can be explained as stellar photons absorbed and re-emitted with a doppler shift corresponding to the velocity of the disc material falling onto the surface of the star (in a process similar to that which occurs in a stellar wind but with blue-shifted emission and red-shifted absorption). As density in the disc is very high then a strong blue-shifted emission will appear. At phase 0.5, when the disc is seen face-on the blue-shifted emission disappears. The emission appearing in the red wings of the former lines could be explained as the effect of the scattering of stellar photons by the wind material confined by the magnetic field and accreting onto the disc (see figure 6.10).

The disc will also have continuum emission that will affect the total continuum flux received from the star. This effect will be maximum when the disc is face-on because the emitting region is larger at this phase. The variability observed in He I,

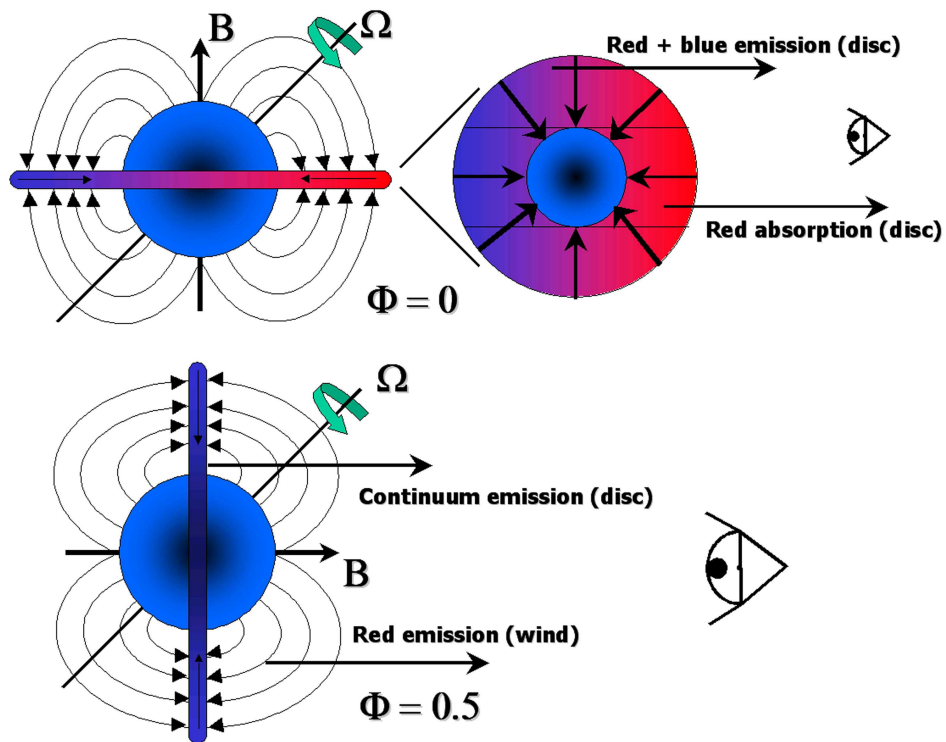


FIGURE 6.11 — This figure illustrates the geometry proposed for θ^1 Ori C corresponding to two different phases ($\phi = 0$ and 0.5). See text for a further explanation. This model considers that the stellar wind is confined by a dipolar magnetic field through the magnetic equator. Consequently, a cool disc with material falling back to the stellar surface is formed. The magnetic pole is inclined 45° from the rotation axis (which is inclined 45° from the line of sight). Top: Phase zero: the disc is seen edge on. Bottom: Phase $\phi = 0.5$: the disc is seen face on.

He II and metal lines (except for the emission in He I $\lambda 4686$) is only a consequence of this effect. As the total continuum flux is varying with the phase, the normalized spectrum will be affected. All absorption lines will be artificially weaker when the disc continuum emission is at maximum.

This variability in the lines can allow us to estimate the amount of continuum flux that comes from the disc, and then the visual magnitude variability. By assuming that at phase zero the lines are not affected by the continuum emission from the

disc, we have scaled the spectra at the other phases to fit in the former spectrum; the scaling factor (f) will be related to the ratio of visual fluxes (i.e. the difference in magnitudes) between the stellar component and the stellar+disc contribution:

$$y_i = (y_0 - 1)f + 1 \quad (6.1)$$

$$\Delta m_i = 2.5 \log f \quad (6.2)$$

where y_i and y_0 are the normalized flux values for the core of a given line at phases ϕ_i and ϕ_0 respectively, and f the scaling factor applied to the spectrum in phase ϕ_i to fit the reference spectrum. See Appendix B for further description of this effect. From this study we would expect a variability of ~ 0.16 magnitudes (see Figure 6.12). Kukarkin et al. (1971), in their catalogue of suspected variable stars, found a change in m_v of 0.06 magnitudes (5.10 - 5.16) for θ^1 Ori C. Hipparcos has also classified this star as variable; although Hipparcos data do not show any clear pattern, the median magnitude in Hipparcos system is 4.61 mag and the variability of this magnitude varies between 4.56 and 4.70, that is in agreement with our study.

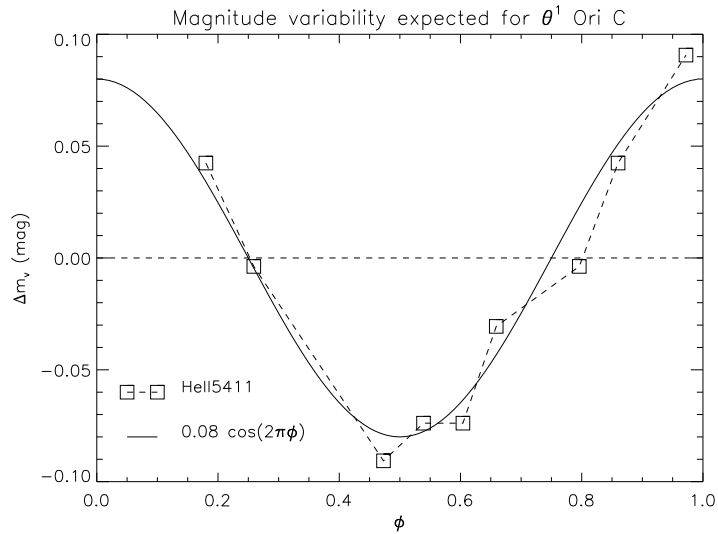


FIGURE 6.12 — Magnitude variability expected from the study of the He II $\lambda 5411$ line. The other He I-II lines follow a similar behavior. The presence of a disk could be responsible of this variability (see text for details). The solid line corresponds to a sinusoidal curve with a maximum change in m_v of 0.16, presented for comparison.

6.5.3 Determination of the $v \sin i$ of θ^1 Ori C

It is very important to have a good determination of the projected rotational velocity of this star as it is supposed that the spectral variability of θ^1 Ori C is related with its rotation. The derived $v \sin i$ should be independent on the phase and should be coherent with a period of ~ 15.4 days.

In Section §6.5.2, it has been shown that the profiles of metal as well as He I and He II lines are dependent on the phase, however this is only an artificial dependence due to the presence of the disk. Once the spectra of different phases are corrected for the effect of dilution by the disc continuum emission, all the metal, He I and He II lines are independent of the phase (except those related to the line emission from the disc, see Figure 6.10).

Previous determinations by Stahl et al. (1996) and Howarth et al. (1997) imply too large projected rotational velocities (50 km s^{-1} and 56 km s^{-1} respectively) to be consistent with a rotational period of ~ 15.4 days. They argue that an extra broadening may be affecting the lines in the spectrum of this star. The Fourier method allows us to separate pure rotational broadening from other broadening mechanisms affecting the shape of the lines. This method has been applied to some metal lines at phase $\phi \sim 0$ (see Table 6.5), deriving a $v \sin i = 24 \pm 3 \text{ km s}^{-1}$. Figure 6.13 shows an example of the application of the Fourier method in the determination of the $v \sin i$ of θ^1 Ori C.

Table 6.5 offers a comparison of $v \sin i$ values obtained with the Fourier and FWHM methods. It can be seen that the Fourier method gives more consistent values for all considered lines. Differences within the FWHM method may reach a factor of 2 and, in fact, some problems are found when trying to fit the profile of some of the lines with a gaussian profile for measuring their linewidth. The derived value for $v \sin i$ through the Fourier method is also more coherent with a O7V star rotating with a 15.422 days period. Considering $R \sim 11 R_{\odot}$, the upper limit for $v \sin i$ is $\sim 35 \text{ km s}^{-1}$ and therefore the inclination of the rotational pole is $i \sim 45^{\circ}$, in agreement with the models proposed by Stahl et al. (1996) and Donati et al. (2002) (see also next section).

The differences found between the $v \sin i$ derived from both methods imply that the lines are affected by an extra broadening. In next section it will be shown that this extra broadening is needed to fit the synthetic H and He lines with the observations.

Line	$v \sin i$ (km s^{-1})	
	Fourier	FWHM
C III 4056	23	42 ± 10
N III 3998	23	28 ± 7
N IV 4057	22	33 ± 7
N IV 5200	20	32 ± 10
Si IV 4089	23	62 ± 14
Si IV 4654	30	47 ± 10
O III 4081	21	52 ± 10
O III 4376	26	31 ± 4
O III 4435	25	32 ± 5
O III 4454	27	34 ± 4
O III 5592	25	45 ± 6

TABLE 6.5 — Projected rotational velocities derived through Fourier and FWHM methods for some metal lines present in the spectrum of θ^1 Ori C. Values were derived at phase 0.972 (see explanation in text).

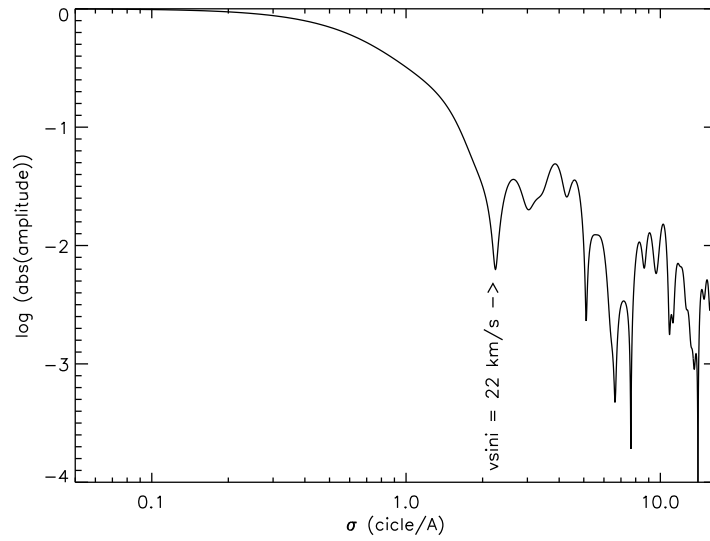


FIGURE 6.13 — Fourier analysis of the N IV $\lambda 4057$ line in θ^1 Ori C (phase 0.972). A $v \sin i = 22 \text{ km s}^{-1}$ is inferred from the first zero in the Fourier transform.

6.5.4 Modeling of θ^1 Ori C

Once the spectral variability of θ^1 Ori C is understood and its $v \sin i$ has been derived, we can proceed to model its stellar atmosphere and wind through the observed spectrum of the star. The lines used for this analysis are shown in Figure 6.14; basically they are the ones used in the other analyses plus He I 5875 Å. Some of the lines are contaminated by emission from the disc (see Sect. §6.5.2), so this must be taken into account. The H $_{\delta}$ and H $_{\gamma}$ lines have been selected as the most reliable lines for deriving $\log g$ (they are less contaminated than H $_{\beta}$ and H $_{\alpha}$); The whole set of He I-II lines has been considered except He II λ 4686; however it must be taken into account that the strength of all these lines vary with the phase. Phase 0.972 will be used for determining the stellar parameters (the effect of the continuum emission of the disc is assumed to be smaller at this phase, see Section §6.5.2).

Although in Section §6.5.3 it has been shown that the rotational velocity (derived from Fourier analysis) is $\sim 24 \text{ km s}^{-1}$, when this broadening is considered all synthetic lines appear narrower than the observed ones. Even if we try to solve the problem by means of a different $v \sin i$ value, it does not work because then the shape of the synthetic line profiles do not fit the observed ones (the cores of the modeled profiles are too wide when the FWHM of the He lines is fitted). An extra-broadening mechanism with a different characteristic profile has to be included. When a gaussian macroturbulent broadening (Gray 1973) is used, the fit clearly improves. However in this case the H I and He II lines cannot be fitted simultaneously with the He I ones; when the former are fitted (for a $T_{\text{eff}} = 39000 \text{ K}$), some of the synthetic lines in the latter appear stronger and narrower than observed. A better fitting for the He I lines is obtained if a higher T_{eff} is considered, but then the synthetic He II lines appear too strong. There is no way to solve this problem in this region of the parameter space either by changing the rotational velocity, the macroturbulence or the microturbulence.

In section 6.4.2, Figure 6.8 shows that the fitting of the He I-II lines could follow a similar behavior in the case of the O7V star HD 47839 (selected as reference star). A variation of 1000 K in the effective temperature change strongly the strength of the He I lines. For this spectrum it also occurs that when the He I lines appear fitted, the He II lines are slightly stronger than observed, and if the He II lines are fitted, the He I lines are stronger than observed.

Puls et al. (2005) have shown that there is a discrepancy for the He I singlets between the synthetic FASTWIND and CMFGEN lines for effective temperatures between 36000 and 41000 K (being the CMFGEN profiles shallower). Therefore the He I triplet system can be considered more reliable (i.e. the He I λ 4471 line). Knowing

this discrepancy, we have considered the He I $\lambda 4471$ line for the fitting with FAST-WIND synthetic profiles.

Our best model corresponds to $T_{\text{eff}} = 39000 \pm 1000$ K and $\log g = 4.1$ dex. From these values, the modeled spectral energy distribution and $M_v = -4.9 \pm 0.3$, a stellar radius $R = 9.9 \pm 1.5 R_{\odot}$ is derived, and then an inclination of the rotational axis of $i = 44 \pm 12^{\circ}$. This value is in agreement with previous independent studies (Stahl et al. 1996; Donati et al. 2002), although our derived $v \sin i$ is more reliable and our radius is not obtained from a SpT - R calibration but is a result of the spectral analysis of the star.

6.6 Stellar abundances in Orion B0.5V stars

Three of the stars studied in Orion are perfect targets for a stellar abundance analysis as they have many narrow unblended lines. These are HD 37020, HD 37023 and HD 37042 (θ^1 Ori A, θ^1 Ori D and θ^2 Ori B respectively), three B0.5V stars. Following the methodology presented in Chapter 3 and the guidelines resulting from the study of the B0.2V star τ Sco (Chapter 5), a very detailed oxygen and silicon abundance study has been performed for these stars. The main purpose of this study is to compare the stellar results with those obtained from the analysis of the nebular spectrum.

The other two Orion stars have been ruled out: HD 37041 (θ^2 Ori A) has a relatively high projected rotational velocity, so metal lines are broadened and then they appear blended; HD 37022 (θ^1 Ori C), being an O7V star, does not have enough oxygen and silicon lines for an accurate abundance analysis.

For comparison purposes, a similar analysis has been done for two reference stars: the O9V star 10Lac, and the previously mentioned B0.2V star τ Sco.

6.6.1 Oxygen abundance determination

In Chapter 5 it was shown that it is important to choose a suitable set of lines to derive reliable stellar oxygen abundances. For this aim, the slow rotating star τ Sco was used. The set of O II lines used for the abundance analyses of the Orion's targets and the other two reference stars (by means of FASTWIND and the oxygen model atom A10HHe023-3) is presented in Table 6.6. The bulk of the suitable lines comes from transitions between configurations $2p^2 ({}^3P) 3s - 2p^2 ({}^3P) 3p$ — multiplets 64, 65 and 72 —, and $2p^2 ({}^3P) 3p - 2p^2 ({}^3P) 3d$ — multiplets 90, 148 and 130 —. As commented in Section §5.3.2 (Chapter 5), lines coming from multiplets 118, 161 and 188 are not considered in the analyses. Although lines from multiplet 90 (O II $\lambda\lambda$ 4072, 4076, 4078, located in a spectral range where the τ Sco CASPEC spectrum has lower *SNR*) do not give coherent results in the analysis of the τ Sco CASPEC spectrum, this is not the case for the Orion stars, therefore they will be included in the analyses of these stars. Note that some of the lines that appear unblended in the spectrum of τ Sco cannot be used in the analyses of the other stars; they have larger rotational broadening and then appear blended (or lie in the wings of H or He lines).

Line	EW_o	$\epsilon(O)^a$	$\Delta\epsilon(O)$	EW_o	$\epsilon(O)$	$\Delta\epsilon(O)$									
HD 149438 ($\xi_t = 8.7$)															
(32000, 4.0)															
$(T_{\text{eff}}, \log g)$															
O II 4638	85	8.75	0.04	—	—	—	—	—	—	—	—	—	—	—	—
O II 4641	127	8.65	0.04	74	8.80	0.05	—	—	—	—	—	—	—	—	—
O II 4661	90	8.70	0.04	45	8.80	0.06	80	—	—	—	—	—	—	—	—
O II 4676	79	8.71	0.05	47	8.96	0.06	82	8.59	0.06	76	8.60	0.06	88	8.56	0.06
O II 4317	92	8.69	0.03	45	8.80	0.05	107	8.67	0.04	65	8.59	0.06	82	8.63	0.06
O II 4319	86	8.71	0.04	44	8.85	0.06	100	8.69	0.05	78	8.59	0.05	98	8.60	0.07
O II 4366	80	8.61	0.04	57	8.97	0.05	96	8.62	0.05	75	8.63	0.05	95	8.66	0.07
O II 4416	100	8.62	0.04	—	—	—	120	8.65	0.05	93	8.62	0.05	103	8.62	0.08
O II 4452	37	8.67	0.07	—	—	—	48	8.64	0.07	32	8.58	0.09	60	8.67	0.10
O II 4072	—	—	—	87	8.83	0.05	118	8.61	0.12	99	8.57	0.09	119	8.71	0.10
O II 4076	—	—	—	93	8.93	0.12	133	8.59	0.12	114	8.57	0.09	—	—	—
O II 4078	—	—	—	23	8.83	0.05	46	8.67	0.17	33	8.59	0.09	48	8.68	0.10
O II 4941	38	8.64	0.06	—	—	—	50	8.68	0.07	35	8.60	0.09	43	8.60	0.08
O II 4943	60	8.62	0.04	—	—	—	67	8.58	0.06	55	8.59	0.07	56	8.48	0.07
O II 4956	17	8.73	0.12	—	—	—	20	8.67	0.14	13	8.58	0.20	22	8.71	0.13
O II 4891	24	8.75	0.10	—	—	—	27	8.68	0.11	18	8.59	0.15	27	8.65	0.12
O II 4906	34	8.64	0.07	—	—	—	42	8.63	0.08	31	8.59	0.10	47	8.72	0.08
$\epsilon(O) = 8.70 \pm 0.10$															
$\epsilon(O) = 8.86 \pm 0.20$															
$\epsilon(O) = 8.65 \pm 0.10$															
$\epsilon(O) = 8.59 \pm 0.10$															
$\epsilon(O) = 8.64 \pm 0.10$															

^a $\epsilon(O) = \log(O/H) + 12$

TABLE 6.6 — Equivalent widths and derived line abundances for the set of O II lines used in our analysis. Line abundances refer to the microturbulence given in brackets for each star (ξ_t in km s^{-1}). Uncertainties in the line abundances come from the propagation of the uncertainties of the equivalent width measurements (see text). Some of the O II lines of the Orion stars have not been used as they appear blended. O II $\lambda\lambda$ 4072, 4076 and 4078 lines were ruled out in the analysis of τ Sco due to the poor quality of the CASPEC spectrum in this region. Final oxygen abundances for each star have been calculated through a weighted mean of the linear values. Errors represent the statistical deviation for these mean values.

The microturbulence derived from the zero slope for each one of the studied stars is presented in Table 6.6. This table also summarizes the observed equivalent widths of the various lines along with the line abundance values obtained for the considered microturbulence. A final abundance value for each star is calculated through a weighted mean of the linear individual line abundances ($10^{\epsilon_i - 12}$). The contribution of the uncertainty in the microturbulence to the total oxygen abundance uncertainty is, for these cases, ~ 0.05 dex. In Chapter 5 it was shown that the uncertainty due to a change of 1000 K in effective temperature and 0.1 dex in $\log g$ is ~ 0.08 dex and ~ 0.01 dex respectively. All these sources of error are added quadratically for deriving the final abundance uncertainty.

6.6.2 Silicon abundance determination

A different approach has been used to derive the silicon abundances. In this case, only three Si III lines are considered reliable for the abundance analysis (see below). However, there are also two or three Si IV lines that complete the set of silicon lines. In Chapter 5 the problems that appear in the silicon abundance analysis of early B main sequence stars were commented (i.e. the different abundances given by the Si III $\lambda\lambda$ 4552, 4567, 4574 and Si III $\lambda\lambda$ 4813, 4818, 4828 triplets, and the smaller microturbulence derived from the silicon and oxygen line analysis). There, it was decided to use the Si III $\lambda\lambda$ 4552, 4567, 4574 triplet and the microturbulence derived from them for deriving the silicon abundance. It is also important, when deriving silicon abundances from Si III and Si IV lines, that the Si IV/Si III ionization equilibrium should be fulfilled.

Tables 6.7 to 6.10 show the silicon abundances resulting from the analysis of the Si III and Si IV lines for different values of T_{eff} and $\log g$ in the Orion stars and 10 Lac. The corresponding table for τ Sco has been presented in Chapter 5 (Table 5.8). For all the cases a microturbulence of $\sim 1 \text{ km s}^{-1}$ is derived, so $\xi_t = 1 \text{ km s}^{-1}$ is the value used for the analyses. The final silicon abundances refer to the ionization equilibrium value.

HD 37020: The Si III/Si IV ionization equilibrium is achieved for $T_{\text{eff}} = 30000 \text{ K}$ and $\log g = 4.1 \text{ dex}$ (in agreement with the values derived from the HHe analysis). The final silicon abundance is $\epsilon(\text{Si}) = 7.55$

HD 37023: The Si III/Si IV ionization equilibrium is achieved for $T_{\text{eff}} = 31000 \text{ K}$ and $\log g = 4.2 \text{ dex}$ (vs. $T_{\text{eff}} = 32000 \text{ K}$, $\log g = 4.2 \text{ dex}$, derived from the HHe analysis). The final silicon abundance is $\epsilon(\text{Si}) = 7.45$

HD 37042: The Si III/Si IV ionization equilibrium is achieved for $T_{\text{eff}} = 29000$ K and $\log g = 4.1$ dex (in agreement with the values derived from the HHe analysis). The final silicon abundance is $\epsilon(\text{Si}) = 7.64$

τ Sco: The Si III/Si IV ionization equilibrium is achieved for $T_{\text{eff}} = 31000$ K and $\log g = 4.0$ dex (vs. $T_{\text{eff}} = 32000$ K, $\log g = 4.0$ dex, derived from the HHe analysis). The final silicon abundance is $\epsilon(\text{Si}) = 7.67$

10 Lac: The Si III/Si IV ionization equilibrium is achieved for $T_{\text{eff}} = 34000$ K and $\log g = 3.8$ dex (vs. $T_{\text{eff}} = 36000$ K, $\log g = 3.9$ dex, derived from the HHe analysis). The final silicon abundance is $\epsilon(\text{Si}) = 7.65$

	$\log g = 4.0$ dex	$\log g = 4.2$ dex
$T_{\text{eff}} = 29000$ K	Si III: 7.44 ± 0.05 Si IV: 7.77 ± 0.08	Si III: 7.38 ± 0.03 Si IV: 7.83 ± 0.05
$T_{\text{eff}} = 30000$ K	Si III: 7.57 ± 0.03 Si IV: 7.47 ± 0.05	Si III: 7.50 ± 0.04 Si IV: 7.60 ± 0.06
$T_{\text{eff}} = 31000$ K	Si III: 7.65 ± 0.02 Si IV: 7.47 ± 0.05	Si III: 7.65 ± 0.04 Si IV: 7.37 ± 0.06

TABLE 6.7 — Effect of varying the stellar parameters on the silicon abundances in the analysis of HD 37020. Si III and Si IV analysis has been considered separately for a microturbulence of 1 km s^{-1} . Uncertainties correspond to the dispersion in line abundances.

	$\log g = 4.0$ dex	$\log g = 4.2$ dex
$T_{\text{eff}} = 31000$ K	Si III: 7.51 ± 0.03 Si IV: 7.28 ± 0.06	Si III: 7.47 ± 0.04 Si IV: 7.43 ± 0.06
$T_{\text{eff}} = 32000$ K	Si III: 7.68 ± 0.03 Si IV: 7.11 ± 0.05	Si III: 7.64 ± 0.03 Si IV: 7.25 ± 0.06
$T_{\text{eff}} = 33000$ K	Si III: 7.92 ± 0.03 Si IV: 6.98 ± 0.06	Si III: 7.81 ± 0.03 Si IV: 7.12 ± 0.06

TABLE 6.8 — As Table 6.7 for HD 37023

	log $g = 4.0$ dex	log $g = 4.2$ dex
$T_{\text{eff}} = 29000$ K	Si III: 7.76 ± 0.05 Si IV: 7.65 ± 0.08	Si III: 7.62 ± 0.03 Si IV: 7.75 ± 0.05
$T_{\text{eff}} = 30000$ K	Si III: 7.76 ± 0.02 Si IV: 7.38 ± 0.06	Si III: 7.74 ± 0.03 Si IV: 7.51 ± 0.06
$T_{\text{eff}} = 31000$ K	Si III: 7.80 ± 0.02 Si IV: 7.11 ± 0.07	Si III: 7.89 ± 0.03 Si IV: 7.28 ± 0.06

TABLE 6.9 — As Table 6.7 for HD 37042

	log $g = 3.8$ dex	log $g = 4.0$ dex
$T_{\text{eff}} = 34000$ K	Si III: 7.63 ± 0.04 Si IV: 7.67 ± 0.07	Si III: 7.47 ± 0.05 Si IV: 7.67 ± 0.06
$T_{\text{eff}} = 35000$ K	Si III: 7.91 ± 0.05 Si IV: 7.71 ± 0.06	Si III: 7.80 ± 0.05 Si IV: 7.67 ± 0.06
$T_{\text{eff}} = 36000$ K	Si III: 8.28 ± 0.10 Si IV: 7.79 ± 0.06	Si III: 8.14 ± 0.06 Si IV: 7.71 ± 0.06

TABLE 6.10 — As Table 6.7 for 10 Lac

6.6.3 Oxygen and silicon abundances in the reference stars

Stellar abundances for the reference stars have been derived elsewhere in the literature (τ Sco – Hardorp & Scholz 1970, Kane et al. 1980, Peters & Polidan 1985, Schönberner et al. 1988, Becker & Butler 1988, Kilian 1992, Martin 2004, see Table 6.11; 10 Lac – Schönberner et al. 1988, Becker & Butler 1988, Gies & Lambert 1992, Daflon et al. 2001, Villamariz et al. 2002, see Table 6.12). Tables 6.11 and 6.12 summarize the oxygen and silicon abundances appeared in the literature for these stars. The abundances derived in this work are also presented for comparison.

For the case of τ Sco, the derived value for the oxygen abundance is compatible with previous results but a bit higher than most of them. This difference can be easily explained taking into account that for this range of stellar parameters, the oxygen abundance derived through O II lines is very sensitive to a change in T_{eff} and log g (the lines become fainter when a higher T_{eff} is considered and then the derived oxygen abundance is higher). As mentioned before, the difference in the derived oxygen abundance due to a change of ~ 1000 K in T_{eff} (around 32000 K) is ~ 0.08 dex.

In the case of 10 Lac, there are less O II lines available for the analysis. The weakest O II lines present in the spectra of the early B-type main sequence stars are even weaker (and hence can be hardly distinguished from the noise) in this O9V star. Nevertheless, it is still possible to obtain the microturbulence and the oxygen abundance from the remaining strong lines. The dependence of the strength of these lines on the stellar parameters is somewhat larger than those of the early B stars, which results in a larger uncertainty associated with the final abundance (a change of 1000 K in effective temperature implies a $\Delta \log \epsilon(\text{O}) \sim 0.18$). Additionally, the adopted microturbulence may affect drastically the final abundance (see Section §5.4.1, Chapter 5). Taking into account these considerations, it can be concluded that the oxygen abundance derived in this work is consistent with the other results presented in the literature.

The derived oxygen abundance for 10 Lac is somewhat larger than that obtained for τ Sco. Note that this difference may disappear if a somewhat lower T_{eff} is considered for 10 Lac. In Section §6.6.2 it has been shown that the Si IV/Si III ionization balance is sometimes achieved for a somewhat lower temperature than obtained by He II/He I. Considering a $T_{\text{eff}} = 35000$ K the corresponding derived oxygen abundance for 10 Lac would be $\epsilon(\text{O}) = 8.66$ dex (a value that would be in agreement with that obtained from τ Sco).

One has to be very careful when comparing silicon abundance values from different studies. In Chapter 5 (Section §5.4.1) it has been shown that the mean value given by the Si III $\lambda\lambda 4552, 4567, 4574$ triplet is very dependent on the adopted microturbulence (up to 0.3 dex smaller when the microturbulence changes from 1 km s^{-1} to 5 km s^{-1}). Therefore, the final silicon abundance is very dependent on the criterion considered for adopting the microturbulence. We have adopted a microturbulence of 1 km s^{-1} (this is the value which produces a zero slope for the Si III $\lambda\lambda 4552, 4567, 4574$ triplet) for deriving the silicon abundances. This is the main reason why our results produce larger silicon abundances in comparison with other works. These studies are using the microturbulence derived from the O II lines analysis, that is somewhat larger; therefore their final silicon abundances are smaller than the values we derive.

Additionally, if only Si III lines are used, the uncertainty associated with the silicon abundance due to uncertainties in the derived stellar parameters is ~ 0.2 dex (see Section §5.4.2). In this work, the final silicon abundance has been determined using both Si III and Si IV lines, and hence the final abundance is better constrained.

Work	T_{eff} (K)	$\log g$	$\epsilon(\text{O})$	$\epsilon(\text{Si})$	ξ_t (km s^{-1})
Hardorp & Scholz	30900	4.05	8.70	7.60	—
Kane et al.	30300	3.95	8.6	—	—
Peters & Polidan	31500	4.3	8.72 ± 0.26	7.43 ± 0.4	—
Schönberner et al.	33000	4.15	8.5	—	5
Becker & Butler	33000	4.15	$8.70 \pm 0.19^{(1)}$	—	5
			$8.63 \pm 0.17^{(2)}$	—	10
Kilian et al.	31400	4.24	8.61 ± 0.12	7.40 ± 0.02	3
Martin	30000	3.75	8.58 ± 0.17	7.49 ± 0.32	7
This work	32000	4.0	8.70 ± 0.10	$7.67 \pm 0.20^{(3)}$	8

TABLE 6.11 — Comparison of stellar parameters and abundances derived for τ Sco in previous studies found in the literature and in this work. ⁽¹⁾ NLTE, ⁽²⁾ LTE. ⁽³⁾ A microturbulence of 1 km s^{-1} has been considered for the silicon abundance determination.

Work	T_{eff} (K)	$\log g$	$\epsilon(\text{O})$	$\epsilon(\text{Si})$	ξ_t (km s^{-1})
Schönberner et al.	38000	4.25	9.00	—	—
Becker & Butler	38000	4.25	$9.03 \pm 0.18^{(1)}$	—	5
			$8.85 \pm 0.28^{(2)}$	—	10
Gies & Lambert	34370	4.29	$8.97 \pm 0.29^{(1)}$	7.19 ± 0.04	8
			$8.82 \pm 0.28^{(2)}$	—	12
Daflon et al.	33720	4.42	$8.58 \pm 0.12^{(1)}$	7.53 ± 0.04	11
			$8.64 \pm 0.10^{(2)}$	7.53 ± 0.03	11
Villamariz et al.	37500	4.00	8.69 ± 0.27	7.93 ± 0.21	22.5
This work	36000	3.9	8.86 ± 0.20	$7.65 \pm 0.20^{(3)}$	7

TABLE 6.12 — Comparison of stellar parameters and abundances derived for 10 Lac in previous studies found in the literature and in this work. ⁽¹⁾ NLTE, ⁽²⁾ LTE. ⁽³⁾ A microturbulence of 1 km s^{-1} has been considered for the silicon abundance determination.

6.6.4 Oxygen and silicon abundances in the Orion stars

Table 6.13 summarizes the derived oxygen and silicon abundances for the B0.5V stars in Orion. These stars have been previously studied by Cunha & Lambert (1992, 1994). These authors presented carbon, nitrogen, oxygen and silicon abundances from LTE and NLTE analyses for these stars. Their results for the oxygen and silicon abundances are also presented in Table 6.13. Finally, our derived abundances for the reference stars are also presented for comparison.

The abundances derived for HD 37020, HD 37023 and HD 37042 are representative of the oxygen and silicon abundances associated with the stellar content of the Orion nebula. From the study of the star HD 37023 slightly lower abundances have been inferred (but still compatible with the other abundances). Note that in Section §6.4.2 it was also shown that the fitting of the H and He lines in this star is not so good as for the other B0.5V stars (observed lines appear slightly broader).

The oxygen and silicon abundances in the Orion stars are similar, though systematically lower, than those derived for the reference stars. The derived values are in agreement with those obtained by Allende-Prieto et al. (2001) for the oxygen and silicon solar abundances. This result, along with the agreement with the oxygen nebular gas-phase abundance in the Orion nebula (see next Section) points towards the disappearance of the "solar abundance discrepancy", which indicated that the abundances from nearby H II regions and local B stars were significantly smaller than the solar abundances.

Our oxygen abundances are systematically lower than the NLTE abundances by Cunha & Lambert (1994). In that paper these authors comment that the LTE abundances are slightly more reliable than the NLTE abundances they present. The differences between their LTE abundances and our results are even higher. These differences can be in part associated with the different stellar parameters used for the abundance analysis. While the stellar parameters which we use have been consistently calculated with the same stellar atmosphere code used for the abundance analysis, theirs are calculated using a photometric calibration. Since the T_{eff} and $\log g$ obtained by these authors are higher than ours (see Table 6.3), the oxygen abundances they derive are obviously higher.

Contrarily, our silicon abundances are systematically larger than the NLTE abundances by Cunha & Lambert (1994). These authors base their results on the Si III $\lambda\lambda 4552, 4567, 4574$ triplet. Additionally, they derive the microturbulence separately for O II, N II and Si III and adopt a mean value for the abundance analysis of

the various elements. The difference in the stellar parameters and the adopted microturbulence explain the discrepancy in the derived abundances (see Section §6.6.2).

We consider our values more reliable, since we have found a very good agreement between the silicon abundances given by both Si III and Si IV lines for those stellar parameters.

Object	N	ξ_t (km/s)	$\log(\text{O}/\text{H})+12$	N	$\log(\text{Si}/\text{H})+12$
This work					
HD 149438	14	8.7 ± 1.2	8.70 ± 0.10	6	$7.67 \pm 0.20^{(1)}$
HD 214680	10	6.7 ± 1.6	8.85 ± 0.20	5	$7.65 \pm 0.20^{(1)}$
HD 37020	15	6.5 ± 1.3	8.65 ± 0.10	5	$7.55 \pm 0.20^{(1)}$
HD 37023	15	7.4 ± 3.0	8.59 ± 0.10	5	$7.45 \pm 0.20^{(1)}$
HD 37042	14	5.5 ± 2.0	8.64 ± 0.10	5	$7.64 \pm 0.20^{(1)}$
Cunha & Lambert (LTE)					
HD 37020	6	7.0	8.92 ± 0.05	3	7.40 ± 0.01
HD 37023	7	7.5	8.76 ± 0.04	4	7.34 ± 0.07
HD 37042	7	6.0	8.97 ± 0.04	4	7.67 ± 0.01
Cunha & Lambert (NLTE)					
HD 37020	7	5.0	8.83 ± 0.12	3	7.16 ± 0.05
HD 37023	6	7.0	8.87 ± 0.08	4	7.18 ± 0.08
HD 37042	6	6.0	8.85 ± 0.06	4	7.33 ± 0.08
Allende-Prieto et al. (Sun)					
			8.69	7.54	

TABLE 6.13 — Oxygen and silicon abundances for the three B0.5V stars inside the Orion nebula and the reference stars τ Sco (HD 149438, B0.2V) and 10Lac (HD 214680, O9V). LTE and NLTE abundances derived by Cunha & Lambert (1994) for the Orion stars and the solar abundances from Allende-Prieto et al. (2001) are also presented for comparison. ⁽¹⁾ A microturbulence of 1 km s^{-1} has been considered for the silicon abundance determination (see text).

6.7 Comparing with nebular results

Much work has been devoted to studying the chemical abundances of the Orion nebula from optical lines (viz. Peimbert & Torres-Peimbert 1977; Rubin et al. 1991; Baldwin et al. 1991; Osterbrock et al. 1992; Esteban et al. 1998) or even ultraviolet and infrared lines (viz. Rubin et al. 1993; Simpson et al. 1998).

The most complete and recent analysis is that of Esteban et al. (2004), who used a wide variety of collisional and recombination lines from high resolution, wide wavelength coverage spectroscopic observations obtained with VLT-UVES. These authors derived ionic abundances of O^+ and O^{2+} from collisionally excited lines (CELS). Additionally, the large sensitivity and spectral coverage of their spectroscopic observations allowed them to obtain values for those ions from recombination lines (RLs).

The final oxygen gas-phase abundance that Esteban et al. (2004) propose is $\epsilon(O) = 8.65 \pm 0.03$ dex. This value is calculated considering the O^{2+} abundance derived from RLs, and the O^+ abundance calculated with CELS and a temperature fluctuation parameter $t^2 = 0.022$.

Our stellar oxygen abundances are in very good agreement with those obtained by Esteban et al. (2004) for the gas-phase. This is an important result due to the fact that the same oxygen abundance has been obtained through the study of two different astrophysical objects. Additionally, this result suggest a low amount of oxygen depleted onto dust grains for the Orion nebula.

In a previous work (Esteban et al. 1998), these authors estimate the dust depletion by comparing Si and Fe nebular abundances with those obtained by Cunha & Lambert (1994) for B stars in the Orion association. Taking into account that correction, the final gas+dust oxygen abundance Esteban et al. (2004) propose is $\epsilon(O) = 8.73 \pm 0.03$ (an oxygen abundance correction by dust ~ 0.08 dex is applied). This dust+gas corrected oxygen abundance seems to be too high compared with our stellar abundances, although still marginally consistent within the uncertainties.

The determination of gas-phase silicon abundances in H II regions depends strongly on FUV observations (for this element, the most important lines are Si III] $\lambda\lambda 1883, 1892 \text{ \AA}$, and Si II] $\lambda\lambda 2335-50 \text{ \AA}$), and the assumption of ICFs from theoretical models. In the case of the Orion nebula, models by Rubin et al. (1991) and Baldwin et al. (1991) predict that Si^{2+} is the dominant ionization state of Si with fractional ionization of 0.79 and 0.83, respectively. Rubin et al. (1993) have determined the

Si abundance of the Orion nebula gas-phase, using the Si III] lines from IUE observations. They argue that the gas-phase abundance ratio Si/C may be determined more reliably than the ratio of either C or Si relative to H, so the Si abundance value they estimated is obtained from Si/C = 0.016 and C/H = 2.8×10^{-4} ratios. The final value they propose is $\epsilon(\text{Si}) = 6.65$. Garnett et al. (1995) propose a range for the silicon abundance in Orion between 6.60 and 7.15 dex. These authors use the same Si III] lines, but infer the final silicon abundance through the ratios Si/C, C/O and O/H. For the Si/C ratio they use a different ICF than Rubin et al. (1993), deriving a significantly higher value. For C/O and O/H they assume the possibility of considering the effect of temperature inhomogeneities (by means of the parameter t^2).

Our stellar silicon abundance is larger than the proposed values for the nebular gas-phase silicon abundance (even taking into account the uncertainties). This result, along with the fact that from the comparison of stellar and nebular gas-phase oxygen abundances a small depletion of oxygen onto dust grains could be inferred, could suggest that the molecules that Esteban et al. used to estimate the O dust depletion in Orion cannot be present in large amounts in this nebula. Consequently, Si, Mg and Fe have to form other molecules without oxygen.

Object	N	ξ_t (km/s)	$\log(\text{O}/\text{H})+12$	N	$\log(\text{Si}/\text{H})+12$
This work					
HD 37020	15	6.5 ± 1.3	8.65 ± 0.10	5	$7.55 \pm 0.20^{(1)}$
HD 37023	15	7.4 ± 3.0	8.59 ± 0.10	5	$7.45 \pm 0.20^{(1)}$
HD 37042	14	5.5 ± 2.0	8.64 ± 0.10	5	$7.64 \pm 0.20^{(1)}$
Esteban et al. (2004)					
Gas-phase			$8.65 \pm 0.03^{(a)}$		—
Gas+dust (assumed)			$8.73 \pm 0.03^{(b)}$		—
Other nebular studies (M42)					
Peimbert & Torres-Peimbert (1977)			$8.75^{(c)}$		—
Rubin et al. (1991)			$8.60^{(d)}$		—
Rubin et al. (1993)			—		$6.65^{(e)}$
Osterbrock et al. (1992)			$8.47^{(f)}$		—
Garnett et al. (1995)			—		$6.60 - 7.15^{(g)}$

TABLE 6.14 — Comparison of oxygen and silicon abundances derived through stellar and nebular studies. ⁽¹⁾ A microturbulence of 1 km s^{-1} has been considered for the silicon abundance determination (see Table 6.13). ^(a) O^{2+} from RLS, and O^+ from CELS and $t^2 = 0.022$. ^(b) an oxygen abundance correction by dust ~ 0.08 dex is applied ^(c) CELS and $t^2 = 0.035$; ^(d) model; ^(e) UV Si III] lines + ICF; ^(f) CELS and $t^2 = 0$; ^(g) UV Si III] lines + ICF;

THE NEAREST APPARENTLY SPHERICAL H II REGION: M43

*El valor y la utilidad de un experimento
dependen de lo apropiado que sea el material
para el objeto con que se emplea.*

Experimentos de hibridación en plantas – Gregor Mendel –

M43 is an apparently spherical H II region ionized by a single star (HD 37061, B1V). This well resolved H II region has been selected to build a tailored model of the nebula, comparing photoionization code results with many different observational constraints. The stellar parameters and the emergent flux of the ionizing star have been derived from a detailed spectroscopic analysis of HD 37061 by means of state-of-the-art stellar atmosphere codes. Photometric and morphological nebular parameters have been obtained from narrow band imagery. Finally, results from long-slit nebular spectral observations at different positions along the nebula have allowed us to derive the physical parameters and abundances of the nebular gas-phase as well as to use the ratio of several nebular lines as constraints for the photoionization model.

7.1 Introduction

THE de Marian's nebula (M43, NGC1982) is an apparently spherical Galactic H II region ionized by a single star (HD 37061, B1V). It is located at the North of the well known Orion nebula (M42, see Figure 2.7 in Chapter 2). Its distance from Earth is assumed to be ~ 450 pc, similar to its companion nebula, which results in an apparent projected size of $\sim 5 \times 5$ arcmin.

Despite that this nebula (along with the Orion nebula) has been extensively observed for many years, this is not a very well studied H II region. Thum et al. (1978), Smith et al. (1987) and Subrahmanyan (1992) explored M43 in the radio and infrared. The most recent studies are those by Rodríguez (1999, 2002), who analyzed long-slit optical spectroscopic data in five different slit positions along the nebula, deriving the physical parameters (T_e and N_e) and O, S, Cl, N, Ar, He, C and Fe abundances of the nebular gas.

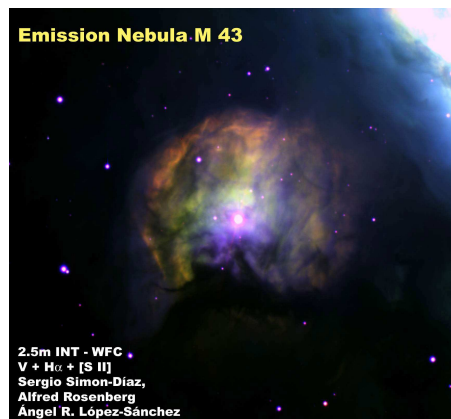


FIGURE 7.1 — False color image of M43 constructed with the combination of several INT-WFC images.

M43 appears to be a good example of a standard "spherically symmetric H II region around a single ionizing star". Moreover, the energy balance of the nebula can be studied without any assumptions about the number and type of the exciting stars. Therefore it is a perfect target for developing a detailed study of the interplay between massive stars and their surrounding interstellar medium, as well as testing the predictions of the stellar atmosphere codes of hot stars using observed nebular constraints in an extremely well defined situation.

The present chapter describes a very detailed study of the galactic H II region M43 and its ionizing source, the B1V star HD 37061. The chapter is structured as follows: the stellar model atmosphere codes FASTWIND and WM-*basic* are used in Section §7.2 to perform a spectroscopic analysis of the ionizing star, deriving its stellar parameters and modeling its spectral energy distribution. In Section §7.3, some INT-WFC narrow band images are used to photometrically characterize M43, deriving its size, total H_α luminosity and surface brightness profiles in various nebular lines. In Section §7.4, nebular spectra in various slit positions along the nebula are used to derive its physical parameters and gas-phase abundances. Finally, all this information is considered in the modeling of the nebula with the photoionization code CLOUDY. In Section §7.5, various models are compared with the observational constraints. This section also presents a comparison with the predictions of the pseudo-3D code CLOUDY-3D. Finally, a summary and the conclusions of this work are presented in Section §7.6.

7.2 Spectroscopic analysis of the ionizing source

HD 37061 (NU Ori, Par 2074) is the ionizing source of M43. This is a B1V variable star ($m_v = 6.50-7.80$, Kukarkin et al. 1971) with a period of $19^d.139$ (Abt et al. 1991). Using bispectrum speckle interferometry, Preibisch et al. (1999) found a companion at ~ 470 mas with a flux ratio in the K-band of 0.03 ± 0.02 .

The spectroscopic observations of HD 37061 were carried out with the Isaac Newton 2.5 m. Telescope (INT) at El Roque de los Muchachos observatory in La Palma in 21th of December 2002 (see Chapter 2 for details). The observed spectrum covers the spectral region between 4000 and 5050 Å and the H_α region with an effective spectral resolution $R \sim 8000$ and $SNR \sim 200-300$.

7.2.1 Stellar parameters

The $v \sin i$ of the star has been determined applying the Fourier method to the He lines, obtaining a $v \sin i = 220 \text{ km s}^{-1}$. The stellar parameters of this B1V star have been derived through a visual comparison of the observed H, He I and He II line profiles with those synthetic ones obtained with FASTWIND (following the habitual technique presented in Chapter 3). It has been found that the observed H Balmer lines are systematically stronger than the synthetic ones (both the He I and He II lines are affected in the same way). This is an effect that appears in binary systems when the cooler and smaller component partially eclipses the hotter component. The global combined flux is lower than that corresponding to the primary if it was isolated, hence the normalized spectrum is affected, resulting on an increase of the strength of the lines¹. In addition, since there is not any line from the companion appearing in the observed spectrum, it can be assumed that the flux of the secondary is negligible compared with the primary flux.

It is not easy to determine the actual correction factor that has to be applied to the observed normalized spectrum. This depends on the ratio of the effective temperatures and radii of the two components as well as the area of the primary star eclipsed by the secondary (see Appendix B). However, the cores of the H_δ and H_γ lines can be used for correcting this effect by comparing them with synthetic lines from a stellar atmosphere model. The strength of these lines is not much affected by changes in T_{eff} , $\log g$, $\epsilon(\text{He})$ or wind characteristic (if these changes are not very strong). As shown in Figure 7.2 the cores of these lines are also less affected by the emission nebular lines. A correction factor $f \sim 0.85$ has to be applied to the observed spectrum to obtain agreement between synthetic and observed H_δ and H_γ

¹This effect is more extensively described in Appendix B

lines. This correction factor suppose a difference in visual magnitude of $\sim 0^m.17$ between this phase and that in which the primary eclipses the secondary. Kukarkin et al. (1971) observe a maximum variation in the visual magnitude of $1^m.3$, hence the latter value is compatible with a partial eclipse of the primary. When this correction factor is applied the whole set of H and He I-II synthetic lines fits perfectly the observed profiles for the parameters shown in Table 7.1. This table also shows the remaining stellar parameters that result from the spectral analysis of HD37061.

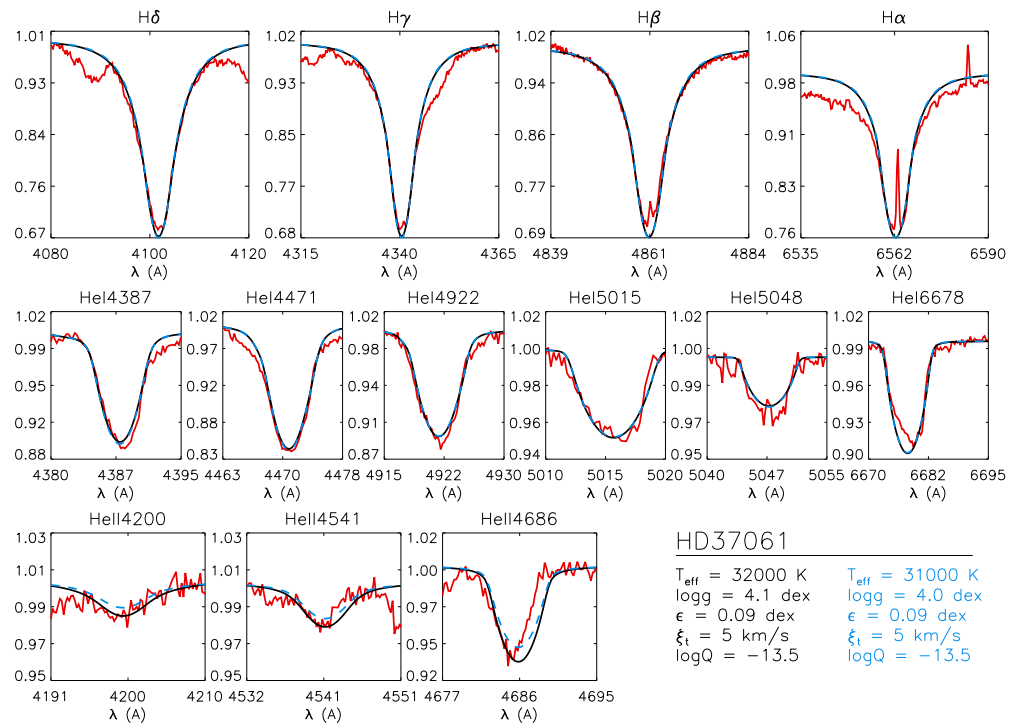


FIGURE 7.2 — Fitting of the observed H and He I-II stellar optical lines with the synthetic FASTWIND profiles for two different values of T_{eff} and $\log g$. The core of the H_{α} and H_{β} lines are clearly contaminated by the narrow nebular emission component. The blue wing of the H_{α} line is affected by a broad diffuse interstellar band (see Chapter 2); the wings of the H_{γ} and H_{δ} lines are contaminated by very broad Si IV and O II stellar absorption lines, due to the high $v \sin i$ of this star.

T_{eff}	32000 ± 1000 K
$\log g$	4.1 ± 0.1 dex
$\epsilon(\text{He})$	0.09
ξ_t	5 km s^{-1}
$\log Q$	-13.5
m_v	6.84 ± 0.01
A_v	2.09 ± 0.03
M_v	-3.5 ± 0.3
$R (R_{\odot})$	6.1 ± 0.8
$\log L/L_{\odot}$	4.54 ± 0.13
$M (M_{\odot})$	17 ± 6

TABLE 7.1 — Stellar parameters derived through the analysis of the optical spectrum of HD 37061. Photometric data are from Preibisch et al. (1999). M_v has been calculated assuming a distance to the nebula $d = 450 \pm 50$ pc.

T_{eff}	32000 K
$\log g$	4.1 dex
R	$6.1 R_{\odot}$
$\epsilon(\text{He})$	0.09
κ	0.188
α	0.599
δ	0.10
$\log L/L_{\odot}$	4.54
$M (M_{\odot})$	17.1
$\dot{M} (M_{\odot} \text{ yr}^{-1})$	0.49×10^{-7}
$v_{\infty} (\text{km s}^{-1})$	2300

TABLE 7.2 — Input parameters considered in WM-*basic* model (top). The second set of parameters (bottom) are derived by the code from the previous input parameters.

7.2.2 Spectral energy distribution

The derived stellar parameters (T_{eff} , $\log g$ and R) have been used as input in WM-*basic* (Pauldrach et al. 2001) to obtain a detailed emergent spectral energy distribution for HD 37061. No wind shocks were considered in the model and the initial set of force multiplier parameters were selected to produce values for \dot{M} and v_{∞} to be consistent with the value of $\log Q = -13.5$ used in FASTWIND model. Table 7.2 summarizes the input parameters considered in WM-*basic* model along with the other inferred stellar and wind parameters.

Figure 7.3 shows a comparison of the emergent fluxes from WM-*basic* and FASTWIND in the Lyman continuum range ($\lambda < 912 \text{ \AA}$). The fluxes have been normalized to correspond to the effective temperature at the photospheric radius. In order to allow for a meaningful comparison between WM-*basic* and FASTWIND modeled SEDs, the high resolution frequency grid provided by WM-*basic* has been re-mapped while keeping the corresponding flux-integrals conserved (see Chapter 3, §3.4.2). Four different fluxes have been plotted in the figure: (a) original WM-*basic* model with line-blanketing, (b) smoothed WM-*basic* line-blanketed model, (c) FASTWIND model with an approximated treatment of line-blanketing, (d) blackbody with a temperature $T = 32000$ K, scaled to have the same number of Lyman continuum photons than the previous models.

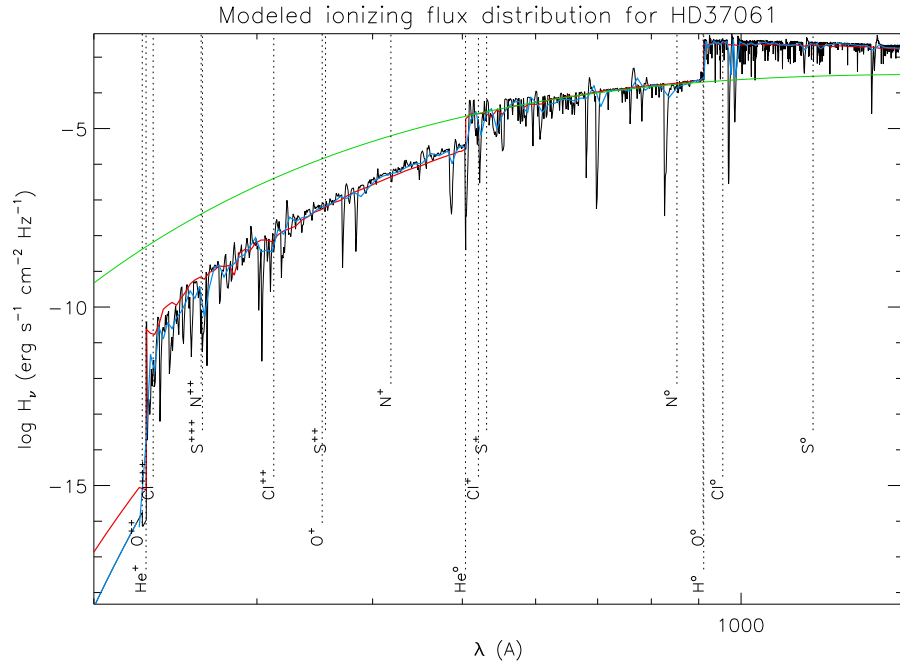


FIGURE 7.3 — Modeled ionizing emergent flux distribution for HD 37061 from FASTWIND and *WM-basic*. The stellar parameters considered for the models are those presented in Table 7.1. Fluxes have been normalized to correspond to the effective temperature at the photospheric radius. (Black) Original *WM-basic* model with line-blanketing, (red) FASTWIND model with an approximate treatment of line-blanketing, (blue) smoothed *WM-basic* model with line-blanketing. Green curve represents the SED of a blackbody with $T_{\text{eff}} = 32000$ K, scaled to have the same number of ionizing photons than *WM-basic* model. Vertical dotted lines show the ionization edges of H, He, Cl, O, S, and N in various ionization stages.

The agreement between the SEDs from both FASTWIND and *WM-basic* models is rather well, except for some strong absorptions and emissions not considered in FASTWIND and the region below 300 \AA (see Puls et al. 2005). The blocking predicted by *WM-basic* between 300 \AA and the He II Lyman jump is stronger; below this edge, *WM-basic* also predicts a lower emergent flux (although the strength of the He II Lyman jump is quite similar in both cases). These differences should be negligible in terms of the number of H^0 ionizing photons, but could be relevant for the ionization of other ions. Table 7.3 shows the effect of these discrepancies over the number of ionizing photons for several ions ($Q(X^{+i})$). Only those ions whose ionization has consequences on the nebular lines used as observational constraints in the modeling of M43 (see Section §7.5) have been considered. Results are better illustrated in Figure 7.4, which shows the difference in logarithm between $Q(X^{+i})$ for

	FASTWIND	WM- <i>basic</i>	FASTWIND	WM- <i>basic</i>
	(32000 K, 4.1 dex, 6.1 R_{\odot})		(31000 K, 4.0 dex, 6.3 R_{\odot})	
H ⁰	2.6e+47	2.4e+47	1.8e+47	1.5e+47
O ⁰	2.6e+47	2.3e+47	1.8e+47	1.4e+47
N ⁰	2.0e+47	1.8e+47	1.3e+47	1.1e+47
S ⁺	6.7e+45	5.3e+45	3.7e+45	2.4e+45
Cl ⁺	4.4e+45	4.0e+45	2.2e+45	1.7e+45
He ⁰	1.1e+45	1.4e+45	5.8e+44	5.7e+44
N ⁺	1.6e+44	1.7e+44	7.9e+43	6.7e+43
O ⁺	1.6e+43	1.8e+43	8.0e+42	8.1e+42

TABLE 7.3 — Number of ionizing photons for several ions predicted by FASTWIND and WM-*basic*. Two models with different T_{eff} and $\log g$ have been considered to study the effect of the stellar parameters on $Q(X^{+i})$.

the considered ions predicted by both models (smoothed blanketed WM-*basic* model is taken as reference). Two main discrepancies are found. The first one is related to the presence of strong absorption lines in WM-*basic* model, not considered in FASTWIND. This makes the number of ionizing photons associated with some ions (viz. H⁰, O⁰, N⁰, S⁺, Cl⁺) being larger for the case of FASTWIND model (up to 25%). The emergent flux between Lyman HeI edge and $\sim 300 \text{ \AA}$ is slightly lower in FASTWIND, producing the difference in number of ionizing photons for He⁰, N⁺ and O⁺. Note that, although the largest discrepancies would be found for ions with ionization edges below 300 \AA (see Figure 7.3), these will produce negligible effects in terms of the ionization structure of the nebula.

THE EFFECT OF THE STELLAR PARAMETERS

In Figure 7.2 it has been shown that two models with slightly different T_{eff} and $\log g$ can fit the observed H and He optical line profiles. Therefore it is important to know which is the effect of a small variation of the stellar parameters (within the uncertainties) on the emergent ionizing flux predicted by the stellar atmosphere models. To this purpose, in Table 7.3 two extra columns with the various $Q(X^{+i})$ inferred from FASTWIND and WM-*basic* models with $T_{\text{eff}} = 31000 \text{ K}$ and $\log g = 4.0 \text{ dex}$ are presented for comparison. Both sets of models have different radii, considering the respective SEDs and $M_V = -3.5$. The effect of the variation of T_{eff} and $\log g$ on $Q(X^{+i})$ depends on the considered ion; for example, for this case there is a difference $\sim 37\%$ in $Q(\text{H}^0)$, but $\sim 60\%$ for $Q(\text{He}^0)$. This is because the slope of the emergent ionizing flux distribution also varies with the stellar parameters.

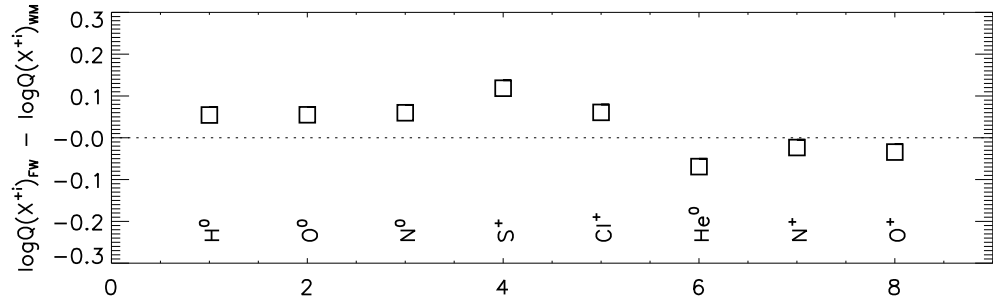


FIGURE 7.4 — Comparison of the number of ionizing photons predicted by FASTWIND and WM-*basic* for different ions (See text).

Therefore, the uncertainty associated with $Q(\text{H}^0)$ will take into account the uncertainty in the stellar parameters along with that associated with the radius (due to ΔM_V). A total uncertainty of 40% will be considered for this case. Note that taking into account this uncertainty associated with the stellar parameters, it can be concluded that the agreement between the number of hydrogen ionizing photons predicted by both FASTWIND and WM-*basic* codes is quite good.

COMPARING WITH OTHER STELLAR ATMOSPHERE CODES

Figure 7.5 compares the number of ionizing photons corresponding to the various WM-*basic* and CMFGEN models indicated in Table 7.4. The radii have been calculated from the respective SED, assuming a $M_V = -3.5$. This Figure illustrates that the number of Lyman continuum photons predicted by a CMFGEN model with $T_{\text{eff}} = 31000$ K and $\log g = 4.0$ is $\sim 80\%$ larger than the one predicted by a WM-*basic* model with the same stellar parameters. The other $Q(X^{+i})$ follow a similar pattern.

Figure 7.6 shows some of the H and He lines used to derive the stellar parameters. In this range of stellar parameters, the He I are quite insensitive to changes in T_{eff} or $\log g$. This is not the case for the He II lines. Although these lines are quite weak, they are very sensitive to changes in the stellar parameters (i.e. the ionization structure of the stellar atmosphere region where the lines are formed). In Figure 7.6 it can be seen that when two CMFGEN and FASTWIND models with the same stellar parameters are considered, CMFGEN model results in a stronger He II $\lambda 4200$ line. To fit the line profiles predicted by CMFGEN, FASTWIND requires a model

	CMFGEN	FASTWIND	
$T_{\text{eff}}(\text{K})$	31000	31000	33000
$\log g$	4.0	4.0	4.1
$R (R_{\odot})$	6.2	6.2	5.8
$\log L/L_{\odot}$	4.50	4.50	4.56
$\log Q(\text{H}^0)$	47.53	47.16	47.54

TABLE 7.4 — CMFGEN and FASTWIND models used for the comparison presented in this section.

with $T_{\text{eff}} = 33000$ K and $\log g = 4.1$. Therefore, since a FASTWIND model with $T_{\text{eff}} = 31000$ K fits the observed H-He optical spectrum of HD 37061, a somewhat lower effective temperature than 31000 K would be derived with CMFGEN. This may be related to the amount of blanketing that is considered by each code.

A better agreement between $Q(\text{H}^0)$ and the other $Q(\text{X}^{+i})$ is found when predictions from a CMFGEN model with $T_{\text{eff}} = 31000$ K and $\log g = 4.0$, and from a WM-*basic* model with $T_{\text{eff}} = 33000$ K and $\log g = 4.1$ are compared. Therefore it can be concluded that similar results can be achieved when the analysis is done consistently, either by using CMFGEN or a combined use of FASTWIND and WM-*basic*². Although there is a difference in the T_{eff} derived from both CMFGEN and FASTWIND codes, the $Q(\text{X}^{+i})$ predicted by CMFGEN and WM-*basic* for the corresponding T_{eff} values are quite similar (at least for the considered ions).

From this comparison it can be concluded that one has to be very careful when comparing results from different stellar atmosphere codes or even using these codes as black boxes. For example, one should be aware that the $T_{\text{eff}} - Q(\text{H}^0)$ calibration may be slightly dependent on the stellar atmosphere code that has been considered. Martins et al. (2005) find that $Q(\text{H}^0)$ values predicted by CMFGEN are somewhat larger than the values predicted by WM-*basic* for dwarfs with $T_{\text{eff}} \leq 40000$ K. The study presented here reinforces the suggestion by these authors that the discrepancy may be due to a shift in T_{eff} .

²Note that WM-*basic* aims mainly at the prediction of EUV/UV fluxes and profiles. Optical lines predicted by this code are not reliable for diagnostic purposes. FASTWIND is hence used to this aim.

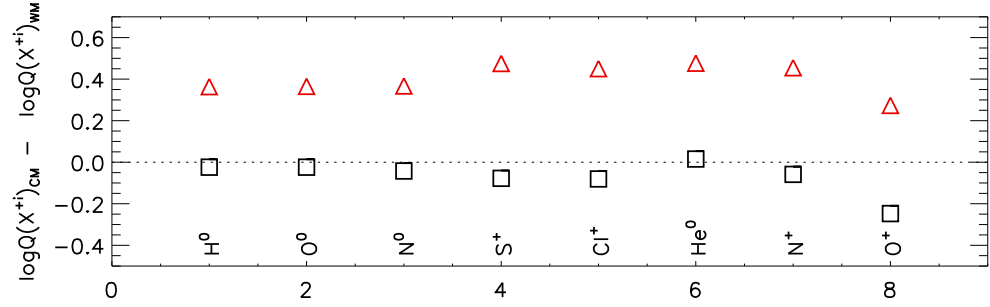


FIGURE 7.5 — Comparison of the number of ionizing photons predicted by CMFGEN and WM-*basic* for the ions considered in Figure 7.4. Red triangles compares the predictions of a CMFGEN model with $T_{\text{eff}} = 31000$ K, $\log g = 4.0$, $R = 6.1 R_{\odot}$ and a WM-*basic* model with the same stellar parameters. Black squares compares the predictions of the same CMFGEN model with a WM-*basic* model with $T_{\text{eff}} = 33000$ K, $\log g = 4.1$, $R = 5.8 R_{\odot}$.

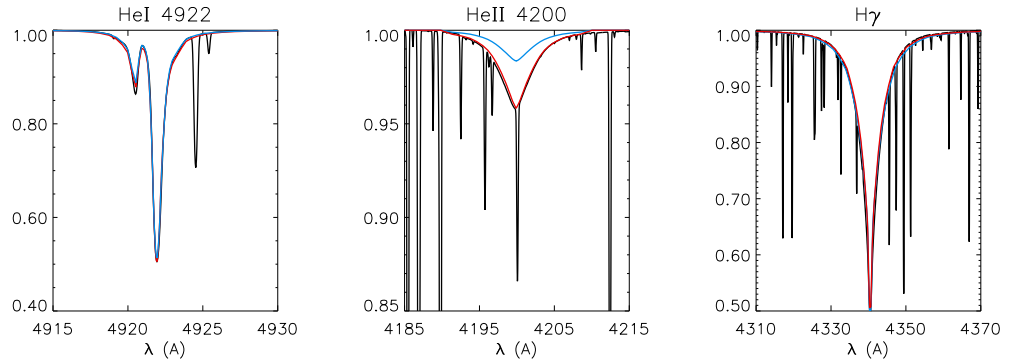


FIGURE 7.6 — H, He I and He II lines from CMFGEN and FASTWIND models summarized in Table 7.4. (Black) CMFGEN model with $T_{\text{eff}} = 31000$ K, $\log g = 4.0$; (red) FASTWIND model with $T_{\text{eff}} = 33000$ K and $\log g = 4.1$; (blue) FASTWIND model with $T_{\text{eff}} = 31000$ K and $\log g = 4.0$.

7.3 Obtaining useful information from the INT-WFC images

Figure 7.7 shows three logarithmic grey scaled INT-WFC images of M43, taken through filters isolating H_{α} + [N II] $\lambda\lambda 6548, 6584$ (top), [O III] $\lambda 5007$ (center) and [S II] $\lambda\lambda 6717, 6731$ (bottom). The observational data-set is described in Chapter 2. Note the apparently spherical distribution of the gas around the ionizing star in the three images. The size of M43 in both H_{α} and [S II] images is roughly the same, indicating a diameter of ~ 5 arcmin, or 0.65 pc if a distance of 450 pc to nebula is considered. This is not the case for the [O III] image, where the nebula appears smaller, a fact that is consistent with the low T_{eff} of the ionizing star (see previous section). Although H_{α} and [S II] images show the nebular material radially distributed around HD 37061, it appears more like a clumpy medium than a filled density distribution. Note the bright emission in the top right corners of the images, corresponding to the northern edge of the Orion nebula. This nebula can be responsible of the foreground emission contaminating the M43 nebula (see next section). A dark lane is present in the eastern side of M43. The dark cloud is located in the foreground and hence blocks the nebular light coming from behind.



FIGURE 7.7 — Logarithmic grey scaled INT-WFC images of M43 taken through narrow band filters: (top) H_{α} ; (center) [O III] $\lambda 5007$; (bottom) [S II] $\lambda 6723$

Position	$\tau_{\text{H}\alpha}$
Pos-1	1.14 ± 0.01
Pos-2	1.20 ± 0.08
Pos-3	1.3 ± 0.2
Pos-4	1.23 ± 0.08
Pos-5	1.16 ± 0.08

TABLE 7.5 — Optical depths at $\lambda=6563 \text{ \AA}$ for the various slit positions.

7.3.1 Total H $_{\alpha}$ luminosity and H $_{\alpha}$ surface brightness profile

In Chapter 2 it is described how the images taken with the H $_{\alpha}$ and Sloan r' filters have been used for obtaining the flux calibrated, pure H $_{\alpha}$ image of M43. Prior to derive the total H $_{\alpha}$ luminosity and surface brightness profile, this image has to be corrected by distance and extinction. Considering $F_{\text{H}\alpha}$ as the nebular flux received at Earth, the corresponding extinction corrected H $_{\alpha}$ luminosity can be derived from:

$$L_{\text{H}\alpha} = 4\pi d^2 F_{\text{H}\alpha} e^{\tau_{\text{H}\alpha}} = 4\pi d^2 F_{\text{H}\alpha} e^{C_{\text{H}\beta} f(\text{H}\alpha)/0.434} \quad (7.1)$$

Where d is the distance to the nebula ($450 \pm 50 \text{ pc}$), $\tau_{\text{H}\alpha}$ the optical depth at the wavelength corresponding to H $_{\alpha}$, $C_{\text{H}\beta}$ is the usual logarithmic extinction coefficient at H $_{\beta}$, and $f(\text{H}\alpha)$ is the value of the extinction law for H $_{\alpha}$ (Cardelli et al. 1989).

The extinction correction has been estimated using Mónica Rodríguez's spectroscopic dataset and Cardelli's extinction law with $R_v = 5.5$ (see also Rodríguez 1999 for further details). Since the H $_{\alpha}$ and H $_{\beta}$ lines are located in different observed spectral ranges, the non-extinction corrected H $_{\alpha}$ /H $_{\beta}$ line ratios for the various slit sections have been calculated using the line intensity of [N II] $\lambda 5755$, present in both blue spectral ranges. Those line ratios have been compared with the theoretical ones (corresponding to case B) to estimate the values of $C_{\text{H}\beta}$. Finally a value of $f(\text{H}\alpha) = 0.857$ has been considered to calculate the $\tau_{\text{H}\alpha}$ values (see Table 7.5). A mean value $\tau_{\text{H}\alpha} = 1.14 \pm 0.09$, derived from the various slits results, has been assumed to correct the H $_{\alpha}$ image for extinction.

Some IDL programs have been implemented to calculate the required photometric information. These are based on the calculation of the integrated H $_{\alpha}$ luminosity corresponding to sectors of circular areas of radius r and whose center is HD 37061 – $L_{\text{H}\alpha}(r)$. It is necessary to consider a sector and not the whole circular area to

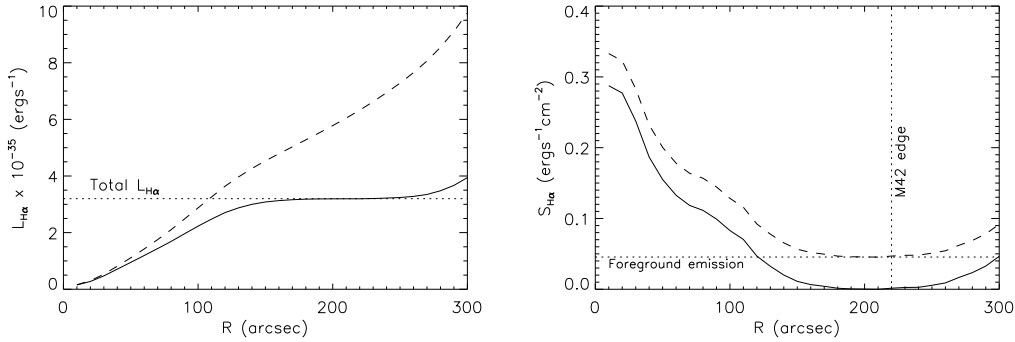


FIGURE 7.8 — Integrated H_{α} luminosity and the surface brightness profiles. Solid lines: foreground emission subtracted profiles. Dashed lines: original profiles without foreground emission subtraction. Radii greater than 210 arcsec are affected by M42 emission.

take into account the presence of the dark lane located at the east of M43. The final luminosities correct for the missing sector by assuming an angle-independent H_{α} emission. Finally, the surface brightness profile is calculated by applying:

$$S_{H\alpha}(r) = \frac{L_{H\alpha}(r + \Delta r) - L_{H\alpha}(r)}{\pi(r + \Delta r)^2 - \pi r^2} \quad (7.2)$$

Figure 7.8 shows the integrated H_{α} luminosity and surface brightness profiles. The main nebular emission centered on HD37061 is contaminated by foreground emission, as can be clearly seen in Figure 7.8. When this foreground emission is subtracted from the H_{α} image, the integrated H_{α} luminosity profile becomes more consistent with what would be expected if the nebula were isolated (for radii greater than the size of the apparently spherical nebula the integrated H_{α} luminosity remains constant). From these plots, a total H_{α} luminosity $\sim 3 \times 10^{35} \text{ ergs}^{-1}$ and a size ~ 130 arcsec (corresponding to ~ 0.28 pc at a distance of 450 pc) can be derived. It is also important to estimate the uncertainties related to the H_{α} luminosity and size, taking into account uncertainties associated with the distance, flux calibration and extinction correction. The final values for these quantities are $L_{H\alpha} = (3.0 \pm 0.8) \times 10^{35} \text{ ergs}^{-1}$ and $R_{\text{neb}} = 0.28 \pm 0.04$ pc.

In section §7.2 it has been shown that the total number of hydrogen ionizing photons predicted by *WM-basic* for the derived stellar parameters of HD37061 is $Q(H^0) = (2.4 \pm 1.0) \times 10^{47} \text{ ph s}^{-1}$, and hence $\frac{\epsilon}{\alpha_B} Q(H^0) = (3.4 \pm 1.4) \times 10^{35} \text{ ergs}^{-1}$. This value is comparable to the observed integrated nebular H_{α} luminosity. Although the H_{α} luminosity of the nebula is slightly lower than that predicted by the stellar

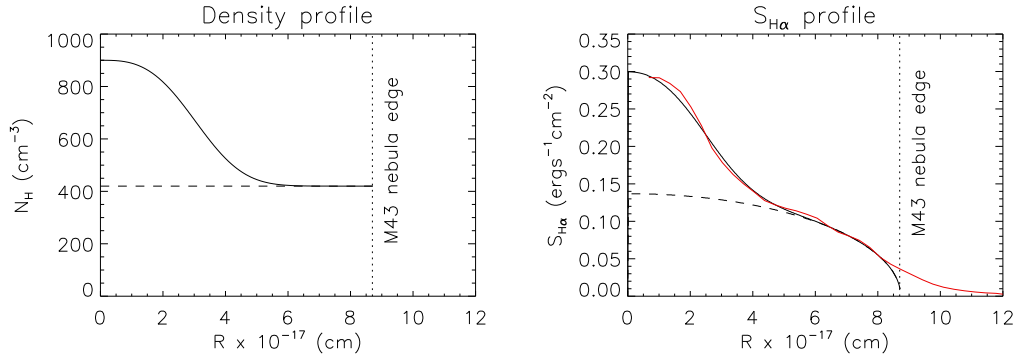


FIGURE 7.9 — Density law described in text and its corresponding H_{α} surface brightness profile (solid lines). The H_{α} surface brightness represented as a dashed line corresponds to a spherical constant density nebula with $N(H)=420 \text{ cm}^{-3}$. Red line is the observed H_{α} surface brightness profile.

model atmosphere, no firm conclusion about the escape of photons from the nebula can be made because both estimations are consistent within the errors. Indeed, the nebula may be considered as radiation bounded.

As mentioned in Chapter 4 (Section §4.4), the H_{α} surface brightness profile can be used to determine the nebular hydrogen density distribution (N_H) once a nebular geometry is assumed. Here, a density law has been estimated from $S_{H_{\alpha}}$, assuming a spherical geometry. By trial and error it has been found that the observed H_{α} surface brightness profile is well reproduced by a spherical model with a hydrogen density distribution described by:

$$N_H(r) = A e^{(-r/B)^3} + C \quad r \leq r_{\max} \quad (7.3)$$

with $A = 480 \text{ cm}^{-3}$, $B = 0.11 \text{ pc}$, $C = 420 \text{ cm}^{-3}$, and $r_{\max} = 0.28 \text{ pc}$. Figure 7.9 shows this density distribution and its corresponding H_{α} surface brightness profile.

7.3.2 Other narrow band filters

The same procedure has been followed for calculating the $[O \text{ III}]$ and $[S \text{ II}]$ surface brightness profiles. These images have not been either flux calibrated or continuum subtracted, however the information provided by the profiles normalized to their central values is also useful to constraint the density distribution and physical geometry of the nebula. Figure 7.10 shows a comparison between the three surface brightness profiles. These plots assume that the surface brightness distributions are

angle-independent; from images presented in Figure 7.7 it can be concluded that this assumption is good to a first order.

Note that both $S_{[\text{SII}]}$ and $S_{[\text{OIII}]}$ are also affected by foreground emission, following a similar behavior to that one shown in Figure 7.8 for the case of $S_{\text{H}\alpha}$. Surface brightness profiles presented in Figure 7.10 have been corrected for this foreground emission.

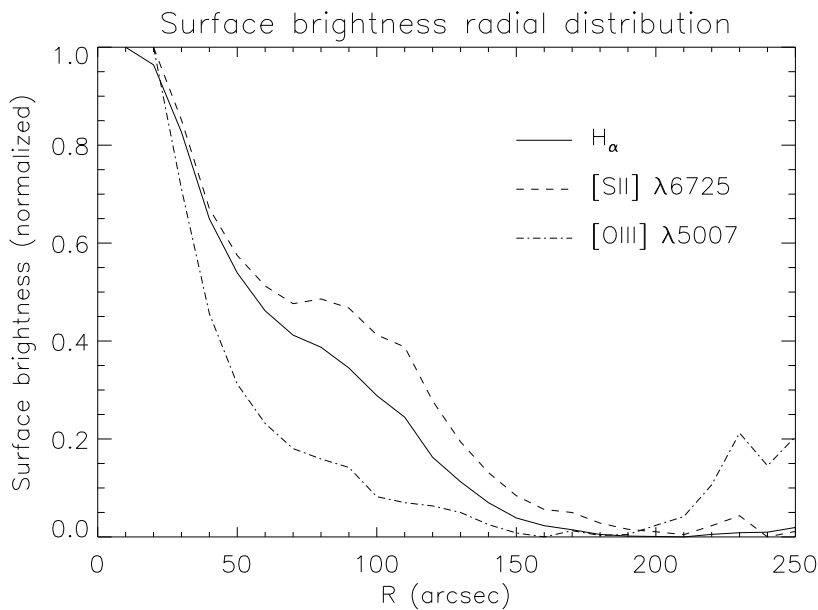


FIGURE 7.10 — Surface brightness profiles corresponding to $\text{H}\alpha$, $[\text{SII}]\lambda 6725$ and $[\text{OIII}]\lambda 5007$ emission. Since the $[\text{SII}]$ and $[\text{OIII}]$ images have not been flux calibrated, the three surface brightness distributions have been normalized to their central values for comparison purposes.

7.4 Nebular physical parameters and abundances revised

For the spectroscopic study of M43, INT-IDS longslit data from Mónica Rodríguez's thesis have been used (Rodríguez 1998; see also Rodríguez, 1999, 2002). The spectroscopic data-set has been presented in Chapter 2 (Section 2.3.1); five spectra at different positions from the central star were obtained by dividing the original ~ 2 arcmin length slit into shorter sections (see Figure 2.5 and Table 2.3).

Rodríguez (1999) derived the physical parameters and abundances of the nebular gas-phase of M43. She used the version of May 1997 of the `NEBULAR` package

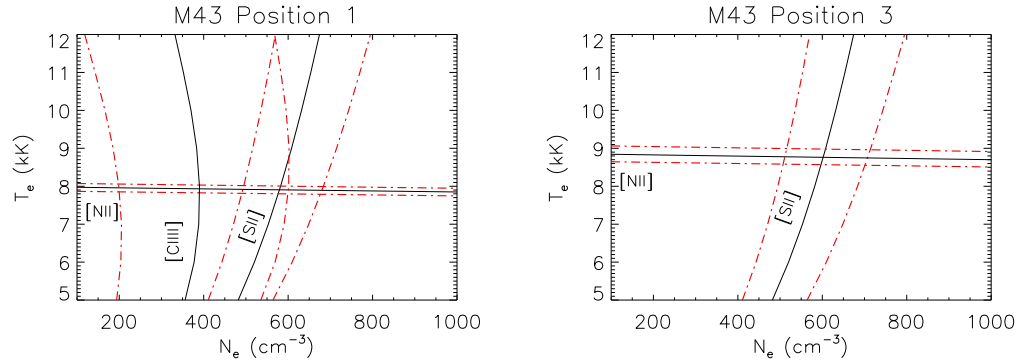


FIGURE 7.11 — Examples of nebular diagnostic diagrams for the determination of T_e and N_e . Red lines show the uncertainties associated with the T_e and N_e determinations due to the uncertainties in the measurement of the corresponding line intensities.

Position	$T_e[\text{N II}]$ (K)	$N_e[\text{S II}]$ (cm^{-3})	$N_e[\text{Cl III}]$ (cm^{-3})
Pos-1	7880	580	390
Pos-2	8265	560	269
Pos-3	8750	600	—
Pos-4	7870	580	—
Pos-5	7840	650	427

TABLE 7.6 — Nebular physical properties derived from the nebular diagnostic plots.

implemented in IRAF. These results have been revised for the present work using the latest version of NEBULAR (February 2004) including some changes in the atomic data that will be discussed below (see also comments on García-Rojas et al. 2005). Figure 7.11 shows examples of the diagnostic diagrams used for the determination of the nebular physical parameters. Only one temperature indicator is available from the spectrum of M43 ($T_e[\text{N II}]$). The low degree of ionization of this nebula makes the $[\text{O III}] \lambda 4363$ line too weak and hence the $T_e[\text{O III}]$ indicator cannot be derived. To determine the electron density, two indicators are available, $N_e[\text{S II}]$ and $N_e[\text{Cl III}]$. Table 7.6 summarizes the derived physical parameters. Note that $N_e[\text{Cl III}]$ gives systematically lower densities than $N_e[\text{S II}]$ does, however the uncertainties associated with this indicator are larger and hence it is less reliable than $N_e[\text{S II}]$. The revised physical parameters are basically the same than the ones obtained by Rodríguez (1999) because the N^+ , S^+ and Cl^{++} atomic data have not been changed in the latest version of NEBULAR.

To derive nebular abundances it has been considered that the various positions have an electron temperature and density inferred from the $T_e[\text{N II}]$ and $N_e[\text{S II}]$ indicators. Nebular abundances have also been revised considering the latest version of `NEBULAR` (except for Cl^+ , see García-Rojas et al. 2004). Table 7.7 summarizes the ionic abundances for the various slit positions.

Ion	Rodríguez					This work				
	S1	S2	S3	S4	S5	S1	S2	S3	S4	S5
O^+	-3.60	-3.57	-3.42	-3.57	-3.55	-3.59	-3.50	-3.37	-3.51	-3.50
O^{++}	-5.13	-5.00	-4.52	-5.10	-5.02	-5.13	-4.96	-4.51	-5.08	-5.01
S^+	-5.66	-5.48	-5.46	-5.62	-5.70	-5.65	-5.47	-5.45	-5.61	-5.69
S^{++}	-5.38	-5.39	-5.55	-5.37	-5.24	-5.39	-5.39	-5.54	-5.36	-5.25
N^+	-4.38	-4.36	-4.36	-4.35	-4.37	-4.37	-4.34	-4.32	-4.33	-4.35
Cl^+	-7.14	-7.02	-7.00	-7.16	-7.22	-7.14	-7.02	-7.00	-7.16	-7.22
Cl^{++}	-7.24	-7.30	-7.35	-7.21	-7.14	-7.24	-7.29	-7.21	-7.20	-7.14
Ar^+	-7.00	-6.96	-6.51	-6.96	-6.32	-7.00	-6.92	-6.49	-6.96	-6.29

TABLE 7.7 — Nebular abundances in units of $\log(X^m/\text{H}^+)$.

As pointed out by Rodríguez (1999), the spectra of M43 are greatly affected by dust-scattered stellar light, in such a way that some He I lines are completely swallowed up by the stellar absorption. Therefore, only a lower limit to the He^+ abundance was obtained from the least affected He I lines $\lambda 5876$ and $\lambda 6678$ ($\text{He}^+/\text{H}^+ > 0.015$).

7.5 Photoionization models

The main purpose of the study presented in this chapter is to reproduce the various observational constraints available for M43 using photoionization models. The spectroscopic information resulting from five slit sections, located at different distances to the stellar ionizing source, along with the photometric information derived from narrow band imagery will be compared with the output of photoionization models with different characteristics. Some spherical models have been calculated with version 96.01 of `CLOUDY`, last described by Ferland et al. (1998). The main characteristics of this code are summarized in Chapter 4. The pseudo-3D photoionization code `CLOUDY-3D` (C. Morisset, private communication) has also been used to compare results from spherical and blister type geometries.

In Section §7.2, the stellar parameters of the ionizing source of M43 have been obtained through the analysis of the optical spectrum of the star, and its spectral energy distribution has been modeled. Information about the nebular physical characteristics and abundances has been derived in Section §7.4 from the nebular spectrum. In this section, all this information is used as input of the photoionization models.

7.5.1 Characteristics and input of the models

GEOMETRY AND DENSITY DISTRIBUTION

Two possible geometries can reproduce the apparent shape of M43 shown by the images: a spherical geometry and a blister-type geometry (see Morisset et al. 2005). Figure 7.12 illustrates these two possibilities. Both cases consider a single ionizing source. The star is embedded inside the nebular material in the spherical case, while this material is illuminated by the star from a certain distance if a blister geometry is considered. Note that the blister-type geometry is not actually a plane-parallel geometry because the ionizing source is not located at infinity, and hence the dilution effect of the stellar flux is important. The free parameters associated with these geometries are the internal radius (R_i) in the spherical case and the minimum distance (d) from the star to the nebular material in the blister case.

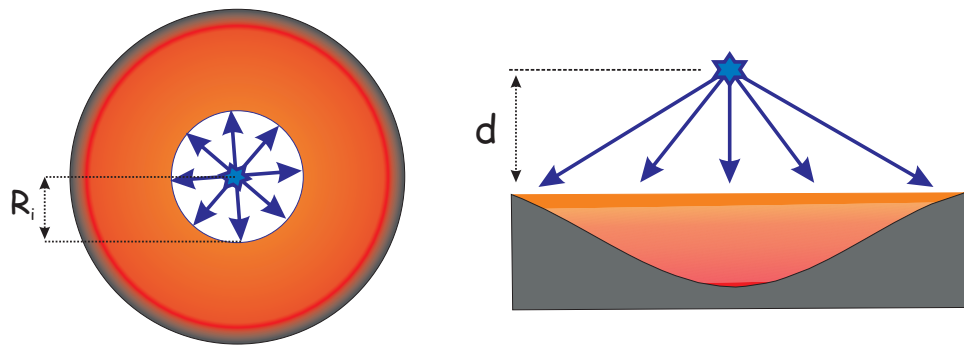


FIGURE 7.12 — Two possible 3D geometries that reproduce the apparently spherical shape of M43. (Left) Spherical model. (Right) Blister model. Red and orange colors represent ionized material; grey color represents molecular material.

The photoionization code `CLOUDY` only allows to consider either spherical or plane parallel geometries. To calculate blister models the code `CLOUDY-3D` will be used .

Two different types of density laws will be assumed for the spherical models in the study performed below: either a constant density or the density law indicated by equation 7.3. For the blister case, only constant density models will be considered.

SPECTRAL ENERGY DISTRIBUTION OF THE IONIZING SOURCE

In Section §7.2, a detailed study of the optical spectrum of HD37061 with the stellar atmosphere code `FASTWIND` has made it possible to derive its stellar parameters and to model the shape of the SED. In addition, a detailed emergent ionizing flux distribution has been obtained using the stellar atmosphere code *WM-basic*.

Table 7.8 summarizes the parameters of the stellar atmosphere models that will be used in the modeling of M43. Note that the best model that results from the spectroscopic analysis of the ionizing star with `FASTWIND` is M2. The stellar luminosity associated with each model has been calculated using the corresponding SED and a $M_v = -3.5$.

Following the procedure indicated in Chapter 4, the spectral energy distributions have been translated to the input format required by `CLOUDY`.

Label	M1	M2	M3
$T_{\text{eff}}(\text{K})$	31000	32000	33000
$\log g$	4.0	4.1	4.1
$\log L/L_{\odot}$	4.49	4.54	4.56
$\log Q(\text{H}^0)$	47.15	47.37	47.54

TABLE 7.8 — *WM-basic* models considered for the ionizing source in the modeling of M43.

STOPPING CRITERIA

Two stopping criteria are considered in `CLOUDY` spherical models: $T_e(\text{min}) = 4000 \text{ K}$ and $R_{\text{ext}} = 0.28 \text{ pc}$. The calculation will stop when the first one is met.

NEBULAR ABUNDANCES

Table 7.9 summarizes the abundances considered in all the models (with the exception of those with enhanced or depleted abundances). These are calculated from the mean values of the results obtained for the different slit positions (see Section §7.4). Only oxygen, nitrogen, sulfur, argon and iron abundances can be directly derived from the M43 INT+IDS nebular spectrum, so for C and Ne, Orion nebula abundances will be considered (Esteban et al. 2004). Since only a lower limit to the He abundance can be derived from the M43 spectra, the abundance derived by Esteban et al. (2004) for the Orion nebula will also be considered as a standard value for this element. These are not very crucial decisions, since some previous test have shown that varying the abundances of elements other than O, N and S does not affect the ionization structure resulting from the models (even if the logarithmic abundances are varied in ± 0.3 dex).

M43						M42		
N	O	S	Ar	Cl	Fe	He	C	Ne
-4.36	-3.56	-5.16	-6.65	-6.87	-5.91	-1.01	-3.58	-4.22

TABLE 7.9 — Nebular abundances considered in the photoionization models. M42 nebular abundances by Esteban et al. (2004) have been considered for He, C and Ne. Iron abundance from Rodríguez (2002)

7.5.2 Observational constraints and strategy

Table 7.10 summarizes the observational constraints that will be used to compare with the output predicted by the photoionization codes. Along with the global constraints (R_{neb} , $L_{\text{H}\alpha}$, and the surface brightness profiles in $\text{H}\alpha$, $[\text{S II}] \lambda\lambda 6717 + 6731$ and $[\text{O III}] \lambda 5007$ lines), other interesting constraints result from various line intensity ratios. These are, the temperature and density constraints $T_e[\text{N II}] 5755/6584$, $N_e[\text{S II}] 6731/6716$ and $N_e[\text{Cl III}] 5538/5518$; the ratio of lines from different ionization states of the same element ($[\text{S III}] / [\text{S II}]$, $[\text{Cl III}] / [\text{Cl II}]$, and $[\text{O III}] / [\text{O II}]$); and the line intensity from different ions relative to $\text{H}\alpha$, $\text{H}\beta$ or Pa12.

Following the procedure indicated in Chapter 4 (Section §4.5.2), the volume emissivities predicted by the CLOUDY models as function of depth into the cloud are used to derive quantities directly comparable with the observational constraints.

COMMENTS ON THE NEBULAR CONSTRAINTS

The H_α surface brightness constraint has been presented in Figure 7.9. Normalized [S II] and [O III] surface brightness profiles are shown in Figure 7.10. The remaining constraints are presented in Figures 7.13 to 7.15. In these Figures, stars show the observed values for the line ratios in the various slit positions, with vertical lines representing their uncertainties and horizontal lines, the size of the slits. Note that the order of the slit sections is M43-4, M43-5, M43-1, M43-2, M43-3³, according to increasing projected distance from the star to the center of the slit section (see Figure 2.5 in Chapter 2).

Some comments on the spectroscopic nebular constraints are presented below:

- Slit position M43-5 is located on a region where the H_α surface brightness is locally enhanced (see Figure 2.5 in Chapter 2). Figure 7.13 shows that the density inferred from the $N_e[\text{S II}]$ indicator is larger for this position, a fact that explains the higher S_{H_α} .
- The ionization degree indicated by the ionization structure constraints for position M43-4 is smaller than the one associated with the slit position M43-5 (see Figure 7.14). Additionally, $\text{He I } \lambda 6678/H_\alpha$ line ratio is smaller for position M43-4 than M43-5 (Figure 7.15). Due to the fact that the distances of these two slits to the star are quite similar, it would be expected that both positions have similar values for the ionization structure constraints and the $\text{He I } \lambda 6678/H_\alpha$ line ratio. Note however that slit position M43-4 is located toward the west of HD 37061, while M43-5 is located toward the east. This effect may be explained by the fact that M42-4 is located close to the foreground dark lane of dust. Additionally, it may be indicating the presence of inhomogeneities in the nebula, or even that the nebula is not actually spherically symmetrical.
- The value of the line ratios $\text{He I } \lambda 6678/H_\alpha$, $[\text{O III}] \lambda 5007/H_\beta$ and $[\text{Cl III}] \lambda 5518/H_\beta$ for M43-3 do not follow the extrapolated behavior from the rest of the slit sections. While it is expected that the intensity of lines $\text{He I } \lambda 6678$, $[\text{O III}] \lambda 5007$ and $[\text{Cl III}] \lambda 5518$ decrease with increasing distance to the ionizing star, the values of these line ratios for M43-3 are too high compared to those associated with the other slit positions. This may suggest that the nebular emission in these lines could be contaminated by the contribution of the Orion nebula (see also Section §7.3).

³This nomenclature follows the original identification labels presented in Rodríguez (1999).

NEBULAR OBSERVATIONAL CONSTRAINTS					
GLOBAL MORPHOLOGICAL AND PHOTOMETRIC CONSTRAINTS					
Apparently spherical geometry					
$R_{\text{neb}} = 0.28 \pm 0.04$ pc					
$L_{\text{H}\alpha} = (3.0 \pm 0.8) \times 10^{35}$ erg s ⁻¹					
H α , [S II] and [O III] surface brightness profiles					
Slit section	M43-4	M43-5	M43-1	M43-2	M43-3
TEMPERATURE AND DENSITY CONSTRAINTS					
[N II] 5755/6584	6.8×10^{-3}	6.9×10^{-3}	7.3×10^{-3}	7.3×10^{-3}	7.4×10^{-3}
[S II] 6731/6716	1.008	1.038	1.005	1.000	1.012
[Cl III] 5538/5518	0.63	0.75	0.75	0.73	0.44
IONIZATION STRUCTURE CONSTRAINTS					
[S III] λ 6312 / [S II] λ 6731	0.023	0.036	0.024	0.016	0.011
[Cl III] λ 5518 / [Cl II] λ 8579	0.65	0.77	0.58	0.41	0.54
[O III] λ 5007 / [O II] λ 7325	2.61	2.89	2.57	3.07	6.23
ABUNDANCE CONSTRAINTS ⁽¹⁾					
He I λ 6678 / H α	0.070	0.338	0.08	0.063	0.24
[S II] λ 6731 / H α	8.42	6.966	8.23	12.39	13.21
[S III] λ 6312 / H α	0.19	0.25	0.20	0.20	0.14
[O I] λ 6300 / H α	0.6	0.46	0.61	0.94	1.96
[O II] λ 7325 / Pa12	321	334	326	387	550
[O III] λ 5007 / H β	8.98	10.92	8.88	13.07	37.6
[N II] λ 6584 / H α	39.64	37.60	38.64	41.45	41.9
[Cl II] λ 8579 / Pa12	37.0	31.9	39.2	53.9	57.0
[Cl III] λ 5518 / H β	0.259	0.28	0.237	0.22	0.344

TABLE 7.10 — Nebular observational constraints used to be compared with the predictions of the photoionization models. The position of the different slit sections is shown in Figure 2.5 (Chapter 2). Note that the order of the slits has been changed according to their projected distance to the ionizing star. ⁽¹⁾ Normalized to H α = 100, H β = 100 or Pa12 = 100. It has been decided to present the line ratios relative to H α , H β or Pa12, depending on the spectral range in which the line is located, in order to minimize possible errors related to the extinction correction.

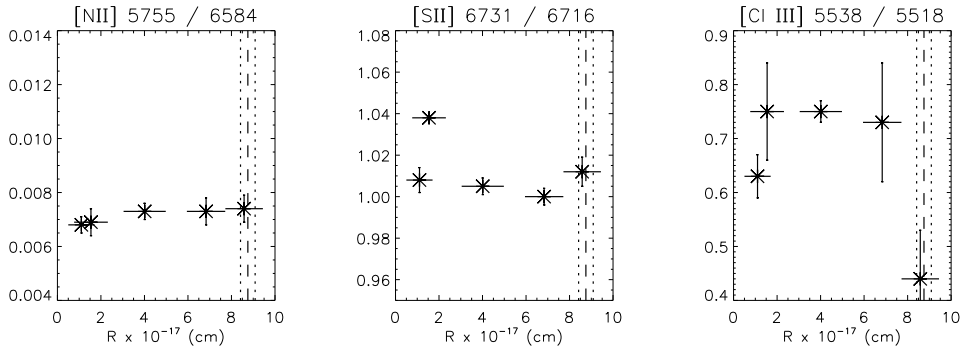


FIGURE 7.13 — Temperature and density constraints. Vertical dashed line represents the nebular size constraint. The observed values for the line ratios in the various slit positions are shown as \times , with vertical lines representing their uncertainties and horizontal lines, the size of the slits. Note that the order of the slit sections, according to increasing projected distance from the star, is M43-4, M43-5, M43-1, M43-2, M43-3

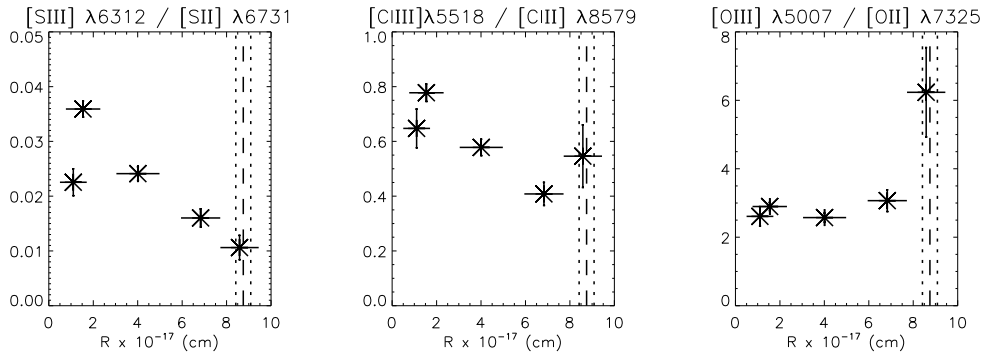


FIGURE 7.14 — The same as in Figure 7.13 but for the ionization structure constraints.

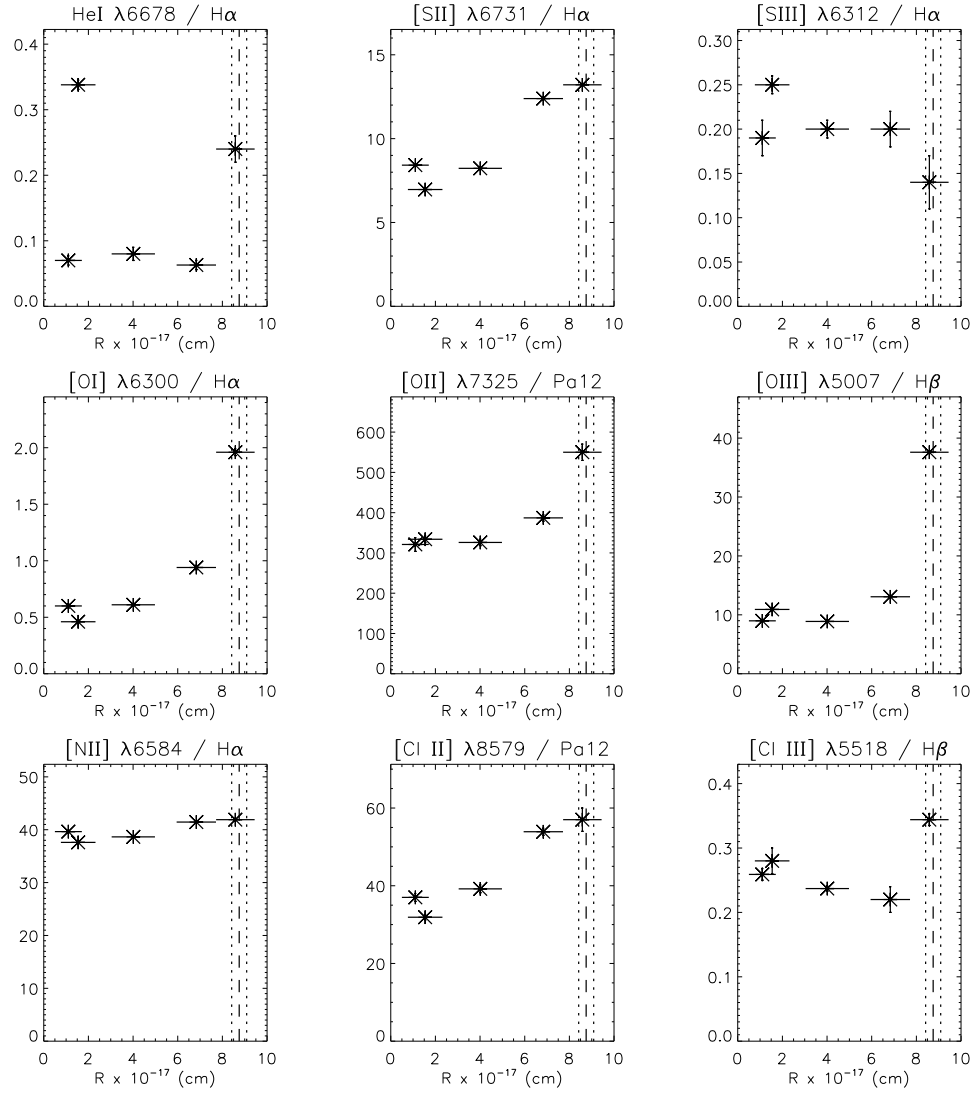


FIGURE 7.15 — The same as in Figure 7.13 but for the abundance constraints. Values for the various line ratios have been normalized to $H_\alpha = 100$, $H_\beta = 100$ or $Pa12 = 100$.

7.5.3 Spherical constant density models

The first photoionization models that will be considered for M43 are constant density models with spherical symmetry. The constant density assumption is reinforced by the information provided by the $N_e[\text{S II}]$ indicator, which indicates roughly the same density for the different slit positions.

A first set of CLOUDY spherical models was calculated with $N(\text{H}) = 600, 550$ and 500 cm^{-3} . The other inputs considered in these models were: the *WM-basic* spectral energy distribution for the model M2 indicated in Table 7.8, an internal radius of 10^{-3} pc and the set of nebular abundances summarized in Table 7.9. Finally, these models do not include dust grains.

In Figure 7.16, the output of the models for the density and temperature indicators are compared with the corresponding observed constraints. From these plots it can be pointed out:

- The model with $N(\text{H}) = 550 \text{ cm}^{-3}$ is the one that better fits the $N_e[\text{S II}]$ indicator. Note that the density inferred from slit positions M43-3 and M43-5 is $\sim 50 \text{ cm}^{-3}$ larger than the value derived from the remaining ones. This may be related to local density inhomogeneities.
- From the $N_e[\text{Cl III}]$ indicator, a somewhat lower density is inferred, although a $N(\text{H}) = 550 \text{ cm}^{-3}$ is acceptable within the uncertainties. Slit positions M43-3 and M43-4 produce extremely low $N_e[\text{Cl III}]$ values. A similar result was previously found in the nebular spectroscopic analysis (see Section §7.4).
- Although the $T_e[\text{N II}]$ constraint is fitted for the inner slit positions, the values predicted by the models for the outer ones is too high. This behavior of the apparent T_e for the models is intrinsically associated with the fact that these are ionization bounded spherical models. At larger distances from the star, the spectrum of the ionizing radiation becomes harder by absorption in the nebula; the radiation nearest the series limit is most strongly attenuated because of the frequency dependence of the absorption coefficient. Therefore, the higher energy photons penetrate further into the gas, and the mean energy of the photoelectrons produced at larger distances from the star is higher. As a consequence, in a spherical nebula, the apparent T_e to be higher at larger projected distances from the star.

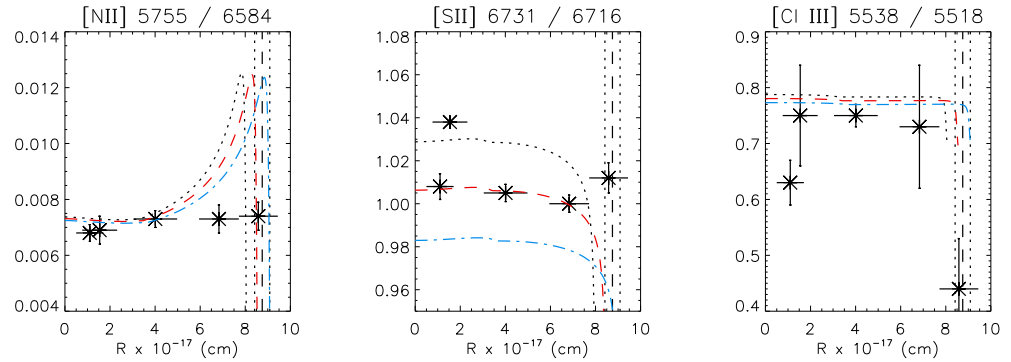


FIGURE 7.16 — Temperature and density constraints. Three constant density spherical models with different densities are compared. Dotted black, dashed red and dot-dashed blue curves correspond to $N(\text{H}) = 600, 550$ and 500 cm^{-3} respectively. The model with $N(\text{H}) = 550 \text{ cm}^{-3}$ is the one that better fits the observed $N_e[\text{S II}]$ constraint.

Figure 7.17 shows a comparison of the $\text{H}\alpha$, $[\text{O III}]$ and $[\text{S II}]$ surface brightness profiles predicted by these models. The $S_{\text{H}\alpha}$ constraint has also been plotted for comparison. Since $[\text{O III}]$ and $[\text{S II}]$ images have not been flux calibrated (see Chapter 2), only the shape of the surface brightness profiles can be used as constraint. As expected, the surface brightness profiles resulting from the models do not fit the observations (neither $S_{\text{H}\alpha}$ nor $S_{[\text{S II}]}$). This is an important deficiency of the constant density models. Nevertheless, following the suggestion presented in Figure 7.9, which shows that the outer part of the $\text{H}\alpha$ surface brightness profile can be fitted assuming $N(\text{H}) = 420 \text{ cm}^{-3}$, the constant density assumption will be further explored. Spherical models with a non-constant density distribution will be considered in a forthcoming section.

The model with $N(\text{H}) = 550 \text{ cm}^{-3}$ predicts the outer part of the $\text{H}\alpha$ surface brightness profile to be higher than the observed constraint. One can try to diminish this $S_{\text{H}\alpha}$ by considering a lower $Q(\text{H}^0)$. This can be achieved either by assuming a ionizing star with lower T_{eff} or a lower stellar luminosity, however both options would result in a smaller nebula. A filling factor smaller than 1 would be needed in this case to enlarge the modeled nebular size to fit the observations. Alternatively, a model with the original stellar properties and a filling factor smaller than 1 can be considered. This model requires a density bounded nebula (i.e some ionizing photons escape from the nebula). Finally, a similar result can be achieved considering a covering factor smaller than 1.

Figure 7.18 compares results from three models. All these models assumes a constant density $N(\text{H}) = 550 \text{ cm}^{-3}$, along with the same stellar properties than the previous

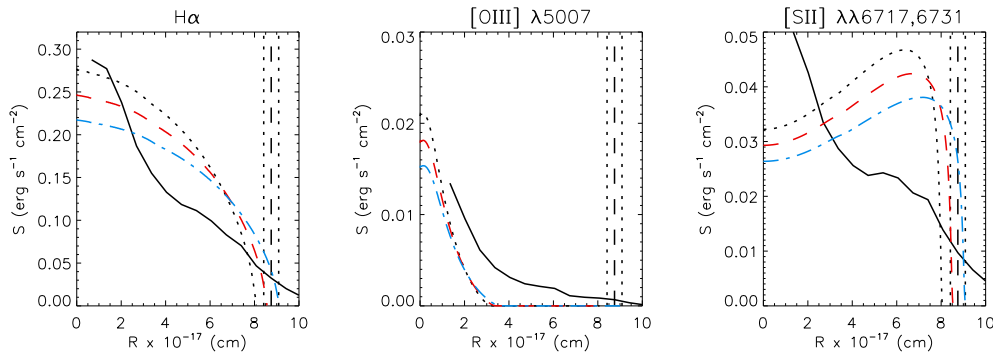


FIGURE 7.17 — $H\alpha$, $[O\text{ III}]\lambda 5007$ and $[S\text{ II}]\lambda\lambda 6717,6731$ surface brightness constraints. Black solid lines: observed surface brightness profiles; note that the $[O\text{ III}]$ and $[S\text{ II}]$ observed profiles have been normalized to a maximum value of 0.013 and 0.05, respectively. Three constant density models with different densities are compared (see comments on Figure 7.16). The $H\alpha$ surface brightness predicted by the model with $N(\text{H}) = 550\text{ cm}^{-3}$ is larger than the observed value

models. The first model is one considered previously (i.e. $\epsilon = 1$, $cf = 1$, and ionization bounded); the second one assumes a filling factor $\epsilon = 0.6$ and a $R_{\text{neb}} = 0.28\text{ pc}$. Finally, the third model considers a covering factor $cf = 0.6$ and no filling factor. Physically, the second model represents a sphere with a clumpy distribution of nebular material; the nebula is density bounded in all directions ($\sim 40\%$ of the ionizing photons are escaping from the nebula). Although in the model with covering factor $\sim 40\%$ of the ionizing photons are also escaping, the situation is different. In this case only $\sim 40\%$ of the nebula is density bounded. This model may be equivalent to a slab of nebular material ionized by a star located just in the edge of the nebula that is closer to the observer. This model is similar to the one that will be considered in Section §7.5.5 having a blister type geometry.

Both models, either with filling factor or covering factor fit perfectly the outer part of the $S_{H\alpha}$ profile (Figure 7.18). However, an this is an interesting point, the model with filling factor less than 1 does not reproduce the $[S\text{ II}]\lambda\lambda 6731/6716$ density constraint. This result can be easily explained taking into account that the value of a line ratio at a given projected distance to the star (R) is determined by the contributions of the part of the nebular material intersected by the line of sight passing through this point. In a density bounded nebula, the high energy ionizing photons are escaping before producing the strong heating of the material located in the ionization front, and hence a smaller "mean" $T_e(R)$ is achieved. The $N_e[S\text{ II}]$ indicator varies consequently, since for a given density, the smaller the value of the $[N\text{ II}]\lambda\lambda 5755/6584$ line ratio, the larger the value of the $[S\text{ II}]\lambda\lambda 6731/6716$ line ratio.

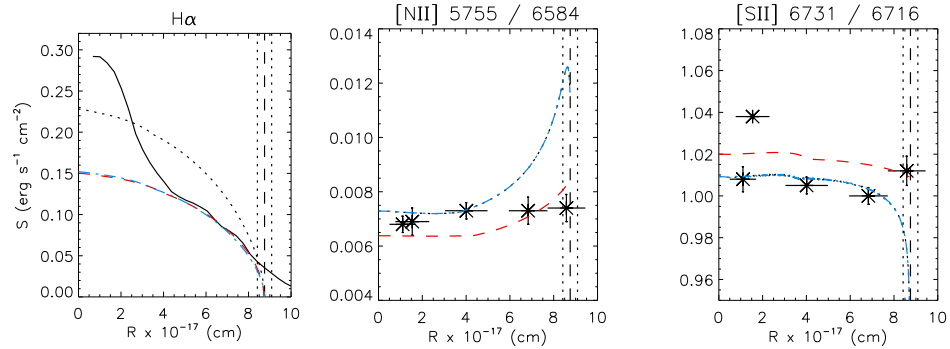


FIGURE 7.18 — $H\alpha$ surface brightness, temperature and density constraints. Three constant density spherical models with $N(\text{H}) = 550 \text{ cm}^{-3}$ and different values for the filling factor (ϵ) and covering factor (cf) are compared. Black dotted lines: $\epsilon = 1$, $cf = 1$; red dashed lines: $\epsilon = 0.6$, $cf = 1$; blue dash-dotted lines: $\epsilon = 1$, $cf = 0.6$. The dotted and dash-dotted lines are overlapped in the $[\text{N II}] 5755/6584$ and $[\text{S II}] 6731/6716$ diagrams.

In the case of the model with covering factor, this effect does not occur because the nebula is not totally density bounded and hence a ionization front is still formed (though some ionizing photons are also escaping in this model). This model has a higher "mean" T_e than the previous model, due to the presence of the ionization front in the ionization bounded part of the nebula.

Obviously, these models do not fit the total nebular $L_{H\alpha}$ constraint. This is due to the fact that the inner part of the nebula, with the largest $S_{H\alpha}$ is not being considered.

Having the deficiencies of the spherical constant density models in mind (namely, the fact that it is not possible to reproduce the shape of the whole $S_{H\alpha}$ profile, and to fit the $T_e[\text{N II}]$ constraint for the outer slit positions), it can be concluded that the best fit to the density and surface brightness constraints is achieved by the photoionization model with $N(\text{H}) = 550 \text{ cm}^{-3}$ a covering factor of 0.6, and a filling factor of 1. Figures 7.19 and 7.20 show the predictions of this model for the other observational constraints. The agreement between both model and observations is surprisingly good for most of the constraints.

IONIZATION STRUCTURE CONSTRAINTS

Figure 7.19 shows the comparison between the line intensity ratios indicating the ionization structure of the nebula and the predictions of a constant density spherical model with $N(\text{H}) = 550 \text{ cm}^{-3}$, $cf = 0.6$ and $\epsilon = 1$. The agreement is quite good for the $[\text{S III}]/[\text{S II}]$ line ratio. In the other two constraints the model predictions depart from the observed values in the outer slit sections. This could be explained if it is considered that the emission of M43 in $[\text{Cl III}] \lambda 5518$ and $[\text{O III}] \lambda 5007$ lines is contaminated by the contribution of the Orion nebula (see Section §7.5.2 and comment below). Note that the ionization degree indicated by the slit section that is closer to the star is too small compared to the predicted value.

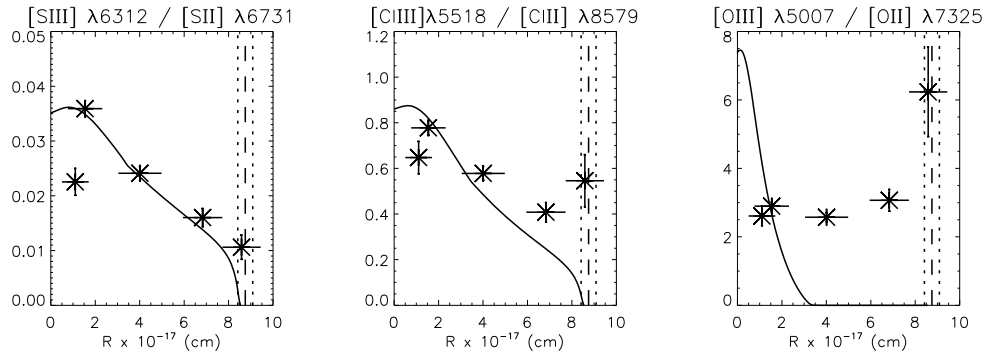


FIGURE 7.19 — Comparison between the line intensity ratios indicating the ionization structure of the nebula and the predictions of constant density spherical models with $N(\text{H}) = 550 \text{ cm}^{-3}$, $cf = 0.6$ and $\epsilon = 1$.

ABUNDANCE CONSTRAINTS

Figure 7.20 shows the comparison between different observed line intensity ratios and the predictions of the previous model. Again, the agreement is quite good for most of the cases, however there are some interesting points to comment:

- The discrepancy found in the apparent T_e for the outer slit sections is also appearing here. Since the intensity of the collisionally excited lines is very dependent of the temperature, and a higher apparent T_e is predicted by the models, the resulting line intensity for these lines is higher than the observed ones.

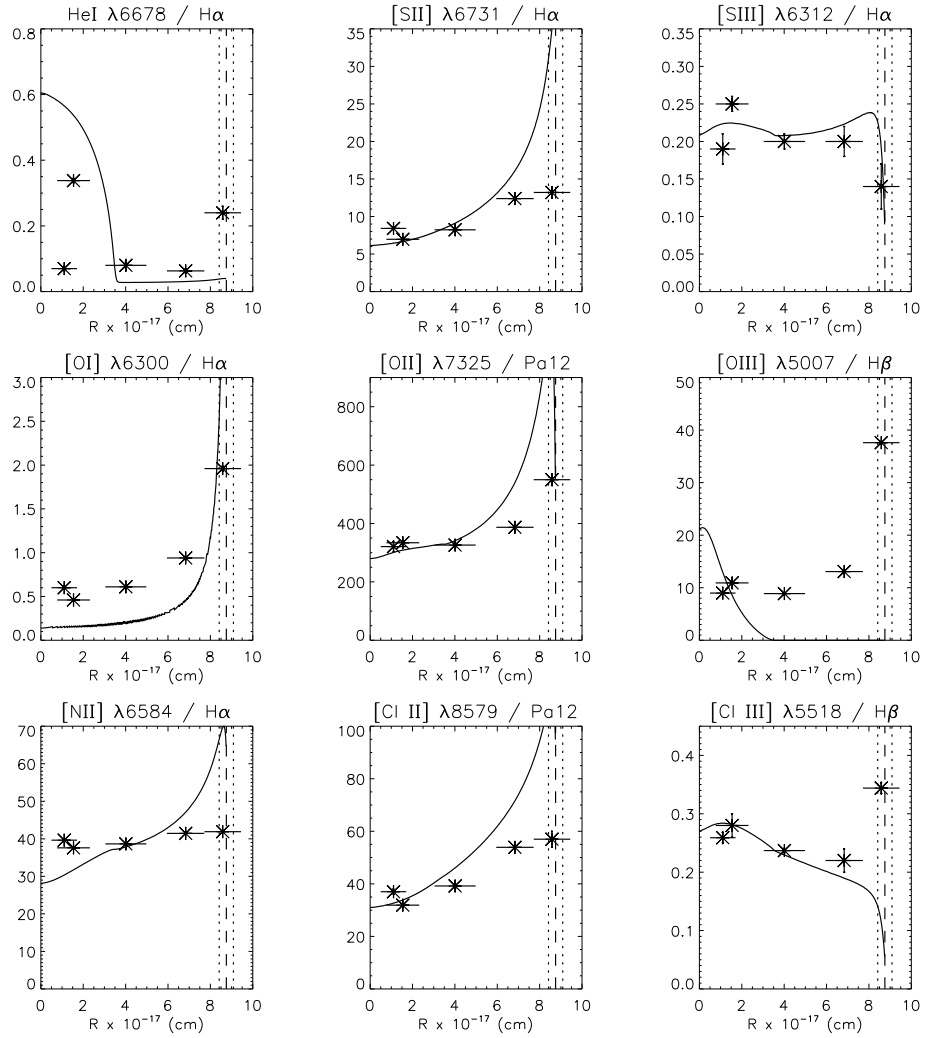


FIGURE 7.20 — Comparison between different observed line intensity ratios and the predictions of constant density spherical models with $N(H) = 550 \text{ cm}^{-3}$, $cf = 0.6$ and $\epsilon = 1$.

- It is clear from the $[\text{O III}] \lambda 5007 / \text{H}_\beta$, $[\text{Cl III}] \lambda 5518 / \text{H}_\beta$ and $\text{He I } \lambda 6678 / \text{H}_\alpha$ diagnostic diagrams that there is some external emission affecting the outer slit sections.
- The size of the He Strömberg sphere is well reproduced by the model, however the predicted $\text{He I } \lambda 6678 / \text{H}_\alpha$ line intensity in the inner part of the nebula is too large compared to the observations. Note also comment on the inner slit section in Section §7.5.2.

MODELS WITH MODIFIED STELLAR PARAMETERS

To illustrate the effect of the stellar parameters on the ionization structure of the nebula, three stellar atmosphere models with different effective temperature ($T_{\text{eff}} = 31, 32$ and 33 kK) have been considered as input of CLOUDY. The characteristics of these models have been summarized in Table 7.8. The nebular density has been fixed to a constant value $N(\text{H}) = 550 \text{ cm}^{-3}$, and a covering factor of 0.6 has been assumed.

For a meaningful comparison, the photoionization models have been treated to reproduce the same R_{neb} : a certain filling factor has been considered for the model with $T_{\text{eff}} = 31000$ K; the model with $T_{\text{eff}} = 33000$ K produces a nebular size that is too large, so the R_{neb} stopping criterion has been considered.

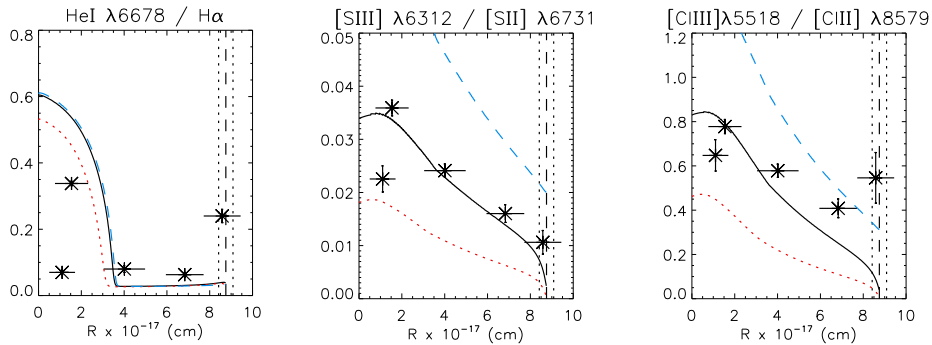


FIGURE 7.21 — Comparison between the line intensity ratios indicating the ionization structure of the nebula and the predictions of constant density spherical CLOUDY models. Three stellar atmosphere models with different effective temperatures, $T_{\text{eff}} = 31000, 32000$ and 33000 K (dotted red, solid black, and dashed blue lines, respectively) have been considered as input of the photoionization code

Figure 7.21 shows the $\text{He I } \lambda 6678 / \text{H}\alpha$, $[\text{S III}] \lambda 6312 / [\text{S II}] \lambda 6731$ and $[\text{Cl III}] \lambda 5518 / [\text{Cl II}] \lambda 8579$ diagrams. These constraints allow to discriminate between models with different stellar effective temperature. No final conclusion can be derived from the $\text{He I } \lambda 6678 / \text{H}\alpha$ diagram. However, the other two diagrams are clearly illustrative. The model that considers a star with $T_{\text{eff}} = 32000$ K fits very well the $[\text{S III}] \lambda 6312 / [\text{S II}] \lambda 6731$ and $[\text{Cl III}] \lambda 5518 / [\text{Cl II}] \lambda 8579$ observed line ratios for the different slit positions (note however the previous comment on the values for the slit positions M43-3 and M43-4, the outer and inner ones respectively). The radiation strength of the star with $T_{\text{eff}} = 33000$ K is too hard and the one corresponding to a star with $T_{\text{eff}} = 31000$ K is too soft. This result is in perfect agreement with the one derived from the analysis of the optical HHe spectra of the ionizing star (see Section §7.2).

MODELS WITH MODIFIED NEBULAR ABUNDANCES

A set of models with modified nebular abundances was generated to study the effect of the abundance of certain elements on the physics of the nebula. The main conclusions of this study are presented below:

- A variation of ± 0.1 dex in the He abundance does not affect the structure of the nebula. Among all the considered constraints, only the $\text{He I } \lambda 6678 / \text{H}\alpha$ line ratio is modified (see Figure 7.22). The other nebular constraints remain unaffected. The best fit is achieved for $\log(\text{He}/\text{H}) = -1.11$. However we consider this value very uncertain since it is based in only one point. Note that this is somewhat larger than the lower limit to the He^+ / H^+ abundance given by Rodríguez (1999), $\log(\text{He}^+ / \text{H}^+) > -1.82$.

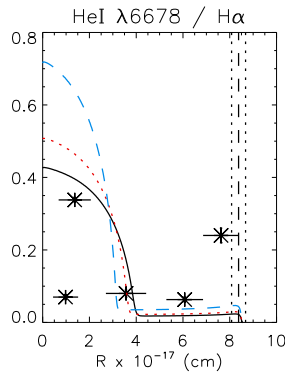


FIGURE 7.22 — Comparison between observational constraints and constant density spherical CLOUDY models with different He abundances. Solid black line: $\log(\text{He}/\text{H}) = -1.11$; dotted red line: $\log(\text{He}/\text{H}) = -1.01$; dashed blue line: $\log(\text{He}/\text{H}) = -0.91$.

- A similar result was found when a variation of ± 0.2 dex was considered in certain elements (viz. Cl, Ar, Fe, Ne, C). Figure 7.23 illustrate the effect of varying the Cl abundance on the ionization structure constraints. The higher the Cl abundance, the larger the $[\text{Cl II}] \lambda 8579 / \text{Pa}12$ and $[\text{Cl III}] \lambda 5518 / \text{H}\beta$ line ratios, however the $[\text{Cl III}] / [\text{Cl II}]$ line ratio is not affected by changes in the Cl abundance.
- There are certain elements (O, N, S) which abundance also affect the physical properties of the nebula. These are the main cooling elements of the nebula. The thermal losses due to the emission of collisionally excited lines of these elements have an effect on the temperature of the nebula and hence on the intensity ratios of all the collisional lines. As it is known, the intensity ratios of recombination lines are almost independent of temperature, and hence the $\text{H}\alpha$ emission and the $\text{He I } \lambda 6678 / \text{H}\alpha$ line ratio are only slightly affected. Figures 7.24 and 7.25 illustrate the effect of a change of ± 0.2 dex in the S abundance.
- The best fit to the S, O, N and Cl observational abundance constraints, as well as the other considered constraints, is achieved for the set of abundances indicated in Table 7.9. Note comment below on the Cl II atomic data considered by CLOUDY.

From this study it can be concluded that the agreement found between the S, O, N and Cl nebular abundances derived through the standard spectroscopic analysis of the nebular spectrum and by means of photoionization modeling is quite good.

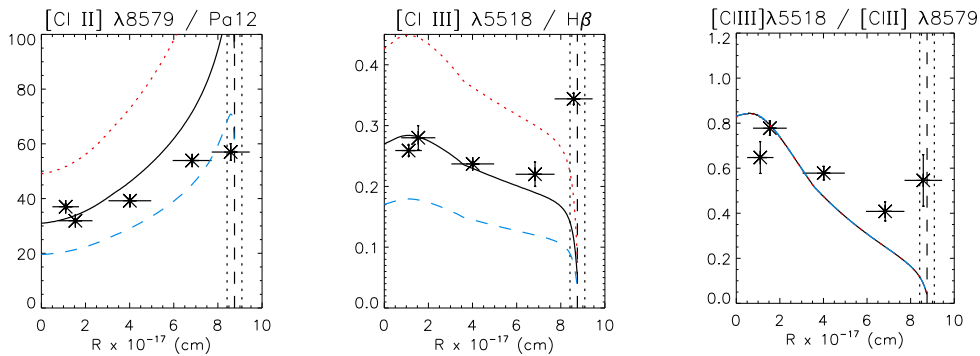


FIGURE 7.23 — Comparison between observational constraints and constant density spherical CLOUDY models with different Cl abundances. Solid black line: $\log(\text{Cl}/\text{H}) = -6.87$; dotted red line: $\log(\text{Cl}/\text{H}) = -6.67$; dashed blue line: $\log(\text{Cl}/\text{H}) = -7.07$.

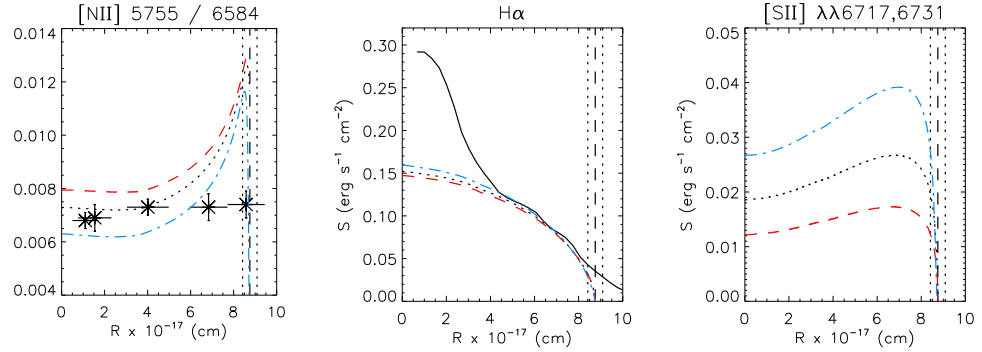


FIGURE 7.24 — Comparison between observational constraints and constant density spherical CLOUDY models with different S abundances. Solid black lines: $\log(S/H) = -5.36$; dotted red lines: $\log(S/H) = -4.96$; dashed blue lines: $\log(S/H) = -5.16$.

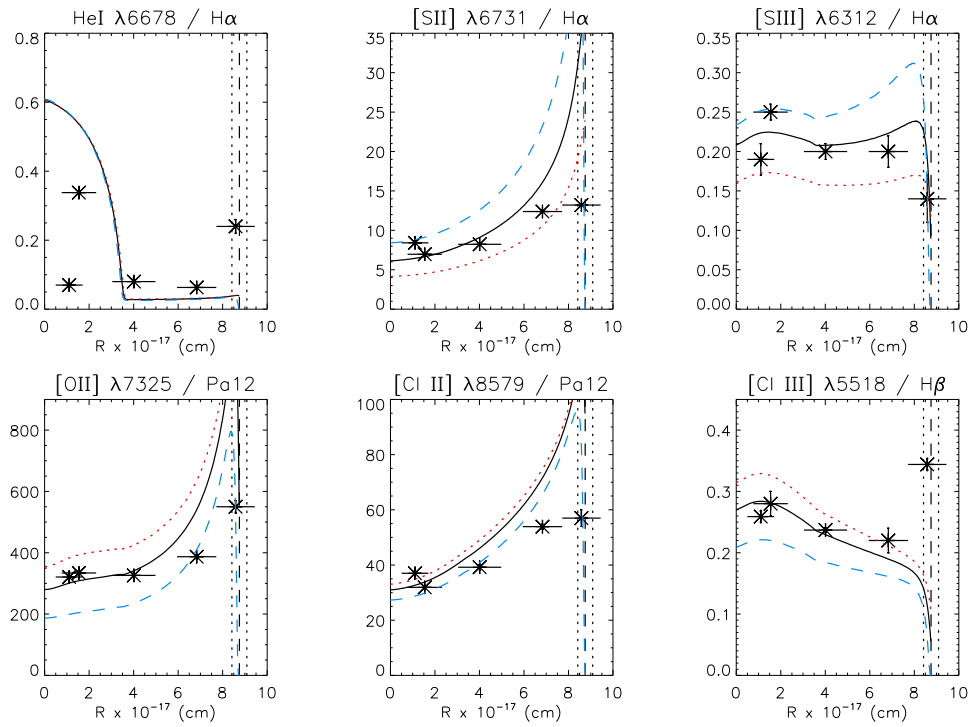


FIGURE 7.25 — The same than in Figure 7.24 but for other spectroscopic constraints.

NOTE ABOUT THE ATOMIC DATA CONSIDERED IN CLOUDY FOR ClII

In the first approaches to the study presented here, it was found that although the best constant density model with spherical symmetry fitted very well the $[S\text{III}]/[S\text{II}]$ constraint, the other ionization structure constraint $[Cl\text{III}]/[Cl\text{II}]$ was not properly fitted (the model produced lower values for this line ratio). Additionally, although the $[Cl\text{III}]/H\beta$ line ratio was fitted, the corresponding model produced too large values for the $[Cl\text{II}]/Pa12$ line ratio. This problem has been solved by changing the ClII collisional data associated with the transitions involving terms 3P , 1D and 1S (see Figure below) considered in CLOUDY (version 96.01).

The original values considered in CLOUDY are those by Wilson & Bell (2002). A better agreement with the observational constraints is found if these values are changed to those proposed by Mendoza et al. (1983). Table 7.11 compares both sets of ClII atomic data. Figure 7.26 illustrates the effect of the different atomic datasets.

	A_{ij} (s^{-1})	γ_{ij} (WB02)	γ_{ij} (M83)
$^3P_1 - ^1D_2$	0.133	8.389	3.86
$^3P_1 - ^1S_0$	1.33	1.01	1.15
$^1D_2 - ^1S_0$	2.06	1.49	0.456

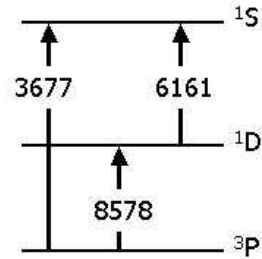


TABLE 7.11 — Atomic data for the ClII transitions indicated in the attached figure. Collisional transitions from Wilson & Bell (2002) and Mendoza et al. (1983).

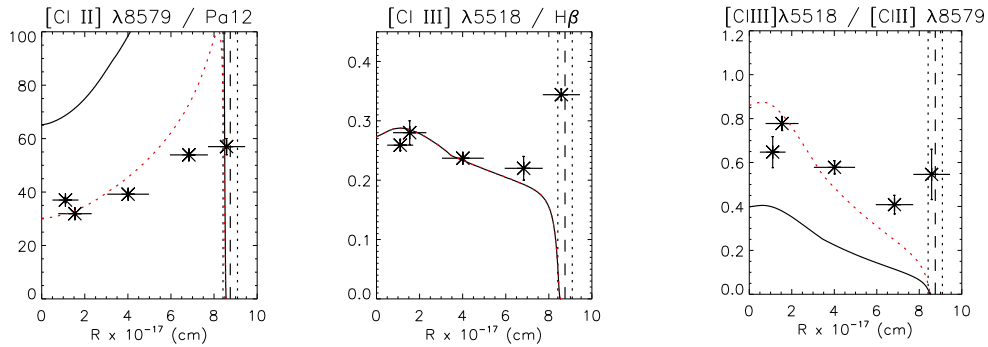


FIGURE 7.26 — Effect of the variation of the ClII collisional data fixing the rest of parameters. Solid line: Wilson & Bell (2002); dotted red: Mendoza et al. (1983)

7.5.4 Density law models

In the previous section it has been shown that although the constant density models fit fairly well the major part of the observational constraints, they have an important deficiency, the observed H_α and [S II] surface brightness profiles are not properly fitted. In Section §7.3.1, a density distribution that reproduces the observed H_α surface brightness profile has been determined for the case of a spherical geometry. This density law, defined by the equation 7.3, has been used as input of CLOUDY to generate spherically symmetric density law models. For these models, the SED corresponding to the stellar atmosphere model M2 has been considered (see Table 7.8). The abundances included in the models are those summarized in Table 7.9.

Figures 7.27 to 7.29 show the diagnostic diagrams for two density law models. The first one assumes the values $A = 480 \text{ cm}^{-3}$, $B = 0.11 \text{ pc}$ and $C = 420 \text{ cm}^{-3}$ for the density law. This model reproduces the H_α surface brightness profile, however predicts too low values for the $N_e[\text{S II}]$ indicator (see Figure 7.28). A second model with enhanced density is hence generated assuming that models that differ in density and filling factor but have the same value of the product $N^2\epsilon$, where ϵ is the volume filling factor, will produce the same H_α surface brightness profile. This second model considers $\epsilon = 0.65$, $A = 595 \text{ cm}^{-3}$ and $C = 520 \text{ cm}^{-3}$.

The first stopping criterion that is reached by these models is the external radius criterion (i.e. these are density bounded models).

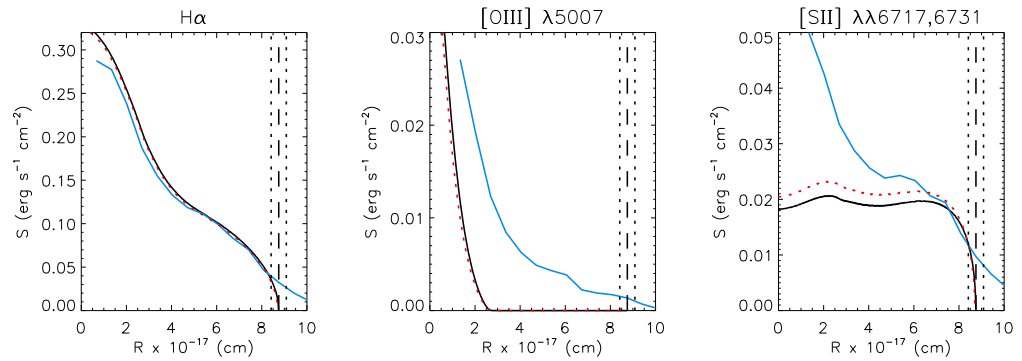


FIGURE 7.27 — Comparison between the observed surface brightness profiles and those predicted by spherical models with a density law (see text). Black solid lines: model with $\epsilon = 1$. Red dotted lines: model with $\epsilon = 0.65$. The product $N^2\epsilon$ remains constant in both models. Blue solid lines: observed surface brightness profiles; note that the [O III] and [S II] observed profiles have been normalized to a maximum value of 0.027 and 0.05, respectively.

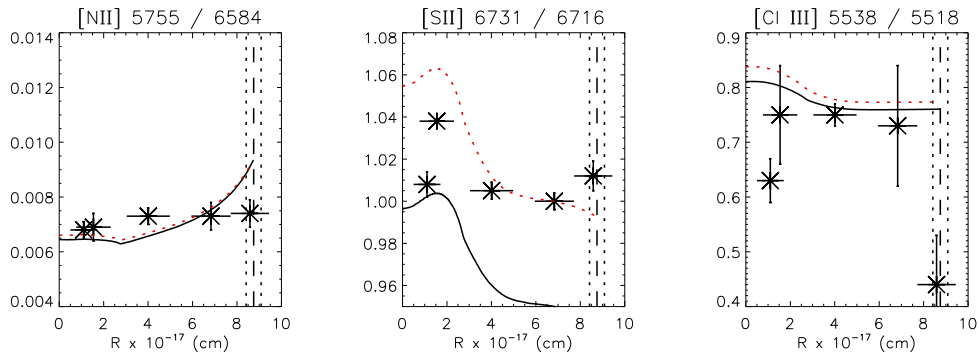


FIGURE 7.28 — The same than in Figure 7.27 but for the temperature and density constraints

These models do not improve the results predicted by the constant density models. Moreover, the agreement with the observations is even worse for some of the constraints (e.g. the ionization degree is too large in the inner part of the nebula, see Figure 7.29). Another interesting result is that the [SII] surface brightness profile is not correctly reproduced either by these models (see Figure 7.27).

These models seem to produce a better agreement with the T_e and abundance observational constraints for the outer slit sections, however this is only an artificial result that is related to the fact that they are density bounded models (see previous section and Figure 7.18). The main deficiency of these models is that they produce too high average ionization for the inner slit sections.

Therefore, although these models reproduce the inner part of the H_α surface brightness profile, they are not fitting correctly the other spectroscopic observational constraints corresponding to this nebular region.

Note that these models consider a density law which was calculated assuming a spherical nebula. However, as it was shown in Section 7.5.1, there are other possible nebular 3D geometries that would produce an apparently spherical nebula. Under the assumption of other type of geometries (e.g. a blister type geometry) the corresponding density distribution that would reproduce the H_α surface brightness distribution may be different.

Following the ideas presented in Morisset et al. (2005), the first steps on the comparison of the observational constraints with a blister type model will be presented in next section.

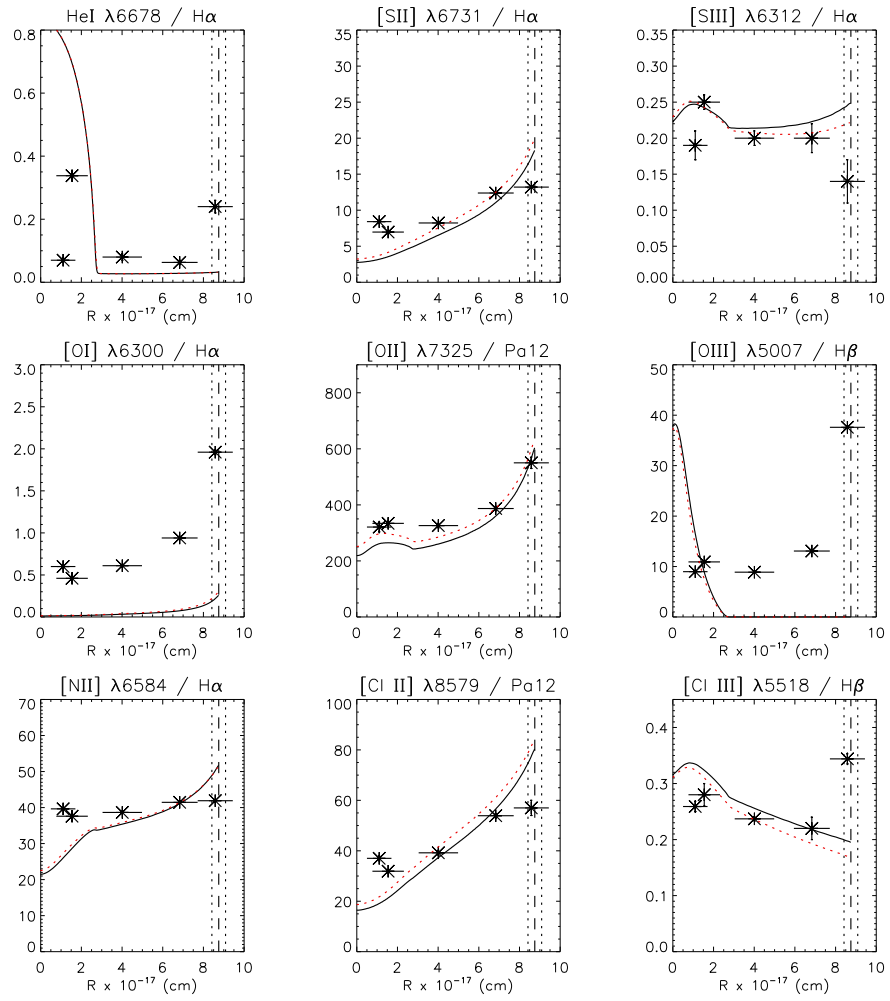


FIGURE 7.29 — The same than in Figure 7.27 but for the abundance constraints

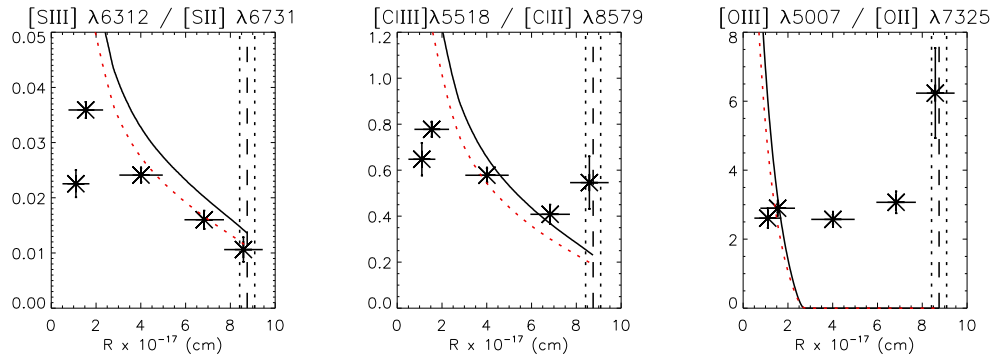


FIGURE 7.30 — The same than in Figure 7.27 but for the ionization structure constraints

7.5.5 Spherical vs. blister models

Morisset et al. (2005) have recently presented a comparison of the apparent physical properties of two photoionization models which, having the same ionizing star and chemical composition, result on the same total $H\beta$ luminosity and surface brightness distribution but have very different geometries. These are a blister model and a spherical model (its spherical impostor). The properties of these two models differ drastically in many respects (e.g. the variation of some "apparent" parameters like the T_e and N_e determined from different line ratios).

The M43 nebula is a perfect observable to test which one of these two possible geometries produce a better fit to a real, very simple $H\text{II}$ region.

In Section §7.5.3 it was shown that a constant density model with spherical symmetry and a covering factor ~ 0.6 (which actually can be assumed to be a blister model with the ionizing star located on the edge of the slab of nebular material) reproduces quite well practically the whole set of observational constraints. However, although this model predicts that the "apparent" electron temperature has to increase with the projected distance to the star, this is not actually observed. This result may be achieved considering a model with a blister type geometry (see Morisset et al. 2005).

Some blister models have been generated with a very recent version of `CLOUDY-3D` (C. Morisset, private communication). The philosophy of this pseudo-3D photoionization code is basically the same as that characterizing `NEBU-3D` (Morisset et al. 2005). It was decided to use `CLOUDY-3D` instead of `NEBU-3D` for a better comparison with the results of the spherical models calculated with `CLOUDY`.

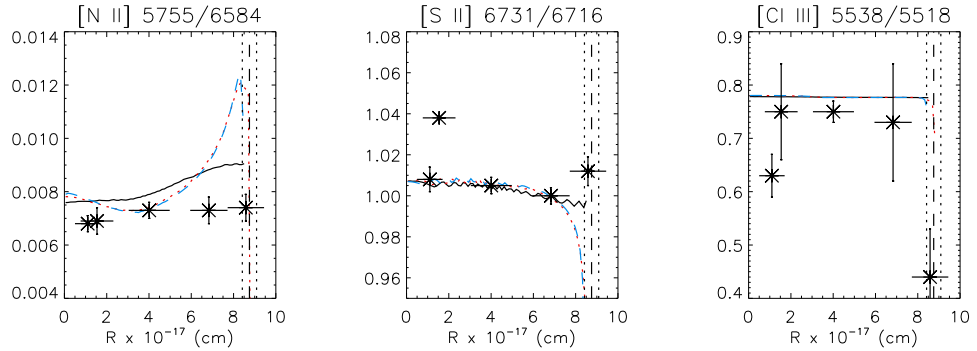


FIGURE 7.31 — Comparison between the observed temperature and density constraints and the predictions of the models considered in Section §7.5.5. Solid black lines: blister model with the star located 0.1 pc to the slab. Red dotted lines: blister model with the star located close to the slab of nebular material. Blue dash-dotted lines: spherical model.

The models assume a constant density $N(H) = 550 \text{ cm}^{-3}$, the spectral energy distribution of the ionizing star predicted by the *WM-basic* model M2 (see Table 7.8), the set of nebular abundances indicated in Table 7.9, and no dust grains.

An important free parameter of the blister models is the distance between the star and the slab (see Figure 7.12). To show the effect of this parameter, two different values have been considered for it: a very small distance (10^{-3} pc) and a distance $d_i = 0.1$ pc.

The diagnostic diagrams for these models are presented in Figures 7.31 and 7.32. The predictions of a spherical model with constant density ($N(H) = 550 \text{ cm}^{-3}$) are also presented for comparison. Note that the Cl II atomic data have not been changed in the version of *CLOUDY* that has been used to calculate these models, therefore the $[Cl II]/Pa12$ line ratios predicted by the models are too large.

The first conclusion that can be emphasized is that a blister model with the star located very close to the slab and a spherical model produce very similar results. When the star is located at a larger distance to the slab the predictions corresponding to some of the nebular spectroscopic constraints are quite different:

- In the blister case, the predicted $T_e[N II]$ is higher than in the spherical case for the inner slits. However the mean $T_e[N II]$ along the nebula is roughly constant, without the large enhancement predicted by the spherical models at the edge of the nebula (Figure 7.31).

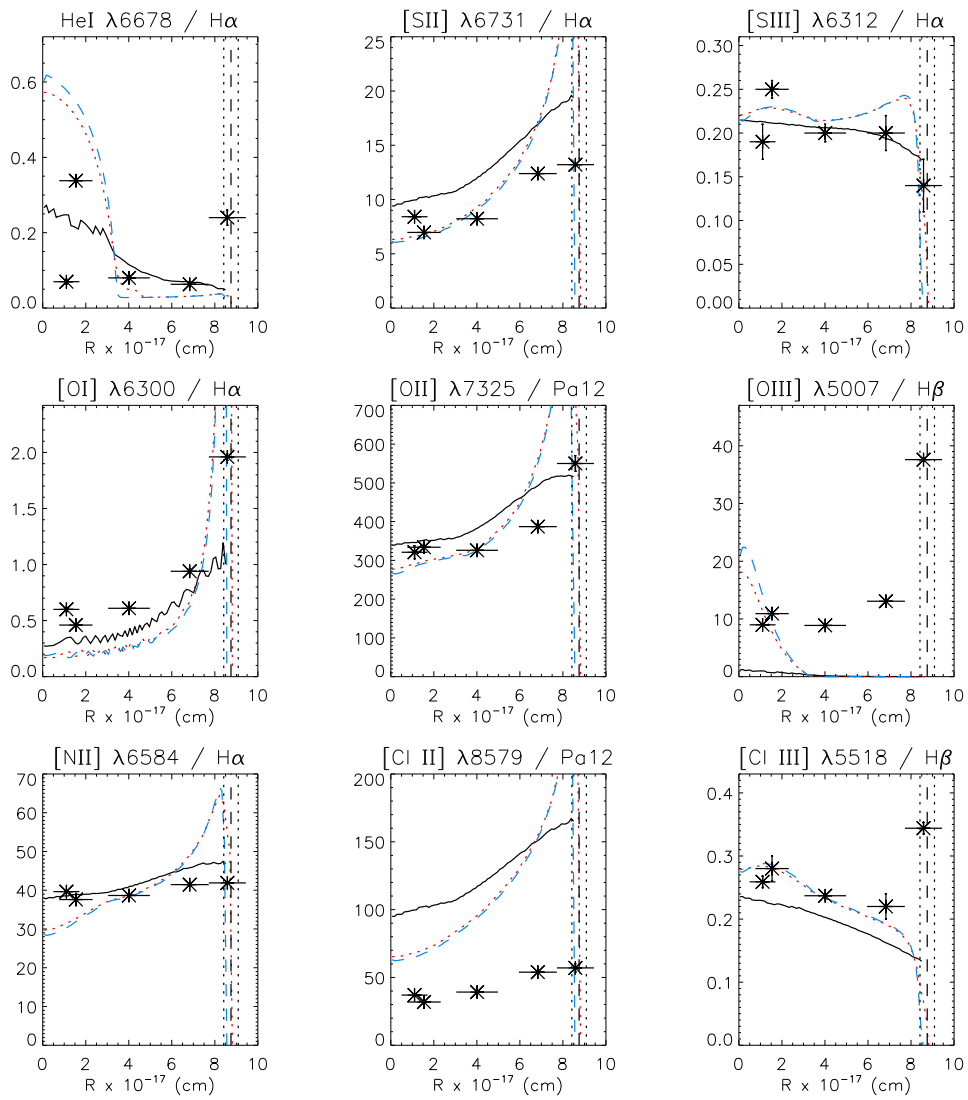


FIGURE 7.32 — The same than in Figure 7.31 but for other spectroscopic constraints

- The $\text{He I } \lambda 6678 / \text{H}_\alpha$ and $[\text{O III}] \lambda 5007 / \text{H}_\beta$ line ratios resulting from both spherical and blister models are quite different. The blister model predicts lower values for these line ratios close to the star. In addition these line ratios decrease more slowly in the blister model (for the spherical model the descent is more abrupt). This is an effect of the considered geometry. In the spherical case the stellar photons which are capable to ionize the He^0 and O^+ ions interact with the nebular material which is close to the star and hence are exhausted. Therefore at larger distances no He^+ and O^{++} are found. In the blister case those stellar photons can reach larger projected distances to the star since no nebular material is in between the star and the slab.
- The $[\text{O III}] \lambda 5007 / \text{H}_\beta$ line ratio predicted by the blister model is by far too low compared to the observations. This may be indicating that the strength of the ionizing radiation predicted by the stellar atmosphere model below the O^+ ionization edge (35.12 eV) is too low, however no general conclusion can be derived since other effects, like the considered distance between the star and the slab of nebular material, may be important.
- The $[\text{S III}] / [\text{S II}]$ and $[\text{Cl III}] / [\text{Cl II}]$ line ratios predicted by the blister model are smaller than those resulting from the spherical model. The agreement with the observational constraints is better for the spherical models. Again a strongest stellar ionizing flux is required to fit the predictions of the blister model to the ionization structure observational constraints (or alternatively, a smaller distance between the star and the slab of nebular material).

Obviously, this new hypothesis about the nebular geometry opens many different possibilities to be taken into account in the photoionization modeling of the nebula (for example the consideration of slabs of nebular material with different shapes, the presence of density gradients across the slab). The opened field is large, but the methodology proposed is strong and the tools we have used are powerful to achieve the study of the different possibilities.

7.6 Summary and conclusions

In this chapter, the well resolved Galactic H II region M43 has been selected to build a tailored model of the nebula, comparing photoionization code results with many different observational constraints. The stellar parameters and the emergent flux of the ionizing star have been derived from a detailed spectroscopic analysis of HD 37061 by means of state-of-the-art stellar atmosphere codes (*FASTWIND* and *WM-basic*). Photometric and morphological nebular parameters have been obtained from narrow band imagery.

A very good agreement between the total number of Lyman continuum photons predicted by the stellar atmosphere code *WM-basic* (for the corresponding derived stellar parameters) and the observed total nebular H_α luminosity has been found. This also indicates that the nebula can be considered as ionization bounded.

Results from long-slit nebular spectral observations at different positions along the nebula have allowed us to derive the physical parameters and abundances of the nebular gas-phase.

Finally, these nebular spectroscopic observations have also allowed us to use the ratio of several nebular lines as constraints for the photoionization models.

Three different types of models have been considered:

- **Spherical models with constant density:** These models fit very well most of the constraints when a $N(H) = 550 \text{ cm}^{-3}$ is considered. However they are limited by the fact that the H_α surface brightness profile cannot be reproduced. In addition, the T_e deduced from the models for the more distant slit sections is too large compared to the observations. This has effects on the predicted line intensity ratios of the collisional lines relative to an H I line.
- **Spherical models with density law:** These models are fixed to reproduce the H_α surface brightness profile by considering a density law. These models require a certain filling factor to fit the N_e constraints and the H_α surface brightness profile at the same time. In addition the nebula must be density bounded to fit the nebular size constraint. However these models produce too high average ionization for the internal slit sections.
- **Blister models:** As previously shown by Morisset et al. (2005), the apparent properties of blister models may differ drastically in many aspects from those resulting from spherical models. These models predict a shallower variation of the apparent T_e with the projected distance to the star and produce the values of the $\text{He I } \lambda 6678/H_\alpha$ and $[\text{O III}] \lambda 5007/H_\beta$ line ratios to be lower close to the star and decrease more slowly with projected distance to the star compared to the spherical models.

In these blister models, the distance between the star and the slab of nebular material is an important free parameter. Only the first steps have been taken in the consideration of blister models, due to the fact that they open new possibilities to be taken into account (for example, the density law across the slab or the shape of this slab of material).

In addition some other interesting points can be remarked from this study:

1. Indicators like the $[\text{S III}] \lambda 6312 / [\text{S II}] \lambda 6731$ line ratio have allowed to constraint the T_{eff} of the ionizing star. The derived value is in very good agreement with that derived from the analysis of the optical spectrum of the star.
2. It has been found that the atomic data proposed by Wilson & Bell (2002) for the Cl II collisional transitions produce too large $[\text{Cl II}] \lambda 8579 / \text{Pa}12$ line ratios. The corresponding atomic dataset by Mendoza et al. (1983) produces a better fit to the observational constraint.

CONCLUSIONS

THE main effort of this thesis has been devoted to study two different aspects of the interplay between massive OB-type stars and associated H II regions. Firstly, the consistency between nebular and stellar abundances was studied. Following this, the predictions of hot star model atmosphere codes were compared to observed nebular constraints in a well defined situation. The comparison of abundances in stars and nebulae has been carried out in the star forming region associated with the Orion nebula (M42). For the second task of this thesis, the de Marian's nebula (M43), an apparently spherical galactic H II region ionized by a single star has been selected. Several types of observables have been used, comprising stellar and nebular spectroscopy and narrow band imagery. We review here the conclusions of this work.

τ SCO: A BENCHMARK TEST

The star τ Sco has been used as a *benchmark test* for the oxygen and silicon absolute abundance analyses of early B-type stars with the stellar atmosphere code FASTWIND. After the identification of the oxygen and silicon lines present in the spectral range 4000 - 5000 Å, which may be useful for the abundance studies in

these stars, a detailed analysis by multiplets has been performed. This study has allowed us to establish a suitable set of O II, Si III and Si IV lines for the abundance analyses of early B-type stars, and to identify common problems associated with the determination of mean abundances by means of the usual curve of growth method:

- It has been argued that it is feasible to use the whole set of O II lines to determine the microturbulence if firstly a detailed analysis by multiplets is performed to identify problematic lines (i.e. blended lines or lines which are incorrectly modeled).
- There has been a problem identified in one of the versions of the oxygen model atom (A10HHe0Si+op) that was used for the oxygen abundance analyses with FASTWIND. This problem was related to the way the data from the OPACITY PROJECT were included in a previous version of the oxygen model atom. It has been decided not to use that problematic version (A10HHe0+op), but a previous one (A10HHe023-3).
- It has been found that the microturbulence derived from the silicon analysis is $\sim 5-7 \text{ km s}^{-1}$ smaller than the one derived from the oxygen analyses. This discrepancy has been previously found for the case of B-type supergiants.
- It has been concluded that the use of different microturbulences for each element allows a more accurate abundances to be derived.
- The dependence of the oxygen and silicon abundances on the stellar parameters has been shown. For this range of stellar parameters, the uncertainties associated with a change of 1000 K and 0.1 dex in effective temperature and gravity are 0.08 dex and 0.01 dex respectively for oxygen and 0.2 dex and 0.05 dex respectively for silicon.
- It has been shown that the Si IV / Si III ionization balance is achieved for a $T_{\text{eff}} \sim 1000 \text{ K}$ lower than the value derived from the He II/He I analysis.
- The oxygen abundance results from various stellar atmosphere codes have been compared. It has been found that the results are compatible once the problematic lines are dismissed and it is taken into account that the different codes can lead to slightly different stellar parameters.

MASSIVE STARS IN ORION NEBULA

The study of the OB-type stars belonging to the Orion nebula cluster has led to several interesting conclusions.

- Projected rotational velocities have been obtained through the Fourier method. This method has been extensively used for late type stars, but not very widely applied to early type stars. The agreement is very good when comparing with results from the line-width method. As the line-width method only estimates the degree of the total broadening of the line (i.e. rotational, macroturbulence, etc.) the result indicates that the influence of macroturbulence in the line broadening of these stars is small (except for the case of θ^1 Ori C).
- Applying the Fourier method to the high resolution θ^1 Ori C FEROS spectra, has allowed us to derive a very accurate $v \sin i$ that is in agreement with the period of variability of some spectral features in this star. This study has illustrated the strength of the Fourier method to distinguish between rotational broadening and other broadening mechanisms that can be present in early type stars (i.e. macroturbulence).
- The stellar parameters for the Trapezium cluster stars (θ^1 Ori A, C, D along with the nearby stars θ^2 Ori A, B) and three other targets selected for comparison, have been determined by means of a detailed spectroscopic analysis using the stellar atmosphere code FASTWIND.

The previous study of τ Sco has laid the foundations to develop a reliable abundance study of three B0.5V stars belonging to the Orion nebula cluster. The derived stellar abundances have been compared with those derived in previous nebular studies from the spectrum of the H II region M42.

- The oxygen abundances derived for these stars are $\log(O/H) + 12 = 8.65$, 8.59 and 8.64 dex (θ^1 Ori A, θ^1 Ori D and θ^2 Ori B respectively). The related uncertainties are 0.10 dex. The adopted microturbulence (derived from the whole set of O II lines) is $\sim 5-8 \text{ km s}^{-1}$.
- Our oxygen abundances are systematically lower than the NLTE abundances by Cunha & Lambert (1994). These difference can be in part associated with differences in the stellar parameters used for the stars in the abundance analysis. The effective temperatures used by these authors are based on photometric calibrations.
- Our stellar oxygen abundances are compatible with those obtained by Esteban et al. (2004) for the gas-phase. This a very important result since the same oxygen abundance has been derived by means of two different astrophysical objects and different techniques.

- Given the excellent agreement between stellar and nebular results for the oxygen abundance in M42 it can also be concluded that the amount of oxygen depleted onto dust grains is very small. Therefore the oxygen depletion factor is lower than previous estimations for the Orion nebula.
- The silicon abundances derived for the Orion stars are $\log(\text{Si}/\text{H}) + 12 = 7.55$, 7.45 and 7.64 dex (θ^1 Ori A, θ^1 Ori D and θ^2 Ori B respectively). The related uncertainties are 0.20 dex. A microturbulence $\xi_t = 1 \text{ km s}^{-1}$ (derived from the Si III $\lambda\lambda$ 4552, 4567, 4574 multiplet) has been considered for the silicon analyses
- These silicon abundances are systematically larger than those determined by Cunha & Lambert (1994). The difference is related with the different stellar parameters and microturbulence values considered in the silicon abundance analysis.
- Our stellar silicon abundances are larger than those nebular abundances derived by Rubin et al. (1993) and Garnett et al. (1995).
- This result suggest a certain amount of nebular silicon depleted onto dust grains, however the exact determination of the silicon depletion factor is complicated due to the uncertainties and possible systematic errors associated with the derived silicon abundances, both stellar and nebular.

TAILORED PHOTOIONIZATION MODELS FOR M43

The photoionization code CLOUDY has been used to build tailored photoionization models for M43. The required input for the models, concerning the spectral energy distribution of the ionizing star, the nebular abundances and the photometric and geometrical characteristics of M43, have been previously determined from spectroscopic observations and imagery.

- The stellar parameters of the ionizing star (HD 37061) have been accurately determined using FASTWIND. These stellar parameters have been used as input to the stellar atmosphere code WM-basic, to obtain a detailed spectral energy distribution for this star. From this SED a total number of Lyman photons $Q(\text{H}^0) = (2.4 \pm 1.0) \times 10^{47} \text{ ph s}^{-1}$ is deduced.
- The integrated $\text{H}\alpha$ luminosity and the size of M43 have been calculated from the $\text{H}\alpha$ images of the nebula. The final values for these quantities (assuming a distance to the nebula of 450 pc) are $L_{\text{H}\alpha} = (3.0 \pm 0.8) \times 10^{35} \text{ ergs}^{-1}$ and $R_{\text{neb}} = 0.28 \pm 0.04 \text{ pc}$.

- Although the H_α luminosity of the nebula is slightly lower than that which would correspond to the previous $Q(H^0)$ value, no firm conclusion about the escape of photons from the nebula can be made because both estimations are consistent within the errors.

The output of the models have been compared with nebular spectroscopic observations corresponding to five slit sections located at different positions along the nebula. Three different types of models have been considered:

- The spherical models with constant density fit very well most of the constraints when a $N(H) = 550 \text{ cm}^{-3}$ is considered. However they are limited by the fact that the H_α surface brightness profile cannot be reproduced. In addition, the T_e deduced from the models for the more distant slit sections is too large compared to the observations. This has effects on the predicted line intensity ratios of the collisional lines relative to a $H\text{I}$ line.
- By assuming a spherical geometry, a radial density law has been obtained from the H_α surface brightness profile. This has been used to generate spherical models with a density law. Although the H_α surface brightness profile is obviously reproduced by these models, they produce too high average ionization for the internal slit sections.
- In addition to the above two models, the first steps have been taken in the consideration of blister models. These models predict a shallower variation of the apparent T_e with the projected distance to the star and produce the values of the $\text{He I } \lambda 6678/H_\alpha$ and $[\text{O III}] \lambda 5007/H_\beta$ line ratios to be lower close to the star and decrease more slowly with projected distance to the star compared to the spherical models. In these blister models, parameters like the distance from the star to the slab, the shape of the slab, or the density law along the slab of nebular material are important parameters to be studied.

Some other interesting points can be remarked from this study:

- Indicators like the $[\text{S III}] \lambda 6312/[\text{S II}] \lambda 6731$ line ratio have allowed to constraint the T_{eff} of the ionizing star. The derived value is in very good agreement with that derived from the analysis of the optical spectrum of the star.
- It has been found that the atomic data proposed by Wilson & Bell (2002) for the Cl II collisional transitions produce too large $[\text{Cl II}] \lambda 8579/\text{Pa}12$ line ratios. The corresponding atomic dataset by Mendoza et al. (1983) produces a better fit to the observational constraint.

THE FOURIER METHOD IN THE DETERMINATION OF STELLAR $V \sin i$

Accurate determination of stellar rotational velocities is a very important task in Astrophysics. Actual evolutionary stellar models take this rotational velocity into account, considering it as an important parameter in the stellar evolution, along with the stellar mass, the chemical composition and the wind characteristics of the star (Maeder & Meynet 2000). The presence of convective layers near the surface of the star in the case of late spectral type stellar objects affect the initial rotation of the star slowing it to equatorial velocities of a few km s^{-1} . However these external convective layers are not present in early OB stars. These objects could then reach high rotational velocities that affect not only the shape of the star, but also their evolutionary time-scale and the presence of nuclear processed material at the stellar surface.

The only information we have about the stars is contained in their spectra. The rotational velocity of the stars affects the stellar spectrum through Doppler effect. This is why, in principle, only the projection of the equatorial velocity along the line of sight ($v \sin i$) can be achieved.

There is not an unique, well established method for extracting the information contained in the stellar spectrum about its projected rotational velocity. They are summarized below:

- Method 1: The observed line profiles are compared with synthetic ones calculated from model atmospheres which are convolved with the corresponding broadenings. Although this is a very accurate method, too much computational time is required.
- Method 2: The observed spectrum is cross-correlated against a *template* spectrum. The Gaussian width of the cross-correlation function is directly related to the projected rotational velocity of the star if rotation is the dominant broadening mechanism of the photospheric lines.
- Method 3: By measuring the FWHM of the observed line profile and relating it with the $v \sin i$ (FWHM-method).
- Method 4: The Fourier technique, firstly described by Gray (1976).

Penny (1996) and Howarth et al. (1997) did an impressive work by applying the cross-correlation technique to IUE spectra of 177 O stars and 373 O-type and early B supergiants respectively. Although the cross correlating method, along with the FWHM-method, are very fast and easy to use they do not allow to separate rotational broadening from other possible extra broadenings (e.g. macroturbulence). The fitting with broadened synthetic profiles make it possible to distinguish between different broadenings and also determine other stellar parameters, but as it has been commented before, too much computational time is needed. Conti & Ebbets (1977) applied this method to measure the $v \sin i$ of a sample of 205 O-type stars in the norther and southern hemisphere and suggest the presence of some extra-broadening (apart from rotational broadening) affecting the line profiles, especially in the case of giants and supergiants. Recently Ryans et al. (2002) have analyzed the high quality spectra of twelve B-type supergiants. They compare observed and synthetic broadened lines using a χ^2 technique and find for their survey of B supergiants that a model where macroturbulence dominates and rotation is negligible is acceptable, but models dominated by rotation provide unsatisfactory fits.

Being also very fast and easy to use the Fourier method has only been marginally applied in the study of OB stars. This technique allows the projected rotational velocity to be easily derived independently of any other broadening mechanism which may affect the line profile. Some work has been devoted for using this method in the determination of $v \sin i$ in late type stars (viz. Smith 1976; Gray 1980; Royer et

al. 2002ab; Reiners et al. 2003). However there is not a comprehensive study that applies this technique to early type stars except that by Ebbets (1979).

In this thesis, the Fourier method has been applied to derive the projected rotational velocity of a set of OB stars (see Chapter 6, Section §6.4). To this aim, we have implemented a very easy-to-use tool in IDL. We have also tested the method with theoretical and observational cases. Some notes on the characteristics and applicability of the Fourier method are presented here.

A.1 Testing the Fourier method. Some theoretical cases

A.1.1 The Fourier method

In a pioneering study, Gray (1973) examined the possibility of using Fourier transforms of profiles to discriminate among three types of atmospheric Doppler broadening mechanisms: microturbulence, macroturbulence, and rotation. Fourier method for the determination of $v \sin i$ is based in the fact that in the Fourier space convolutions transform in products. Between rotation, macroturbulence, natural and instrumental profile, only rotation function has zeroes in its Fourier transform. The zeroes will appear in the total transform function. Carroll (1933) showed that the position of the zeroes are related with the $v \sin i$. Actually the frequency of the first zero (σ_1) is related to the rotational velocity through:

$$\frac{\lambda}{c} v \sin i \sigma_1 = 0.660 \quad (\text{A.1})$$

The microturbulence can also add zeroes, when strong lines are considered, due to the boxiness caused by it in saturated lines (Gray 1973). Sidelobes arising from saturation in the Fourier space appear at higher frequencies than those for rotation, so there is rarely any confusion between them, except those cases with low $v \sin i$.

A.1.2 Rotational and macroturbulent profiles

The usual formulation adopted for the rotational broadening (Carroll 1933) consider the rotational profile, that will be convolved with the other flux profiles, defined by:

$$V(x) = \frac{1}{1 + 2\beta/3} \left[\frac{2}{\pi^{1/2}} (1 - x^2)^{1/2} + \frac{\beta}{2} (1 - x^2) \right] \frac{1}{\Delta\lambda_0} \quad (\text{A.2})$$

$$x = \Delta\lambda / \Delta\lambda_0 \quad \Delta\lambda_0 = \lambda_0 v \sin i / c$$

where β is limb darkening parameter ($0 \leq \beta \leq 1.5$).

In this study we will consider a gaussian-angle-dependent profile (see Gray 1976) for the macroturbulence. This author considered the possibility of two components in the macroturbulent broadening (radial and tangential). Each one of them has similar expressions but a different value of the macroturbulent velocity:

$$M(\Delta\lambda) = A_R\Theta_R + A_T\Theta_T$$

where

$$\Theta_i = \frac{2}{\pi^{1/2}\Delta M_i} x_i \left[-\pi^{1/2} + \frac{e^{-x_i^2}}{x_i} + \pi^{1/2} \operatorname{erf}(x_i) \right] \quad (\text{A.3})$$

$$x_i = \Delta\lambda/\Delta M_i \quad \Delta M_i = \lambda_0\theta_i/c$$

being θ_R and θ_T the radial and tangential components of the macroturbulent velocity and $A_R^2 + A_T^2 = 1$.

A.1.3 The Fast Fourier Transform (FFT) and its computational properties

Although the theoretical base of this methodology was well established by Gray (1973) and used by some other authors, they were limited by computational and observational constraints. Photographic plates did not allow to have enough spectral resolution. They also claimed for the development of new computational technics that made possible the calculation of the Fourier transform reducing the computational time. Nowadays this is feasible; almost all computational packages include the Fast Fourier Transform (FFT) as a basic program, and the charged coupled devices (CCDs) allows to have enough spectral resolution.

Because we are talking about computational methods, we have to consider computational limitations. One of these is related with the sampling of the function we want to make the transform. This value imposes a limit in the maximum σ value that can be calculated: $\sigma_{\max} = (2\Delta\lambda)^{-1}$. From Formula A.1 and this computational limitation it can be derived that it is not possible to determine a $v \sin i$ lower than $1.320 c \Delta\lambda/\lambda$. The other limitation is that the sampling of the FFT function depends on the number of points into which the λ -function is sampled, the more points are considered in this function the better is the sampling of the FFT function: $\Delta\sigma = (N\Delta\lambda)^{-1}$.

The only way to improve the σ_{\max} , this is obtaining a higher σ_{\max} and then be able to reach higher frequencies, is to have observations with better spectral dispersion, $\Delta\lambda$. It is not possible to improve the σ_{\max} by trying to have a better sampling

of the λ function by interpolation from the original data (either linear or spline). However, it is possible to improve the sampling of the FFT function, not by interpolation but by extrapolation of the continuum (fixed to 1). The better the sampling of this function the more accurate the zeroes of the function can be determined.

A.1.4 Some theoretical tests

Before applying the Fourier method to determine the $v \sin i$ of our sample of OB stars (see Chapter 6, Section §6.4) we have done some theoretical tests to study how well does it work and to establish the accuracy of the methodology.

For this study we have used FASTWIND (Santolaya-Rey et al. 1997, Puls et al. 2005) theoretical profiles from a model with $T_{\text{eff}} = 30000$ K, $\log g = 4.0$ (an early B Main Sequence star) convolved with different broadening functions. Thermal and microturbulence broadenings are included in the line calculation in the usual way. For the rotational and macroturbulent broadenings we have used the functions defined in Formulae A.2 and A.3. In some cases it has been added noise to the synthetic spectra; we have used a Poissonian distribution of noise generated with RANDOMN in IDL.

The first test is related to the possibility to disentangle between the rotational and the macroturbulent broadenings affecting a stellar line profile. Figure A.1 shows an illustrative example for this study. Three sets of rotational and macroturbulent broadenings have been considered: $(v \sin i, \Theta_T) = (50, 100)$, $(90, 50)$ and $(50, 0)$ km s^{-1} . The $v \sin i$ derived through the FWHM method is 100, 100 and 50 km s^{-1} respectively for the solid, dashed and dashed-dotted cases. This method does not allow us to distinguish if the broadening of the line is due to rotation or macroturbulence (i.e. for the first two cases a wrong value of $v \sin i$ is derived). The difference clearly appears in the Fourier space. It can be seen that although the solid and dashed broadened lines are hardly distinguished in the λ -space (left), the Fourier transforms of the lines are clearly different (right). The first zero in the solid line corresponds to a $v \sin i$ of 50 km s^{-1} ($\sigma \sim 0.9$) while the first zero in the dashed line corresponds to a $v \sin i$ of 90 km s^{-1} ($\sigma \sim 0.5$).

Once we know which is the $v \sin i$, the λ -space can help us to decide if there is an extra-broadening of the line. Comparing the solid and the dashed-dotted lines it appears obvious that a extra-broadening, apart from rotational broadening, is needed for the solid line. From the Fourier transform a $v \sin i = 50 \text{ km s}^{-1}$ is derived for this solid profile, but this rotational broadening is not sufficient for fitting the lines in the λ -space.

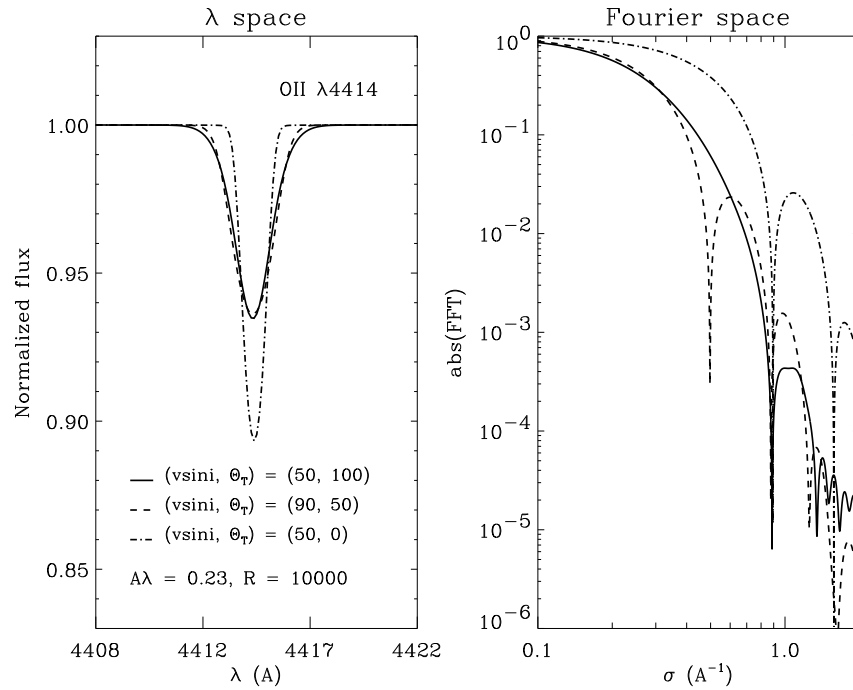


FIGURE A.1 — A synthetic O II line has been convolved with an instrumental ($R = 10000$) profile, and three different sets of rotational and a macroturbulent profiles. See section A.1.4 for explanation.

A second test has been performed to study how well does this method work when different lines in the spectrum are considered. For comparing results from different lines a $\sigma\lambda$ baseline has to be used, as the position of the first zero associated with the $v \sin i$ depends on the λ of the line (see Eq. A.1). Figure A.2 shows the result of this study. The Fourier technique has been applied to several FASTWIND synthetic lines from different elements and ionization states. As can be seen, the agreement between the different lines is almost perfect (even when the line He I $\lambda 4471$ is used).

Finally, we wanted to study the accuracy of the method when different values of SNR and $v \sin i$ are considered. Figure A.3 resumes this study. The same O II line has been broadened to different values of $v \sin i$ and different levels of noise have been added to each one of the broadened profiles. This way we can study how does the noise affect to the determination of the projected rotational velocity through the Fourier method.

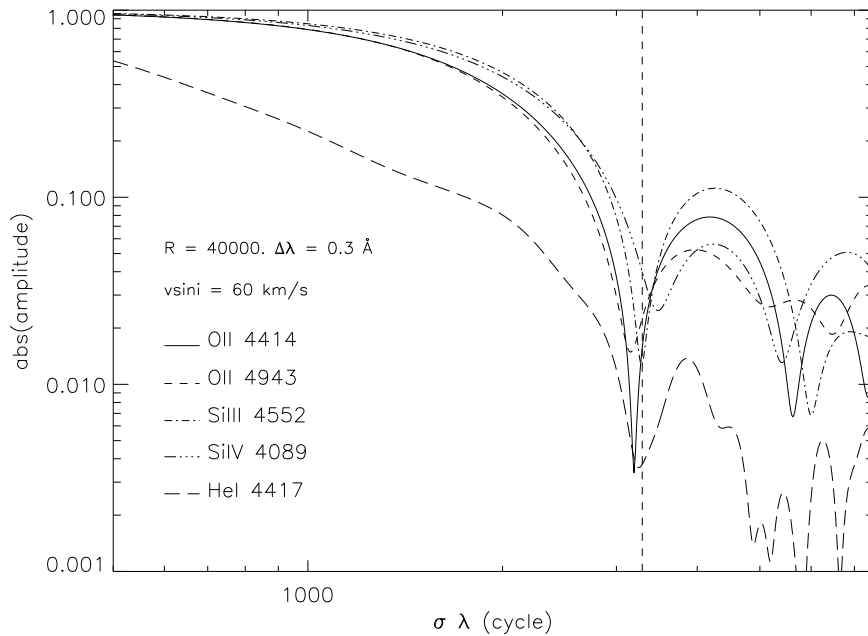


FIGURE A.2 — Five different synthetic lines generated with FASTWIND have been convolved with a $v \sin i$ of 60 km s^{-1} and degraded to a SNR ratio of 200. The different lines show the Fourier transform of the lines on a $\sigma\lambda$ baseline. The first zero is very near the theoretical value for all the lines. It is quite remarkable how the Fourier transform can detect the $v \sin i$ feature even for the He I $\lambda 4471$ line.

Three $v \sin i$ and five different SNR (ranging from poor to high quality spectra) have been considered. The main results of this theoretical study is that a SNR of 50 is not sufficient for derive accurately the $v \sin i$ from this O II line. With higher values of SNR (even 100) the first zero is well defined both for the low projected rotational velocity and for the other two cases. This result can also be affected by the presence of macroturbulence or even the resolution of the spectrum.

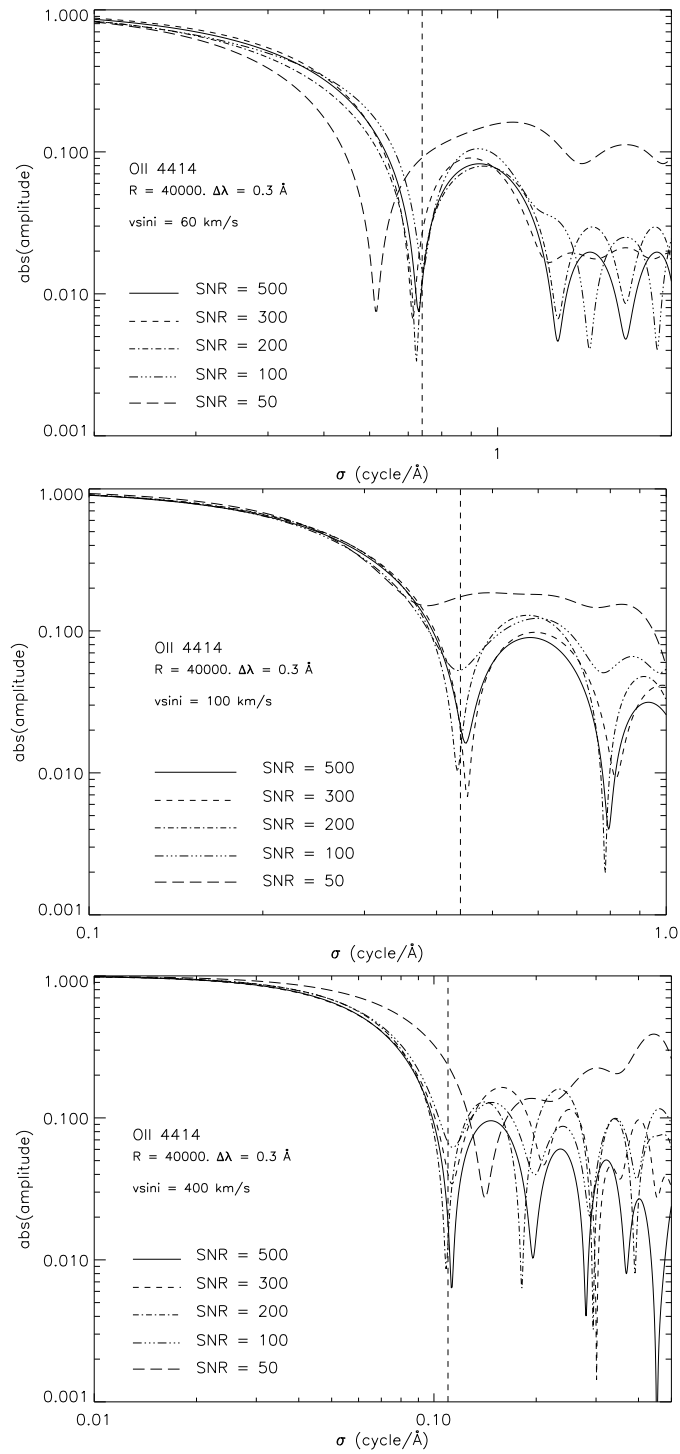


FIGURE A.3 — Different levels of noise have been added to the O II $\lambda 4414$ line, which has previously broadened to $v \sin i = 60, 100$ and 400 km s^{-1} . Vertical lines correspond to the theoretical σ value associated with the corresponding $v \sin i$ (derived from Eq. A.1). See section A.1.4 for explanation.

A.2 Applying the Fourier method to real OB stellar spectra

Figures A.4 to A.7 show examples of the application of the Fourier method to real OB stellar spectra. Four of the stars studied in Chapters 6 and 7 have been selected as illustrative examples (see also the study of θ^1 Ori C in Section §6.10, Chapter 6).

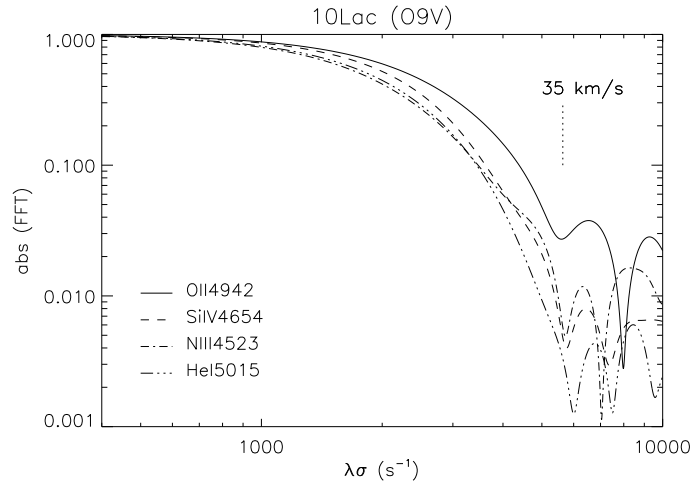


FIGURE A.4 — The following four figures (A.4 to A.7) show examples of the application of the Fourier method to some of the stars studied in this thesis (Chapters 6 and 7). In this Figure, the study of the star 10 Lac is presented.

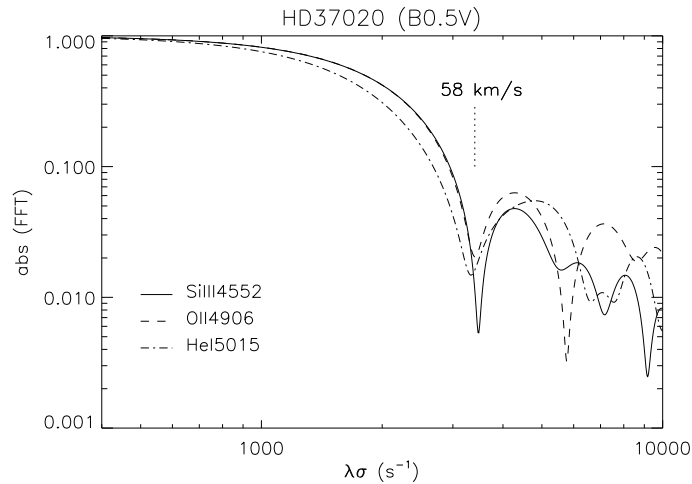


FIGURE A.5 — Application of the Fourier method to the star HD 37020.

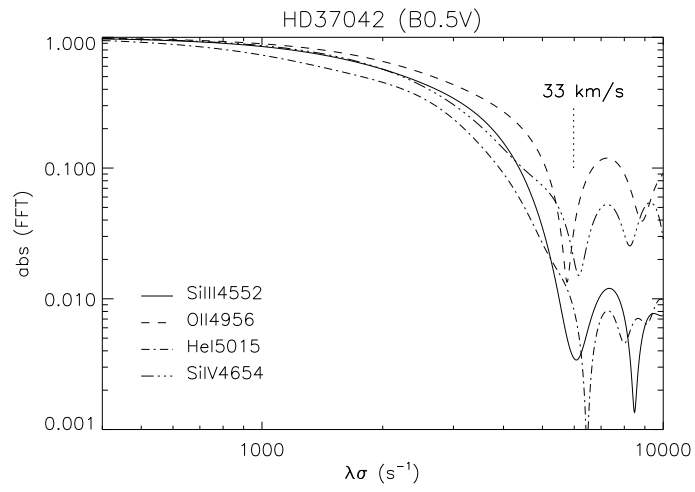


FIGURE A.6 — Application of the Fourier method to the star HD 37042.

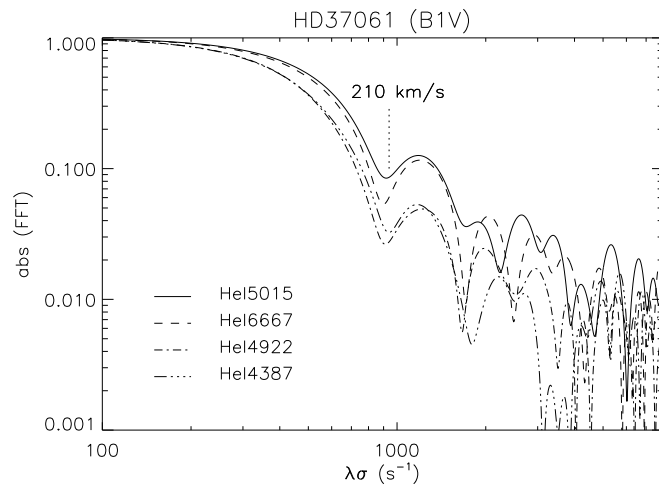


FIGURE A.7 — Application of the Fourier method to the star HD 37061.

STELLAR SPECTROSCOPY OF BINARY SYSTEMS

CONSIDERING a binary system with an OB Main Sequence star as the primary, the other star must have the same or lower mass. If the secondary has lower mass, it must be Main Sequence (this is, not evolved), so it must have lower T_{eff} and $R_1 \geq R_2$.

For the three cases considered in Figure B.1:

$$\frac{F_B}{F_A} \leq 1 \quad (\text{B.1})$$

$$\frac{F_C}{F_A} \geq 1 \quad (\text{B.2})$$

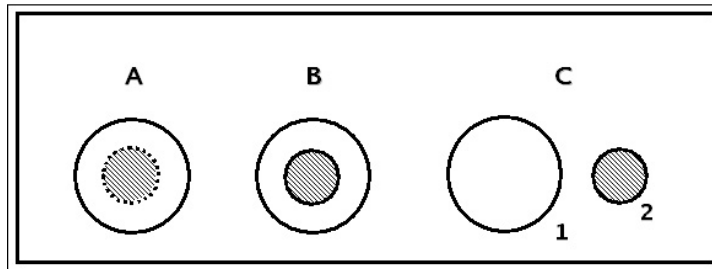


FIGURE B.1 — In a binary system, while the stars are orbiting, there can be considered three different extreme positions: (A) The secondary star is hidden behind the primary star. (B) The secondary star is located in front of the primary; the secondary partially eclipses the primary. (C) Both components can be visually separated.

When a binary system is spectroscopically observed, it sometimes occurs that the two components cannot be spatially resolved, and hence both stars lie inside the slit or the fiber. In that case, a combined spectrum is obtained, and the lines of the primary are affected by the presence of the other component depending of the relative position of both stars:

- If the system is observed when the primary star is eclipsing the secondary (case A), only the spectral lines of the primary will appear in the combined spectrum, as if it was isolated.
- If the system is observed when the cooler star is eclipsing the primary star (case B), the spectral lines of the primary will appear stronger.
- If the system is observed out of eclipse (case C), the spectral lines of the stars will appear fainter in the global spectra.

This effect can be quantified taking into account:

$$I_{12} = K (F_1 A_1 + F_2 A_2) \quad (\text{B.3})$$

with:

$$\text{Case A :} \quad A_1 = \pi R_1^2 \quad A_2 = 0 \quad (\text{B.4})$$

$$\text{Case B :} \quad A_1 = \pi R_1^2 - \pi R_2^2 \quad A_2 = \pi R_2^2 \quad (\text{B.5})$$

$$\text{Case C :} \quad A_1 = \pi R_1^2 \quad A_2 = \pi R_2^2 \quad (\text{B.6})$$

$$(\text{B.7})$$

In case A, when the spectrum is normalized, one have for a given line:

$$y_{1n}^A = \frac{K y_1 A_1}{K F_1 A_1} = \frac{y_1}{F_1} \quad (\text{B.8})$$

meanwhile, for cases B and C:

$$y_{1n}^{B,C} = \frac{K y_1 A_1 + K F_2 A_2}{K F_1 A_1 + K F_2 A_2} = \frac{y_1 A_1 + F_2 A_2}{F_1 A_1 + F_2 A_2} = \frac{\frac{y_1}{F_1} + \frac{F_2 A_2}{F_1 A_1}}{1 + \frac{F_2 A_2}{F_1 A_1}} = \quad (\text{B.9})$$

$$= \frac{y_{1n}^A - 1 + 1 + \frac{F_2 A_2}{F_1 A_1}}{1 + \frac{F_2 A_2}{F_1 A_1}} = (y_{1n}^A - 1) \left(1 + \frac{F_2 A_2}{F_1 A_1}\right)^{-1} + 1 \quad (\text{B.10})$$

On the other hand:

$$m_{B,C} - m_A = -2.5 \log\left(\frac{F_1 A_1 + F_2 A_2}{F_1 A_1}\right) = 2.5 \log\left(1 + \frac{F_2 A_2}{F_1 A_1}\right)^{-1} \quad (\text{B.11})$$

Therefore, if a correction factor f has to be applied to the lines in a normalized spectrum, this is equivalent to a change in magnitude respect to the case when the star is isolated:

$$y_{1n}^{B,C} = (y_{1n}^A - 1)f + 1 \quad (\text{B.12})$$

$$m_{B,C} - m_A = 2.5 \log f \quad (\text{B.13})$$

where:

$$f = \left(1 + \frac{F_2 A_2}{F_1 A_1}\right)^{-1} \quad (\text{B.14})$$

$$F_\nu \propto T_{\text{eff}} \quad (\text{B.15})$$

GLOSSARY OF TERMS

TELESCOPES AND INSTRUMENTS

FLAMES	Fibre Large Array Multi Element Spectrograph
VLT	Very Large Telescope
INT	Isaac Newton Telescope
IDS	Intermediate Dispersion Spectrograph
WFC	Wide Field Camera
CASPEC	Cassegrain Echelle Spectrograph
ESO	European Southern Observatory
FEROS	Fiber-fed Extended Range Optical Spectrograph

INSTITUTES AND ASTRONOMY GROUPS

ESO	European Southern Observatory
IAC	Instituto de Astrofísica de Canarias
ING	Isaac Newton Group
CSIC	Centro Superior de Investigaciones Científicas
IEM	Instituto de Estructura de la Materia
QUB	Queen's University of Belfast

GENERAL DEFINITIONS

ISM	Interstellar Medium
UV	Ultraviolet
EUV	Extreme ultraviolet
IR	Infrared
FIR	Far infrared
IMF	Initial mass function
SFH	Star formation history
SpT	Spectral type
LTE	Local thermodynamic equilibrium
NLTE	Non local thermodynamic equilibrium
<i>SNR</i>	Signal-to-noise ratio
DIB	Diffuse interstellar band
SED	Spectral energy distribution
m_v	Apparent visual magnitude
A_v	Visual extinction
M_v	Absolute visual magnitude
<i>EW</i>	Equivalent width

STELLAR DEFINITIONS

T_{eff}	Effective temperature
$\log g$	Logarithmic surface gravity
v_∞	Stellar wind terminal velocity
Q	Stellar wind-strength parameter
ξ_t	Microturbulence
$\epsilon(X)$	Abundance of the element X (in units of $\log(X^m/H^+) + 12$)
Z	Metallicity
\dot{M}	Mass loss rate
H_ν	Eddington flux
$Q(H^0)$	Number of hydrogen ionizing photons
$Q(X^{+i})$	Number of ionizing photons for the ionic specie X^{+i}
$v \sin i$	Projected rotational velocity

NEBULAR DEFINITIONS

T_e	Electron temperature
N_e	Electron density
ORL	Optical recombination line
CEL	Collisionally excited lines
$S_{H\alpha}$	Surface brightness in H_α line
$C_{H\beta}$	Logarithmic extinction at H_β
$f(H_\alpha)$	Value of the extinction law for H_α
R_v	Ratio of visual extinction to colour-excess
$\tau_{H\alpha}$	Optical depth at the wavelength corresponding to H_α
$\alpha_B(H, T_e)$	H recombination coefficient to the excited states
$\epsilon_{H\alpha}$	Emission coefficient of H_α
N_H	Hydrogen density
$N(H)$	Hydrogen density
ϵ	Filling factor
cf	Covering factor
ICF	Ionization correction factor

ATOMIC DEFINITIONS

RBF	Radiative bound-free (transition)
OP	Opacity project
τ_R	Rosseland optical depth
$\log gf$	Degeneracy of level \times oscillator strength (in logarithm)
τ_ν	Monochromatic optical depth
τ_ν^c	Monochromatic optical depth for the continuum
τ_ν^l	Monochromatic optical depth for the line
κ_ν^c	Continuous absorption coefficient
σ_ν^c	Continuous scattering coefficient
χ_ν^l	Line absorption coefficient
A_{ij}	Radiative bound-bound transition coefficient
γ_{ij}	Collisional bound-bound transition coefficient

BIBLIOGRAPHY

- Abt, H.A., Wang, R., & Cardona, O. 1991, ApJ, 367, 155
- Afflerbach, A., Churchwell, E., & Werner, M.W. 1997, ApJ, 478, 190
- Allende-Prieto, C., Lambert, D.L., & Asplund, M. 2001, ApJ, 556, L63
- Anderson, L.S. 1989, ApJ, 339, 558
- Babel, J., & Montmerle, T. 1997, ApJ, 485, L29
- Baldwin, J.A., Ferland, G.J., Martin, P.G., Corbin, M.R., Cota, S.A., Peterson, B.M., Slettebak, A. 1991, ApJ, 374, 580
- Becker, S.R., & Butler K. 1988, A&A, 201, 232
- Becker, S.R., & Butler, K. 1990, A&A, 235, 326
- Bianchi L., & García M. 2002, ApJ, 581, 610
- Blaauw, A. 1964, ARA&A, 2, 213
- Bresolin, F., Kudritzki, R.-P., Mendez, R.H., Przybilla, N. 2001, ApJ, 548, 159
- Bresolin, F., Garnett, D.R., Kennicutt, R.C., Jr. 2004, ApJ, 615, 228
- Bouret, J.-C., Lanz, T., Hillier, D.J., Heap, S.R., Hubeny, I., Lennon, D.J., Smith, L.J., & Evans, C.J. 2003, ApJ, 595, 1182
- Butler, K., & Giddings, J.R. 1985, Coll. Comp. Project No. 7 (CCP7), Newsletter 9, London, p. 7
- Caillault, J.P., Gagne, M., & Stauffer J.R. 1994, ApJ, 432, 386
- Cardelli, J.A., Clayton, G.C., & Mathis, J.S. 1989, ApJ, 345, 245
- Carroll, J.A. 1933, MNRAS, 93, 478
- Castor, J.I., Abbott, D.C., & Klein, R.I. 1975, ApJ, 195, 157
- Cedr s, B., Urbaneja, M.A., & Cepa, J. 2004, A&A, 422, 511

- Cerviño, M., Luridiana, V., & Castander F.J. 2000, A&A, 360, L5
- Cerviño, M., Valls-Gabaud, D., Luridiana, V., Mas-Hesse, J. M. 2002, A&A, 381, 51
- Conti, P.S. 1972, ApJ, 174, L79
- Conti, P.S., Ebbets, D. 1977, ApJ, 213, 438
- Crowther, P.A., Hillier, D.J., Evans, C.J., Fullerton, A.W., De Marco, O., & Willis, A.J. 2002, ApJ579, 774
- Cunha K., & Lambert D.L. 1992, ApJ, 399, 586
- Cunha K., & Lambert D.L. 1994, ApJ, 426, 170
- Daflon, S., Cunha K., & Becker, S.R. 1999, ApJ, 522, 950
- Daflon, S., Cunha K., Becker, S.R., & Smith, V.V. 2001, ApJ, 552, 309
- Daflon, S., & Cunha K. 2004, ApJ, 617, 1115
- Deharveng, L., Peña, M., Caplan, J., & Costero, R. 2000, MNRAS, 311, 329
- Díaz, A.I., & Pérez-Montero, E. 2000, MNRAS, 312, 130
- Donati, J.F., Babel, J., Harries, T.J., et al. 2002, MNRAS, 333, 55
- Dufton, P. L., McErlean, N.D., Lennon, D.J., Ryans, R.S.I. 2000, A&A353, 311
- Dufton, P.L., Ryans, R.S.I, Trundle, C., Lennon. D.J., Hubeny, I., Lanz, T., Allende Prieto, C., A&A, in press -astroph/0412367
- Ebbets, D. 1979, ApJ, 227, 510
- Ehrenfreund, P., & Charnley, S.B. 2000, ARA&A, 38, 427
- Esteban, C., Peimbert, M., Torres-Peimbert, S., & Escalante, V. 1998, MNRAS, 295, 401
- Esteban, C. 2002, in Ionized Gaseous Nebulae, Eds. W.J. Henney, J. Franco, M. Martos, & M. Peña, RMxAASC, 12, 56
- Esteban, C., Peimbert, M., Peimbert, A., & Rodríguez, M., 2002, ApJ, 581, 241
- Esteban, C., Peimbert, M., García-Rojas, J., Ruiz, M. T., Peimbert, A., & Rodríguez, M., 2004, MNRAS, 355, 229
- Esteban, C., García-Rojas, J., Peimbert, M., Peimbert, A., Ruiz, M.T., Rodríguez, M., & Carigi, L. 2005, ApJ618, 95
- Evans, C.J., Crowther, P.A., Fullerton, A.W., Hillier, D.J. 2004, ApJ, 610, 1021
- Ferland, G.J., Korista, K.T., Verner, D.A., Ferguson, J.W., Kingdon, J.B., Verner, E.M. 1998, PASP, 110, 761

- Ferland G.F. 2001, *PASP*, 113, 165
- Ferland G.F. 2003, *ARA&A*, 41, 517
- Gabler, R., Gabler, A., Kudritzki, R. P., Puls, J., & Pauldrach, A.W.A 1989, *A&A*, 226, 162
- Gagné, M., Caillault, J.P., Stauffer, J.R., et al. 1997, *ApJ*, 478, L87
- García, M. & Bianchi, L. 2004, *ApJ*, 606, 497
- García-Rojas, J., Esteban, C., Peimbert, M., Rodríguez, M., Ruiz, M. T., & Peimbert, A. 2004, *ApJS*, 153, 50
- García-Rojas, J., Esteban, C., Peimbert, A., Peimbert, M., Rodríguez, M., & Ruiz, M. T. 2005, *MNRAS*, in press
- Garnett, D.R., Dufour, R.J., Peimbert, M., Torres-Peimbert, S., Shields, G.A., Skillman, E.D., Terlevich, E., & Terlevich, R.J. 1995, *ApJ*, 449, 77
- Gies, D.R., Lambert, D.L. 1992, *ApJ*, 387, 673
- Gies, D.R., Mason, B.D., Hartkopf, W.I., et al. 1993, *AJ*, 106, 2072
- Giveon, U., Sternberg, A., Lutz, D., Feuchtgruber, H., & Pauldrach, A. W. A. 2002, *ApJ*, 566, 880
- Gray, D.F. 1973, *ApJ*, 184, 461
- Gray, D.F. 1976, *The observation and analysis of stellar photospheres*, New York, Wiley-Interscience.
- Gray, D.F. 1980, *PASP*, 92, 154
- Grevesse, N. & Sauval, A.J. 1998, *Space Sci. Rev.*, 85, 161
- Gummersbach, C.A., Kaufer, A., Schaefer, D.R., Szeifert, T., & Wolf, B. 1988, *A&A*, 338, 881
- Hardorp, J., Scholz, M. 1970, *ApJS*, 19, 193
- Henry, R.J.W. 1970 *AJ*, 161, 1153
- Herbig, G.H. 1995 *ARA&A*, 33, 19
- Herbig, G.H., & Terndrup, D.M. 1986, *ApJ*, 307, 609
- Herrero, A., Kudritzki, R.P., Vilchez, J.M., Kunze, D., Butler, K., & Haser, S. 1992, *A&A*, 261, 209
- Herrero, A., Puls, J., & Najarro, F. 2002, *A&A*, 396, 949
- Herrero, A. 2003, *ASPC*, 304, 10

- Herrero, A., Simón-Díaz, S., Najarro, F., et al. 2004, proceedings of the International Workshop on Massive Stars in interacting binaries (2004, Quebec, Canada), in press
- Herrero, A., & Najarro, F. 2005, proceedings of the Workshop on Stellar population (2005, Cancun, Mexico). Eds. D. Vals & M.Chávez, ASP, in press
- Hillenbrand L.A. 1997, *AJ*, 113, 1733
- Hillenbrand L.A., & Hartmann L.W. 1998, *ApJ*, 492, 540
- Hillier, D.J., & Miller, D.L. 1998, *ApJ*, 496, 407
- Hillier, D.J., Lanz, T., Heap, S.R., Hubeny, I., Smith, L.J., Evans, C.J., Lennon, D.J., & Bouret, J. C. 2003, *ApJ*, 588, 1039
- Howarth, I.D., Siebert, K.W., Hussain, G.A.J., Prinja, R.K. 1997, *MNRAS*, 284, 265
- Howarth, I.D., & Prinja, R.K. 1989, *ApJS*, 69, 527
- Howarth, I.D. 2004, proceedings of the IAU Symposium No. 215 on Stellar Rotation (2002, Cancun, Yucatan, Mexico). Eds. A. Maeder & P. Eenens. ASP, p.33
- Hubeny, I. 1988, *Computer Physics Comm.*, 52, 103
- Hubeny, I., & Lanz, T. 1992, *A&A*, 262, 501
- Hubeny, I., Lanz, T., & Jeffery, C.S. 1994, in *Newsletter on Analysis of Astronomical Spectra No. 20*. Ed. C.S. Jeffery, St. Andrews University, p. 30
- Hubeny, I., & Lanz, T. 1995, *ApJ*, 39, 875
- Hunter, I., Dufton, P.L., Ryans, R.S.I., Lennon, D.J., Rolleston, W.R.J., Hubeny, I., & Lanz, T. 2005, *A&A*, 436, 687
- Humphreys, R. 1978, *ApJS*, 38, 309
- Israel, F.P. 1978, *A&A*, 70, 769
- Jamet, L., Pérez, E., Cerviño, M., Stasińska, G., González-Delgado, R.M., & Vílchez, J.M. 2004, *A&A*, 426, 399
- Kane, L., McKeith, C.D., & Dufton, P.L. 1980, *A&A*, 84, 115
- Kennicutt, R.C., Jr., Bresolin, F., & Garnett, D.R. 2003, *AJ*, 591, 801
- Kilian, J., Becker, S.R., Gehren, T., et al. 1991, *A&A*, 244, 419
- Kilian, J. 1992, *A&A*, 262, 171
- Kilian, J. 1994, *A&A*, 282, 867
- Kobulnicky, H.A., Kennicutt, R.C., Jr., & Pizagno, J.L. 1999, *ApJ*, 514, 544

- Korn, A.J., Becker, S.R., Gummersbach, C.A., & Wolf, B. 2000, *A&A*, 353, 665
- Korn, A.J., Keller, S.C., Kaufer, A., Langer, N., Przybilla, N., Stahl, O., & Wolf, B. 2002, *A&A*, 385, 143
- Kubát, J., Puls, J., & Pauldrach, A.W.A. 1999, *A&A*, 341, 587
- Kudritzki, R.P., Pauldrach, A., Puls, J., & Abbott, D.C. 1989, *A&A*, 219, 205
- Kudritzki, R.P., & Puls, J. 2000, *ARA&A*, 38, 613
- Kukarkin, B.V., Kholopov, P.N., Pskovsky, Y.P., Efremov, Y.N., Kukarkina, N.P., Kurochkin, N.E., & Medvedeva, G.I. 1971, *General Catalogue of Variable Stars*, 3rd ed.
- Kunze, D., Kudritzki, R.P., & Puls, J. 1992, in "The Atmospheres of Early Type stars", Eds. U. Heber, C.S. Jeffery, *Lecture Notes in Physics* 401, Springer-Verlag, p. 45.
- Kunze, D. 1994, PhD thesis, Ludwig Maximilians Universität, Munich, Germany
- Kurucz, R.L. 1979, *ApJS*, 40,1
- Kurucz, R.L. 1991, in "Stellar Atmospheres: Beyond Classical Models", NATO ASI Series C, Vol 341, Eds. L. Crivellari, I. Hubeny, D.G. Hummer, p 441
- Kurucz, R.L. 1992, *AAS*, 180, 3202
- Lanz, T., & Hubeny, I. 2003, *Stellar Atmosphere Modeling*, ASP Conference Proceedings, Vol. 288. Abstracts from a conference held 8-12 April 2002 in Tuebingen, Germany. Eds. I. Hubeny, D. Mihalas, & K. Werner. ASP, p.117
- Lanz, T., & Hubeny, I. 2003, *ApJS*, 146, 417
- Lennon, D.J., Becker, S.T., Butler, K., Eber, F., Groth, H. G., Kunze, D., Kudritzki, R.-P. 1991, *A&A*, 252, 498
- Lenorzer, A., Mokiem, M.R., de Koter, A., & Puls, J. 2004, *A&A*, 422, 275
- Lee, J.-K., Rolleston, W.R.J., Dufton, P.L., & Ryans, R.S.I. 2005, *A&A*, 429, 1025
- Liu, X.W. 2002, *RMxAA*, 12, 70
- Liu, X.W. 2003, in Sutherland, R., Kwok, S., Dopita, M.A., eds. *Procs. IAU Symp. 209*, ASP, 339
- Lohsen, E. 1975, *IBVS*, 988, 1
- Lucy, L.B., & Solomon, P.M. 1970, *ApJ*, 159, 879
- Luridiana, V., Peimbert, M., & Leitherer, C. 1999, *ApJ*, 527, 110
- Maeder, A., & Meynet, G. 2000, *ARA&A*, 38, 143

- Martin, J.C. 2004, AJ, 128, 2474
- Martins, F., Schaerer, D., Hillier, D.J., & Heydari-Malayeri, M. 2004, A&A, 420, 1087
- Martins, F., Schaerer, D., & Hillier, D.J. 2002, A&A, 382, 999
- Martins, F., Schaerer, D., & Hillier, D.J. 2005, A&A, in press
- Massey P., Bresolin F., Kudritzki R.P., Puls J., Pauldrach A.W.A. 2004, ApJ, 608, 1001
- Mathis, J.S., & Rosa, M.R. 1991, A&A, 245,6225
- Matthews T.A., & Sandage A.R. 1963, ApJ, 138, 30
- McErlean, N.D., Lennon, D.J., & Dufton, P.L. 1999, A&A, 349, 553
- McGaugh, S.S. 1994, ApJ, 426, 135
- McNamara, D.H., & Larsson H.J. 1962, ApJ, 135, 748
- Mendoza, C., & Zeppen, C. J. 1983, MNRAS, 202, 981
- Meynet G., & Maeder A. 2003, A&A, 404, 975
- Mihalas., D. & Auer L.H. 1970, ApJ, 160, 1161
- Monteverde, M.I., Herrero, A., Lennon, D.J., & Kudritzki, R.-P. 1997, ApJ, 474, 107
- Monteverde, M.I. & Herrero, A. 1998, ApJS, 263, 171
- Monteverde, M.I., Herrero, A., & Lennon, D.J. 2000, ApJ, 545, 813
- Moore, C.E. 1971, *Atomic energy levels, Vol 1*, NSRDS-NBS 35, Washington, U.S. Dept. of Commerce
- Morisset, C., Schaerer, D., Martín-Hernández, N. L., Peeters, E., Damour, F., Baluteau, J.-P., Cox, P., & Roelfsema, P. 2002, A&A, 386, 558
- Morisset, C., Schaerer, D., Bouret, J.-C., & Martins, F. 2004, A&A, 415, 577
- Morisset, C., Stasińska, G., & Peña, M., 2005, MNRAS, 360, 499
- Nahar, S.N. 2003, Stellar Atmosphere Modeling, ASP Conference Proceedings, Vol. 288. Abstracts from a conference held 8-12 April 2002 in Tuebingen, Germany. Eds. I. Hubeny, D. Mihalas, & K. Werner. ASP, p.651
- Najarro, F., Kudritzki, R.P., Cassinelli, J.P., Stahl, O., & Hillier, D.J. 1996, A&A, 306, 892
- Najarro, F., Figer, D.F., Hillier, D.J., & Kudritzki, R.P. 2004, ApJ, 611, 105
- Oey, M.S., & Kennicutt, R.C., Jr. 1997, MNRAS, 291, 827

- Oey, M.S., Dopita, M.A., Shields, J.C., & Smith, R.C. 1999, *ApJS*, 128, 511
- Oey, M.S., & Shields, J.C. 2000, *ApJ*, 539, 687
- O'Dell, C.R. 2001, *PASP*, 113, 290
- Osterbrock, D.E. 1989, *Astrophysics of Gaseous Nebulae and Active Galactic Nuclei* (Mill Valley: University Science Books)
- Osterbrock, D.E., Tran, H.D., Veilleux, S. 1992, *ApJ*, 389, 305
- Pagel, B. E. J., Edmunds, M. G., Blackwell, D. E., Chun, M. S., Smith, G. 1979, *MNRAS*, 189, 95
- Palla, F., & Stahler, S.W. 1999, *ApJ*, 525, 772
- Pauldrach, A.W.A., Puls, J., & Kudritzki, R.-P. 1986, *A&A*, 164, 86
- Pauldrach, A.W.A., Lennon, M., Hoffmann, T.L., Sellmaier, F., Kudritzki, R.-P., & Puls, J. 1998, *ASPC*, 131, 258
- Pauldrach, A.W.A., Hoffmann, T.L., Lennon, M. 2001, *A&A*, 375, 161
- Penny, L. R. 1996, *ApJ*, 463, 737
- Peña, M., Stasińska, G., Esteban, C., Koesterke, L., Medina, S., & Kingsburgh, R. 1998, *A&A*, 337, 866
- Peimbert, M. 1967, *ApJ*, 150, 825
- Peimbert, M. & Torres-Peimbert, S. 1977, *MNRAS*, 179, 217
- Peters, G.J., & Polidan, R.S. 1985, *IAUS*, 111, 417
- Pilyugin, L. S. 2000, *A&A*, 362, 325
- Pilyugin, L. S. 2001, *A&A*, 369, 594
- Pilyugin, L. S. 2003, *A&A*, 401, 557
- Preibisch, T., Balega, Y., Hofmann, K.H., Weigelt, G., & Zinnecker, H. 1999, *NewA*, 4, 531
- Przybilla, N., & Butler, K. 2004, *ApJ*, 609, 1181
- Puls, J., Kudritzki, R.-P., Herrero, A., Pauldrach, A.W.A., Haser, S.M., Lennon, D.J., Gabler, R., Voels, S.A., Vilchez, J.M., Wachter, S., & Feldmeier, A. 1996, *A&A*, 305, 171
- Puls, J., Urbaneja, M.A., Venero, R., Repolust, T., Springmann, U., Jokuthy, A., & Mokiem, M.R. 2005, *A&A*, submitted
- Rauch, T., & Deetjen, J.L. 2003, *Stellar Atmosphere Modeling*, ASP Conference Proceedings, Vol. 288. Abstracts from a conference held 8-12 April 2002 in Tuebingen, Germany. Eds. I. Hubeny, D. Mihalas, & K. Werner. ASP, p.103

- Reiners, A., & Schmitt, J., H., M., M. 2003, *A&A*, 398, 647
- Relaño, M., Peimbert, M., & Beckmann, J.E. 2002, *ApJ*, 564, 704
- Rix, S.A., Pettini, M., Leitherer, C., Bresolin, F., Kudritzki, R.-P., & Steidel, C.C. 2004, *ApJ*, 615, 98
- Repolust, T., Puls, J., & Herrero, A. 2004, *A&A*415, 349
- Rodríguez, M. 1998, "La abundancia de Hierro en regiones HII galácticas", thesis, University of La Laguna
- Rodríguez, M. 1999, *A&A*351, 1075
- Rodríguez, M. 2002, *A&A*389, 556
- Rolleston, W.R.J., Brown, P.J.F., Dufton, P.L., & Howarth, I.D. 1996, *A&A*, 315, 95
- Rolleston, W.R.J., Smartt, S. J., Dufton, P.L., & Ryans, R.S.I. 2000, *A&A*, 363, 585
- Royer, F., Gerbaldi, M., Faraggiana, R., & Gómez, A. E. 2002a, *A&A*, 381, 105
- Royer, F., Grenier, S., Baylac, M.-O., Gómez, A. E., & Zorec, J. 2002b, *A&A*, 393, 897
- Rubin, R.H., Simpson, J.P., Haas, M.R., Erickson, E.F. 1991, *ApJ*, 374, 564
- Rubin, R. H., Dufour, R. J., & Walter, D. K. 1993, *ApJ*, 413, 242
- Ryans, R.S.I., Dufton, P.L., Rolleston, W.R.J., Lennon, D.J., Keenan, F.P., Smoker, J.V., Lambert, D.L. 2002, *MNRAS*, 336, 577
- Salpeter, E. E. 1955, *ApJ*, 121, 161
- Santolaya-Rey, A. E., Puls, J., & Herrero, A. 1997, *A&A*, 323, 488
- Sellmaier, F., Yamamoto, T., Pauldrach, A.W.A., & Rubin, R.H. 1996, *A&A*, 305, L37
- Schaerer & de Koter 1997, *A&A*, 322, 598
- Schaller, G., Schaerer, D., Meynet, G., & Maeder, A. 1992, *A&AS*, 96, 269
- Schönberner, D., Herrero, A., Becker, S., Eber, F., Butler, K., Kudritzki, R.P., & Simon, K. P. 1988, *A&A*, 197, 209
- Shaver, P.A., McGee, R.X., Newton, L.M., Danks, A.C., & Pottasch, S.R. 1983, *MNRAS*, 204, 53
- Simón-Díaz, S., Herrero, A., & Esteban, C. 2003, *RMxAC* 18, 123
- Simón-Díaz, S., Herrero, A., Esteban, C., & Najarro, F. 2005, *A&A*, submitted

- Simpson, J.P., Rubin, R.H., Erickson, E.F., Haas, M. R 1998, ApJ, 311, 895
- Skillman, E. D. 1989, ApJ, 347, 883
- Smartt, S.J., Dufton, P.L., & Rolleston, W.R.J. 1996, A&A, 310, 123
- Smartt, S.J., & Rolleston, W.R.J. 1997, ApJ, 481, 47
- Smartt, S. J., Venn, K.A, Dufton, P.L., Lennon, D.J., Rolleston, W.R.J., & Keenan, F.P. 2001, A&A, 367, 86
- Smartt, S.J., Crowther, P.A., Dufton, P.L., Lennon, D.J., Kudritzki, R.P., Herrero, A., McCarthy, J.K., Bresolin, F. 2001, MNRAS, 325, 257
- Smith, J., Harper, D.A., & Loewenstein, R.F. 1987, 314, 76
- Smith, L.J.; Norris, R.P.F. & Crowther, P.A. 2002, MNRAS, 337, 1309
- Smith, M. A. 1976, ApJ, 208, 487
- Stahl, O., Wolf, B., Gäng, Th., et al. 1993, A&A, 274, L29
- Stahl, O., Kaufer, A., Rivinius, T., et al. 1996, A&A, 312, 539
- Stasińska, G. 1990, A&AS, 83, 501
- Stasińska, G., & Leitherer, C. 1996, ApJS, 107, 661
- Stasińska, G., & Schaerer, D. 1997, A&A, 322, 615
- Stasińska, G., & Schaerer, D. 1999, A&A, 351, 72
- Stasinska, G., & Izotov, Y. 2003, A&A, 297, 71
- Stasinska, G. 2002, RMxAA, 12, 70
- Stasińska, G. 2004, lectures on Cosmochemistry. The melting pot of the elements. XIII Canary Islands Winter School of Astrophysics, (Tenerife, Spain), November 19-30, 2001, Eds. C. Esteban, R. J. García López, A. Herrero & F. Sánchez. Cambridge contemporary astrophysics. Cambridge, UK: Cambridge University Press, 2004, p. 115 - 170
- Stasińska, G. 2005, A&A, 434, 507
- Subrahmanyam, R. 1992, MNRAS, 254, 719
- Tenorio-Tagle, G. 1979, A&A, 71, 59
- Thum, C., Lemke, D., Fahrback, U., & Frey, A. 1978, A&A, 65, 207
- Torres-Peimbert, S., & Peimbert, M. 1977, RMxAA, 2, 181
- Torres-Peimbert, S., & Peimbert, M. 2003, in Sutherland, R., Kwok, S., Dopita, M.A., eds. Procs. IAU Symp. 209, ASP, 339

- Trundle, C., Dufton, P.L., Lennon, D.J., Smartt, S.J., & Urbaneja, M.A. 2002, *A&A*, 395, 519
- Trundle, C. 2004, "Spectroscopic studies of the atmospheres and winds of B- type supergiants", thesis, Queens University of Belfast 217
- Trundle, C., Lennon, D.J., Puls, J., & Dufton, P.L. 2004, *A&A*, 417, 217
- Trundle, C., & Lennon, D.J. 2005, *A&A*, 434, 677
- Urbaneja, M.A., Herrero, A., Bresolin, F., Kudritzki, R.-P., Gieren, W., & Puls, J., 2003, *ApJ* 584, 73
- Urbaneja, M.A. 2004, "B Supergiants in the Milky Way and nearby galaxies: models and quantitative spectroscopy", thesis, University of La Laguna
- Urbaneja, M.A., Herrero, A., Bresolin, F., Kudritzki, R.P., Gieren, W., Puls, J., Przybilla, N., Najarro, F., & Pietrzynski, G. 2005a, *ApJ*, 622, 826
- Urbaneja, M.A., Herrero, A., Kudritzki, R.P., Najarro, F., Smartt, S.J., Puls, J., Lennon, D.J., & Corral, L.J. 2005b, *ApJ*, submitted
- Vacca W.D., Garmany C.D., & Shull J.M. 1996, *ApJ*, 460, 914
- Venn, K.A., McCarthy, J.K., Lennon, D.J., Przybilla, N., Kudritzki, R.P., & Lemke, M. 2000, *ApJ*, 541, 610
- Venn, K.A., Brooks, A.M., Lambert, D.L., Lemke, M., Langer, N., Lennon, D.J., & Keenan, F.P. 2002, *ApJ*, 565, 571
- Vilchez, J.M., & Esteban, C. 1996, *MNRAS*, 280, 720
- Vilchez, J.M., Pagel, B.E.J., Díaz, A.I., Terlevich, E., & Edmunds, M.G. 1988, *MNRAS*, 235, 633
- Villamariz, M.R., & Herrero, A. 2000, *A&A*, 357, 597
- Villamariz, M.R., Herrero, A., Becker, S.R, & Butler, K. 2002, *A&A*, 388, 940
- Walborn, N.R. 1972a, *AJ*, 77, 312
- Walborn, N.R. 1972b, *ApJ*, 176, 119
- Walborn, N.R., & Nichols, J.S. 1994, *ApJ*, 425, L29
- Walborn, N.R., Howarth, I.D., Herrero, A., & Lennon, D.J. 2003, *ApJ*, 617, 61
- Walborn, N.R., & Fitzpatrick, E.L. 1990, *PASP*, 102, 379
- Wilson, N.J., & Bell, K.L. 2002, *MNRAS*, 331, 389
- Zurita, A., Rozas, M., & Beckmann, J. 2000, *A&A*, 363, 9